Datura Stramonium Leaf Extract Mediated Co_3O_4@ZnO, Co_3O_4@NiO, and Co_3O_4@CuO Core-Shell Nanostructures: Investigation of their Anticancer, Antibacterial, and Antioxidant Activities

Gezahegn Tadesse Ayanie

A Dissertation Submitted to

The Department of Applied Chemistry

College of Applied Natural Science

Presented in Partial Fulfillment of the Requirement for the Degree of Doctor of Philosophy in Bioinorganic Chemistry

Office of Postgraduate Studies

Adama Science and Technology University

December, 2024

Adama, Ethiopia

Datura Stramonium Leaf Extract Mediated Co_3O_4@ZnO, Co_3O_4@NiO, and Co_3O_4@CuO Core-Shell Nanostructures: Investigation of their Anticancer, Antibacterial, and Antioxidant Activities

Gezahegn Tadesse Ayanie

Supervisors:

Main Supervisor: Prof. Tegene Desalegn

Co-Supervisor: Prof. H C Ananda Murthy

A Dissertation Submitted to

The Department of Applied Chemistry

College of Applied Natural Science

Presented in Partial Fulfillment of the Requirement for the Degree of Doctor of Philosophy in Bioinorganic Chemistry

Office of Postgraduate Studies

Adama Science and Technology University

November, 2024

Adama, Ethiopia

DECLARATION

I hereby declare that this Dissertation entitled '***Datura Stramonium*** **Leaf Extract Mediated Co_3O_4@ZnO, Co_3O_4@NiO, and Co_3O_4@CuO Core-Shell Nanostructures: Investigation of their Anticancer, Antibacterial, and Antioxidant Activities**' is my original work. It has not been submitted for the award of any academic degree, diploma, or certificate in any other university. All sources of materials used for this dissertation have been duly acknowledged through appropriate citations.

Gezahegn Tadesse Ayanie _____ _____

Name of student Signature Date

APPROVAL OF SUPERVISORS

We hereby certify that the dissertation entitled '***Datura Stramonium*** **Leaf Extract Mediated Co_3O_4@ZnO, Co_3O_4@NiO, and Co_3O_4@CuO Core-Shell Nanostructures: Investigation of their Anticancer, Antibacterial, and Antioxidant Activities'** submitted in partial fulfillment of the requirements for the degree of Doctor of Philosophy in Bioinorganic chemistry, the Graduate program of the Department of Applied Chemistry, and has been carried out by Gezahegn Tadesse Ayanie, ID. No PGR19466/12 under our supervision. Therefore, we recommend that the student fulfill the requirements and hence hereby he can submit the dissertation to the department.

Prof. Tegene Desalegn	_____	_____
Main Supervisor	Signature	Date
Prof. H C Ananda Murthy	_____	_____
Co-supervisor	Signature	Date

APPROVAL SHEET OF BOARD OF EXAMINERS FOR DISSERTATION

We hereby certify that the recommendation and suggestion made by the board of examiners are appropriately incorporated into the final PhD Dissertation entitled "***Datura Stramonium* Leaf Extract Mediated Co_3O_4@ZnO, Co_3O_4@NiO, and Co_3O_4@CuO Core-Shell Nanostructures: Investigation of their Anticancer, Antibacterial, and Antioxidant Activities**" by Gezahegn Tadesse.

Prof. Tegene Desalegn (PhD)		
Supervisor	Signature	Date
Prof. H C Ananda Murthy (PhD)	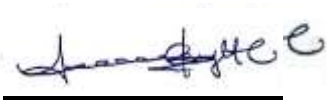	
Co-supervisor	Signature	Date

We, the undersigned, members of the board of examiners of the final open defense by **Gezahegn Tadesse** have read and evaluated his dissertation entitled "***Datura Stramonium* Leaf Extract Mediated Co_3O_4@ZnO, Co_3O_4@NiO, and Co_3O_4@CuO Core-Shell Nanostructures: Investigation of their Anticancer, Antibacterial, and Antioxidant Activities**" and examined the candidate. This is, therefore, to certify that the dissertation has been accepted in partial fulfillment of the requirement for the Degree of Doctor of Philosophy in Bioinorganic Chemistry.

Dr. Defaru Negera (PhD)		
Chairperson	Signature	Date
Dr. Fedlu Kedir (PhD)		
Internal Examiner	Signature	Date
Dr. Enyew Amare (PhD)		
Internal Examiner	Signature	Date
Prof. Sisay Tadesse (PhD)		
External Examiner	Signature	Date

Dr. Negash Getachew (PhD)  _____

External Examiner Signature Date

Final approval and acceptance of the dissertation is contingent upon submission of its final copy to the Office of Postgraduate Studies (OPGS) through the Department Graduate Council (DGC) and College Graduate Committee (CGC).

Department Head	Signature	Date
College Dean	Signature	Date
Office of Postgraduate Studies, Dean	Signature	Date

ACKNOWLEDGEMENTS

First and foremost, I am grateful to my main supervisor Prof. Tegene Desalegn, and co-supervisor Prof. H C Ananda Murthy for their comprehensive guidance and mentorship from the beginning to the end of the work. I would like to acknowledge Ethiopian Ministry of Education (MoE) for financial support. I would like to thank the Department of Applied Chemistry, the Department of Material Science and Engineering, and the Department of Applied Biology of Adama Science and Technology University for laboratory provision, characterization, and for the measurement of anticancer, antibacterial, and antioxidant activities.

My gratitude goes to Bahir Dar University for the TGA-DTA analysis and Ethiopia Leather Industry for the FT-IR and XRD characterization. Furthermore, I would like to thank Dr. Lemma Teshome Tufa for characterizing my samples using SEM, EDX, TEM/HR-TEM/SAED and STEM at the Department of Chemistry, Chemistry Engineering and Applied Chemistry, Chungnam National University, Daejeon 34134, Republic of Korea, C. R. Ravikumar for SEM, TEM/HR-TEM characterization at Research Centre, Department of Science, East West Institute of Technology, Bangalore 560091, Karnataka, India.

I also thank Mr. Addisalem Abebe and his staff for their kind support for anticancer test and SEM, TEM/HR-TEM, and UV-Vis characterization at the School of Chemical Science, Indian Institute of Technology (IIT), Mandi, H.P. India.

Besides, I appreciate the entire academic and research assistant of the Department of Applied Chemistry, College of Natural Science, Adama Science and Technology University for their continued and friendly assistance throughout my work.

Furthermore, I am grateful to all academic and research assistants of the Department of Applied Chemistry, College of Natural Science, Adama Science and Technology University, for their ongoing and courteous cooperation during my research.

Finally, I would like to thank my wife Almaz Tsegaye and my partner Medehen Abera has all been financially and psychologically supportive of me throughout.

TABLE OF CONTENTS

Table of Contents

LIST OF TABLES

LIST OF FIGURES

LIST OF ABBREVIATIONS AND ACRONYMS

A549	Human lung adenocarcinoma
Caco-2	Human colon adenocarcinoma
CCD-112	Human colon fibroblast cell
CDK1/2	Cyclin-dependent kinase 1/2
CSNs	Core-shell nanostructure
DMEM	Dulbecco's Modified Eagle Medium
DMSO	Dimethylsulfoxide
DNA	Deoxyribonucleic acid
DPPH	2,2-diphenyl-1-picrylhydrazyl
DTA	Differential thermal Analysis
EDX	Energy Dispersive X-ray analysis
ER	Estrogen receptor
FBS	Fetal Bovine Serum
FDA	Food and Drug Administration
FFT	Fast Fourier Transform
FT-IR	Fourier Transform Infrared Spectroscopy
FWHM	Full Width at Half Maximum
HCT-116	Human colorectal cancer cell-116
HDF	Human Dermal Fibroblast
HEK-293	Human Embryonic Kidney-293
Hep-G2	Human liver cancer cell
HER2	Human epidermal growth factor receptor 2
HFF	Human Foreskin Fibroblast
HR-TEM	High Resolution Transmission Electron Microscopy
HT-29	Colon cancer cell
hTERT	Human Telomerase Reverse Transcriptase
IC_{50}	Half-maximal inhibitory concentration
IFFT	Inverted Fast Fourier Transform
LSPR	Localized surface plasmon resonance
MCF-7	Michigan Cancer Foundation-7

MONPs	Metal oxide nanoparticles
MTT	Dimethyl thiazolyl diphenyl tetrazolium
MTX	Methotrexate
NADPH	Nicotinamide adenine dinucleotide phosphate
NPs	Nanoparticles
OD	Optical density
PBMC	Peripheral blood mononuclear cells
PEG	Polyethylene Glycol
PR	progesterone receptor
PVP	Polyvinylpyrrolidone
RBCs	Red blood cells
ROS	Reactive oxygen species
SAED	Selected Area Electron Diffraction
SEM	Scanning Electron Microscopy
TEM	Transmission Electron Microscopy
TGA	Thermal Gravimetric Analysis
TNBC	Triple-negative breast cancer
UV-Vis	UV-Visible spectroscopy
WHO	World Health Organization
XRD	X-ray Diffraction

ABSTRACT

Investigating potent anticancer, antibacterial, and antioxidant core-shell nanostructures (CSNs) using the green method is highly preferred as it is an environmentally friendly approach. In this work, Co_3O_4@ZnO (CZ), Co_3O_4@NiO (CN), and Co_3O_4@CuO (CC) CSNs, as well as Co_3O_4, ZnO, NiO, and CuO metal oxide nanoparticles (MONPs) were synthesized employing D. stramonium leaf extract. The XRD confirmed the formation of the cubic Co_3O_4, hexagonal wurtzite ZnO, face-centered cubic NiO, and monoclinic CuO MONPs, as well as cubic-hexagonal CZ, cubic-face-centered cubic CN, and cubic-monoclinic CC CSNs. The average crystallite size of Co_3O_4(11), ZnO(11), NiO(11), and CuO(11) MONPs was found to be 11, 17, 12, and 13 nm, whereas CZ(11), CN(11), and CC(11) CSNs were 22, 13, and 15 nm, respectively. The diffraction peaks of the core and shell were slightly shifted, which suggests the formation of core-shell nanostructures. The spherical CZ, prismatic CN, and cylindrical CC CSNs with particle sizes of 21.1, 16.99, and 11.07 nm were revealed from TEM analysis, respectively. Additionally, the HR-TEM image reveals a less-contrast shell enclosing a dark core, and lattice fringes are found in both regions. The polycrystalline nature of CZ, CN, and CC CSNs was also revealed from SAED analysis. The in vitro cytotoxicity of CZ, CN, and CC CSNs and the Epirubicin drug against MCF-7 cancer cells at 800 µg/mL were found to be 95.22, 81.38, 97.72, and 96.15%, whereas against PBMC they were 66.44, 51.94, 62.43, and 65.18%, respectively. The CC CSNs showed stronger anticancer activity even than the Epirubicin drug with less cytotoxicity. The IC_{50} of CZ, CN, and CC CSNs was revealed to be about 18.3, 21.25, and 17.8%, respectively. The in vitro antibacterial activity of Co_3O_4(11), ZnO(11), NiO(11), and CuO(11) NPs against S. aureus showed IC_{50} values of 22.22, 18.36, 28.55, and 17.21 µg/mL and against E. coli were 33.3, 27, 36, and 26 µg/mL, respectively. The low IC_{50} of CuO(11) NPs indicates the high inhibition activity of CuO NPs in contrast to the other. CZ, CN, and CC CSNs showed IC50s of 11.6, 23.46, and 14 µg/mL against S. aureus, but 17.55, 26, and 21.76 µg/mL against E. coli, respectively. The percentage scavenging activity of Co_3O_4, ZnO, NiO, and CuO NPs and CZ, CN, and CC CSNs against DPPH radical at 500 µg/mL were 63.308, 75.385, 57.0769, 74.872, 86.87, 65.98, and 76.32%, respectively. *As a result, CSNs exhibit stronger antibacterial and antioxidant activity than corresponding individual MONPs due to basic features and synergistic effects within the core-shell structure.*

Keywords: Antibacterial, Anticancer, Antioxidant, Core-shell, *Datura stramonium*

1. INTRODUCTION

1.1. Background of the Study

Nowadays, cancer, bacterial infection, and oxidative stress are being reported to be among major health challenges worldwide. Cancer is non-communicable disease caused by physicochemical and biological carcinogenic interactions with the human body cells that cause genetic change and result in uncontrolled growth of abnormal cells (S. Khan *et al*., 2015, Mousa *et al*., 2023). It is the second most protruding cause of death in the world next to cardiovascular disease. In a cancerous cell, the abnormal cells invade the healthy parts of the body and are capable of altering the biochemical and cellular functions and finally causing death. In 2019, about 18 million new cases of cancer and 8.8 million with a death rate of 15.7% were reported (Hussain *et al*., 2019, Siegel *et al*., 2022). Additionally, the World Health Organization (WHO) report shows that cancer is expected to rise from 14 million in 2012 to 22 million deaths in the coming 20 years (Al-Sheddi *et al*., 2018, Nabil *et al*., 2020). The most common cancer diseases that cause an increment in the number of deaths per year are lung cancer, colon cancer, bladder cancer, breast cancer, colorectal cancer, kidney cancer, prostate cancer, and pancreatic cancer. Of these cancer diseases, breast cancer is the second leading cause of cancer death among women (Pugazhendhi *et al*., 2019, Aboeita *et al*., 2022).

In 2020, the International Agency for Research on Cancer, WHO reported about 2.26 million new cases of breast cancer worldwide which became the most common cancer by replacing lung cancer. As mentioned in some reports, the preference used for the prevalence rate of breast cancer increased from 16.7 to 33.6 per 100,000 women in 2000 and 2009, respectively. As per the report of 2018, out of 2.1 million cancer deaths worldwide, 6.6% of deaths are due to breast cancer (Abu‐Serie & Eltarahony, 2021, Vinardell & Mitjans, 2015, Mubarik *et al*., 2022). Additionally, breast cancer caused 685,000 deaths in women in 2020 worldwide. Furthermore, the report of WHO indicated that about 1.7 million new cases of breast cancer recorded in 2015 are expected to double in 2030 (Torres-Román *et al*., 2023). Due to this, several therapies such as chemotherapy, radiotherapy, proton beam therapy, hormone therapy, targeted drug therapy, clinical trials, immunotherapy, etc. have been used to medicate this devastating disease, that causes so much suffering (Tao *et al*., 2021, Perumal *et al*., 2024 , Aboeita *et al*., 2022, J. Wang *et al*., 2017, Wang *et al*., 2017, Mousa *et al*., 2023, van Beek *et al*., 2021, Van den Bosch *et al*.,

2021). However, these treatment methods have significant adverse effects on normal cells with limited efficacy, toxic and non-selective toward cancerous cells (Nagajyothi, Pandurangan, *et al*., 2017, Zubair *et al*., 2021).

Therefore, it is imperative to develop a potent, high efficacy, non-toxic, cost effective, selective, and biocompatible drug for breast cancer treatment (Amina *et al*., 2020, Y. Huang *et al*., 2023). In the treatment of breast cancer, the most challenging problem is the side effects of therapies that caused due to the difficulties in differentiating cancerous and normal cells which lead to systematic toxicity. The researchers explore new strategies that led to several promising results with their activity in the diagnosis and treatment of breast cancer (Raj Preeth *et al*., 2019). The advanced and effective strategy for breast cancer treatment is nanoparticles (NPs) that have been developed for cancer treatment for the last three decades. The nanoparticles-based systems, with high biocompatibility, easy surface functionalization, cancer targeting and drug delivery capacity, have demonstrated the potential to overcome these side effects. Among these, metal oxide nanoparticles (MONPs) find significant biomedical applications such as drug delivery, gene therapy, biomarker mapping, targeted therapy, and molecular imaging in the treatment of cancer with minimum side effects (Arsalan *et al*., 2020, Vinardell & Mitjans, 2015, Shalaby *et al*., 2022). The anticancer activity of MONPs such as Co_3O_4 (S. A. Khan *et al*., 2021), Fe_2O_3 (Ramalingam *et al*., 2020, Shanmugasundaram *et al*., 2018, TiO_2 (Maheswari *et al*., 2020), ZnO (Al-Enazi *et al*., 2023), CuO (Elsayed *et al*., 2021), Cu/CuO (Abu‐Serie & Eltarahony, 2021), NiO (Kganyago *et al*., 2018), and TiO_2/ZnO (Chakra *et al*., 2017) have been widely examined.

The other serious public health challenge that emerged over recent years around the world is bacterial infectious diseases. Bacterial infectious diseases are caused by various harmful bacteria strains mainly food pathogens, such as *Escherichia coli*, *Staphylococcus aureus*, *Pseudomonas aeruginosa*, *Shigella flexneri*, *Enterococcus faecalis*, *Salmonella* types, and *Clostridium perfringens* (Sirelkhatim *et al*., 2015, Hussain *et al*., 2019). A variety of antibiotic drugs are being used to treat the infectious diseases caused by these strains. Antibiotics such sulphonamides (Kim *et al*., 2019), β-lactams (Rabiei *et al*., 2020), aminoglycosides (Huth *et al*., 2011), tetracyclines (Jabeen *et al*., 2011), lincosamides (Ahmadi *et al*., 2021) and streptogramins (Johnston *et al*., 2005) are commonly used for bacterial infection treatment. However, some bacteria have developed resistance to these drugs. Antibiotic resistance occurs when the

medication loses its efficiency in killing bacteria and the bacteria keep growing and cause infection. According to the data from WHO, closely about 80% of bacterial drug-resistivity is developed because of overuse, improper use, availability of new antibiotics, and the emergence of new bacterial gene mutations (Rajeshkumar *et al*., 2019, Dubale *et al*., 2023). The morbidity and mortality due to infection caused by multidrug-resistant bacteria increased from time to time. The report showed that the mortality due to infection caused by multidrug-resistant bacteria in 2019 was found to be approximately 5.0 million people (Alavi *et al*., 2022, Barzan *et al*., 2022). Similarly, some studies also showed that drug-resistant bacterial infection caused about 3.0 million and 10 million deaths in developing countries and some tropical countries annually, respectively (Rezk *et al*., 2022).

Among multidrug-resistant bacteria, the Gram-negative bacteria (*E. coli* and *P. aeruginosa*) and gram-positive (S. *aureus* and S. *pyogenes)* have the potential and still cause infection even in the presence of antibacterial drugs (Slavin *et al*., 2017). Due to this, searching for a potential and effective antibacterial agent becomes a serious assignment to work on for researchers all over the world. In recent studies, the antibacterial activities of different metal based nanoparticles (NPs) have been investigated. Among several nanoparticles metal oxide nanoparticles (MONPs) and their composites have become the most promising agents in addressing the antibacterial resistance (Lizundia *et al*., 2020, Dinga *et al*., 2022).

The MONPs have the ability to inhibit the growth of a wide range of Gram-positive and Gram-negative bacteria than other organic NPs due to their durability, high stability, and low mammalian cell toxicity. Some of the MONPs that are capable of combatting bacteria include ZnO (Ogunyemi *et al*., 2019), Ag_2O (Manikandan *et al*., 2017), CuO, Cu_2O (Nagaraj *et al*., 2019), NiO (Hafeez *et al*., 2021), Ti_2O (Aravind *et al*., 2021), WO_3 (Habtemariam, 2021), Al_2O_3 (Ansari *et a*l., 2015) and Co_3O_4 (Hafeez *et al*., 2020) which were examined in the last few decades for both gram-negative and Gram-positive bacteria (De Souza *et al*., 2019, Arsalan *et al*., 2020, Hariharan *et al*., 2017). Mixed metal oxide nanostructures such as CuZnFe (Alzahrani *et al*., 2018), ZnO/SiO_2 (Grigorie *et al*., 2017), ZrO_2/ZnO (Uribe López *et al*., 2019), Fe_2O_3/ZnO (Nabil *et al*., 2020) and ZnO-NiO-CuO (Alqarni *et al*., 2022) were also investigated to possess the potential to reduce cytotoxic effect of monoxide nanoparticles and the ability to inhibit bacterial growth (Asamoah *et al*., 2020).

In addition to cancer and bacterial infection diseases, the global population is confronted with oxidative stress as another health challenge caused by excessive production of reactive oxygen species (ROS) in cells. In normal cellular metabolism, ROS such as superoxide radical ($O_2^{\cdot-}$), hydroxyl radical ($^{\cdot}OH$), singlet oxygen ($^1O_2$), and hydrogen peroxide (H_2O_2) are formed as a byproduct that has a significant role in cell signaling and homeostasis (Slavin & Bach, 2022, S. Yang & Lian, 2020). During times of environmental stress such as high temperature, drought, salinity, chemo-toxicity, radiation, and microbial attack reactive oxygen species are excessively produced. In normal cellular metabolism, the generated ROS are scavenged by natural antioxidants such as superoxide dismutase, catalase, and peroxiredoxins to prevent oxidative damage (Tavassolifar *et al*., 2020), Sundram *et al*., 2022, Alarifi *et al*., 2014). However, the excessive generation of ROS induces oxidative stress which is the imbalance between ROS and antioxidants and causes chronic diseases such: as diabetes, cancer, cardiovascular and neurodegenerative diseases (Snezhkina *et al*., 2020, Pizzino *et al*., 2017). To address this health problem, researchers have taken the initiative to develop various potent antioxidants to prevent oxidative damage. Exogenous delivery of antioxidants holds promise to alleviate oxidative stress to regain the redox balance. There exist reports of the development of natural and synthetic antioxidants. Metal based nanoparticles are among the commonly studied antioxidant agents. Among these, MONPs such as ZnO (Nagajyothi *et al*., 2015, Mahendra *et al*., 2020), CuO (Bukhari *et al*., 2021), Co_3O_4 (Haq, Abbasi, *et al*., 2021), Fe_2O_3 (Üstün *et al*., 2022) and NiO (Barzinjy *et al*., 2020) are proven to be effective in scavenging reactive oxygen species. Even though a lot of research has been carried out and promising results are being achieved, the problem of treating cancer, bacterial infections, and oxidative stress is not fully solved yet. Hence, researchers keep trying to find the most efficient and potent drugs to solve the aforementioned human health issues. As the concept of synthesis and characterization of NPs increases, the researchers gained interesting knowledge in designing a new hybrid nanostructure called core-shell nanoparticles.

In recent developments, literature reports indicate that in contrast to monometallic oxide and metal oxide nanostructures, metal oxide core-shell nanostructures are preferred for biomedical applications due to their low toxicity, high solubility, thermal and chemical stability, less defect, biocompatibility, and high permeability to specific target cells (Ganesan *et al*., 2020, Ramalingam *et al*., 2020). Metal oxide core-shell nanoparticles (MOCSNs) such as:

Co_3O_4@NiO (Q. Yang *et al*., 2014), ZnO/Co_3O_4/NiO (Zhu *et al*., 2021), Fe_3O_4@Co_3O_4 (Alqarni *et al*., 2022) (Shivappa *et al*., 2018), NiO@Co_3O_4@graphene (Yin *et al*., 2019), $Tb(OH)_3$@SiO_2 (Ta *et al*., 2022), Co_3O_4@ZnO (AlTurki, 2018), CuO@ZnO (Tamanis *et al*., 2015), Co_3O_4@CuO (X. Li *et al*., 2017), Co_3O_4@MnO_2 (Tahir *et al*., 2017), Co_3O_4@SiO_2 (Ding *et al*., 2021), and TiO_2@Co_3O_4 (Goutam *et al*., 2020) have been synthesized by using different methods and for several applications. These MOCSNs are synthesized by chemical methods such as sol-gel, hydrothermal, sono-coprecipitation, solvothermal, emulsion polymerization, microemulsion polymerization, ultrasonic microwave, electrochemical, electroless deposition, and a few are by green methods (Shamhari *et al*., 2018, Kolodziejczak-Radzimska & Jesionowski, 2014, Nasrollahzadeh *et al*., 2020, Veisi *et al*., 2019). The chemical method of synthesis is often costly, and potentially harmful to the environment and living organisms. Thus, in search for safe, eco-friendly, cost-effective, rapid, easily available, high stability, and biocompatible synthesis, researchers were motivated to develop green synthesis methods (S. U. Khan *et al*., 2018, Vasantharaj *et al*., 2019). Among chemically synthesized core-shell nanostructure (CSNs) Co_3O_4@ZnO (Zhang *et al*., 2019), NiO/ZnO (Juma *et al*., 2017), and CuO/ZnO (Zhao *et al*., 2010, Xu *et al*., 2019) caught the attention of researcher due to their parent essentiality, less toxicity, high dispersibility, biocompatibility, good conjugation with bioactive molecules and high thermal and chemical stability. However, core-shell nanoparticles Co_3O_4@ZnO, Co_3O_4@NiO, and Co_3O_4@CuO have not been synthesized by the green approach, and their anticancer, antibacterial, and antioxidant activities are not reported yet.

Green synthesis methods encompass the use of microorganisms and plants part for the miniaturization of metal ions into their nanoscale size (1-100 nm). Nowadays, the method gained comprehensive attention from researchers because of its safety, efficiency, simplicity, economical, eco-friendly, reliable, non-toxic and sustainable for synthesizing various NPs (Murali *et al*., 2021, Carpa *et al*., 2017, Lagashetty *et al*., 2020). The properties of synthesized CSNs are characterized by using UV-Vis-diffuse reflectance spectroscopy (DRS), X-ray diffraction (XRD), Fourier transform infrared spectroscopy (FT-IR), scanning electron microscopy-energy dispersive X-ray spectroscopy (SEM/EDX), transmission electron microscopy-high resolution transmission electron microscopy (TEM/HRTEM), selected electron area diffraction (SAED), X-ray diffraction (XRD), and thermogravimetric analysis-differential thermal analysis (TGA/DTA). In this work, the novel *Datura stramonium* leaf extract-mediated

Co_3O_4@ZnO (CZ), Co_3O_4@NiO (CN), and Co_3O_4@CuO (CC) CSNs were synthesized. Finally, the anticancer, antibacterial, and antioxidant activities of biologically synthesized CSNs were investigated.

1.2. Statement of the Problem

Cancer disease, bacterial infection, and oxidative stress are some of the most serious health challenges that have drawn the public and researchers' attention worldwide as human health threat that prolongs economic and health crises. Cancer is the leading cause of death worldwide; specifically, breast cancer is a major ongoing public health issue among women. Conventional therapies such as surgery, radiotherapy, chemotherapy, and hormone therapy are commonly used for cancer treatment (Tagde *et al*., 2022, Sharifi *et al*., 2020). However, these treatments are unable to stop the propagation of cancer cells and show adverse side effects on healthy cells (Kouhbanani *et al*., 2021). Due to this, searching for effective treatment methods and developing safe and less toxic anticancer drugs are imperative issues worldwide.

Bacterial infectious diseases are caused by a harmful bacterial strain inside or outside the body and can be treated by different antibacterial drugs which show rapid increment as a consequence of the spread of antibacterial-resistant infection disease. However, due to the change in bacterial species and their genetic makeup, the activity of antibacterial drugs against bacteria is resisted (Kamurai *et al*., 2020, Happy *et al*., 2019). Even though the advances in synthesizing new antibacterial drugs used in the formal pharmaceutical industry are still derived, the organisms continue to grow and cause infection. Therefore, finding potent antibacterial drugs has become a critical issue all over the world. Additionally, excess reactive oxygen species produced in normal metabolic processes exert oxidative damaging effects by reacting with nearly every molecule found in living cells and can initiate different degenerative diseases. The oxidative reaction of ROS is controlled by enzymes such as superoxide dismutase, catalase, and antioxidant compounds (Xu *et al*., 2019). However, the excess production of ROS in the body results in oxidative stress which in turn consequences, in diseases like neurological disorders, cancer, emphysema, cirrhosis, atherosclerosis, and arthritis (Al-Snafi, 2017, Alavi *et al*., 2022). Antioxidant drugs in clinical use are not strong enough to reduce excessive production of ROS in cellular metabolic processes and have numerous side effects.

Due to these health problems, with the development of nanotechnology, various types of NPs have been synthesized. The antibacterial and antioxidant activities of several metal oxide nanoparticles have been studied widely. However, the antibacterial and antioxidant activities of Co_3O_4, ZnO, NiO, and CuO NPs synthesized utilizing *D. stramonium* leaf extract have not yet been reported. Furthermore, to address a wide range of challenges in medical fields and the limitations of individual components, researchers designed different mixtures of metal oxide nanoparticles. Amongst, in exploring various options to address these problems, metal oxide core-shell nanoparticles, have emerged as promising candidates due to their low toxicity, biocompatibility, selectivity, high dispersibility, permeability, and thermal stability. Moreover, the synergetic effect that might arise from the combination of the core and shell metal oxides derives interest in designing core-shell type nanostructures. However, the anticancer, antibacterial, and antioxidant activities of *D.stramonium* mediated Co_3O_4@ZnO, Co_3O_4@NiO, and Co_3O_4@CuO CSNs were not yet reported. Therefore, this study investigated the anticancer, antibacterial, and antioxidant activities of *Datura stramonium* leaf extract-mediated CZ, CN, and CC CSNs.

1.3. Objectives

1.3.1. General Objective

To synthesize Co_3O_4@ZnO, Co_3O_4@NiO, and Co_3O_4@CuO CSNs using *Datura Stramonium* leaf extract and investigate their anticancer, antibacterial, and antioxidant activities.

1.3.2. Specific Objectives

To prepare the aqueous extract of the *Datura Stramonium* plant leaf and screen its phytochemical composition.

To synthesize Co_3O_4, ZnO, NiO, and CuO metal oxide nanoparticles and Co_3O_4@ZnO, Co_3O_4@NiO, and Co_3O_4@CuO CSNs.

To characterize the synthesized nanomaterials using TGA/DTA, FTIR, XRD, UV-Vis, SEM-EDX, TEM, HR-TEM, and SAED techniques.

To examine the *in vitro* anticancer activities of the synthesized MOCSNs against breast cancer.

To study the antibacterial activity of synthesized MONPs and MOCSNs against gram-positive (*Staphylococcus aureus* and S*treptococcus pyogenes*) and gram-negative (*Escherichia coli* and *Pseudomonas aeruginosa*).

To study the antioxidant activities of the synthesized MONPs and MOCSNs.

1.4. Significance of the Study

The best achievement of this study was expected to come up with improved nanostructure and ensure the potent anticancer, antibacterial, and antioxidant activities of Co_3O_4@ZnO, Co_3O_4@NiO, and Co_3O_4@CuO CSNs. The work was also expected to provide insight into the biological synthesis of CSNs and alternative approaches to the researchers to synthesize the core-shell nanostructures by utilizing phytochemical constituents of different parts of plants, microorganisms, and bio-based compounds. Furthermore, the result of the study provides significant baseline data for researchers and pharmaceutical industries on the use of MOCSNs as biological agents. Due to their high cytotoxicity to cancer cells, low toxicity to healthy cells, high inhibition efficiency in antibacterial, and strong scavenging activities, the biogenically synthesized CSNs were supposed to contribute to the development of new drugs. The scientific community will also benefit from the publications of the findings.

1.5. Scope of the Study

In this research work, the *D.stramonium* mediated Co_3O_4, ZnO, NiO, and CuO NPs and CZ, CN, and CC MOCSNs were carried out using leaf extract. The *D.stramonium* mediated metal oxide nanoparticles and their CSNs were characterized using advanced instruments such as UV-Vis, FTIR, TGA/DTA, XRD, SEM-EDX, TEM, HR-TEM, and SAED techniques. The antibacterial and antioxidant activity of MONPs and MOCSNs were evaluated. Additionally *in vitro,* cytotoxicity of CZ, CN, and CC MOCSNs to breast cancer cells was studied. The synergistic effect of core-shell nanostructures was seen in antibacterial and antioxidant activity studies. However, this work didn‘t focus on the optimization of core concentration, pH synthesis, and calcination temperature.

2. Literature Review

2.1. Nanoparticles

Nanomaterial technology is the most striking science in the world, which refers to research and technology development since the last century. It was presented in 1959 by Nobel laureate Richard P. Feynman at the annual American Chemical Society meeting and stated "There's Plenty of Room at the Bottom". Richard P. Feynman elaborated on the prospects of manipulating single atoms that behave differently from their parent materials and building nanoscale machines (Guisbiers *et al*., 2012, Turna *et al*., 2014). Since then, the increment of demand for the miniaturization of technology has resulted in an upsurge in nanotechnology research and products containing NPs. In the last two decades, nanotechnology has studied the optical, mechanical, magnetic, and thermal characteristics and the production and application of physical, chemical, and biological systems of NPs (G. Sharma *et al*., 2019, Amaliyah *et al*., 2020).

In the century of nanotechnology, NPs become promising particles owing to their noble physical and chemical properties resulting from their small size and large surface area to volume ratio (S. U. Khan *et al*., 2018). Due to this fact, the NPs are highly reactive, stable in chemical processes, have good mechanical strength, non-toxic, dispersible, and bioavailable. However, the shape, size, and structure of these NPs are different even for the NPs synthesized from the same materials. Example: Gold nanoparticles show distinct color owing to a phenomenon known as localized surface plasmon resonance (LSPR). The colors of gold are a result of the collective oscillation of the conduction electrons in the gold nanoparticles when they are excited by incident light. The incident light causes the electrons to oscillate collectively at a specific frequency, which depends on the size, shape, and composition of gold nanoparticles. This frequency corresponds to a particular color in the visible spectrum and causes the LSPR frequency shifts, resulting in a different color being observed the smaller gold nanoparticles tend to appear red, while larger nanoparticles may appear blue or purple as shown in Figure 1 (X. Huang & El-Sayed, 2010).

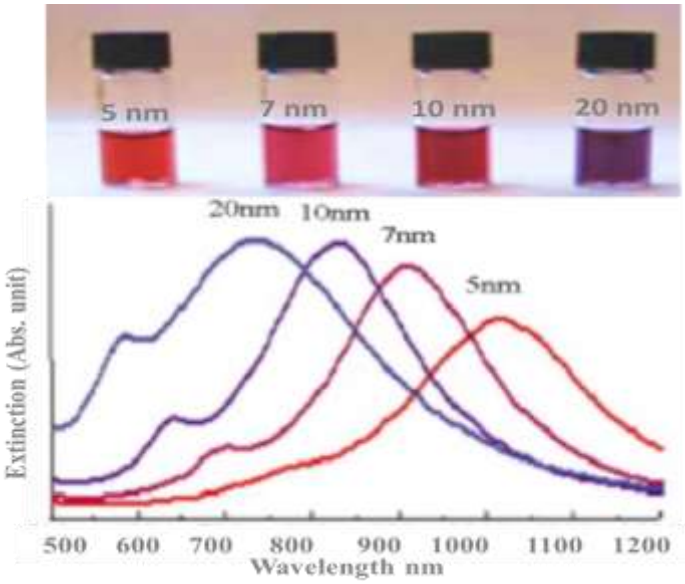

Figure 1: Solutions with gold nanoparticles and color altered as the size of gold nanoparticles increases.

Several NPs are manipulated on an atomic, molecular, and super-molecular level and gain much attention due to their numerous applications in different fields. While nanoparticles offer enormous promise, their safety and possible environmental effect must be thoroughly reviewed during research and deployment to guarantee responsible use (Ganesan *et al*., 2020). The versatility of nanoparticles allows for innovations in multiple sectors, enhancing existing technologies and enabling new solutions to complex challenges. Their unique properties continue to drive research and development, promising even more applications in the future.

In the novel study of NPs, the synthesis method is an imperative issue that enables the customization of nanomaterials for specific applications. Nanoparticles are synthesized by two main approaches, namely top-down and bottom-up as shown in Figure 2. In top-down approaches, the nanoscale particle is obtained by the reduction of bulk material by milling, etching, crushing, grinding, nanolithography, laser ablation, sputtering, and thermal decomposition. In top-down approaches, synthesizing uniform shapes and surface perfection is a big challenge. Wang Y *et al*., (2021) reported that the synthesis of uniform spherical colloids of MONPs within the range of 0.1-1 nm remains an impressive challenge, even though almost all the synthesized NPs are limited to a diameter below 100 nm (Han *et al*., 2016, Baig *et al*., 2021).

Unlike that, bottom-up approaches, which are atom to atom or molecules to molecules assemble and synthesis approaches such as Sol-gel (Sugihartono *et al*., 2019), hydrothermal (Sharifi *et al*., 2020), and biosynthesis (Andleeb *et al*., 2021). Due to this fact, the bottom-up approach is preferred to synthesize uniform shapes and perfect surface structures. In contrast to physical and chemical bottom-up approaches that result in environmental toxicity and are possibly hazardous, the green method synthesis of nanoparticles is environmentally friendly, cost-effective, nontoxic, and rapid synthesis (I. M. Alarifi, 2022, Shafey, 2020, Marslin *et al.*, 2018).

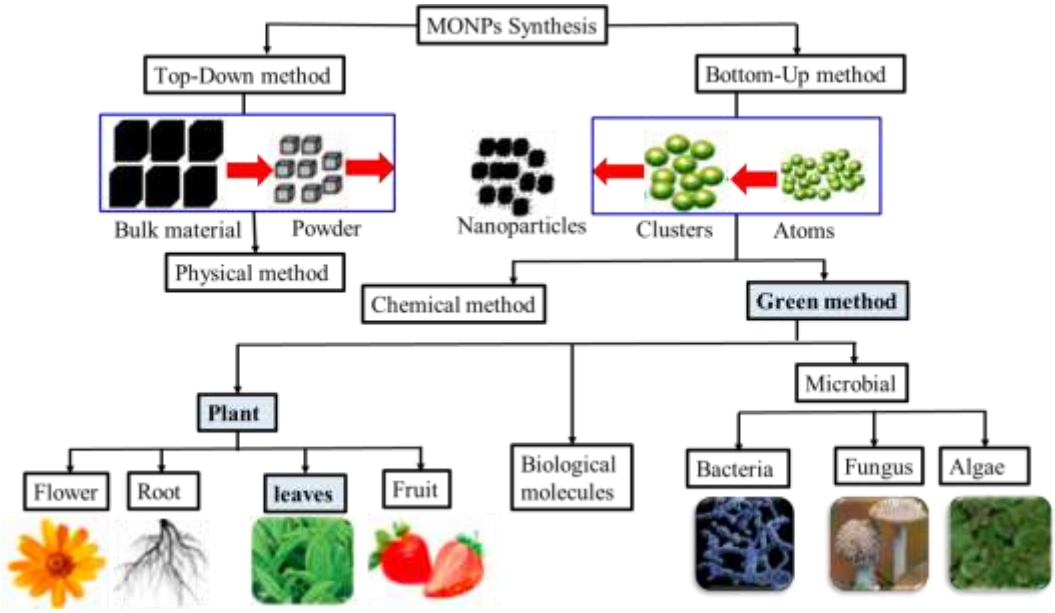

Figure 2: Different methods used for synthesizing nanoparticles.

2.2. Metal Oxide Nanoparticles

Metal oxide nanoparticles (MONPs) have shown remarkable potential in various fields of applications. It signifies a field of nanomaterials chemistry that got great attention a few decades ago because of its special physicochemical properties and numerous applications as shown in Figure 3. MONPs play an important role in the fields of physics, chemistry, biology, engineering, medicine, industry, and material sciences (Usmani 1 *et al*., 2018). Due to the small size and high density of edge surface sites, MONPs exhibit unique physicochemical properties that significantly improve their bioavailability, biocompatibility, and minimize drug toxicity. MONPs are of different types and they have unique physical, chemical, and biological

characteristics that can be easily altered or manipulated (Keat *et al*., 2015, Chung *et al*., 2017; Hussain *et al*., 2019, Hossain *et al*., 2024)

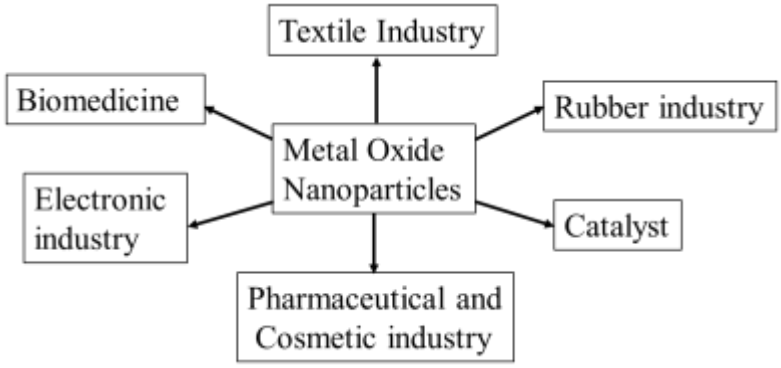

Figure 3: Diverse applications of MONPs in different fields.

In general, the functional properties of MONPs have resulted from parameters such as size, shape, morphology, crystal structure, and surface chemistry. Due to this, several metal oxide nanostructures such as Fe_3O_4, ZnO, Co_3O_4, CuO, MgO, NiO, TiO_2, and MnO_2 MONPs have been studied (Shalaby *et al*., 2022, Jayasimha *et al*., 2024).

Out of these metal oxide nanoparticles Co_3O_4, NiO, CuO, and ZnO NPs have gained great attention due to their novel applications such as anticancer, antibacterial, antioxidant, and antidiabetic (Arsalan *et al*., 2020, Yagoub *et al*., 2022). Investigation of these MONPs is valuable for developing modern nanomaterials with high performance. The synthesis, properties, characterization, structural designing, and their potential application were highly focused by researchers to modify the properties of their respective metal based NPs (Bekele *et al*., 2022)

2.2.1. Cobalt Oxide Nanoparticles (Co_3O_4 NPs)

Nowadays, intense scientific study is focusing on MONPs due to their numerous potential applications in fields of the space industry, solar cells, sensors, catalysis, cosmetics, fuel cells, biomedicines, electrochemistry, biotechnology, energy devices, agriculture, food technology, and optical devices, pharmaceuticals, textile industry, and water treatment (Waris *et al*., 2021). Amongst, metal oxide nanoparticles of transitional metal specifically cobalt attracted numerous researchers due to their low cost and good electro-activity. Cobalt metal can exist in variable oxidation states +2, +3, and +4 making it prominent to be used for different applications (Raeisi *et al*., 2021, Khalil *et al*., 2020). Due to its variable oxidation states and high resistance to corrosion and oxidation, it shows potential applications. An antiferromagnetic p-type semiconductor cobalt oxide nanoparticles (Co_3O_4 NPs) attained focus due to its unique properties

such as magnetic, electrical, catalytic, and use in a variety of applications such as energy storage, field emission, sensing, and magnetic semiconductors properties irrespective of bulk materials (Safdar *et al*., 2023, Omran *et al*., 2020). In addition, cobalt oxide NPs show good antioxidant, anticancer, and antibacterial activities and are synthesized by environmentally friendly and non-toxic green approach. In green synthesis of cobalt oxide nanoparticles, plants, bacteria, algae, and fungi are widely used. In contrast, plants are preferred due to their abundance, safe nature, and greater stabilization and reduction capacity (Govindasamy *et al*., 2022, Ajarem *et al*., 2021). Yu *et al*., 2017, also synthesized Co_3O_4 NPs by a green method using leaf extract of *Helianthus annuus* which shows good photocatalytic activity. The synthesized cobalt oxide NPs using *Punica granatum* peel extract and characterized by advanced techniques and their size was in the range of 40-80 nm.

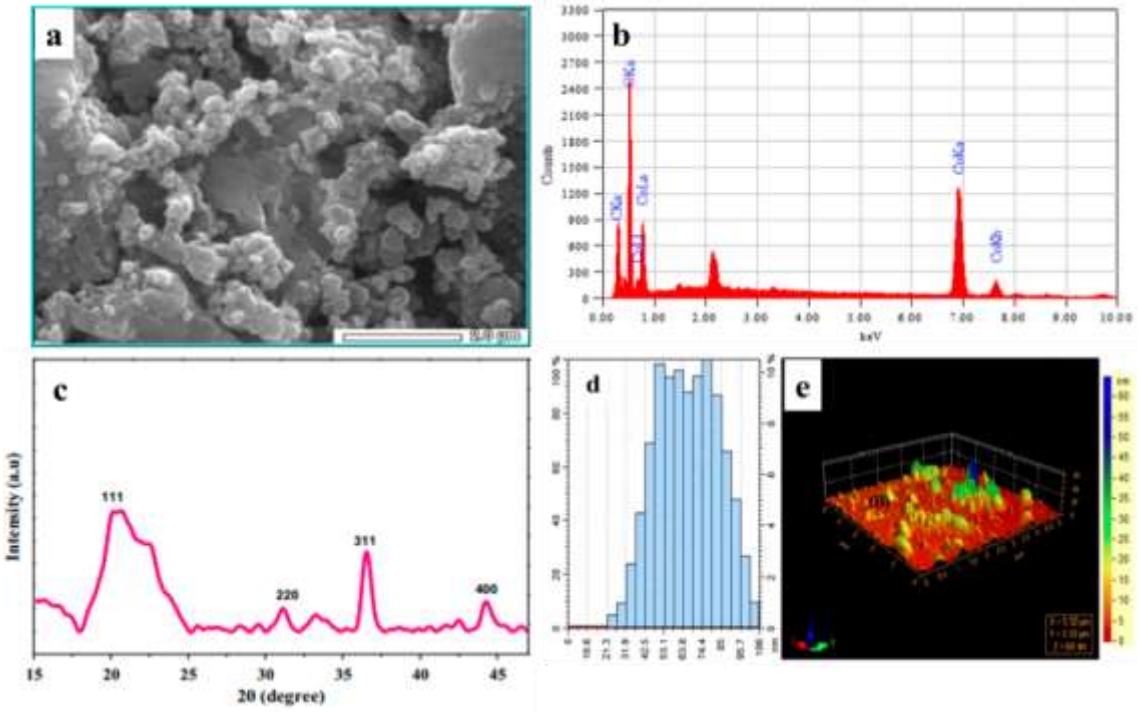

Figure 4: The SEM image (a), EDX spectra (b), XRD pattern (c), particle size distribution (d), and AFM image (e) of Co_3O_4 NPs (Bibi *et al*., 2017).

The XRD diffraction peaks of Co_3O_4 NPs with an average size of 43.78-73.10 nm were reported at 2θ of 20.05 (111), 31.19 (22 0), 36.56 (311), and 44.29 (400) (Bibi *et al*., 2017, Nomura *et al*., 2019, Jia *et al*., 2016). As shown in Figure 4, the spherical shape, elemental composition, and surface topography of Co_3O_4 NPs obtained from SEM images, EDX spectra, and AFM images

were reported. Dewi *et al*., (2019), reported *Euphorbia heterophylla L*. leaves extract mediated Co_3O_4 NPs with ~17 nm size.

2.2.2. Zinc Oxide Nanoparticles (ZnO NPs)

Zinc metal is the most abundant trace element in the mammalian body and is essential to the structure and function of myriad proteins which are classified as regulatory, structural, and enzymatic. Due to the lack of its storage site in the body, it should be added to animal diets. For a few decades ago, numerous MONPs have been widely studied. Of them, zinc oxide nanoparticles (ZnO NPs) which are inorganic metal oxides have been synthesized due to their large range of applications such as biomedical, catalytic, photocatalytic, energy, and environmental treatment (Perumal *et al*., 2024, Chikkanna *et al*., 2019, Samy *et al*., 2019). ZnO NPs are also used in sunscreen and cosmetic yields hence it does not be absorbed via epidermis. Zinc oxide is known by its n-type semiconductor and its nanomaterials acquired remarkable consideration because of its inspiring properties like a wide direct band gap of 3.37 eV at room temperature and high excitation binding energy of 60 meV which have made zinc oxide important both for scientific and industrial applications (Kebede Urge *et al*., 2023, Sundrarajan *et al*., 2015). Its material exhibits semiconducting, piezoelectric, and pyroelectric optical properties. Among several classes of semiconductors, ZnO is a promising oxide owing to its non-hazardous and economical features such as high thermal, chemical immovability, resistivity control, high quantum field, flexible morphologies, and superior electrical properties (Mallikarjunaswamy *et al*., 2020). Moreover, a nanosized ZnO showed potential biological applications such as antibacterial, antifungal agents, bio-imaging probes, and drug carriers. The most prominent characteristics of ZnO NPs are bioavailability and low toxicity which is why it is potent antibacterial, antimicrobial, anticancer, and good scavengers of reactive molecules (Mahendra *et al*., 2020, Jiang *et al*., 2018, Bayat *et al*., 2019).

Nowadays, it can be synthesized by using green methods under different parameters and characterized by different techniques such as UV-Vis, SEM, TEM, XRD, HRTEM, and EDX.

Sundrarajan *et al*., 2015, reported that ZnO NPs synthesized using *Pongamia pinnata* plant extract show good activity against *Staphylococcus aureus* (gram-positive) and *Escherichia coli* (gram-negative) organisms. The hexagonal phase and high purity of green synthesized ZnO NPs are characterized by XRD and EDX techniques.

2.2.3. Nickel Oxide Nanoparticles (NiO NPs)

Nickel oxide is an attractive p-type semiconductor with of band gap energy of 3.6 eV and a conduction band energy is 1.8 eV. Due to its basic properties, the researcher reduced the bulky size of nickel metal and metal oxide to its nanoscale (Sabouri *et al*., 2021). The nano-size nickel oxide has fascinating features such as being optical, magnetic, electrical, and catalytic with good thermal stability, specific capacitance, stable endurance for resistive switching, rapid switching time for resistance-based memory, excellent durability, electrochemical stability, and chemical properties when compared to their bulk state (Olajire & Mohammed, 2020). In addition to this, NiO NPs have also been widely used in biomedical applications which is due to their unique surface area, Ni^{+2} ion releasing and adsorbing ability, and cytotoxic effects. As a result of its great uses, NiO NPs have been synthesized by different chemical and biological methods. The chemical methods are complex and use unsafe and toxic chemicals that are costly and take a long time to give the desired product (Barzinjy *et al*., 2020). Because of this, the researchers developed an environmentally benign technique called the green method. The green synthesized NiO NPs have potential antibacterial, anticancer, antidiabetic, and antifungal activities (Wardani *et al*., 2019).

2.2.4. Copper Oxide Nanoparticles (CuO NPs)

Copper is an inorganic transition metal and is widely used for nanomaterials manufacturing due to its low cost and high abundance in nature, stability and has been used in applications such as sensors, catalysis, biotechnologies, and nontoxicity (Sharmila, Sakthi Pradeep, *et al*., 2018). Copper which is an active metal is used in many redox processes in animal and plant cells. In plants, it is used as part of regulatory proteins, a cofactor of phenol oxidases, ascorbate oxidase, superoxide dismutase (SOD), and participates in electron transport in the respiratory and photosynthetic chains. In addition to copper metal, copper oxide has also been used in different fields of applications that as energy conversion and storage through environmental science, electronics, and sensors (Ijaz *et al*., 2017).

Recently, CuO NPs have attracted considerable attention and explored in electronics, air and liquid filtration, ceramics, wood preservation, textiles, bioactive coatings, skin products, films,

lubricant oils, and in inks medical therapeutics, particularly as antimicrobial, antibacterial, anticancer agents and drug delivery systems (A. Singh *et al*., 2017).

The existing results did not provide clear information about the effect of CuO NPs on plant cells. The action of CuO NPs on plant cells has not been studied satisfactorily. However, it is known that nanopowders are successfully used as microfertilizers and pesticides. CuO NPs have distinct physicochemical and biological properties due to the large surface area to volume ratio (Benhammada & Trache, 2021, Nagajyothi, Muthuraman, *et al*., 2017). CuO NPs can be fabricated by chemical methods (direct precipitation, sol-gel, solvothermal, thermal decomposition, emulsion precipitation, and hydrothermal) and biological methods. The most preferred green synthesis attains much more consideration, in which active biomolecules like *aloe barbadensis*, *Carica papaya*, *Eucalyptus globules*, *Tecoma castanifolia*, *Corymbia itriodora*, *Nephelium lappaceum L*., *Lycopersicon esculentum*, bacteria, and fungi were used for the synthesis of CuO NPs. CuO NPs synthesis is much less expensive in contrast to gold and silver nanoparticles which have potent anti-microbial activity due to their unusual crystal (Nagajyothi *et al*., 2015).

2.3. Core-Shell Nanostructures

Recently, metal oxide NPs in various forms and morphology have been discovered to be efficient in different applications which are primarily attributed to their size, shape, and crystal structures. Several MONPs and their composite have been developed for a variety of applications. Among composite NPs, core-shell metal oxide nanostructure (MOCSNs) are recently developed and play a significant role in various fields such as catalyst, industrial, and biomedical (B. Sharma *et al*., 2013, Rajith Kumar *et al*., 2020). The CSNs are distinguished by their biphasic inner core and outer shell components. They may have varying core sizes and shapes, as well as shell thicknesses and surface morphologies. The CSNs have distinct features that result from the arrangement of various components inside the structures. The CSNs are constructed such that shell components increase the core part's reactivity, oxidative stability, and thermal stability while reducing flaws throughout the structure.(Nomoev *et al*., 2015, Pathak *et al*., 2019).

Due to the unique properties that developed from layer by layer arrangement of core and shell material, geometry, and design, the CSNs attract the researcher’s attention. The combination of

one core and two or more shell nanomaterials can be termed core-shell, core@shell, or core/shell. The CSNs are designed based on the purpose of the study and their application can be varied by changing the individual components (Kalska-Szostko *et al.*, 2015, B. Sharma *et al.*, 2013). Unlike other nanostructures, the CSNs are separated layer by layer as shown in Figure 5. Researchers synthesized spherical core/shell nanoparticles for the first and later different types of CSNs have been developed based on core shape. The non-spherical shape of core nanoparticles leads to the formation of different shapes of particles. These structures are synthesized by layering the shell over core material which is used as a physical separation from the surrounding environment and prevents the direct involvement of surface chemistry (Rakgalakane & Moloto, 2011, Costas *et al.*, 2020, Gawande *et al.*, 2015).

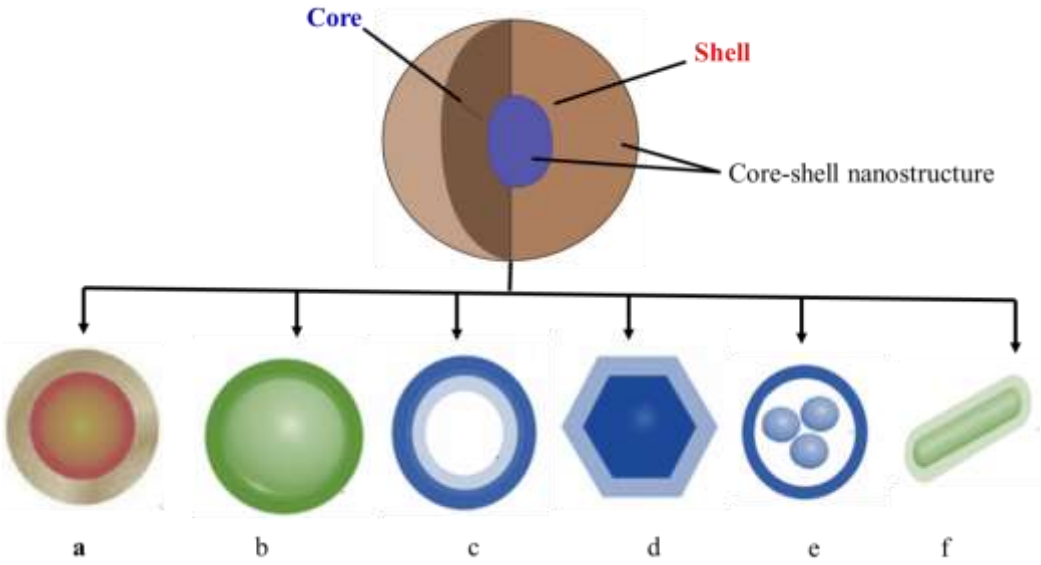

Figure 5: Different structures of core-shell nanoparticles: (a) spherical core/shell nanoparticles, (b) nano matryoshka material, (c) Core double-shell particles or core multi-shell nanoparticles, (d) hexagonal core-shell nanoparticles, (e) multiple small core materials coated by single shell material and, (f) Rod core-shell nanoparticles (El-toni *et al.*, 2023).

The core-shell nanoparticles are the most appropriate and operative ways to have a synergetic effect of metal-metal, metal-metal oxide, and metal oxide-metal oxide inorganic NPs combination for multifunctional applications. In addition to this, shell nanoparticles layered the core phase to manage its migration and aggregation (Bekele *et al.*, 2022, El-Toni *et al.*, 2016).

The decorating of a benign shell nanomaterial on the surface of a core nanoparticle is used to improve properties such as less toxicity, high dispersibility, biocompatibility, cyto-compatibility, good conjugation with other bioactive molecules, and high thermal and chemical stability. Due to the unique structural feature consisting of a distinct core and shell makes core-shell nanoparticles (CSNP) and modified properties, CSNs are used in various applications such as energy harvesting, environmental, catalysis, drug delivery, cell therapy, anti-microbial and cancer treatment (Costas *et al*., 2020, Yilmaz & Yilmaz, 2020). The physical and chemical properties of core-shell hybrid structures have been modified in contrast to single components and received incredible research interest in recent years exhibiting the modifiable materials properties (AlTurki, 2018). Recently, several CSNs such as Cu@ZnO (Chang *et al*., 2016), Fe_3O_4@Ag (Nalluri *et al*., 2019), ZnO@Polymer (Xiong *et al*., 2008), Au@PVP (XU *et al*., 2016), CuO@NiO (Bayal & Jeevanandam, 2012) Au@Ag (G. Li & Tang, 2014) (Samal *et al*., 2013), Co_3O_4@NiO (R. X. Chen *et al*., 2015), ZnO-Cu_xO (Florica *et al*., 2019), CuO-ZnO (Costas *et al*., 2020), ZnO@ZnS (Sadollahkhani *et al*., 2014), NiO@ZnO (Han *et al*., 2016), PbO/ZnO (Pathak *et al*., 2019), CdSe/ZnO (Rakgalakane & Moloto, 2011), have been synthesized by several methods.

For example, Sadollahkhani *et al*., (2014) synthesized ZnO@ZnS core-shell nanoparticles step by step, in which ZnO NPs co-precipitation firstly and then afterward covered with ZnS using a solution-based chemical method at low temperature (Sadollahkhani *et al*., 2014). The core-shell nanowire structure of Co_3O_4@NiO is synthesized in two steps. The Co_3O_4 NPs are synthesized by the hydrothermal method and have a diameter of 70 nm with a length of approximately 10 μm. The Co_3O_4 nanowire structure is used as a core for successive deposition of NiO nanoflakes with a thickness of about 10 nm (Xia *et al*., 2012). Ning-Ning *et al*., (2016) synthesized Au@PVP NPs using the hydrothermal method and obtained uniform size with controlled shell-thickness. The synthesized Au@PVP has an optimal shell-thickness and shows appropriate adsorption time with high sensitivity toward malachite green (XU *et al*., 2016). Bayal *et al*., (2012) reported the monoclinic phase of CuO NPs and cubic phase of NiONPs of CuO@NiO core-shell synthesized using a homogeneous precipitation method (Bayal & Jeevanandam, 2012). Xiong *et al*., (2014), reported Au@Cu_2O core-shell nanoparticles synthesized by solution method and determined their sensitivity to carbon monoxide. In this hybrid of nanostructure Au nanorods (10-15 nm width and 40-60 nm length) were used as core and 30-60 nm Cu_2O shell

layer were deposited to form bricks and spherical shape Au@Cu_2O core@shell nanostructures. With morphological and orientation control the Au NPs cores have channeled the growth of Cu_2O shells. The (111) planes of Cu_2O and Au were layered over one another while the (200) planes of Cu_2O can grow on the (200) facets of gold to form the interfaces. The core which is Au has an exact plane orientation with the Cu_2O shells. The (100), (110), and (111) plane orientations of cores were parallel to the corresponding planes of the Cu_2O shells (J. S. Chen *et al.*, 2010). Rakgalakane and Moloto, (2011) reported the CdSe/ZnO core-shell nanoparticles synthesized by an electrochemical deposition method (Rakgalakane and Moloto, 2011).

2.4. Synthesis of Metal Oxide Nanoparticles

Over the last several years, green synthesis of MONPs has captured the interest of researchers and emerged as the most pursued strategy. The procedures have mostly been developed by employing various microbial and plant extract portions (Ruiz-Garcia *et al*., 2020). Amongst, plant extract to synthesize NPs is the most preferred which offers an alternative to microbes that is not easily available, and needs safe environmental conditions and proper culturing methods. Due to this, green synthesis of MONPs using plant extract which follows a simple procedure, is fast in production rate, easily available, and cost-effective has been developed (Bouafia *et al*., 2020, Nasrollahzadeh *et al*., 2020, Rahman *et al*., 2022).

Plant extracts are used to reduce metal salt to their corresponding MONPs. The good reducing capacity of plant extract is due to several bioactive constituents found in different parts of plants. The most common bioactive molecules are the polyphenolics which consist of flavonoids and phenolic acids which form the building up of polymeric tannins (Wanjala Wafula *et al*., 2023). Furthermore, phytochemicals such as alkaloids, terpenoids, amino acids, vitamins, polysaccharides, and protein molecules contribute to the synthesis of MONPs by reducing their precursor salts and stabilizing the generated NPs in the complicated redox-mediated process (Ogunyemi *et al*., 2019, Widatalla *et al*., 2022, Jacob & P, 2019). In the green synthesis of nanoparticles, a variety of plant parts are used for reduction purposes and as a capping agent. The plant parts preferred for synthesis are properly cleansed to remove dust particles and contaminants before drying in the shade. Finally, the phytochemical was extracted by heating a mixture of plant powder and a specified solvent at temperatures ranging from 40-50 ℃ and utilized for reduction as shown in Figure 6.

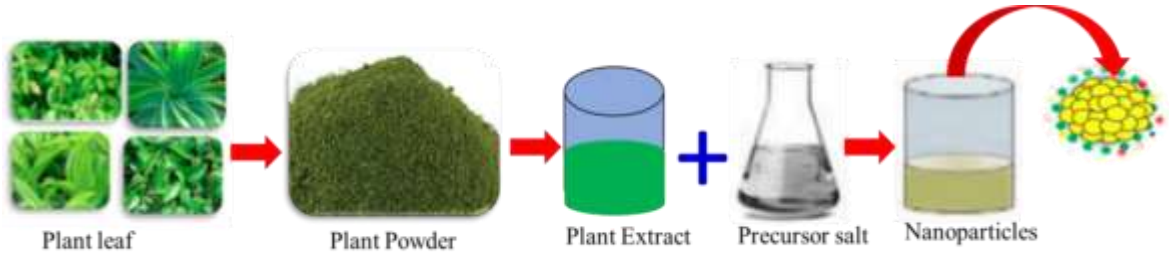

Figure 6: Green synthesis nanoparticles using plant leaf extract.

Phytochemicals with reducing properties include polyphenols, flavonoids, terpenoids, and alkaloids. They may transfer electrons to metal ions, decreasing them from ionic to zero-valent states. This decrease is frequently shown by a color shift in the solution, as metal nanoparticles usually have unique hues due to surface plasmon resonance. After the metal ions are reduced to zero-valent atoms, they can aggregate to form nanoparticles. Phytochemicals can also be used as stabilizing or capping agents, preventing nanoparticles from avoiding particle agglomeration. Functional groups found in phytochemicals, including hydroxyl (-OH), carboxyl (-COOH), amino (-NH_2), and others, can adsorb onto the surface of nanoparticles, giving stability and influencing the size and form of the particles. The metal cations of precursor salt will be saturated to form hydroxyl complexes and grow up to form crystallite with oxygen after supersaturation as depicted in Figure 7 (Khalil *et al*., 2020, Robertson *et al*., 2019, Mittal *et al*., 2013, Mendes *et al*., 2022).

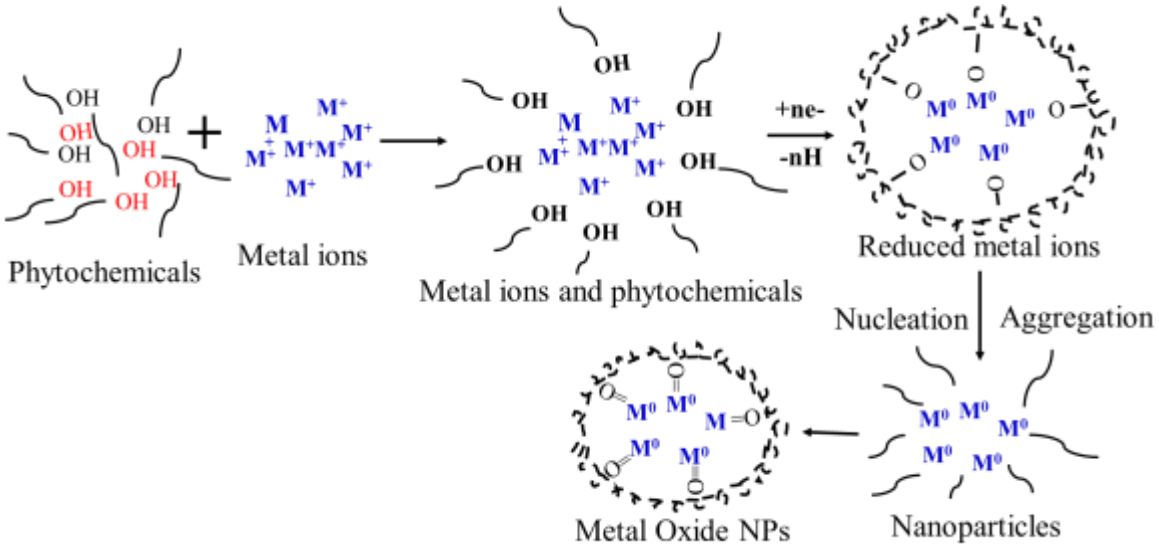

Figure 7: Schematic illustration of mechanism involved in phytochemical mediated MONPs

Incidentally, nanoparticles are incorporated into numerous fields by giving innovative solutions in the world (Mohd Yusof *et al*., 2019). There are several types of NPs including metal, metal oxide, polymers, ceramic, quantum dots, fullerenes, and nanotube nanoparticles. Among these NPs, MONPs are of special interest due to their multifunction. The research interest in the MONPs become an imperative issue, because of their distinctive physical and chemical properties and their noble application (Aziz *et al*., 2019).

Dewi *et al*., (2018) synthesized the Co_3O_4 NPs using *Euphorbia heterophylla* leaves extract and obtained a spherical shape and 17 nm size nanoparticles from transmission electron microscopy. The size of Co_3O_4 NPs obtained by the Debye Scherer equation was 39.99 nm with 1.53 eV band gap energy (Dewi *et al*., 2019). Hafeez *et al*., (2020) reported that the Co_3O_4 NPs were synthesized by using leaves extract of *Populus ciliata* and cobalt nitrate hexahydrate precursor salt and characterized using x-ray diffraction (XRD), transmission electron microscopy (TEM), and scanning electron microscopy (SEM) (Hafeez *et al*., 2020). Ullah *et al*., (2020) synthesized Cobalt-oxide nanoparticles using *Punica granatum* peel extract using cobalt nitrate hexahydrate precursor salt and characterized them using methods such as XRD, SEM, EDX, AFM, FTIR, and UV-Vis spectroscopy. The particles showed a spherical shape and 40-80 nm size(Waris *et al*., 2021).

Selam *et al*., (2020) synthesized ZnO NPs using *Deverra tortuosa* plant extract as a reducing agent and confirmed by using UV-Visible (UV-Vis) spectroscopy. The absorption spectrum of *Deverra tortuosa* plant extract mediated ZnO NPS showed a characteristic peak at 374 nm (Dagne *et al*., 2019). Al-Ameer *et al*., (2019) synthesized ZnO NPs using *Olea europaea* leaves extract as a bioreductant agent and obtained 20-50 nm size with a spherical shape (Alrubaie & Kadhim, 2019,. Sharmila *et al*., 2018) synthesized CuO NPs using *Tecoma castanifolia* leaf extract and obtained a spherical shape and a size < 100 nm from TEM analysis. The copper precursor salt is reduced by phytochemicals like polyphenols, hydrocarbons, resins, and volatile oils of *Tecoma castanifolia* plant leaf. The formation of CuO NPs through bioreduction of copper sulphate salt by using *Bauhinia tomentosa* leaf extract and observed the spherical shape with size of 22-40 nm (Sharmila, Sakthi Pradeep, *et al*., 2018).

Similarly, Ananda Murthy *et al*., (2018) reported that the spherical CuO NPs with an average size of 20–30 nm are synthesized by reducing agents such as flavonoids, triterpenoids, steroids, cardenolides, and alkaloids of *Calotropis gigantea* leaves (Ananda Murthy *et al*., 2018).

2.5. Synthesis of Core-Shell Nanostructure

CSNs are synthesized by creating nanoparticles with a core made of one substance and a shell made of another. These structures can be constructed to have unique qualities that are not present in the individual components. The core-shell design enables the use of various materials to provide certain functionality, such as increased stability, controlled release, or improved biocompatibility (Sanad *et al*., 2021). The core/shell nanostructures are typically manufactured by reducing metal salts in one or two steps using appropriate reducing agents. The core/shell nanoparticles were synthesized in one-step via simultaneous reduction, which involves reducing both metal precursors at the same time to form core/shell structures. In this instance, the development of shell particles on the core is beyond one's control (A. Ali *et al*., 2021). In a two-step procedure, the core is formed, and the second material is coated on the core as shell particles by serial reduction using a suitable agent for each phase (Khatami *et al*., 2018).

Recently, Co_3O_4 NPs which exhibit numerous oxidation states and ZnO NPs which are semiconductors are becoming interesting in the research area. AlTurki, (2018) prepared CZ CSNs by using the sol-gel method and obtained the spherical shape with 12 nm size of NPs from TEM analysis (AlTurki, 2018). The peaks located at (2θ) match with the refection of crystal planes in the left side panel of Figure 8, whereas in the right panel side of the XRD pattern, the peaks are attributed to Co_3O_4 core and ZnO shell. D.Y. Han, *et al*., (2015) reported the NiO@ZnO CSNs prepared by using a microemulsion system. The result of the XRD pattern demonstrated that the particles were exactly indexed to a cubic rock salt structure of NiO and ZnO as depicted in Figure 8(a). The morphological feature of the CSNs obtained by TEM was also reported as shown in Figure 8(b) D.Y. Han, *et al*., (2015).

Jinglong Bai, *et al*., (2021) reported that all of the diffraction peaks in NiO@ZnO CSNFs are in good agreement with the wurtzite ZnO (JCPDS no. 36-1451) and cubic NiO (JCPDS no. 04-0835). In the report, there is no distinct peak index to other phases, except for ZnO or NiO, which indicates the formation of NiO@ZnO CSNs. as shown in Figure 8(c). As shown in Figure 8(d), the SEM pictures show that following deposition, NiO NPs are covered by ZnO layers (~20 nm) with wrinkled surfaces. AlTurki, (2018) synthesized Co_3O_4@ZnO CSNs at low temperatures by using the sol-gel method. According to the study, the XRD for Co_3O_4@ZnO CSNs revealed that the major peaks correspond to the ZnO hexagonal wurtzite structure, which

is consistent with JCPDS card 36-1451, as shown in Figure 8(e). Furthermore, as seen in Figure 8(f) of the HR-TEM picture, the Co_3O_4 cores are darker than the ZnO shell. HR-TEM pictures reveal a definite interface between the core and the shell, with the edge of the shell showing lower intensity than the core (AlTurki, 2018).

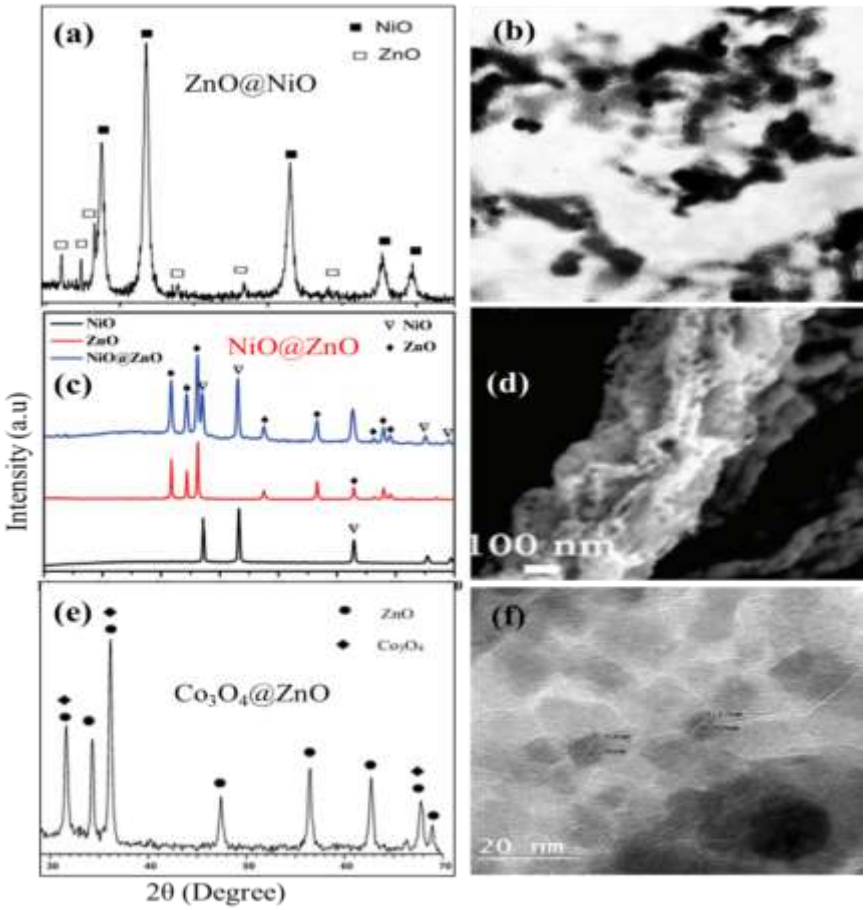

Figure 8: XRD pattern of (a) ZnO@NiO, (c) NiO@ZnO, (e) Co_3O_4@ZnO, and (b) the SEM image of ZnO@NiO, TEM image of (d) NiO@ZnO and (f) Co_3O_4@ZnO CSNs

In addition to this, Cai *et al*., (2014) synthesized Co_3O_4@ZnO core-shell using hydrothermal/sol-gel routes. The Co_3O_4@ZnO core-shell particles were characterized by TEM and 22 and 56 nm were obtained for the Co_3O_4 core and ZnO shell respectively (Cai *et al*., 2014). Zhang *et al*., (2019) synthesized ZnO@Co_3O_4 core-shell on Ni foil by using a mild photo-deposition method which has a larger electrochemical active surface area. The ZnO@Co_3O_4 core-shell showed bundle-like nanostructure from SEM image with diameters of 50-80 nm. In

$ZnO@Co_3O_4$ CSNs the core and shell components are identified by using TEM in which the ZnO core is fully covered by the Co_3O_4 NPs (El-Toni *et al*., 2016).

A p-type semiconductor NiO can form a shell nanostructure. Co_3O_4@NiO CSNs are a particular type of nanostructured particles and their characteristics depend on the volume of CSNs. Han *et al*., (2015) synthesized NiO@ZnO CSNs of core NiO and shell ZnO by using thermal oxidation in air. The core-shell particles have 35 nm with a thickness size of ZnO shell ~15 nm for NiO-ZnO. NiO@ZnO CSNs were successfully prepared in Triton X-100/n-hextnol/cyclohexane/water microemulsion system (Han *et al*., 2016, Paul *et al*., 2020). The NiO@ZnO CSNs that consist of NiO core and ZnO shell with a diameter of 200-300 nm showed the interfaces of the crystallite NiO and ZnO crystal lattices. The interplanar distance of 0.26 nm coincides with the lattice spacing of the (002) plane of ZnO, while the lattice spacing of 0.241 nm corresponds to the interplanar spacing of the (111) plane of cubic NiO. Moreover, the distinct interface and continuity of lattice fringes observed between the NiO and ZnO nanostructures indicate the formation of p-n heterojunction between NiO and ZnO in CSNs (Han *et al*., 2016).

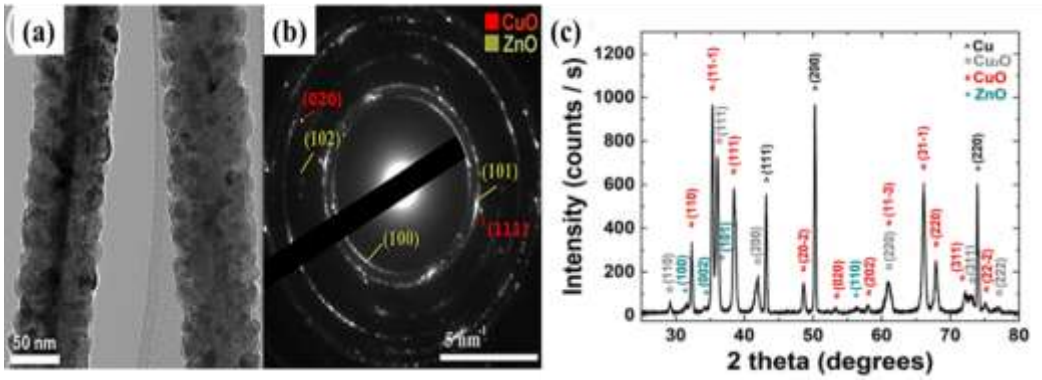

Figure 9: The TEM image (a), SAED image (b), and XRD pattern (c) of CuO-ZnO NPs.

Costas *et al*., (2020) synthesized CuO@ZnO CSNs of core CuO and shell ZnO by using thermal oxidation in air and magnetron sputtering respectively (Costas *et al*., 2020). In the report, the core nanomaterials have a monoclinic structure and the shell film has a hexagonal wurtzite structure. In XRD analysis the Cu showed the diffraction maxima and, Cu_2O film and the CuO showed peaks at 2θ: 31.7°, 34.4°, 36.2° and 56.6° corresponding to the Miller indexes of the reflecting planes for ZnO in hexagonal wurtzite phase: (100), (002), (101) and (110) proving the presence of the ZnO shell as shown in Figure 9(c) (Florica *et al*., 2019).

The TEM image of a CuO-ZnO core-shell nanoparticle indicates that the cylindrical shape of the CuO core is conserved after the coating with the ZnO shell. Moreover, the CuO core has a diameter of about 50 nm and the entire CuO-ZnO core-shell nanowire diameter is about 80 nm, the thickness of the ZnO shell being evaluated at ~15 nm. The component of monoclinic for the CuO core and hexagonal wurtzite for the ZnO shell. The SAED implies that CuO-ZnO core-shell particles exhibit both components polycrystalline structures, monoclinic for the CuO core and hexagonal wurtzite for the ZnO shell Figure 9(b).

Mansournia and Ghaderi (2016) (Mansournia & Ghaderi, 2017) prepared the CuO@ZnO core-shell using a simple two-step hydrothermal method. The photocatalytic effect of CuO@ZnO CSNs was varied with the thickness of the CuO core particle, and the order of degradation rate is as follows: CuO < 50% CuO@ZnO < ZnO < 10% CuO@ZnO < 2% CuO@ZnO ~ 0.4% CuO@ZnO CSNs. Park *et al*., (2012) synthesized ZnO-CuO core-shell nanoparticles in two steps, that ZnO nanoparticles were prepared by hydrolysis and injected in situ to form ZnO-CuO core-shell. The needle-like CuO shell was shown in the TEM image with an mean length of 49 ± 4 nm and a thickness of 8 nm (Chan Park *et al*., 2012).

Table 1: Plant extract mediated Co_3O_4, ZnO, NiO, and CuO NPs.

Types of plants	Salts precursor	Particle size in nm	Morphology of MONPs	Applications	References
Populus ciliata	$Co(NO_3)_2.6H_2O$	15-35	Sqaure like	Antibacterial	(Hafeez *et al*., 2020)
Salvia hispanica	$Co(NO_3)_2.6H_2O$	9.218	Spherical	Antibacterial	(Kiani *et al*., 2021)
Rosmarinus ofcinalis	$CoCl_2.6H_2O$	10	Sheet like	Anticancer	(Raeisi *et al*., 2021)
Punica granatum peel	$Co(NO_3)_2.6H_2O$	40-80	Spherical	Antibacterial	(Bibi *et al*., 2017)
Apium graveolens	$Co(NO_3)_2.6H_2O$	21-72	Cubic	Antibacterial	(Urabe & Aziz, 2019)
Algae	$Co(NO_3)_2.6H_2O$	30	Spherical	Anticancer Antibacterial Antioxidant	(Ajarem *et al*., 2021)
Hibiscus cannabinus	$Co(NO_3)_2.6H_2O$	20.8	Rod-like	Antibacterial	(Waris *et al*., 2021)
Sageretia thea	$Co(NO_3)_2.6H_2O$	43	Spherical	Anticancer	(Khalil *et al*.,

				Antibacterial Antioxidant	2020)
Citrus limon fruit	$CoCl_2.6H_2O$	19	Cubic	Antibacterial	(Anuradha & Raji, 2021)
Moringa oleifera	$Ni(NO_3)_2$	9.69	Spherical	Anticancer Antibacterial	(Angel Ezhilarasi *et al*., 2018)
Calotropis gigantean	$Ni(NO_3)_2$	20-40	Spherical	Antimicrobial	(Din *et al*., 2018)
Gymnema sylvestere	$Ni(NO_3)_2{\cdot}6H_2O$	32	Cubic	Anticancer Antimicrobial	(Vijaya Kumar *et al*., 2019)
Aegle marmelos	$Ni(NO_3)_2$	8-10	Cubic	Antibacterial Anticancer	(Angel Ezhilarasi *et al*., 2018)
Zingiber officinale	$Ni(NO_3)_2$	16–52	Cubic	Antibacterial	(Haider *et al*., 2020)
Allium sativum	$Ni(NO_3)_2$	11–59	Spherical	Antibacterial	(Haider *et al*., 2020)
Rhamnus virgate	$Ni(NO_3)_2$	24	Cubic	Anticancer Antimicrobial Antifungal	(Iqbal *et al*., 2019)
Raphanus sativus	$Ni(NO_3)_2$	13-52	Spherical	Antioxidant Antibacterial	(Haq, Dildar, *et al*., 2021)
Abutilon indicum	$Ni(NO_3)_2{\cdot}6H_2O$	33	Spherical	Anticancer Antioxidant Antibacterial	(S. A. Khan *et al*., 2021)
Pterospermum acerifolium	$Cu(NO_3)_2{\cdot}3H_2O$	46	Spherical	Antibacterial	(Saif *et al*., 2016)
Syzygium alternifolium	$CuSO_4.5H_2O$	17.2	Spherical	Antimicrobial Anticancer	(Yugandhar *et al*., 2017)
cordiamyxa	$CuSO_4.5H_2O$	20-26	Spherical	Antibacterial	(Ali Thamer & Tareq Barakat, 2019)
Camellia japonica	$Cu(NO_3)_2{\cdot}3H_2O$	15-25	Spherical	Antibacterial	(Kumar *et al*., 2020)
Tea leaves	$CuSO_4.5H_2O$	26-40	Spherical	Antibacterial	(Sorbiun *et al*., 2018)
Malva sylvestr	$CuSO_4.5H_2O$	5-30	Spherical	Antibacterial	(Nagajyothi, Muthuraman, et

is leaf					al., 2017)
Acalypha indica	$CuSO_4$	44-52	Spherical	Antibacterial	(Sivaraj *et al*., 2014)
Ormocarpum cochinchinense	$CuCl_2$	20	Spherical	Anticancer	(Gnanavel et al., 2017a)
Tecoma castanifolia	$CuSO_4$	<100	Spherical	Antibacterial	(Sharmila *et al*., 2016)
Galeopsidis herba	$CuSO_4$	5-15	Spherical	Antioxidant	(Dobrucka, 2018)
Hesperidin	$CuSO_4$	20-40	Spherical	Anticancer	(Stephen & Seethalakshmi, 2013)
Parthenium hysterophorus	$ZnSO_4$	22-94	Hexagonal	Antibacterial Anticancer	(Gupta *et al*., 2018)
Aloe vera extracts	$ZnSO_4$	26-73	Hexagonal	Anticancer	(A. Hussain *et al*., 2019)
Moringa Oleifera	$Zn(CH_3CHOO)_2$	52	Hexagonal Wurtzite	Antibacterial	(Pal *et a*l., 2018)
Tecoma castanifolia	$ZnSO_4$	70-75	Spherical	Antioxidant, Antibacterial Anticancer	(Sharmila, Muthukumaran, *et al*., 2018)
Costus pictus	$Zn(NO_3)_2.6H_2O$	29.11	Hexagonal	Antibacterial Anticancer	(Yugandhar *et al*., 2017)
Albizia lebbeck	$Zn(NO_3)_2$	66.25	Spherical	Anticancer	(Kalpana & Devi Rajeswari, 2018)
Deverra tortuosa	$Zn(NO_3)_{2.}6H_2O$	15.22	Hexagonal	Anticancer	(Selim *et al*., 2020)
Pongamia Pinnata	$Zn(NO_3)_{2.}6H_2O$	100	Hexagonal	Antibacterial	*(Sundrarajan et al*., 2015)
Strawberry	$Zn(CH_2COO)_2.2H_2O$	30-40	Spherical	Antibacterial	(Bayat *et al*., 2019)
Olea europaea	$ZnSO_4.7H_2O$	20-40	Spherical	Antibacterial	(Alrubaie & Kadhim, 2019)
Ocimum tenuiflorum	$C_4H_6O_4.Zn.2H_2O$	36.28	Hexagonal	Antioxidant	(Sushma *et al*., 2016)
Catharanthus roseus	$ZnSO_4$	22-94	Hexagonal	Antibacterial	(Gupta *et al*., 2018)
occinia abyssinica	$Zn(CH_2COO)_2.2H_2O$	10.4	Hexagonal	Antioxidant Antibacterial	(Safawo *et al*., 2018)

Rheum rhaponticum	$Zn(CH_2COO)_2.2H_2O$	30	Spherical	Anticancer	(Salari & Neamati, 2019)

2.6. Anticancer Activity

2.6.1. Breast cancer

Cancer is a generic name for diseases known by the development of abnormal cells that grow and divide uncontrollably due to multiple changes in genes and can break into and destroy normal parts of the body tissue (Punnoose *et al.*, 2014). Cancer induces various pathological and metabolic changes in cellular systems and is the second leading cause of death around the globe next to cardiovascular disease. Distressingly cancer kills about 8.8 million people each year, accounting for one out of six deaths and more than the total number of deaths from HIV/AIDS, malaria, and tuberculosis. According to the World Health Organization (WHO) report, cancer caused 7.4 million deaths in 2004, 8.2 deaths in 2012, 9.6 million deaths in 2018, and expected to increase approximately 12 million deaths in 2030. (Kantelhardt *et al*., 2014, Casais-Molina *et al*., 2018).

According to the 2014 World Health Organization report, the number of new cancer cases is expected to increase from 14 million to 22 million, in the coming 20 years (Vinardell & Mitjans, 2015). Among various groups of cancer, lung cancer is the leading cancer that causes 1.5 million deaths, whereas liver, stomach, colorectal, breast, and esophageal cancer causes 745,000, 723,000, 694,000, 521,000, and 400,000 deaths respectively. Breast cancer is the most often diagnosed among all other cancers that develop in the lining of the milk duct. Breast cancer became the most frequent class of fatal cancer in women throughout the world a few decades back.

Nowadays, cancer is treated by chemotherapy, surgery, radiotherapy, and immunotherapy (Al-Sheddi *et al*., 2018). Inappropriately, the existing therapeutic methods for these cancers are unsatisfactory and signify a great challenge as many patients have cancer recurrence and severe side effects. For example, Methotrexate (MTX) is a well-established (antineoplastic or cytotoxic) chemotherapy and immunosuppressant drug used to treat different types of cancer, but its usage requires high doses causing severe side effects. Due to this researchers probe novel drugs with high antitumor efficacy in addition to safety (Nabil *et al.*, 2020, Pugazhendhi *et al*., 2019).

Breast cancer is the most common malignancy and one of the deadliest after lung cancer in women worldwide. It is metastatic cancer that is transferred to different organs such as the bone, liver, lung, and brain, which mainly accounts for its incurability. Breast cancer accounted for approximately 570,000 deaths in 2015 (Pugazhendhi *et al*., 2019; Salari & Neamati, 2019). Over 1.5 million women (25% of all women with cancer) are diagnosed with breast cancer every year throughout the world. In 2016, ~ 61,000 new cases of in situ breast cancer and 249,000 new invasive breast cancer cases were estimated in the USA (Tang *et al*., 2017; Santhoshkumar & Balupillai, 2018). In 2017, it was estimated that 30% of all new cancer cases (252,710) among women cancers are breast cancer in America. In the US, over 266,000 new cases of invasive breast cancer are expected to be diagnosed in women, along with nearly 64,000 new cases of non-invasive breast cancer in 2018. Nowadays, such virulence disease is treated by commonly known methods such as surgery, chemotherapy, and radiotherapy which have adverse side effects on normal cells. Due to this, various NPs have been discovered and synthesized to be able to selectively target tumor cells without causing any harm to the healthy cells (Zubair *et al*., 2021, Rao *et al*., 2016, Sun *et al*., 2017, Azizi *et al*., 2017, Selvakumari *et al*., 2015; Poller *et al*., 2017). Among these, Co_3O_4, NiO, ZnO, and CuO NPs and their composition have been studied. Breast cancer is a complicated illness with several potential causes, and it frequently results from the combination of various elements, such as genetic, hormonal, environmental, and lifestyle factors.

2.6.2. Anticancer Activity of MONPs

MONPs gain diverse applications due to their unique antibacterial, anticancer, antioxidant, antifungal, and enzyme inhibition properties. Among the MONPs, Co_3O_4 NPs find immense applications and attract numerous research interests. Co_3O_4 NPs have a potent potential in cancer treatment, even though their cellular mechanistic interactions are still poorly understood (S. Khan *et al*., 2015).

Huang *et al*., (2020) determined that Co_3O_4 NPs can induce lysosomal function damage by inhibiting lysosomal proteolytic activity (X. Huang *et al*., 2021).

Raeis *et al*., (2021) reported the cytotoxicity effect of green synthesized Co_3O_4 NPs on astrocytoma cells. The activity of NPs depends on their concentration and the IC_{50} value was found to be ~55 µg/mL which indicates the green synthesized Co_3O_4 NPs have an optimal toxicity on U87 cells (Raeisi *et al*., 2021).

Khan *et al*., (2015) reported that the synthesized Co_3O_4 NPs have great anticancer potential against cancerous cell lines; rather they have no significant toxic effect on normal cells. They investigated the potential cytotoxic of Co_3O_4 NPs in human colorectal types of cancerous cells HT29 and SW620 and obtained IC_{50} values of 2.26 and 394.5 μg/mL respectively (Hafeez *et al*., 2020, S. Khan *et al*., 2015).

The cytotoxic activity of *P. guajava* plant extract mediated Co_3O_4 NPs against breast cancer cell lines using the MTT test was investigated. Its percentage cytotoxic activity was observed as 90, 83, 77, 68, 61, 58, and 52% against MCF-7 cells compared to control cells in which the cell viability decreases with concentration increase (Govindasamy, Raja, Singh, Govindarasu, & Sabura, 2022).

ZnO NPs have a unique performance that makes them appropriate for various biomedical applications which approved by the Food and Drug Administration (FDA, USA) vouch for their biocompatible nature. The Zn^{2+} of ZnO NPs can generate ROS when it interacts with the cell and shows higher toxicity against cancer cells. In addition to this, ZnO NPs used as an effective carrier for the targeted delivery of several anticancer drugs into tumor cells (Vinardell & Mitjans, 2015, Sushma *et al*., 2016).

Table 2: The IC_{50} values for cancer (MCF-7) and healthy (HFF & HDF) cells

	Time of Incubation	Cancer cell	Normal cell	
		MCF-7	HF-F	HD-F
IC_{50}	24 hr	12 μg/ml	30 μg/ml	147 μg/ml
	48 hr	11 μg/ml	25 μg/ml	137 μg/ml
	72 hr	8 μg/ml	12 μg/ml	137/ml

Gowdhami *et al*., (2019) reported that the *Gracilaria edulis* plant extract mediated ZnO NPs showed the anticancer potential on cervical cancer cell lines. The particles showed the concentration cytotoxicity with an IC_{50} value of 35 μg/mL in cervical cancer cells which did not show any toxicity towards normal healthy peripheral blood mononuclear cells even at 200 μg/mL concentration. This particle also caused 100% death in HeLa cells at the highest concentration of 200 μg/mL, whereas around 80% of cells were alive at the same concentration in HEK-293 cells.

Selim *et al*., (2020) investigate the potent anticancer activity of *Deverra tortuosa* plant extract mediated ZnO NPs. The activity was *in vitro* probed against human colon adenocarcinoma "Caco-2" and human lung adenocarcinoma "A549" compared to their activities on the human lung fibroblast cell line using the MTT assay. The green synthesized ZnO NPs showed remarkable selective cytotoxicity against these cancer cell lines (Selim *et al*., 2020).

Salari *et al*., (2019) and Salari & Neamati, (2019) examined the anticancer activity of *Rheum rhaponticum* waste extract mediated ZnO NPs on MCF-7 breast cancer cells and the impact on normal (HFF and HDF) cells. The cytotoxicity of ZnO NPs on both cancerous and normal cells was measured in terms of concentration and time dependent treatment.

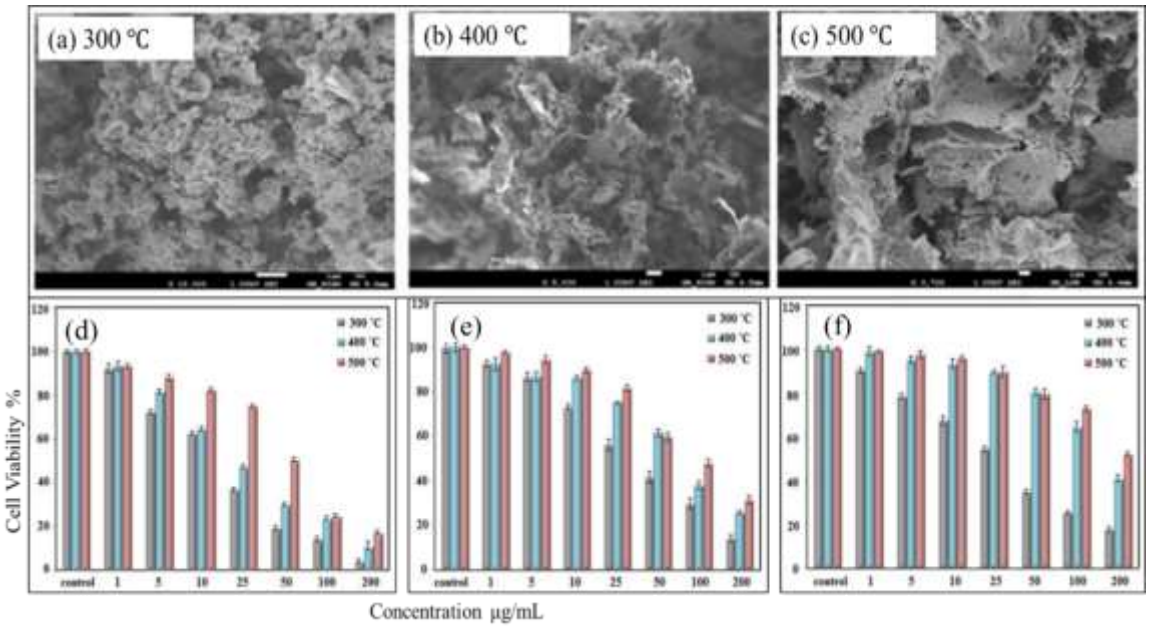

Figure 10: TEM images of NiO NPs synthesized at 300 ˚C (a), 400 ˚C (b) and 500 ˚C (c) and its cell viability against MCF-7 (d), Hep-G2 (e), and HT-29 (f) cancer cell lines (Kouhbanani *et al*., 2021).

The treatment indicated the IC_{50} values of MCF-7 cancer cells are different from those of normal (HFF and HDF) cells. The values of IC_{50} indicate that ZnO NPs have lower cytotoxic effects on healthy (HFF & HDF) cells in contrast to cancerous cells. The anticancer activity of ZnO NPs on MCF-7 (Breast cancer cell) was reported by Shobhaa and his coworkers. The cancerous cell exhibited a 50% reduction at a very low concentration of 31.2 µg/ml (Shobhaa *et al*., 2017).

Nickel oxide nanoparticles attract the attention of researchers, because of their unique properties such as optical, electronic, and physiochemical properties. Nowadays, NiO NPs are synthesized by using green methods (plant, algae, bacteria, and fungi) for different applications like sensors, drug delivery, antimicrobial, anticancer, etc. Among them, anticancer activity green synthesized NiO NPs have been widely studied. Kouhbanan *et al*., (2021) reported the anticancer activities of NiO NPs against human liver cancer cell (Hep-G2), breast cancer cell (MCF-7), and colon cancer cell (HT-29) lines using the MTT assay. In the report, NiO NPs synthesized at 300, 400, and 500 ℃ showed higher cytotoxicity effects. However, NiO NPs synthesized at 300 ˚C have higher cytotoxicity effects than at 400 and 500 ℃ due to their small size as shown in Figure 10 (Kouhbanani *et al*., 2021).

Ezhilarasi *et al*., (2016) also reported the anticancer activity of *Moringa oleifera* extract mediated NiO NPs against HT-29 cancer cells. The small size of NiO nanoparticles causes cytotoxicity in cell lines that showed changes in cell morphology due to the cell swelling and breaking as a result of apoptosis. Unlike that in the controlled cells, NiO NPs caused DNA destruction by apoptotic process (Angel Ezhilarasi *et al*., 2018).

The current treatment methods for cancer are associated with toxicity in healthy tissues, partial therapeutic response, drug resistance, and finally recurrence of the disease. Cancer drugs are challenged by non-specific binding, undesired toxicity in healthy cells, low therapeutic index, and finally poor therapeutic outcome (Nagaraj *et al*., 2019). To overcome the challenge MONPs are being engineered to enhance the transport property of therapeutic agents and diagnostic tools through the complex biological barriers and to aid the interaction with biomolecules. Of them, CuO NPs play a crucial role in filtering the compatibility and bioavailability of natural products in the treatment of cancer due to their specific interaction with and disruption of the mitochondrial respiratory chain (Gnanavel et al., 2017b). It can also disorder mitochondrial function by generating ROS and suppressing ATP synthesis, which leads to DNA damage. The biocompatibility of CuO NPs was evaluated by in vitro cytotoxicity assay for their potential in vivo biomedical applications such as targeted drug delivery, cancer cell diagnostics, and therapeutics (Rehana *et al*., 2017, K. Ali *et al*., 2020).

Akintelu *et al*., (2020) reported that black bean extract mediated CuO NPs reduce the growth of cervical carcinoma cells by altering the mitochondrial structure. It has been also reported green

synthesized CuO NPs using *Ficus religiosa* showed potential anticancer efficiency against the growth of A549 adenocarcinomic human alveolar basal epithelial cells (Sankar *et al*., 2014). The cytotoxicity of *Pterolobium hexapetalum* plant leaf mediated CuO NPs against human breast cancer cell lines clearly showed enhanced effectiveness (Nagaraj *et al*., 2019, Akintelu *et al*., 2020).

Wu *et al*., (2018) investigate the in-vitro cytotoxicity of CuO NPs synthesized by using *Coleus aromaticus* leaf extract. The in-vitro of the synthesized was studied by investigating the cell viability of A549 cell lines (Wu *et al*., 2019).

2.6.3. Anticancer Activity of CSNs

CSNs have attracted considerable interest in the field of cancer therapy due to their unique properties, which can be customized for various anticancer activities. These nanostructures consist of a core material surrounded by a distinct shell, which can be designed to encapsulate drugs, enhance targeting, improve biocompatibility, and provide controlled release of therapeutic agents. CSNs can be designed to precisely target cancer cells by functionalizing the shell with atoms that identify and bind to receptors overexpressed on cancer cells, delivering the encapsulated medications directly to the tumor location while decreasing systemic toxicity. The nanostructure's shell can operate as a barrier, controlling medication release.

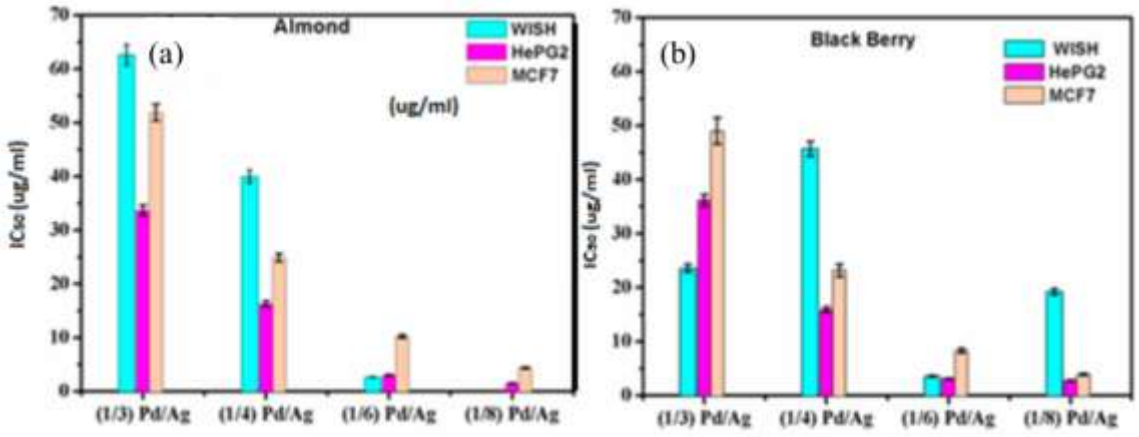

Figure 11: The IC_{50} values of Ag@Pd core-shell NPs (a) Almond and (b) blackberry fruit extract mediated against HEPG2 and MCF-7 cancer cells compared to the normal one *(Abdel-Fattah* et al*., 2017)*.

This is especially important for chemotherapeutic medicines since it enables the drug's continuous release over time, ensuring effective concentrations at the tumor location while

avoiding adverse effects. The size and surface features of CSNs can be adjusted to take advantage of the enhanced permeability and retention effect, which occurs when tumors have leaky vasculature, allowing nanoparticles to aggregate preferentially in tumor tissue (Ahmadi Bakhtiari *et al*., 2022).

Several studies on the anticancer activity of CSNs synthesized using different methods have been reported. The anticancer potential activity of biogenic synthesized Ag@Pd core-shell nanoparticles utilizing blackberry fruit and almond (*Prunusamygdalus*) was reported by Wafa *et al*., 2017, Abdel-Fattah *et al*., 2017). The image size analyzer showed 8 ± 0.26 and 6 ± 0.23 nm for almond (Prunusamygdalus) and black berry fruit extract mediated Ag@Pd core-shell nanoparticles respectively.

The anticancer activity of Ag@Pd core-shell NPs against human breast cancer (MCF-7) and hepatocellular carcinoma (HEPG2) cell lines at different concentrations was investigated by using an MTT assay as depicted in Figure 12. The almond extract mediated Ag@Pd core-shell NPs showed slightly more effectiveness than blackberry fruit extract due to its morphology resulting from the function group belonging to the plants.

Elbaz *et al*., (2016) examined the cytotoxicity of Ag@PVP core-shell nanoparticles against MCF-7 cancer cells and 1BR hTERT normal cells by using MTT assay. The report indicates that Ag@PVP core-shell nanoparticles showed higher cytotoxicity against MCF-7 cancer cells in contrast to normal 1BR hTERT cells. The Ag@PVP core-shell nanoparticles pass through the cell membrane via endocytosis and localize into the lysosomes. In an acidic environment, Ag^{+} of nanoparticle is released ultimately inducing the generation of ROS.

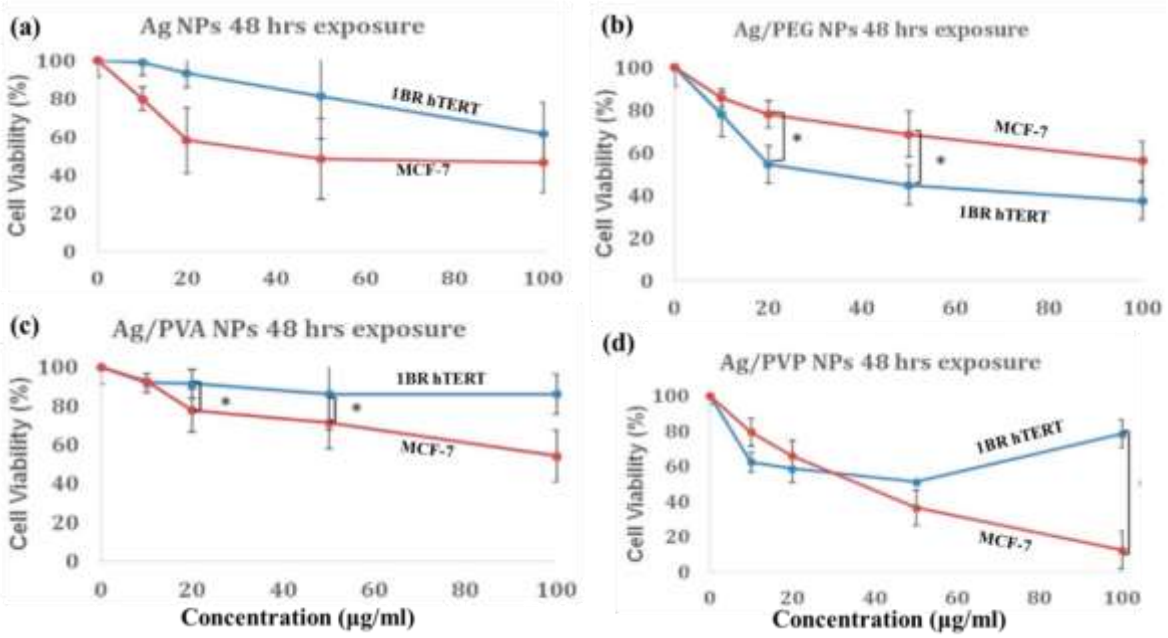

Figure 12: The percentage of viable MCF-7 cells and 1BR hTERT cells treated for 48 h with (a) Ag NPs, (b) Ag/PEG NPs, (c) Ag/PVA NPs, and (d) Ag/PVP NPs (Elbaz *et al*., 2016).

The mitochondria are disrupted by induced ROS and silver ions that result in DNA damage and cell death. The report implies that Ag@PVP core-shell nanoparticles are highly cytotoxic MCF-7 cancer cells and PEG-coated Ag NPs which are more cytotoxic to normal cells as shown in Figure 12 (Elbaz *et al*., 2016).

Kovács *et al*. showed the extraordinary in vivo metastasis-suppressing power of Au@Ag CSNs in metastasis-promoting cells in the reactive stroma (Kovács *et al*., 2020).

The cytotoxic effect of *Garcinia mangostana* peel extract mediated Au NPs and Au@Ag against colon-derived HCT-116 (cancer) and CCD-112 (normal) cells was also reported (Lee *et al*., 2022).

2.7. Antibacterial Activity

Human beings have been living unfriendly with several microorganisms which is a potential cause of different infectious diseases. During the 20th century, the investigation of antibacterial for the treatment of bacteria caused infection was the most prominent. According to WHO, bacteria can be attacked by antibacterial drugs. The first medicine discovered for the treatment of infectious disease specifically syphilis was Salvarsan which is nontoxic to the patients. However, it was not used until the discovery of Penicillin, in 1928 by Alexander Fleming (Peterson &

Kaur, 2018, Reta *et al*., 2019). Several antibacterial were produced between 1930 and 2000However due to they are capable of horizontal gene transfer between different species, enzymatic degradation of antibacterial drugs, alteration of bacterial proteins that are antimicrobial targets and changes in membrane permeability to antibiotics the evolution of new resistant discovery of new molecules with antibacterial activity has become even more challenging to the pharmaceutical industry (Sánchez-López *et al*., 2020, Tanwar *et al.*, 2014).

A recent study indicates even though the struggle to defeat bacterial pathogens continues, bacteria are still resisting several antibiotics as shown in Figure 13. Currently, the profile studies of antimicrobials have proved that bacteria that cause infections become resistant to different groups of antibiotics. The WHO reported that the rate of resisting drugs becomes high in bacteria such as *E. coli* against antibiotics as cephalosporin and fluoroquinolones, *K. pneumoniae* against *cephalosporin* and *carbapenems*, *Staphylococcus aureus* against methicillin, *S pneumoniae* against penicillin, *N Salmonella* against fluoroquinolones, *Shigella* species against fluoroquinolones, *Neisseria gonorrhoeae* against cephalosporin, and *Mycobacterium tuberculosis* against rifampicin, isoniazid, and fluoroquinolone causing common infections (like urinary tract infections, pneumonia, and bloodstream infections) and high percentage of hospital-acquired infections (Bridges *et al*., 2020, Tanwar *et al*., 2014, Sánchez-López *et al.*, 2020).

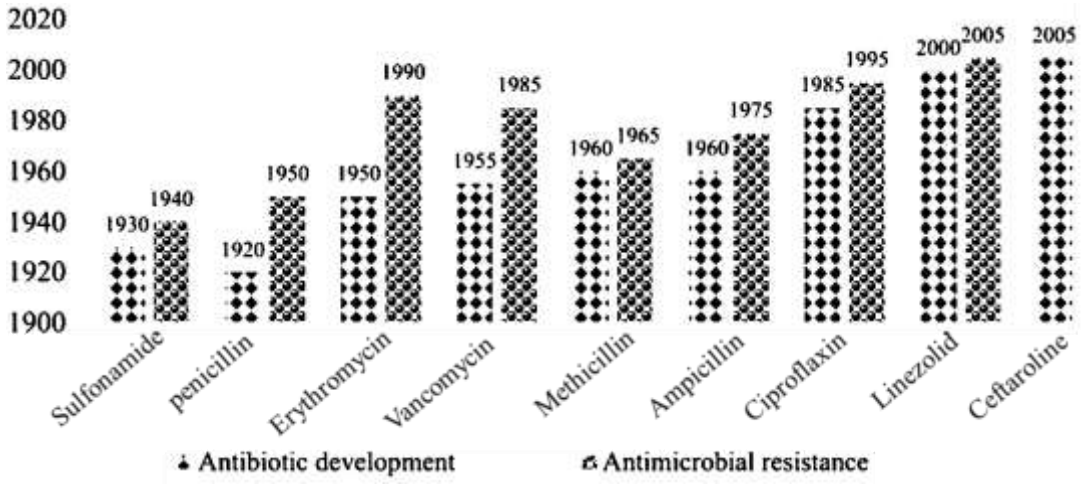

Figure 13: The time of antibiotic development and resistance by bacterial strains.

Thus, the continuous emergence of bacterial resistance has challenged the research community to develop novel antibiotic agents. Among the most promising of these novel antibiotic agents are metal and MONPs, which have shown strong antibacterial activity in a devastating number of studies (Gupta *et al*., 2018).

In contrast to other antibiotics, MONPs with antibacterial activities have the potential to kill or inhibit bacterial growth by targeting multiple biomolecules. A high antimicrobial activity of MONPs depends on the particle size that allows greater surface contact and a direct interaction with the membrane's microorganisms. Nanoparticles smaller than 10 nm highly interact with bacteria and produce electronic effects which improve the reactivity of NPs. Thus, it is proven that the bactericidal effects of NPs are size dependent (Turakhia *et al.*, 2020, Benhammada & Trache, 2021). MONPs are known for their potent capability to inhibit the growth of a wide range of bacteria. MONPs release positively charged ions that interact with the negatively charged surface of bacteria cell walls causing cell wall or membrane disruption. The metal ions enter the cytoplasmic membrane interact and inhibit molecules such as proteins or nucleic acids and then resulting in the generation of ROS that is toxic to the bacteria (Usmani *et al.*, 2018).

The cell membranes of the microorganisms interact with the medium so metal oxide NPs have some interactions to release metal ions that interfere with the processes of deoxyribonucleic acid (DNA) replication, cell membrane formation, and cell division (Kumar *et a*l., 2020). Several studies propose that MONPs attach to the surface of the cell membrane disturbing the permeability and respiration function of the cell. The damage to the cell may be caused by the interaction of NPs with sulfur or phosphorus containing biomolecules in the cell such as DNA. As a result of electrostatic attraction and affinity to sulfur proteins, metal ions can adhere to the cell wall and cytoplasmic membrane (Khandel *et al.*, 2018). The adhered metal ions can enhance the permeability of the cytoplasmic membrane and lead to disruption of the bacterial envelope. After the uptake of free metal ions into cells, respiratory enzymes can be deactivated, generating ROS but interrupting adenosine triphosphate production (Bouafia *et al.*, 2020). ROS can be a principal agent in the provocation of cell membrane disruption and deoxyribonucleic acid (DNA) modification. As sulfur and phosphorus are important components of DNA, the interaction of metal ions with the sulfur and phosphorus of DNA can cause problems in DNA replication, cell reproduction, or even result in the termination of the microorganisms. MONPs also have the ability to penetrate bacterial cell walls and subsequently change the structure of the cell membrane, because of their nanoscale size. The denaturation of the cytoplasmic membrane can rupture organelles, and even result in cell lysis (Din *et al.*, 2017, Dessen e*t al.*, 2001, Lan *et al.*, 2014, Khandel *et al.*, 2018).

2.7.1. Bacterial Strains

From a clinical perspective, the bacteria justifying the term most fully are multi-resistant Gram-positive and Gram-negative species that are classified based on their cell wall structures. The Gram-positive bacteria such as *Staphylococcus aureus* and *Bacillus subtilis* have a thick layer of peptidoglycan in their cell walls which are decorated with teichoic acid polymers and covalently-bound proteins and provide bacterial structure, tensile strength, and counteracting the osmotic pressure imparted by the cytoplasm (Kamurai *et al*., 2020, Teshome *et al*., 2020). In Gram-positive bacteria, the peptidoglycan has a large permeability threshold and is accessible for several molecules. Due to this, such types of bacteria are susceptible to various antibiotics. But the Gram-negative bacteria such as *E coli*, *P. aeruginosa,* and *P. vulgaris* have a thin peptidoglycan layer. However, the Gram-negative bacteria are intrinsically insusceptible to many of these antibacterial agents owing to the presence of a much finer molecular sieve, called the outer membrane that framed a thin peptidoglycan layer (Cox & Wright, 2013, Din *et al*., 2017).

Staphylococcus aureus is both a commensal bacterium and a human pathogen and is the most dangerous of all of the many common staphylococcal bacteria that cause a wide variety of infections such as skin infections, heart valve infections, and bone infections. *Staphylococci* are gram-positive bacteria that are characterized by individual *cocci* that appear to be divided into more than one plane to form grape clusters that are none motile and none spore-forming facultative anaerobes and grow by aerobic respiration or by fermentation pathogenic (Nabera, 2009); (Neupane *et al*., 2018). *S. aureus* is a member of the genus *staphylococci* which is named *aureus* due to its golden color appearance as it grows on solid media. The cell wall of *S.aureus* is 50% peptidoglycan by weight which consists of alternating polysaccharide molecules of N-acetylglucosamine and N-acetylmuramic with 1, 4 – β bonds. The surface features of staphylococcal have a secretory signal sequence at the N terminal, positively charged amino acids that extend into the cytoplasm, a hydrophobic membrane-spanning domain, and a cell-wall–anchoring region, all at the carboxyl terminal. This bacteria can destroy human tissues by producing different enzymes, such as protease, lipase, and hyaluronidase (D.lowy & M.D., 1998, Slavin *et al*., 2017, Tong *et al*., 2015).

Escherichia coli is a Gram-negative bacteria found in the environment, foods, and intestine of humans and animals. It exhibits phospholipids, lipopolysaccharides, colanic acid and about 50%

of its outer membrane consists of proteins attached to the membrane. *E. coli* strains are comparatively easy to grow under both aerobic and anaerobic conditions some of *E. coli* isolates are considered part of the beneficial normal flora of the intestine but some strains appeared to acquire pathogenicity mechanisms to cause disease in humans such as urinary tract infections and sepsis or meningitis (Wang *et al*., 2021, Happy *et al*., 2019).

Bacillus subtilis is a Gram-positive bacterium that was used many years ago as a model to determine the molecular pathways that control biofilm formation. It is known for aerobic, endospore-forming, and rod-shape among the phylum Firmicutes and family Bacillaceae. Peptidoglycan in the cell wall of *B. subtilis* is responsible for shape determination and cellular viability. The peptidoglycan polymer is formed from an irregular sequence of glycan strands of repeating disaccharide residues, cross-linked via peptide side chains which allow a high osmotic pressure inside the cell (Bridier *et al*., 2011, Harwood *et al*., 2001).

Klebsiella is a type of Gram-negative bacteria that can cause infections such as pneumonia, bloodstream infections, urinary tract cystitis, wound or surgical site infections, and meningitis. *Klebsiella pneumoniae* is an encapsulated, non-motile bacterium found in the environment. *K. pneumoniae* strain is the most prevalent multidrug-resistant *Enterobacteriaceae* in hospitals worldwide. The Major factors of *K. Pneumoniae's* extreme harmfulness are the capsule, lipopolysaccharide, and adhesins. The capsule is one of the most important virulence determinants, protecting against serum bactericidal activity, antimicrobial peptides, and phagocytosis (De Souza *et al*., 2019, Tanwar *et al*., 2014).

2.7.2. Antibacterial Activity of MONPs

Co_3O_4 NPs can interact with the sulfur of protein contained in the bacterial cell membrane and DNA. The NPs preferably attack the respiratory chain and cell division of bacteria, finally leading to cell death. The NPs release cobalt oxide in the bacterial cells enhancing their bactericidal activity.

Dewi *et al*., (2020) reported that the potent antibacterial activity of *Populus ciliata* leaf extract mediated Co_3O_4 NPs and the activity was concentration dependent. The green synthesized Co_3O_4 NPs were higher against gram-positive bacteria as compared to gram-negative bacteria (Dewi *et al*., 2019). The maximum inhibition zone 24.5 ± 1.3 against B.subtilis which is gram-positive

and 20.4 ± 0.7 for *Klebsiella pneumoniae* gram-negative bacteria was observed. In this report, the green synthesized Co_3O_4 NPs are more efficient against B.subtilis than antibiotics used as a control during their study. The gram-positive bacteria are more exposed to Co_3O_4 NPs due to the high permeability of porous on the bacteria cell walls in contrast to gram-negative bacteria and such a structure of cell wall facilitates the maximum absorption of NPs.

Saeed *et al*., (2018) synthesized Co_3O_4 NPs using leaves extract of *Salvia hispanica* and evaluated its antibacterial activity. The particle showed noble antibacterial activity in comparison with the standard drugs and control (Nomura *et al*., 2019).

Urabe and Aziz (2019) synthesized Co_3O_4 NPs using Apium graveolens and Camellia sinensis extracts and studied their antibacterial activities against Gram-negative (*P. aerugino*) and Gram-positive (*S. aureus*) bacteria. The Co_3O_4 NPs with 21-72 nm size inhibit Gram-negative (*P. aerugino*) at about 17 mm and Gram-positive (*S. aureus*) at 12 mm and 200 µg/ml (Urabe & Aziz, 2019).

The bacterial inhibition by ZnO NPs could be attributed to its high specific surface charge and ROS generation. Naseer *et al*., (2020) reported the antibacterial activities of ZnO NPs synthesized using *Cassia fstula* and *Melia azadarach* plant extracts against Gram-negative pathogen) *E. coli* and (Gram-positive pathogen) *S. aureus*). In contrast to standard antibiotics, the biosynthesized ZnO nanoparticle showed strong bacterial activity. Gram-negative standard drugs inhibit from 15-20 mm whereas green synthesized ZnO NPs inhibit in the range of 16-40mm. *S. aureus* was resistant to a variety of standard drugs and the zone of inhibition for the rest of the standard drugs ranged from 4-13 mm while that of ZnO NPs was 14-37 mm in range (Naseer *et al*., 2020).

Mahendra *et al*., (2019) determined the antibacterial activity of ZnO NPs synthesized using leaf extracts of *Canthium dicoccum*. The particles are highly effective against *B. subtilis* and less sensitive against *Stapyhlococcus aureus*. The inhibition zone of ZnO NPs is 18.33, 16.33, 15.66, and 15 mm against *B. subtilis*, *E. coli*, *P. aeruginosa* and *S. aureus* respectively. The study indicates that the green synthesized ZnO NPs have antibacterial effective activity in contrast to plant leaf extract reported by (Prashanth *et al*., 2015, Shivappa *et al*., 2018).

Suresh *et al*., (2014) reported the antibacterial activity of green synthesized ZnO NPs against Gram-negative and Gram-positive. The particles showed significant activity on four selected bacterial strains at 500 and 1000 mg concentrations (Suresh *et al*., 2014).

A few decades ago, the prevalence of bacterial borne diseases increased intensely. The continuous placement of antibacterial agents in treating infections caused the development of drug-resistant bacteria. The bacterial borne infections mostly occur around the hospitals, due to the availability of a variety of bacterial strains that enable to copying of genes from one another to develop new gene orders. Bacteria with modified gene order can resist the existing antibacterial agents and cause different infections. Henceforth, the researchers developed a potential antibacterial agent at nanosize. The recently fabricated and widely used nanoparticle is metal oxide nanoparticles. The antibacterial activity of NiO NPs against various bacterial pathogens has been studied (Ezhilarasi *et al*., 2016, R. K. Das *et al*., 2017, Sabouri *et al*., 2021).

Ezhilarasi *et al*., (2018) investigated the antibacterial activity of *Aegle marmelos* leaf extract mediated NiO NPs against two Gram-positive and Gram-negative strains. The report indicated that, the antibacterial activity of NiO NPs against two Gram-positive higher than the Gram-negative bacterial strains. The difference in the inhibition zone of treated bacteria is due to the thin layer cell wall with a single layer of peptidoglycan (Angel Ezhilarasi *et al*., 2018).

Haider *et al*., (2020) reported the antibacterial activity of NiO NPs synthesized using *zingiber officinale* and *allium sativum* extract. The garlic extract mediated NiO NPs showed a high inhibition zone in contrast to the ginger extract mediated against multidrug resistance bacteria due to the synergetic effect of phytochemicals in the plant and reduced NiO NPs (Haider *et al*., 2020).

Copper metal containing nanomaterials have potent applications in contrast to their parent material. P-type semiconductors CuO NPs with band gap energy of approximately 1.7 eV possess unique properties based on particle size, shape, morphology, and orientation (Ijaz *et al*., 2017). Among CuO NP's potent applications, antibacterial is the most common activity. The Cu^{2+} ions released from the CuO NPs have a potent effective nature in antibacterial activity (Bhuvaneshwari *et al*., 2018). The antibacterial activity of *Azadirachta indica* plant extract mediated CuO NPs was reported by Sharma *et al*., (2015). The antibacterial activity of CuO NPs at concentrations of 50 µl, 75 µl and 100 µl against the bacterial strain *E. coli* are observed as 17

± 0.25 mm, 19 ± 0.25 mm, and 20 ± 0.25 mm, respectively as indicated in Figure 14 (J. K. Sharma *et al*., 2015).

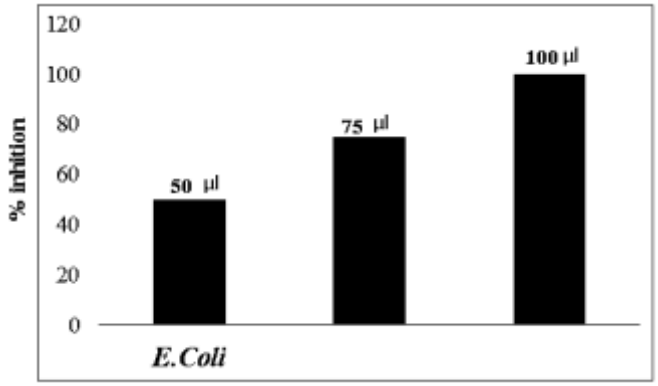

Figure 14: Antibacterial activity of CuO NPs against *E.Coli* (J. K. Sharma *et al*., 2015).

The Cu^{2+} of CuO NPs inhibits the bacteria by interacting with biomolecules such as protein, DNA, and enzymes. The ions released from NPs interact with DNA and break down the DNA strands leading to bacterial death.

Turakhia *et al*., (2020) investigated the antibacterial activity of *Carica papaya* leaf extract mediated CuO NPs against gram-positive and gram-negative bacterial strains. It has been also reported that CuO NPs have more toxicity on bacterial strains in contrast to *Carica papaya* plant extract due to the electrostatic interaction of Cu^{2+} with proteins, DNA, and cell walls that resulted in their denaturation (Singh *et al*., 2017, Turakhia *et al*., 2020).

Vaidehi *et al*., (2018) also reported that CuO NPs synthesized using *Solanum lycopersicum* aqueous leaf extract showed good antibacterial activity. CuO NPs showed different activity against *Bacillus subtilis, S.aureus,* and *E.coli* bacterial strains that increase with the increment of concentration (Bhuvaneshwari *et al*., 2018).

2.7.3. Antibacterial Activity of CSNs

Villalobos-Noriega, J. A., (2021) reported the antibacterial activity of *Rumex hymenosepalus* root extract mediated Au@Ag CSNs against *S. aureus, E. coli* as shown in Figure 15(a) and (b), respectively. The Au and Ag NPs, as well as the Au@Ag CSNs, inhibit the growth of the gram-positive bacteria *S. aureus* almost equally. However, the Au@Ag CSNs show good percent inhibition against *E. coli* in contrast to the parent nanoparticles (Villalobos-Noriega *et al*., 2021).

Additionally, the antibacterial activity of Ag@Pd core-shell NPs synthesized using almond and blackberry fruit extract against *S. aureus*, *E. coli*, and *C. albicans* was evaluated. Almond extract mediated Ag@Pd core-shell NPs showed higher inhibition against *S. aureus* than *E. coli* and *C. Albicans* as shown in Figures 15(c) and (d). Elyamny, S. reported the dose-dependent antibacterial activities of $Ag@Ag_2O$ CSNs on a variety of pathogens. The report demonstrates that at 50 µg/mL, $Ag@Ag_2O$ CSNs suppress *S.aureus, P.aerginosa, and C.vulgaris* biofilm disintegration by about 74.7, 67.8, and 83.5%, respectively.

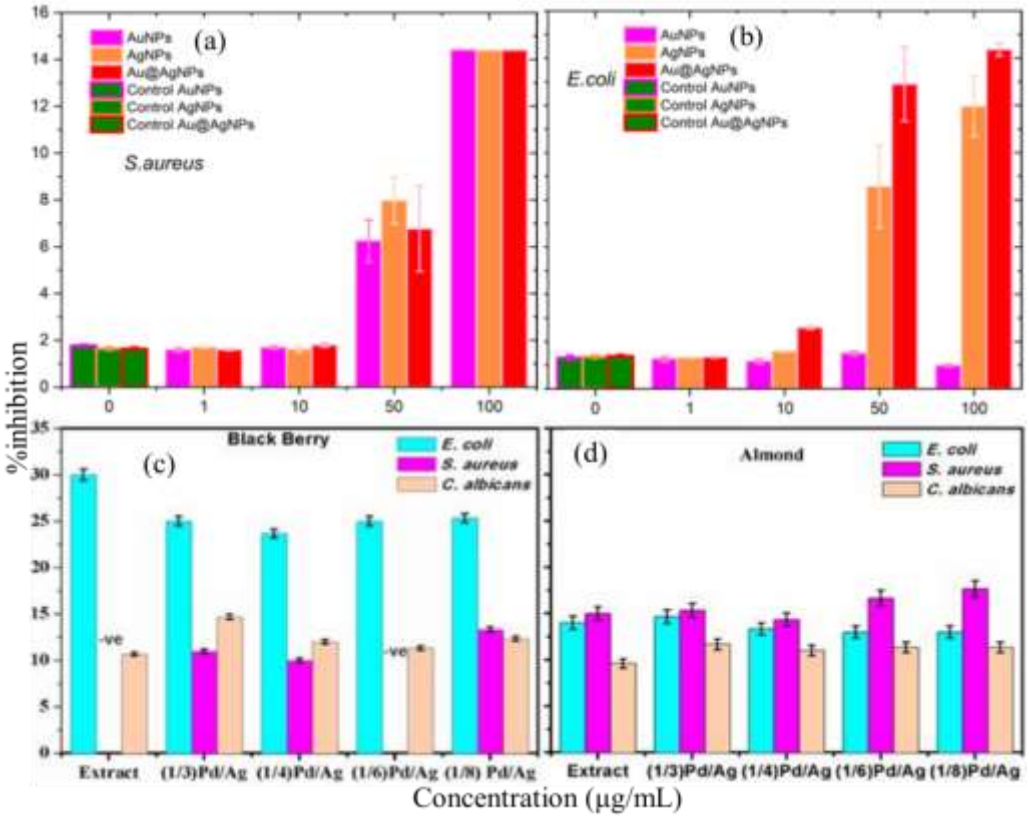

Figure 15: Antibacterial activity of Au@Ag CSNs (a) against *S. aureus*, (b) *E.coli* and antibacterial activities of Ag@Pd CSNs against *S. aureus*, *E.coli*, and *C.albicans* (c) Blackberry mediated and (d) Almond mediated (Abdel-Fattah *et al*., 2017).

2.8. Antioxidant Activity

The oxidative phosphorylation metabolism is processed in mitochondria and generates ROS such as superoxide ($O_2^{\bullet-}$), hydrogen peroxide (H_2O_2), and hydroxyl radical ($HO^{\bullet}$) which is a crucial molecule for cellular actions. The concentration of these reactive molecules is determined by the steadiness between the rate of production and consumption by oxidizing agents in the cell.

Several mechanisms are used by the cell to maintain the redox reaction when exposed to ROS (Navarro-Yepes *et al*., 2014, Pleńkowska *et al*., 2020). On the other hand, when ROS enthusiastically produced, the antioxidant in the cell cannot adjust to the normal level of redox homeostasis, thereby resulting in oxidative stress. The excessively produced ROS can cause indiscriminate damage to biological molecules such as proteins, nucleic acid, membranes, lipids and leading to loss of function and even cell death (Liang *et al*., 2020). The tissues and cells control the excessive production of ROS by using enzymatic components, such as superoxide dismutase, catalase, and glutathione peroxidase, and non-enzymatic such as vitamins C, A, and E, glutathione, and thioredoxin to protect themselves from ROS-induced cellular damage. However, the high increment and endogenously uncontrollable production of ROS causes oxidative stress and results in several diseases such as cancer, diabetes, metabolic disorders, and cardiovascular diseases. In aerobic organisms, ROS are derived from singlet oxygen molecules by receiving a single electron (Murray *et al*., 2021, García-Sánchez *et al*., 2020).

$$O_2 + e^- \rightarrow O_2^{\bullet -} \quad (1)$$

The superoxide ($O_2\bullet^-$) can react with a ferric ion (Fe^{3+}) in the cell and can result in the formation of reactive hydroxyl radical (HO•) by Fenton reaction (Navarro-Yepes *et al*., 2014, Liang *et al*., 2020).

$$O_2^{\bullet -} + H^+ \rightarrow O_2^{\bullet}H \quad (2)$$

$$O_2^{\bullet}H + O_2^{\bullet -} + H^+ \rightarrow H_2O_2 + O_2 \quad (3)$$

$$Fe^{3+} + O_2^{\bullet -} \rightarrow Fe^{2+} + O_2 \quad (4)$$

$$Fe^{2+} + H_2O_2 \rightarrow Fe^{3+} + HO^{\bullet} + HO^- \quad (5)$$

Recently, to combat the excessive production of ROS several organic and inorganic compounds are investigated. Amongst, inorganic substances specifically MONPs are studied and their potent antioxidant activities were assured (Pizzino *et al*., 2017).

2.8.1. Antioxidant Activity of MONPs

The green synthesized Co_3O_4 NPs have potent antioxidant activity due to their superior biomedical applications. The cobalt oxide NPs showed 2, 2-diphenyl-1-picrylhydrazyl (DPPH) free radical scavenging potential. Additionally, the plant extract mediated cobalt oxide NPs showed DPPH stable free radical scavenging potentials and antioxidant capacities. In another study, greener synthesis of cobalt NPs was reported by applying secondary metabolites from

Celosia argentea plant extract and showed antioxidant activities against DPPH radical, and their scavenging power was reportedly accelerated with increasing concentration. It was also reported that the radical scavenging activity of green synthesized Co_3O_4 NPs is dose-dependent (Ajarem *et al*., 2021, Khalil *et al*., 2020, Shaheen *et al*., 2020). Ullaha *et al.*, (2020) reported that the cytotoxic of Co_3O_4 NPs to macrophages (IC_{50}=58.55 mg/mL) than that of RBCs (IC_{50}>200 mg/mL). The report indicates that the green synthesized Co_3O_4 NPs have more potent antioxidant activity (Ullah *et al*., 2019). It has been reported that the *Sageretia thea* leaf extract mediated Co_3O_4 NPs showed strong antioxidant activity Khalil *et al*., 2017, Khalil *et al*., 2020). The highest DPPH radical scavenging (57%) was observed at 200 µg/ml while the scavenging ability decreased at lower concentrations.

ZnO NPs used as a significant antioxidant against reactive free radicals in protecting cellular defense against oxidative stress. Zinc metal ion in ZnO NPs reduces the reactive free radical species to maintain oxidative DNA damage and integrity within the cell (Sushma *et al*., 2016). Sushma *et al*., (2016) determined the antioxidant activity of *Ocimum tenuiflorum* plant leaf extract mediated ZnO NPs using DPPH and obtained the maximum inhibition (65.23%) and absorbance (0.6 a.u). Safawo *et al*., (2018) determine the antioxidant activity of *Occinia abyssinica* extract mediated ZnO NPs (ZnO Nps) which is measured by DPPH assay. In this report, the radical scavenging capacity ZnO Nps slightly lower than standard ascorbic acid in all concentrations. The radical scavenging activities of the particles showed increment with increasing the concentration with IC_{50} value of 127.74 µg/ml (Safawo *et al*., 2018). Lingaraju *et al*., (2016) evaluated the DPPH stable free radical scavenging activity of *Ruta graveolens* herbs mediated ZnO NPs. The absorbance of free radicals decreases as reduction takes place and the radical scavenging activity was reported for ZnO NPs. They also reported that the %inhibition of free radicals by ZnO NPs was obtained with IC_{50} having a value of 9.34 mg/mL as shown in Figure 16(a) (Lingaraju *et al*., 2016).

Raghavebdra *et al*., (2017) also reported that the green synthesized ZnO NPs using *Garcinia gummi-gutta* plant seed extract also showed antioxidant activity. The radical scavenging effects of ZnO NPs were reported at various concentrations (50, 100, 150, and 200 µg/mL) mixed with 1.0 mL of 50% methanolic solution containing 140 µl of 1 mM DPPH solution. The DPPH free radical scavenging activity with an IC_{50} value of 425 µg/mL, indicates ZnO NPs were proved to be potent inhibitors as shown in Figure 16(b). From the report, the difference in the percentage of

inhibition is due to the phytochemical of plants, size, and shape of particles. Previous reports have also shown the antioxidant activity of green synthesized ZnO NPs using different plants such as *Cassia fistula* (Pavan Kumar *et al*., 2015), *Aegle marmelos* (Mallikarjunaswamy *et al*., 2020), *Ocimum tenuiflorum* (Sushma *et al*., 2016), *Polygala tenuifolia* (Nagajyothi *et al*., 2015) and *Ruta graveolens* (Lingaraju *et al*., 2016) extract.

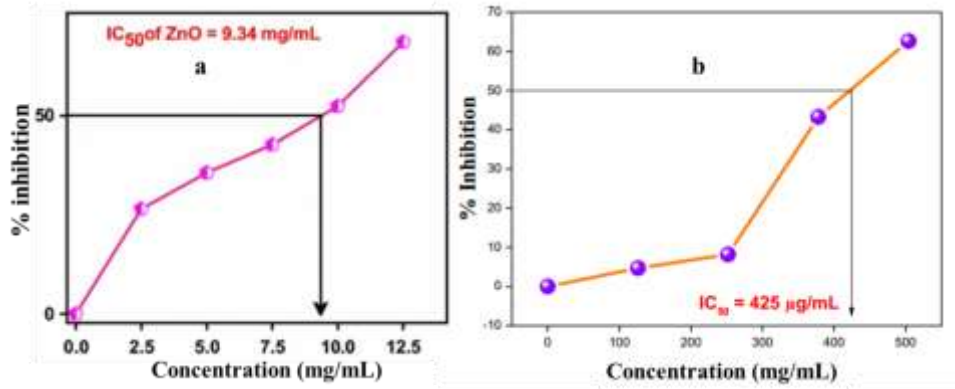

Figure 16: Antioxidant activity of ZnO NPs synthesized using (a) *Ruta graveolens* herbs and (b) *garcinia gummi-gutta* plant seed extract (Raghavendra *et al*., 2017).

The properties of MONPs are achieved by changing their size at the nanoscale which provides the capacity to use them in a variety of fields. Owing to their precise functional features and significance in a wide variety of technical applications, NiO NPs have been used. The numerous rewarding applications of NiO NPs in biomedical have been reported. As reported in some studies, NiO NPs have great potential antioxidant activity (Behera *et al*., 2019).

Khan *et al*., (2021) reported that the green synthesized NiO NPs showed higher antioxidant activity than chemically synthesized. The antioxidant activity of NiO NPs showed a superior linoleic acid peroxidation inhibition percentage compared to chemically synthesized NiO nanoparticles but slightly lower than plant extract and BHT. The greater inhibition observed in green synthesized NiO NPs is due to the synergetic effect of plant phytochemicals and NiO NPs. The report indicated the chemically synthesized NiO NPs had shown a toxic effect on fibroblast cells as many dead cells (Red) appeared compared to NiO NPs plant extract mediated. The bioactive molecules enhance the biocompatibility and dispersibility of green synthesized NiO NPs in cells (S. A. Khan *et al*., 2021). Haq *et al.*, (2021) also reported that the *Raphanus sativus* plant leaf extract mediated NiO NPs have potential antioxidant activity. The antioxidant activity

of the particle is concentration-dependent. As shown in the report, the scavenging activity of NiO NPs increases with their concentration (Dildar, *et al*., 2021)

Recently, CuO NPs have gained considerable interest due to their potential health benefit.
The antioxidant activity of green synthesized CuO NPs by plant extracts such as *Anthemis nobilis*, *Calotropis gigantea*, *Gloriosa superba*, *Cinnamomum camphora*, *Aloe vera,* and *Carica papaya* have been reported (Ghosh *et al*., 2020). Debrucka R. (2018), reported the antioxidant activity of green synthesized CuO NPs using the *Galeopsis speciosa* extract. The CuO NPs reduce the stable free radical DPPH, leading to the decrease in absorbance measured at 515 nm wavelength. The IC_{50} of CuO NPs was 4.12 µg/ml which indicates its high antioxidant activity (Dobrucka, 2018). Ijaz *et al*., (2017) reported that *Abutilon indicum* extract mediated CuO NPs synthesized showed a potential antioxidant activity.

2.8.2. Antioxidant Activity of CSNs

Antioxidants have an important function in maintaining a healthy cell state, as evidenced by extensive studies. The endogenous antioxidant defense mechanism is normally competent in dealing with free radicals in the body, but under disease-developing-threshold situations, the crucial requirement for exogenous antioxidants increases. Core-shell nanostructures can act as efficient antioxidants due to their unique features and the synergistic effects of the core and shell materials. Arriagada *et al*., (2019) reported the antioxidant activity of caffeic Acid grafted on amino-functionalized core-shell silica nanospheres (ACSSNs@CA). The CA enhances the capacity of the core materials to inhibit the DPPH free radicals (Arriagada *et al*., 2019). Mohamed *et al*., (2024) reported the antioxidant activity of *M. suaveolens* extract mediated $CoO@TiO_2$ and$Fe_2O_3@TiO_2$ CSNs was evaluated by DPPH. The report indicates the antioxidant activity was concentration-dependent. The antioxidant activity of $Fe_2O_3@TiO_2$ CSNs was revealed to be 76.34% at 0.11 mg/mL attended by a higher IC_{50} value of 0.055 mg/mL (Hammouda et al., 2024).

2.9. *Datura Stramonium*

Datura stramonium (D. stramonium) is a family of *Solanaceae* and is an annual flowering erect herb distributed in warm regions of the world. *D. stramonium* is known for its unpleasant odor and has a height of 0.6-1.2 m. It has hairy leaves with stalks 4-6 in long, pale green, and ovate

with a lightly hairy branched stem (Carpa *et al*., 2017). It is a common herb in disturbed areas, waste ground, fertile soils in fields, and roadsides and is well known for its potent pharmacological activity with great utility and usage in folklore medicine. Due to the presence of active phytochemicals, some species of *D. stramonium* are widely used in different medical treatments. Traditionally, *D. stramonium* plant extract was used for the treatment of diseases such as asthma, sinus infections, gastrointestinal problems, aches, abscesses, arthritis, boils, headaches, hemorrhoids, rattlesnake bites, sprains, swellings, burns, ulcers, and tumors (Kishore *et al*., 2016, Soni *et al*., 2012, Guo *et al*., 2018). Nowadays, it is added to the medicinal plants list which has a broad range of medicinal applications such as antinociceptive, antioxidant, hypolipidemic, anti-rheumatoid, and hypoglycemic properties (Batool *et al*., 2020, Rahmoune *et al*., 2017).

In addition to its very important medicinal role, it is toxic due to the presence of alkaloid groups: hyoscyamine, atropine, and scopolamine. *D. stramonium* is a hallucinogenic plant that causes serious poisoning. Taking any part of this plant may result in a severe anticholinergic reaction which causes toxicity and occasionally leads to diagnostic difficulties (Carpa *et al*., 2017, S. Das *et al*., 2012). In general, the potential activity in disease treatment and dangerous toxicity of *D. stramonium* plants is due to phytochemicals.

Figure 17: Leaf of *D. stramonium* plants (Kadam *et al*., 2018)

2.9.1. Phytochemical Constituents of *Datura Stramonium*

D. stramonium contains a variety of biologically active phytochemicals like alkaloids, atropine, scopolamine, tannin, fat, Phenols, Saponins, sterols, Steroids, glycosides Flavonoids, carbohydrates, and proteins (Batool *et al*., 2020). As documented in different reports, the leaf

and seed of *D. stramonium* are rich in alkaloids, including atropine, hyoscyamine, and scopolamine.

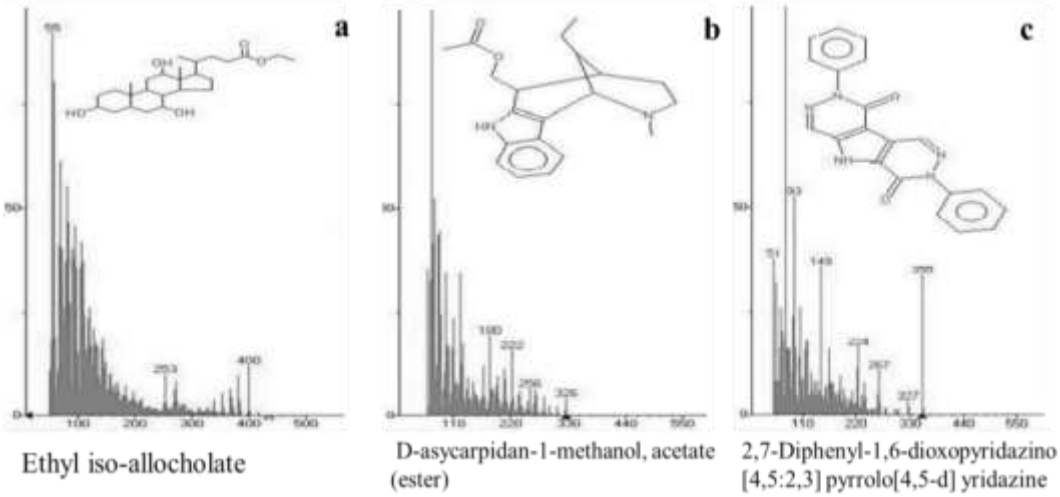

Figure 18: The Structure of Ethyl iso-allocholate (a), D-asycarpidan-1-methanol, acetate (ester) (b) and 2, 7-Diphenyl-1, 6- dioxopyridazino [4, 5:2, 3] pyrrolo [4,5-d] pyridazine (c) present in the leaves extract of *D. stramonium* using GC-MS analysis.

Huda *et al*., (2015) determined compounds of alkaloids ethanolic extract using gas chromatography-mass spectroscopy and investigated the Ethyl iso-allocholate, D-asycarpidan-1-methanol, acetate (ester) and 2,7-Diphenyl-1,6- dioxopyridazino [4,5:2,3] pyrrolo[4,5-d] pyridazine as shown in Figure 18 (Altameme *et al*., 2015). Miraldi *et al*., (2017) also determine the quantitative value of scopolamine and atropine in *D. stramonium* plant. The maximum contents of hyoscyamine and scopolamine in *D. stramonium* were found in the leaves. The maximum average atropine level in the leaves is within the range of 0.831 ± 0.014 μg/mg, while the maximum level of atropine in the flowers is 0.270 ± 0.026 μg/mg. On the other hand, the maximum scopolamine level in the stems and flowers is 0.129 ± 0.014 and 0.106 ± 0.031 μg/mg respectively (Altameme *et al*., 2015). In addition to this *D. stramonium* contains belladonnine, leucine, glutamic acid, enzymes, citric acid, malic acid, etheric oil, mineral salts, etc.

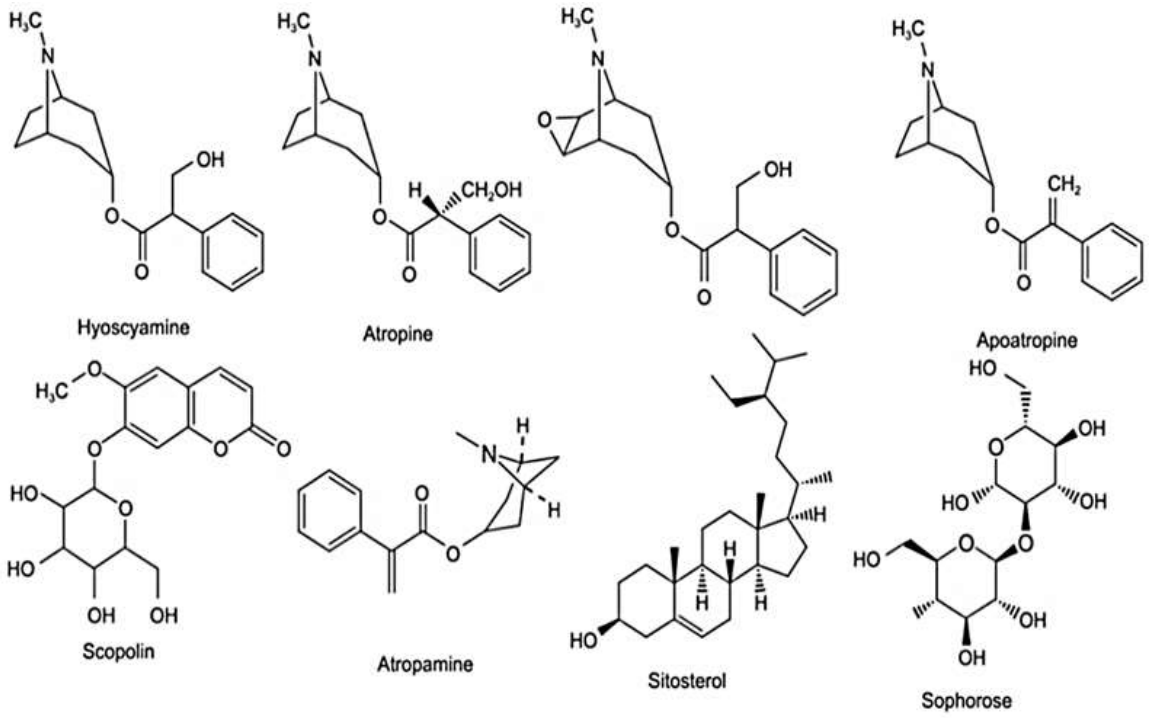

Figure 19: The chemical constituents of *D. Stramonium* plant (Batool *et al*., 2020).

Altameme *et al*., (2015), investigated some phytochemicals found in *D. stramonium* as shown in Table 3. The reported phytochemical study revealed the presence of alkaloids, flavonoids, saponins, tannins, and terpenoids. Furthermore, the quantitative analysis showed saponins (44.61 mg/g) and alkaloids (39.10 mg/g) were the dominant compounds followed by flavonoids (34.71 mg/g) and terpenoids (32.34 mg/g) (Altameme *et al*., 2015).

Table 3: Qualitative and quantitative investigation of *D.stramonium's* phytochemicals.

S.No	Qualitative test			Quantitative test
	Secondary metabolites	Color observation	Methanol extract	Metabolites mg/g
1	Flavonoids	Yellow	++	34.71±0.005
2	Terpenoids	Reddish brown	+	32.34±0.007
3	Saponins	Small bubble	+	44.61±0.007
4	Alkaloids	Reddish brown	++	39.10±0.009

The (+) moderately and (++) highly positive indicate the presence of phytocomponents.

D. stramonium's phytochemical components play an important role in green nanoparticle formation. These bioactive chemicals function as reducing and stabilizing agents, allowing the synthesis of stable, biocompatible nanoparticles with potential uses in a variety of fields. This environmentally friendly method complements the increased emphasis on sustainable and green chemical processes (Carpa *et al*., 2017).

3. Materials and Methods

The purpose of chemicals, materials, and advanced characterization techniques used in this work has been described. Additionally, the experimental procedures used for plant extraction, phytochemical screening, metal oxide nanoparticles, and core-shell nanostructure synthesis were explained. Furthermore, the standard procedures for anticancer, antibacterial, and antioxidant activity tests were explored.

3.1. Chemicals and Reagents

In this study, the precursor salts such as cobalt acetate hexahydrate ($Co(CH_3CO_2)_2.6H_2O$ (Sigma Aldrich), nickel acetate dihydrate ($Ni(CH_3CO_2)_2.2H_2O$) (Sigma Aldrich), copper acetate dihydrate ($Cu(CH_3CO_2)_2.2H_2O$) (Sigma Aldrich), and zinc acetate dihydrate ($Zn(CH_3CO_2)_2.2H_2O$) (Sigma Aldrich) have been used for the synthesis of respective MONPs and CSNs. Chloroform ($CHCl_3$), sulphuric acid (H_2SO_4), ferric chloride ($FeCl_3$), ammonia (NH_3), benzene (C_6H_6), and potassium iodide (KI) which are (Sigma Aldrich) were used for phytochemicals screening. Additionally, ethanol (CH_3CH_2OH) (99.9%, LabTech Chemicals) and sodium hydroxide (NaOH) (Sigma Aldrich) were also used for washing purposes and as precipitating agents, respectively. Distilled water was also used as the synthesis medium. Dimethyl sulfoxide and ampicillin were used as negative and positive controls, respectively. Ascorbic acid and DPPH (Sigma Aldrich) were used as a positive and negative control for antioxidant activity tests, respectively (Ajarem *et al.*, 2022). Dulbecco's Modified Eagle Medium (DMEM), Fetal Bovine Serum (FBS), penicillin-streptomycin, and insulin were used for cancer cell growth in an anticancer study. Additionally, MTT ((3, 4, 5-dimethylthiazol-2-yl)-2-5-diphenyletrazolium bromide) reagent (Sigma Aldrich) was for *in vitro* cytotoxicity study whereas Epirubicin was used as a positive control. All the chemicals and reagents used were of analytical grades and were purchased from the market.

3.2. Materials and Instruments

Materials used in this research work were; spatulas, borosilicate glass, electronic balance, pipet, hotplate, test tube, centrifuge, Erlenmeyer flask, pestle, volumetric flask, mortar, crucible, plastic bottles, funnel, Whatman number 1 filter paper, refrigerator, pH meter, aluminium foil, forceps, watch glass, burette, stand, graduating cylinder, and micro grinding machine. The advanced

characterization instrumental techniques such as; Uv-visible spectroscopy (UV-Vis), fourier transform infrared spectroscopy (FT-IR), scanning electron microscopy-energy dispersive X-ray spectroscopy (SEM/EDX), transmission electron microscopy-high resolution transmission electron microscopy (TEM/HRTEM), selected area electron diffraction (SAED), X-ray diffraction (XRD), and thermogravimetric analysis-differential thermal analysis (TGA/DTA) have been used for sample analysis.

3.3. Collection of *Datura stramonium* Plant Leaf

The Leaf of the *D. stramonium* plant used in this study for the synthesis of the nanoparticles was collected from around Adama city, East Shewa, Oromia regional state. Adama is a city located in the East Shewa zone, Oromia. It is located at 8.54 N 39.27 E, at an elevation of 1712 m, and 99 Km away from Addis Ababa to the southeast of Oromia. The specimen was identified and authenticated at the Addis Ababa University Herbarium (Voucher No. AUGH016) and documented for reference purposes.

3.4. Preparation of Plant Leaf Extract

In this study, the first step in the synthesis of nanoparticles was the preparation of the plant leaf's aqueous extract. Accordingly, the collected *D. stramonium* leaf was washed thoroughly using distilled water to remove dust particles and any contaminants and dried under a shadow area at room temperature for 15 days until all moisture was lost. The dried leaf was ground using a micro grinding machine, and the fine powder of the plant leaf obtained, about 3200 g, was packed in a dry bottle. The aqueous extraction was carried out using a 1000 mL conical flask containing 500 mL of distilled water by taking 30 g of leaf powder from the *D. stramonium* plant. The colloidal suspension of *D. stramonium* was boiled at 40 °C for about 90 min under continuous stirring. The boiled mixture was cooled to room temperature and filtered using Whatman number 1 filter paper (J. K. Sharma *et al*., 2015). Finally, the filtrate was stored in the refrigerator at 4 °C for the synthesis of Co_3O_4, ZnO, NiO, and CuO MONPs and CZ, CN, and CC CSNs (Tilahun *et al*., 2022). The schematic diagram of the leaf extraction is presented in Figure 20.

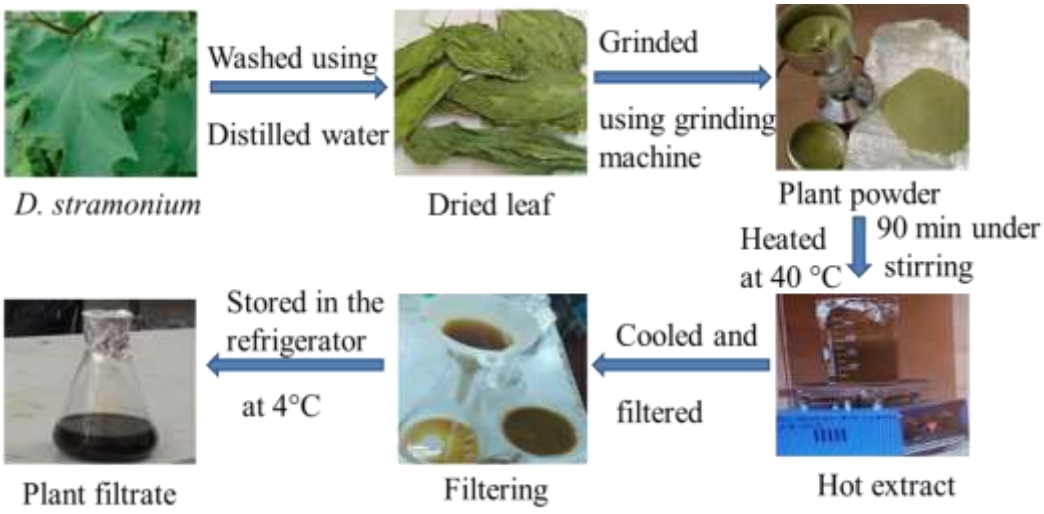

Figure 20: A schematic representation of *D. stramonium* leaf extraction.

3.5. Phytochemical Screening of Aqueous Extract of *Datura Stramonium* Leaf

The plant leaf extract was subjected to assessment for the existence of the phytochemicals by using the following standard methods (Batool *et al*., 2020,)

1. **Tests for Flavonoids (Alkaline Reagent Test)**: 2 mL of 2.0% NaOH mixture was mixed with aqueous plant crude extract; a concentrated yellow color was observed, which became colorless when 2 drops of diluted acid were added to the mixture. This result confirms the presence of flavonoids.

2. **Test for Alkaloids (Wagner's test)**: 2 mL of the *D. stramonium* plant aqueous extract solution was dissolved in Wagner's reagent (Iodine in Potassium Iodide). The formation of a brown/reddish precipitate confirms the presence of Alkaloids.

3. **Test for tannins**: 0.5 g of *D. stramonium* plant extract was boiled in 10 mL of distilled water in a test tube and filtered. 5 drops of 0.1% $FeCl_3$ was added to the filtrate, to give a brownish-green or a blue-black color which confirms the presence of tannins.

4. Test for terpenoids (Salkowski test): 2 mL of aqueous *D. stramonium* plant extract was mixed with 2 mL of chloroform and 3 mL concentrated H_2SO_4 carefully to form a layer. A reddish-brown coloration of the interface formed showed positive results indicative of the presence of terpenoids.

5. Test for Steroids: 2 mL of chloroform and concentrated H_2SO_4 were added with the 5 mL aqueous *D. stramonium* plant crude extract and no color change was observed, which could indicate the absence of steroids.

6. Tests for Glycosides (Salkowski's Test): 2 mL concentrated H_2SO_4 was added to the aqueous plant crude extract. The formation of a reddish-brown color is indicated by the presence of glycosides.

7. Test for phytosterols (Salkowski's test): 2 mL of aqueous plant extract and 10 mL of chloroform were mixed and then filtered. 5 drops of concentrated H_2SO_4 were added to the filtrate; the mixture was shaken and examined for the appearance of a golden yellow color which indicates the presence of phytosterols.

8. Test for Anthraquinones: 10 mL of benzene was added to 6 g of the plant extract in a conical flask and kept for 10 minutes and then filtered. Further, 10 ml of 10% ammonia solution was added to the filtrate and shaken vigorously, and pink, violet, or red color formation indicated the presence of anthraquinones in the ammonia phase.

9. Test for saponins: 0.5 g of plant extract was taken then 5 mL of distilled water was added and shaken while heating to boil. Frothing showed the presence of saponins.

10. Test for phenols: 5 drops of 2% of $FeCl_3$ was added to 2 mL of aqueous plant extract and the formation of a bluish-green to black color indicates the presence of phenols.

3.6. Synthesis of Metal Oxide Nanoparticles

Metal oxide nanoparticles (MONPs) such as cobalt oxide, zinc oxide, nickel oxide, and copper oxide nanoparticles were synthesized using *D. stramonium* plant leaf extract according to modified synthesis procedures (George *et al*., 2022).

3.6.1. Synthesis of Cobalt Oxide Nanoparticles

In this study, cobalt acetate hexahydrate ($Co(CH_3CO_2)_2.6H_2O$) and *D. stramonium* leaf extract were used for the synthesis of cobalt oxide nanoparticles (Co_3O_4 NPs). The Co_3O_4 NPs were prepared in (1:2), (1:1), and (2:1) volume ratios of cobalt acetate hexahydrate ($Co(CH_3CO_2)_2.6H_2O$) to *D. stramonium* leaf extract. Three different metal salt-to-plant leaf

extract volume ratios were Co_3O_4 (50:100 mL), Co_3O_4 (50:50 mL), and Co_3O_4 (100:50 mL) which denoted as Co_3O_4(12), Co_3O_4(11), and Co_3O_4(21), respectively. During Co_3O_4(11) synthesis, 50 mL of *D. stramonium* leaf extract was added dropwise to a 500 mL Erlenmeyer flask containing 50 mL of 0.5 M $Co(CH_3CO_2)_2.6H_2O$ solution and stirred for 4 h at room temperature. The pH of the formed suspensions on stirring was checked after the stirring time was completed and adjusted to pH = 12 by adding some drops of 0.1 M NaOH solution based on the reported procedure (Safdar *et al*., 2023). The formed suspension was further stirred for 30 min to maintain the uniform distribution of the added base. The precipitate formation was enhanced by the addition of NaOH solution. The resulting solution was placed in a refrigerator overnight to enhance precipitate formation. Then, the precipitate was centrifuged at 3000 rpm for 20 min. The supernatant was decanted carefully and washed thrice in all cases by using ethanol and distilled water sequentially. The washed precipitate was collected from the centrifuge tubes on a ceramic crucible dish and placed in a drying oven for 3 h at 100 ℃ and then allowed to cool. The dried precipitate was calcined at 350 ℃ using a muffle furnace for 5 h and stored for further analysis (Kiani *et al*., 2021, Urabe & Aziz, 2019, Nagajothi, 2022, Hashami et al., 2024). Similarly, Co_3O_4(12) and Co_3O_4(21) were also synthesized in 50:100 mL and 100:50 mL volume ratios, respectively, following the same procedure.

3.6.2. Synthesis of Zinc Oxide Nanoparticles

In the synthesis of ZnO NPs, the precursor zinc acetate dihydrate ($Zn(CH_3CO_2)_2.2H_2O$) salt, sodium hydroxide (NaOH), and plant extract were utilized. To synthesize ZnO NPs, 0.5 M of $Zn(CH_3CO_2)_2.2H_2O$ was prepared using distilled water and mixed with *D. stramonium* plant leaf extract. In this case, the three different metal salt-to-plant extract volume ratios (50:100 mL), (50:50 mL), and (100:50 mL) were assigned as ZnO(12), ZnO(11), and ZnO(21), respectively. For instance, in the synthesis of ZnO(11), 50 mL of plant extract was added dropwise into a 1000 mL Erlenmeyer flask containing 50 mL of 0.5 M $Zn(CH_3CO_2)_2.2H_2O$. The mixtures were stirred for 4 h and followed by the addition of 0.1 M NaOH to adjust the pH to 12 based on the previous work in the literature (Hafeez *et al*., 2020). After the dropwise addition of 0.1 M NaOH, the obtained precipitate was stirred for 20 min. The precipitate was centrifuged at 3000 rpm for 20 min and was followed by washing with ethanol and distilled water three times. The washed nanoparticles were collected and placed on a ceramic crucible, which was left to dry in an oven for 3 h at 100 ℃. The oven-dried precipitate was calcined using a muffle furnace at 480 ℃ for 5

h and stored for characterization and applications (Álvarez-Chimal *et al*., 2021). Similarly, ZnO(12) and ZnO(21) were also synthesized by varying their corresponding volume ratios under the same condition and procedure.

3.6.3. Synthesis of Nickel Oxide Nanoparticles

The synthesis of NiO NPs within different three volume ratios was performed by utilizing *D. stramonium* leaf extract and nickel acetate dihydrate ($Ni(CH_3CO_2)_2{\cdot}2H_2O$) precursor salt. The synthesis was carried out using 0.5 M $Ni(CH_3CO_2)_2{\cdot}2H_2O$ and plant leaf extract within NiO(12) (50 mL of precursor:100 mL of extract), NiO(11) (50 mL of precursor:50 mL of extract), and NiO(21) (100 mL of precursor:50 mL of extract) ratios using a separate Erlenmeyer flask. The mixture of precursor salt solution and plant leaf extract was stirred for 4 h at room temperature. The pH of the suspensions was adjusted to 12 by adding 0.1 M NaOH and followed by stirring the three ratios for about 20 min to maintain the homogenized mixture. After completion of the reaction, each of the individually formed suspension were placed in a refrigerator for 12 h. The formed and settled precipitate was centrifuged at 3000 rpm and washed three times using ethanol and distilled water. All the volume ratios of the precipitates were collected on a crucible ceramic dish and dried at 100 °C till the solvents and the reagents were removed. Finally, the samples were calcined for 5 h at 380 °C by using a muffle furnace (S. Hussain *et al*., 2023).

3.6.4. Synthesis of Copper Oxide Nanoparticles

In the presence of an aqueous crude extract of *D. stramonium* leaf and 0.5 M of ($Cu(CH_3CO_2)_2.2H_2O$), CuO NPs were synthesized in three different volume ratios, such that (12) (50 mL precursor: 100 mL extract), (11) (50 precursor mL:50 mL extract), and (21) (100 mL precursor:50 mL extract). To probe the effect of volume ratios on the structure, morphology, and biological activities such as antibacterial and antioxidant with specified volume ratios CuO NPs were synthesized. The synthesis was performed by utilizing the three volume ratios within three different Erlenmeyer flasks. The volume of extract was gradually added to the three Erlenmeyer flasks with the stated volume ratios containing 0.5 M of ($Cu(CH_3CO_2)_2.2H_2O$) precursor salt. The mixtures were stirred for about 4 h. Then the pH of the solution was adjusted to 12 by utilizing 0.1 M NaOH solution. To homogenize the added NaOH, the formed suspension was stirred for an additional 20 min. Then, each of the three Erlenmeyer flasks containing the formed suspension was placed in a refrigerator for 12 h. Each of the suspensions was centrifuged 3 times

at 3000 rpm and washed three times by utilizing distilled water and ethanol. The formed precipitates were then collected on a ceramic dish and dried at 100 °C until the moisture and solvents were removed (Almisbah & Mohammed, 2023). The dried samples were calcined at 300 °C for 5 h.

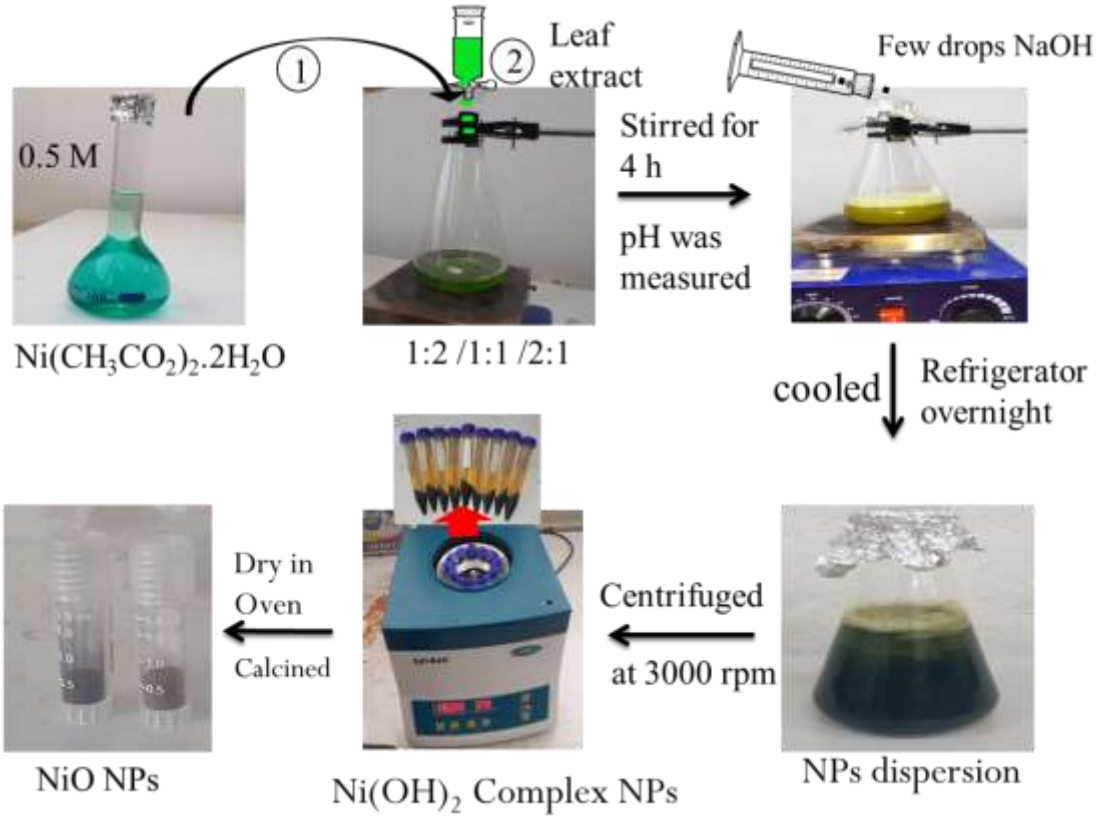

Figure 21: The schematic representation of metal oxide nanoparticles synthesis.

Similarly, Co_3O_4, ZnO, and CuO NPs were also synthesized by utilizing their corresponding precursor salts under the same condition and procedure.

3.7. Synthesis of Core-Shell Nanostructures

In this study, the MOCSNs were synthesized using *D. stramonium* leaf extract and the precursor salts. Cobalt acetate hexahydrate ($Co(CH_3CO_2)_2.6H_2O$) was used to synthesis a core, whereas zinc acetate dihydrate ($Zn(CH_3CO_2)_2{\cdot}2H_2O$), nickel acetate dihydrate ($Ni(CH_3CO_2)_2{\cdot}2H_2O$), and copper acetate dihydrate ($Cu(CH_3CO_2)_2\ 2H_2O$) precursor salts were utilized for respective shell synthesis. The synthesis was performed separately by keeping the concentration of the core

(inner) part material constant and varying the concentration of the shell (outer) material. The volume of plant extract, core, and shell material was constant throughout the synthesis.

3.7.1. Synthesis of Co_3O_4@ZnO Core-Shell Nanostructures

The Co_3O_4@ZnO (CZ) CSNs were synthesized using the *D. stramonium* leaf extract, $Co(CH_3CO_2)_2.6H_2O$, and $Zn(CH_3CO_2)_2.2H_2O$ precursor salts. The synthesis of CZ CSNs, was carried out using an *in-situ* method in three different concentration ratios of precursor salts of core to shell materials as 0.5:0.25, 0.5:0.5, and 0.5:0.75 M which are denoted as CZ(21), CZ(11), and CZ(23), respectively.

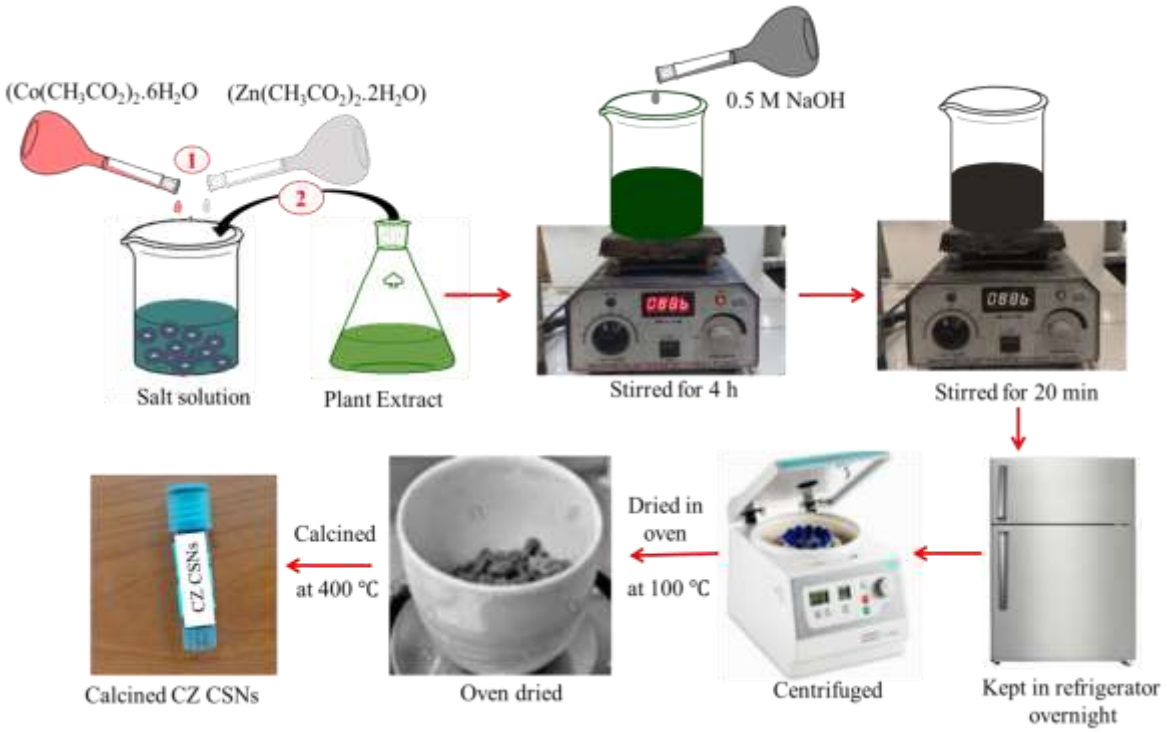

Figure 22: The synthesis of CZ core-shell nanostructures.

In this case, the effect of three different concentration ratios of precursor salt of the shell was studied. Specifically, during the synthesis of CZ(11), 100 mL of the plant leaf extract was gradually added to a 1000 mL beaker containing the mixture of 50 mL of 0.5 M ($Co(CH_3CO_2)_2.6H_2O$) and 50 mL of 0.5 M $Zn(CH_3CO_2)_2$. $2H_2O$ and stirred for about 4 h. Then, 0.1 M of NaOH was added (pH=12) under stirring for 30 min resulting in the precipitation of the CSNs. The precipitate was kept in a refrigerator overnight. The precipitate was centrifuged at 3500 rpm for 20 min and washed three times using ethanol and distilled water. The washed

CZ(11) CSNs was collected on a ceramic crucible and dried in an oven at 100 ℃ and finally calcined at 360 ℃ using a muffle furnace and the obtained crystalline nanostructure was stored for the characterization (Kirubha & Palanisamy, 2014). The same procedure was repeated for the synthesis of CZ(21) and CZ(23) CSNs.

3.7.2. Synthesis of Co_3O_4@NiO Core-Shell Nanostructures

In the synthesis of Co_3O_4@NiO (CN) CSNs, the three different concentration ratios of precursor salts of the core to shell materials CN(21), CN(11), and CN(23) by keeping the concentration of ($Co(CH_3CO_2)_2.6H_2O$) constant (0.5 M) and varying the concentration of ($Ni(CH_3CO_2)_2.2H_2O$) as 0.25, 0.5, and 0.75 M, respectively. Unlike that of the CZ CSNs, the CN CSNs were synthesized in two steps. For example, during the synthesis of CN(11), the first 50 mL of *D. stramonium* leaf extract was gradually added to 50 mL of 0.5 M ($Co(CH_3CO_2)_2.6H_2O$) and stirred for 4 h. To adjust the pH of the mixture and enhance the precipitate formation, 0.1 M of NaOH was added and further stirred for 30 min. At this step, the $Co(OH)_2$ precipitate was formed and followed by the addition of precursor salt solution of shell material.

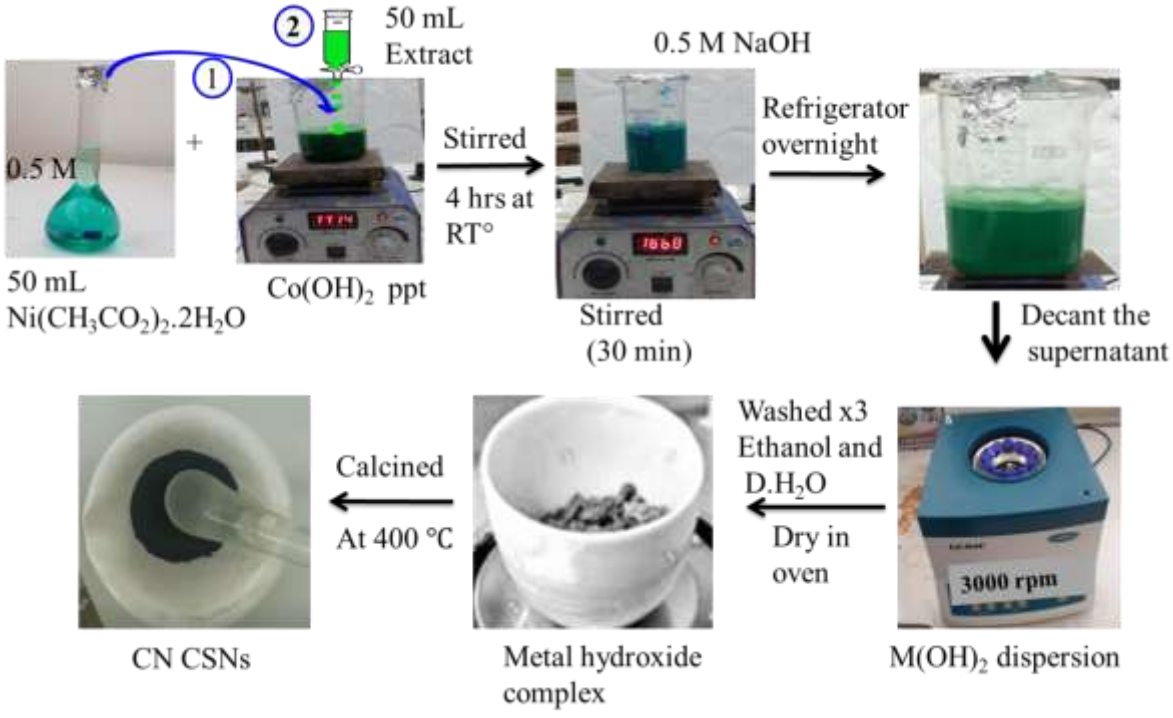

Figure 23: The schematic diagram of CN CSNs synthesis.

To develop the shell materials on the $Co(OH)_2$ precipitate, 50 mL of 0.5 M $Ni(CH_3CO_2)_2.2H_2O$ was added and followed by the gradual addition of 50 mL of plant extract. The mixture was stirred for another 4 h. After the completion of 4 h stirring, 0.1 M of NaOH was added to adjust the pH to 12 and stirred for 30 min. The CN(11) CSNs were kept in a refrigerator for 12 h to enrich precipitate formation and then centrifuged at 3500 rpm for 20 min and washed three times using ethanol and distilled water. The same procedure was repeated for CN(21) and CN(23) CSNs by utilizing 0.25 and 0.75 M of $Ni(CH_3CO_2)_2.2H_2O$ salt, respectively. Finally, the precipitate was collected on the ceramic crucible and dried in the oven at 100 °C. The dried CN CSNs were calcined at 400 °C and kept for further analysis (Rezk *et al*., 2022).

3.7.3. Synthesis of Co_3O_4@CuO Core-Shell Nanostructures

The Co_3O_4@CuO (CC) CSNs were synthesized by utilizing the aqueous extract of *D.stramonium* plant leaf, cobalt acetate hexahydrate ($Co(CH_3CO_2)_2.6H_2O$), and copper acetate dihydrate ($Cu(CH_3CO_2)_2\ 2H_2O$) precursor salts by following the procedure shown in Figure 24. In the synthesis of CC CSNs, the concentration of $Co(CH_3CO_2)_2.6H_2O$ was kept constant (0.5 M) and $Cu(CH_3CO_2)_2\ 2H_2O$ was prepared in three different concentrations as 0.25, 0.5, and 0.75 M and represented as CC(21) CSNs, CC(11) CSNs, and CC(23) CSNs, respectively. In the two step synthesis of CC(21) CSNs, 50 mL of plant leaf extract was added to 50 mL of 0.5 M ($Co(CH_3CO_2)_2.6H_2O$) and stirred for 4 h. Based on the literature, the pH was adjusted to 12 by addition of 0.1 M of NaOH to enhance the precipitate formation and further stirred for 30 min. Then, the shell was synthesized by the addition of 50 mL of 0.25 M $Cu(CH_3CO_2)_2.2H_2O$ precursor salt solution to the $Co(OH)_2$ nanoparticle dispersion formed in the first step followed by the addition of 50 mL of plant extract. The mixture was stirred for 4 h and the pH was readjusted to 12 by the addition of 0.1 M of NaOH and stirred for 30 min. The CC(21) CSNs was kept in a refrigerator for 12 h to enhance precipitate formation and then centrifuged at 3500 rpm for 20 min and washed three times using ethanol and distilled water (Venkateswarlu *et al.*, 2015). The CC(11) and CC(23) CSNs were also synthesized by following the same procedure by utilizing 0.5 and 0.75 M of $Cu(CH_3CO_2)_2.2H_2O$ salt, respectively (Ganesan *et al*., 2020). Finally, the synthesized CSNs were collected on the ceramic crucible and dried in the oven at 100 °C. The dried CC CSNs were calcined at 320 °C and kept for further analysis.

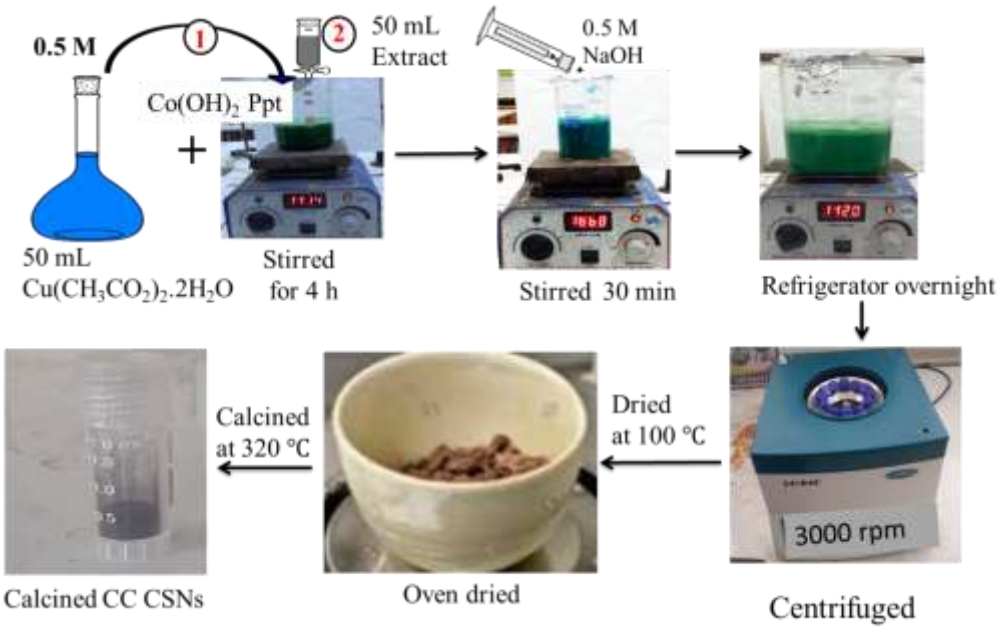

Figure 24: The schematic diagram of CC CSNs synthesis.

3.8. Characterization Techniques

The synthesized MONPs and CSNs by utilizing *D. stramonium* leaf extract have been confirmed by using advanced characterization techniques. The proportion of weight loss of the MONPs and CSNs samples was determined using TGA curves and compared to the relevant thermal changes of the DTA peaks. The calcination temperature of MONPs and MOCSNs samples resulted from the formation and decomposition of different species, as represented in TGA/DTA curves (Ajarem *et al.*, 2021). The appropriate temperature at which no weight loss occurred and thermally stable with constant heat change was determined. At the School of Chemical and Food Engineering, Bahir Dar University, Bahir Dar, thermal gravimetric analysis and differential thermal analysis (HCT-3, Beijing Hengjiu Instrument, China) were used to determine the temperature at which MONPs and MOCSNs have to be become calcined. The heating rate was 10 ℃/min and the hold time were 50 ℃/min.

The MONPs and MOCSNs were also characterized using a UV-Vis spectrophotometer (Lambda 1050 (PerkinElmer, Japan)). The absorption spectra were obtained using a spectrophotometer between the wavelengths of 200 and 800 nm. The absorption band and band gap energy of the synthesized nanoparticles were revealed. During analysis, the MONPs and CSNs dispersed in DMSO solvent, and the blank solution was placed in the lid of the sample champer and scanned

within the selected wavelength range and the absorbance spectrum was recorded. The generated absorbance was drawn as a function of wavelength and furthermore, the band gap energy was also calculated by using Tauc relation.

FT-IR spectroscopy has been used to describe the type of functional group present in the plant's leaf and the synthesized nanoparticles. To determine several functional groups, the synthesized nanostructures were homogenized with a KBr pellet and analyzed using Fourier transform infrared spectroscopy (FT-IR) (Bruker TENSOR27 Spectrometer, Germany) with a scanning range of 4000 - 400 cm^{-1}. The investigated function group resulted from the spectra appearing in the FT-IR analysis.

The crystal structure and average crystallite size of MONPs and CSNs were analyzed by using XRD (XRD-7000, SHIMADZU Corporation, Japan) which is furnished with a Cu metal used for generating a Cu Kα radiation with λ = 0.15406 nm and recorded in the range from 10-80°. The average crystallite sizes of all synthesized MONPs and CSNs were determined using Debye-Scherrer's formula written in equation (1) (Perumal *et al*., 2024)

$$D = \frac{k\lambda}{\beta Cos\theta} \quad (1)$$

Where:

D – the average size of crystallite,

λ – the wavelength of the X-ray with values of 1.5406 Å for CuKα,

K – crystallite constant (0.94)

θ – the peak position (in degrees)

β – the full width at a half-maximum height

The XRD analysis of Co_3O_4(12), Co_3O_4(11), and Co_3O_4(21) NPs was performed using CuKα radiation with a scanning rate of 0.16 deg/s. The characterization was performed at the Department of Material Science and Engineering of Adama Science and Technology University. QualX software was used to determine the JCPDS card number of the samples.

Scanning electron microscopy-Energy dispersive X-ray Analysis (SEM-EDX, model CamScan MV2300, Germany) was used to investigate the morphology and elemental composition of MONPs and CSNs. The characterization was performed at the Research Institute of Materials Chemistry, Chungnam National University, Republic of Korea. The sample was placed in the

sample holder and moved to the instrument's stage. During characterization, the incident electron beam interacts with the sample, and secondary electrons are inelastically scattered from the surface of the sample to provide high-resolution topographical information about the sample surface. Furthermore, the elemental composition of the samples was determined by using EDX. The EDX spectra of MONPs and CSNs samples were evaluated based on their percentage abundance. The peak with the highest percentage of abundance in samples was expected to be the most intense.

The particle size distribution, grain orientation, and shape of synthesized MONPs and CSNs were determined by using TEM/HR-TEM. The TEM employs an electron beam to photograph the picture that was used for identification. TEM can also be used to observe and analyse the core-shell structure. SAED was used to determine the crystallinity nature of MONPs and CSNs. The TEM/HR-TEM (JEM-2100, USA) analysis was performed at the Department of Chemistry, Chemistry Engineering, and Applied Chemistry at Chungnam National University in the Republic of Korea. Finally, the particle size and distribution were determined by using Gatan software and plotted by using origin software.

3.9. Synthesis Mechanism of Metal Oxide Nanoparticles

In the phytochemical mediated MONPs, the mechanistic electron interaction occurs in different stages. Under the controlled temperature and pH, the phytochemicals from the extract donate electrons to reduce metal ions to metal atoms. The π-electron donors such as amine, carboxyl, and hydroxyl functional groups of phytochemicals are potential reducing agents and are subsequently used as a capping agent to stabilize the metal nanoparticles by preventing agglomeration. The initial stage involves complexation, in which phenolic hydroxyl groups (OH) form electrostatic complexes with metal ions, which are then reduced to metal atoms. The resulting metal atoms undergo nucleation and form a cluster of metal nanoparticles. This is followed by the growth and coalescence of separate small nanoparticles into larger ones that occur through the coarsening process. This process continues until the particles become stable in shape and size for nanoparticles. The phytochemicals interact with the metal by electrostatic interaction and form a protective coating that prevents particle growth. In an aqueous medium, metal atoms react with hydroxide ions (OH^-) present in the solution, particularly if the pH is

raised due to the presence of certain compounds in the plant extract as well as alkaline solution added during synthesis. This reaction leads to the formation of metal hydroxides which can further precipitate out of the solution. The metal hydroxide further undergoes oxidation under exposure to an elevated temperature that leads to the formation of MONPs (S. Hussain *et al.*, 2023, H. Singh *et al.*, 2023).

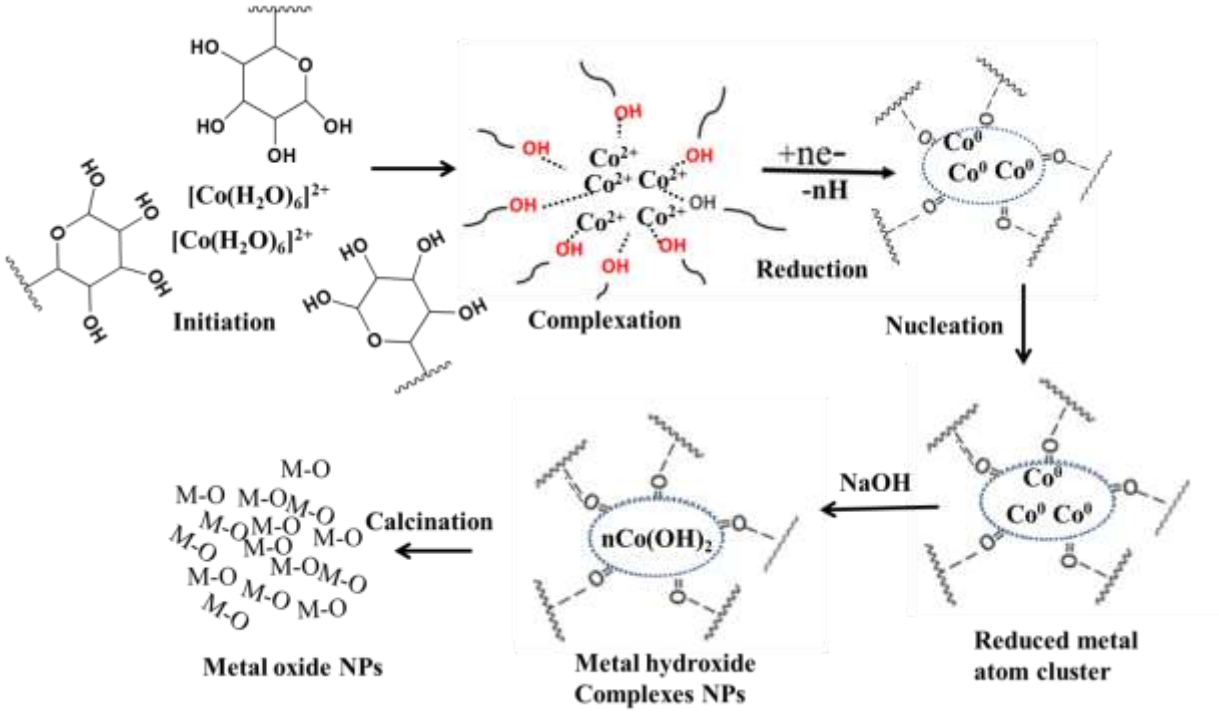

Figure 25: Synthesis mechanism of metal oxide nanoparticles (Thatyana *et al.*, 2023).

3.10. Anticancer Activity

3.10.1. Cell Culture

Human breast cancer cells (MCF-7) and peripheral blood mononuclear cells (PBMC) were used to study the cytotoxicity of synthesized samples. MCF-7 was cultured in DMEM supplemented with 10% fetal bovine serum (FBS), 1% penicillin-streptomycin, and 10 µg/mL of insulin at 37 °C in a humidified incubator with a 5% CO_2 atmosphere. Cells passaged at pre-confluent densities were used for further studies (K. Ali *et al.*, 2020).

3.10.2. Cell Viability Assay

The cell viability was determined by using standard MTT (3-(4, 5-Dimethylthiazol-2-yl)-2, 5-diphenyltetrazolium Bromide) reagent. The MCF-7 and PBMC from the confluent flasks was trypsinized and plated into 96 well tissue culture plates at a density of 3.0 x 10^3 cells/well. The cells were treated with concentrations of 12.5, 25, 50, 100, 200, 400, and 800 µg/mL of CZ, CN, and CC CSNs in triplicates. After 24 h incubation, MTT solution (2.5 µg/mL) was added and further incubated at 37 °C and 5% CO_2 for 4 h. The amount of colored formazan was determined by measuring optical density (OD) using a TECAN microplate reader at 570 nm. OD values were subjected to calculate the percentage of viability by using the following formula (S. A. Khan *et al.*, 2021)

$$\%\ Cell\ viability\ = \frac{OD\ of\ \ Control - \ OD\ of Sample}{OD\ of\ \ Control} * 100 \dots\dots\dots\dots\dots\dots\dots\dots\dots\dots (2)$$

3.11. Antibacterial Activities

The antibacterial activities of the synthesized Co_3O_4, ZnO, NiO, and CuO NPs as well as CZ, CN, and CC CSNs were evaluated using the disc diffusion method. The inhibition efficiency of the biologically synthesized NPs was studied for gram-positive (*S. aureus* and *S. pyogenes*) and gram-negative (*E. coli* and *P. aeruginosa*) bacterial strains. In the disc diffusion method, 12 g of broth agar was prepared in 200 mL of distilled water. The solution of nutrient agar was dispensed onto the petri dish. The poured liquid nutrient agar was solidified on the petri dish and well homogenized and the grown culture of the four bacteria was inoculated and kept on a shaker at 35 °C for 24 h at 200 rpm. The standard drug Ampicillin (positive control) was used in the analysis to determine the antibacterial activities of all biologically synthesized NPs (Nagajothi, 2022). In addition to this, DMSO was used as a solvent and negative control. Then, the biologically synthesized NPs were applied to the gram-positive and gram-negative in four different concentrations (25, 50, and 100 µg/mL). The plates were incubated at 37 °C for about 24 h and checked for the zone of inhibition. The scale of the image was determined in millimeters. The same procedure was followed for all nanoparticles synthesized in this work.

3.12. Antioxidant Activities

The stable purple 2, 2-diphenyl-1-picrylhydrazyl (DPPH) free radical was utilized to investigate the radical scavenging ability of biologically synthesized NPs. The activity was measured following the modified procedure used in the previous work report (Din *et al*., 2017). A 4 mL of 100 µM DPPH was prepared in DSMO and added to methanolic 1000 µL NPs with 50, 100, 200, 300, and 500 µg/mL. The mixture was sonicated and kept in the dark chamber for 30 min and followed by incubation at 37 ± 2 ℃ for the same time. The UV-Vis absorbance of positive control (ascorbic acid) and the mixture of the same concentration were measured at 517 nm. All the experiments were performed in triplicate and the average absorbance for each sample was considered. Finally, the percentage scavenging capacity of NPs was determined using equation (3) (Ajarem *et al*., 2022). The same procedure was followed for all metal oxide nanoparticles and CSNs synthesized in this work.

$$\% \text{ Radical scavenging activity} = \frac{Absorbance\ of\ control - Absorbance\ of\ samle}{Absorbance\ of\ control} * 100 \quad (3)$$

3.13. Data Analysis

The generated data of synthesized NPs were analysed and computed by using Microsoft Excel, 2013, Origin Pro software, ImageJ software, and Gatan Microscopy Suite Software.

4. Results and Discussions

4.1. Phytochemical analysis

The phytochemical constituents found in the aqueous extract of *D. stramonium* plant leaf were qualitatively screened by using the reagents listed in Table 4. All phytochemical analyses showed positive results except steroids as the color change indicates the presence of phytochemical constituents (Dubale *et al*., 2023). The analysis confirmed that alkaloids, flavonoids, tannins, saponins, phenol, phytosterols, glycosides, terpenoids, and anthraquinones were among the major constituents of the *D. stramonium* leaf extract as depicted in (Figure 26 and Table 4) (M. A. Ali & Endalew, 2021, Cornelius *et al*., 2019).

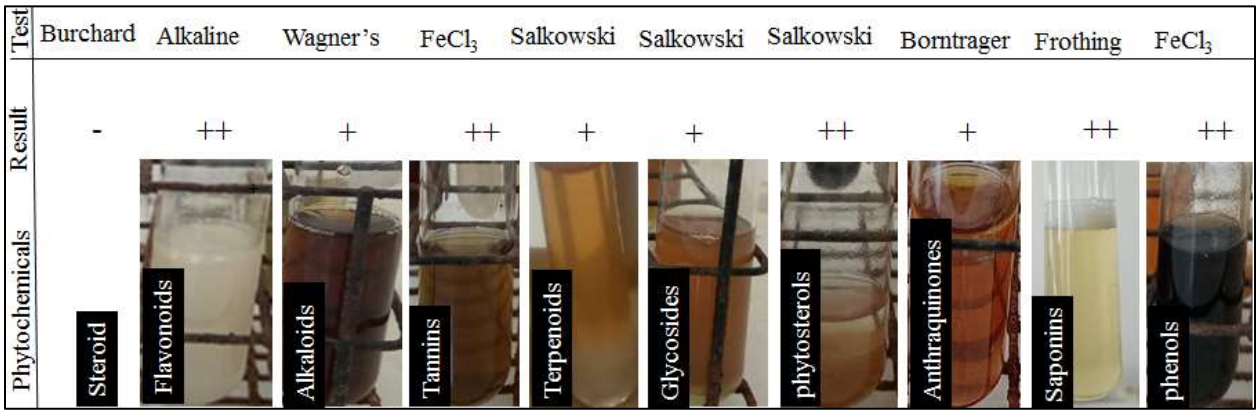

Figure 26: Qualitatively analyzed result of selected phytochemical constituents of *D. stramonium* leaf extract.

In the qualitative screening, alkaloids, flavonoids, tannins, saponins, phenol, steroids, and anthraquinones were tested by utilizing wagners's, alkaline, water, iron chloride, buchard, and Borntrager reagent, respectively. Salkowski reagent was also used to test phytosterols, glycosides, and terpenoids. As shown in Figure 26, the appearance of brown/reddish, white, froth, black, golden yellow, reddish-brown, brown, and red color ensured the presence of alkaloids, flavonoids, tannins, saponins, phenol, phytosterols, glycosides, terpenoids, and anthraquinones phytochemicals, respectively (Rehana *et al*., 2017, Hashmi *et al*., 2021). However, in the steroids test no color change was observed which is indicative of its absence.

Table 4: Some selected phytochemicals screened from aqueous *D. stramonium* leaf extract.

S.No	Phytochemicals	Reagents	Result	Color
1	Alkaloids	Wagner's	+	Brown/reddish
2	Flavonoids	Alkaline	+	White
3	Tannins	$FeCl_3$	+	Green
4	Saponins	Water	++	Froth
5	Phenol	$FeCl_3$	++	Black
6	Phytosterols	Salkowski	+	Golden yellow
7	Glycosides	Salkowski	+	Reddish-brown
8	Steroids	Burchard	-	No change
9	Terpenoids	Salkowski	+	Brown
10	Anthraquinones	Bontrager	+	Red

The (-), (+), and (++) signs indicate the absence, moderate, and high presence of phytochemicals in aqueous leaf extract, respectively.

Similar phytochemical constituents of the *D. stramonium* plant extract were reported in a previous study (M. A. Ali & Endalew, 2021). Among the phytochemicals, the polyphenol groups are used to reduce the metal ions to their zero-valent and as a capping agent to prevent the agglomeration of nanoparticles during their synthesis. Due to this, the aqueous extract of *D. stramonium* was utilized for the synthesis of Co_3O_4, ZnO, NiO, and CuO NPs and CZ, CN, and CC CSNs.

4.2. Characterization of MONPs and CSNs

4.2.1. Thermal (TGA/DTA) Analysis

In this study, the thermal analysis of Co_3O_4, ZnO, NiO, and CuO NPs and CZ, CN, and CC CSNs was operated within a range of $29 - 800$ ℃ using thermogravimetric analysis coupled with differential thermal analysis (TGA-DTA). For each case, 10 mg of the sample was analyzed and the trend of weight loss was recorded as the temperature rose. The TGA curve depicted in Figure 27 showed the removal of thermally unstable substances found in the synthesized metal oxide nanoparticles and the data were used to determine the calcination temperature. The percentage weight loss of chemical constituents of MONPs has been determined from the curve of TGA. The endothermic and exothermic energy changes of the sample were also determined

from DTA curve. The endothermic process evaporates the volatile molecules, while the exothermic process involves chemical changes like oxidation reactions. As shown in Figure 27(a-d), from the TGA curve the percentage weight loss and calcination temperature of the MONPs were determined. Accordingly, the calcination temperatures of Co_3O_4, ZnO, NiO, and CuO NPs were found to be 350, 480, 420, and 300 ℃, respectively (Moavi *et al.*, 2021). The compounds incorporated within the synthesized nanoparticles, such as water and several organic molecules were removed before the temperature reached these calcination points. The TGA curve in Figure 27(a) showed the removal of extremely volatile molecules (1.8%) and water molecules (5.8%) (Fatimah *et al.*, 2016). About 13% of non-volatile organic molecules have been removed within the range of 240-350 ℃.

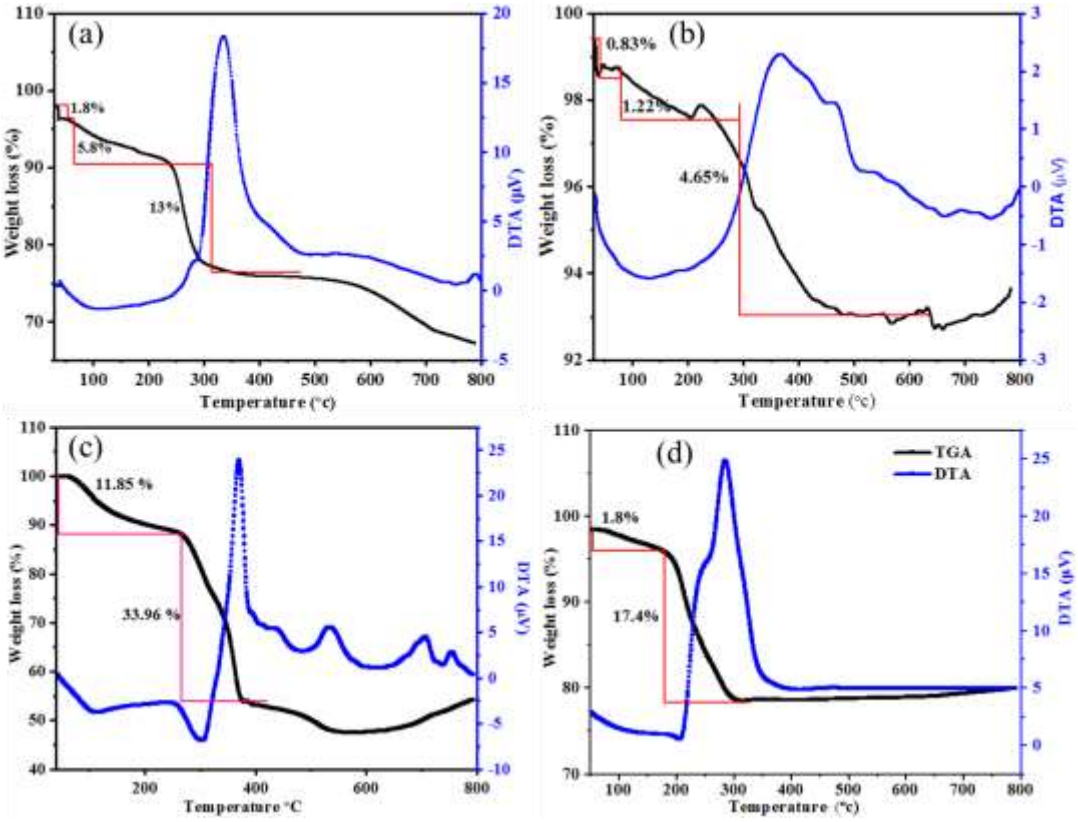

Figure 27: TGA/DTA curves of the synthesized (a) Co_3O_4, (b) ZnO, (c) NiO, and (d) CuO nanoparticles.

Similarly, in the TGA curve of ZnO NPs, 0.83%, 1.22%, and 4.65% weight loss were observed because of the removal of volatile molecules, water, and some organic molecules from plant extract, respectively (Nagajyothi *et al.*, 2015). Unlike Co_3O_4 and ZnO NPs, the TGA curve of

NiO and CuO NPs showed weight loss at two stages. As indicated in Figure 27(c) and (d), the first weight loss about 11.85%, and 1.8% within the range of 30-260, and 30-180 ℃ were found to be water for NiO and CuO NPs, respectively. The loss observed in the second stage was due to the removal of some organic molecules of plant extract utilized during the synthesis of nanoparticles. The percent loss for these organic molecules was found to be 33.96%, and 17.4%, for NiO and CuO NPs within the range of 270-380, and 190-290 ℃, respectively. As shown in the DTA curve, Co-O, Zn-O, Ni-O, and Cu-O MONPs were formed in the temperature range of 300-425, 300-580, 330-580, and 240-400 ℃, respectively.

The complementary information such as thermal change, bond formation, and weight loss of CSNs as a function of temperature were also determined by using TGA/DTA. The analysis was done to determine the calcination temperature for MONPs and CSNs. As depicted in Figure 28, the synthesized CZ, CN, and CC CSNs became thermally stable beyond 360, 400, and 320 ℃, respectively. The exothermic and endothermic heat occasions associated with the heat change of CSNs were determined by using differential thermal analysis techniques. As shown in Figure 28(a) from the DTA peak, the heat was released slightly at 302 °C and highly at 338 °C. Such an intense peak is believed to be due to the formation of metal-oxygen bonds.

In Figure 28(b), it is evident that CN CSNs exhibit heat absorption peaks at 38 °C and 295 °C, facilitating weight loss, and subsequently released absorbed heat at 430°C. The endothermic peak of CC CSNs at 50 °C and 284 °C and the exothermic peak at 206 °C and 390 °C were also presented in Figure 28(c) (Devi *et al*., 2014).

The percentage weight losses of synthesized CSNs were explored from the TGA curve as depicted in Figure 28 The change in physical properties of the CSNs was monitored as a function of controlled temperature change. As shown in the TGA curve plotted in Figure 28(a), CZ CSNs became stable at a temperature of 360 ℃ and onwards. In the curve, the removal of some molecules such as ethanol, water, and organic bioactive molecules from the plant extract was observed at different stages. The first two weight losses of 4.95% and 6.77% recorded were due to the removal of volatile compounds and water respectively, whereas, the remaining two steps (9.01 and 17.2%) were due to the removal of organic molecules of the plant extract. In general, about 37.93% weight of the sample was lost in the thermal analysis of CZ CSNs within the

temperature range of 30-360 ℃. The difference in the stages of weight loss is believed to be the formation of a hydrogel-like structure between metal-phytochemical and phytochemicals-phytochemicals.

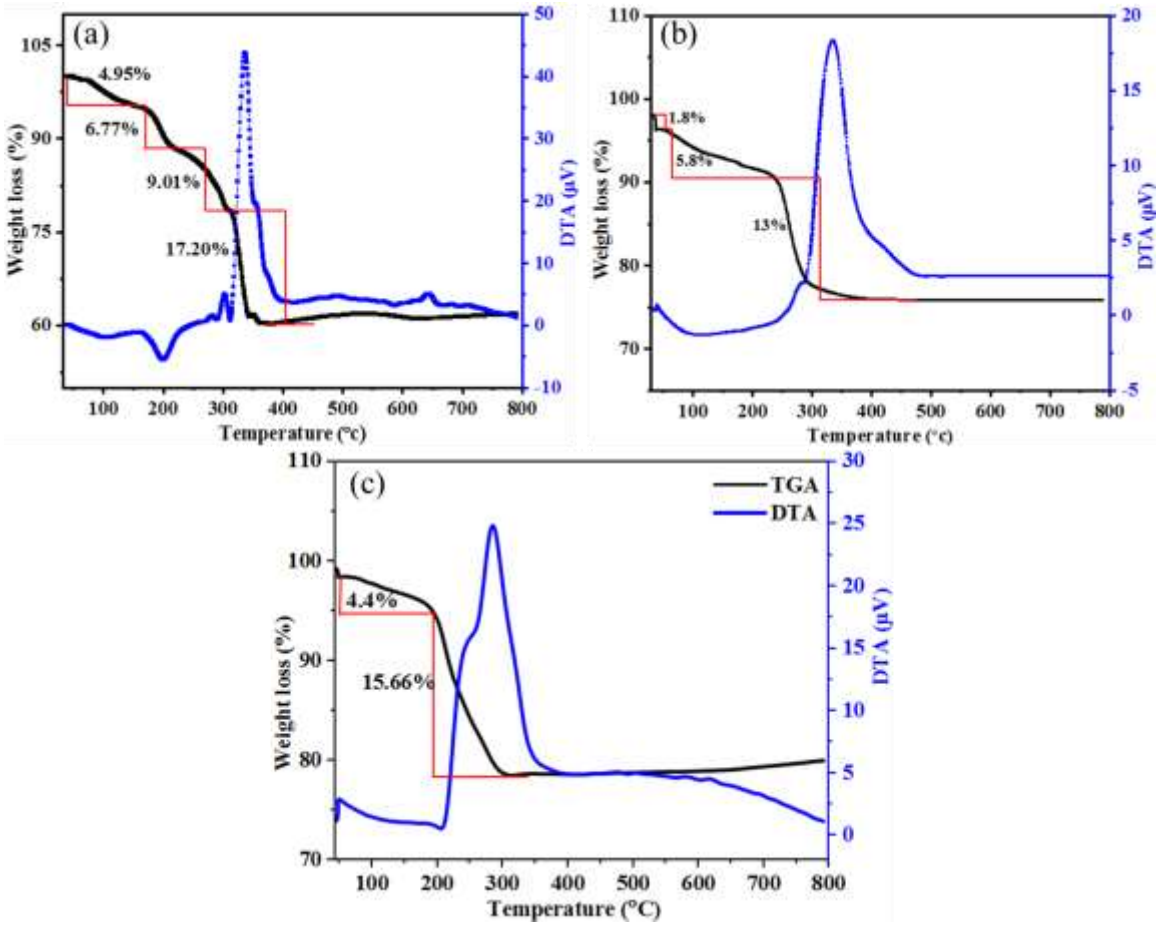

Figure 28: TGA/DTA curve of the synthesized (a) CZ, (b) CN, and (c) CC core-shell nanostructures.

This supported that the CZ CSNs were capped by the phytochemicals of the plant extract. In the TGA analysis shown in Figure 28(b), the curve for CN CSNs showed weight loss at three stages. The weight loss of CN CSNs was found to be about 1.8%, 5.8%, and 13% which was associated with volatile molecules, water, and bioactive molecules from plant extract utilized during synthesis. In the case of CC CSNs, weight loss of about 4.4% and 15.66% were associated with water and bioactive molecules. As depicted in Figure 28(c), from the TGA curve it can be noted that above a temperature of 320 ℃, the CC CSNs were found to be thermally stable (Ong *et al*., 2015).

Generally, as observed from TGA/DTA curve analysis, the synthesized Co_3O_4, ZnO, NiO, and CuO nanoparticles and CZ, CN, and CC CSNs were found to be stable beyond different temperatures. The thermal stability of Co_3O_4 core material was increased when coated with ZnO and NiO shell materials. The arrangement of atoms within the core-shell material was restricted due to the confinement effect. This effect stabilized the CSNs by preventing structural decomposition and transformation at high temperatures. However, in the case of CC CSNs, the lower calcination temperature of the CuO shell affects the overall thermal stability of the CSNs. This is mostly believed to be due to the difference in the coefficient of thermal expansion and compatibility of the Co_3O_4 core and CuO shells (Zhang *et al*., 2014, Rocchetti *et al*., 2016). The exothermic curve of DTA observed in the range of 320-440, 290-440, and 230-380 ℃, indicates the formation of Co/Zn-O, Co/Ni-O, and Co/Cu-O, respectively.

4.2.2. UV-Vis Analysis

The synthesized Co_3O_4, ZnO, NiO, and CuO MONPs and CZ, CN, and CC CSNs were analyzed by using UV-Visible spectroscopy. As shown in Figure 29, the absorption band of MONPs synthesized in (1:1), (1:2), and (2:1) volume ratios were measured. The analysis was done by using UV-Vis spectroscopy within the range of 200-800 nm wavelengths. The absorbed UV-Vis light by the synthesized nanoparticles was recorded and used for band gap energy calculation. From the generated data, the values of absorbance for these nanoparticles varied mainly due to their size. The MONPs absorb UV-Vis light at a specific wavelength and cause electron transition between the valance band and conduction band of nanoparticles. As indicated in Figure 29(a), the absorption spectra of Co_3O_4(11), Co_3O_4(12), and Co_3O_4(21) NPs were measured and their band appeared at two different wavelengths. The absorption bands observed at 230 and 276 nm were associated with Co_3O_4(11) NPs, whereas 288 and 338 nm correspond to Co_3O_4 (12), and 368 and 417 nm belong to Co_3O_4 (21) NPs, respectively. The absorption bands observed relatively at shorter and longer wavelengths in each spectrum were due to the charge transfer from $O^{2-} \rightarrow Co^{2+}$ and $O^{2-} \rightarrow Co^{3+}$, respectively (Ravi Dhas *et al*., 2015). The absorption bands of ZnO(11), ZnO(12), and ZnO(21) NPs were 275, 334, and 382 nm which are represented in Figure 29(b). The broadband shown in the absorption band of ZnO NPs in all the ratios was due to the wide range of particle size distribution. The difference in particle size distribution affects

the distribution of energy levels within the particles and causes the broadening of the absorption spectrum.

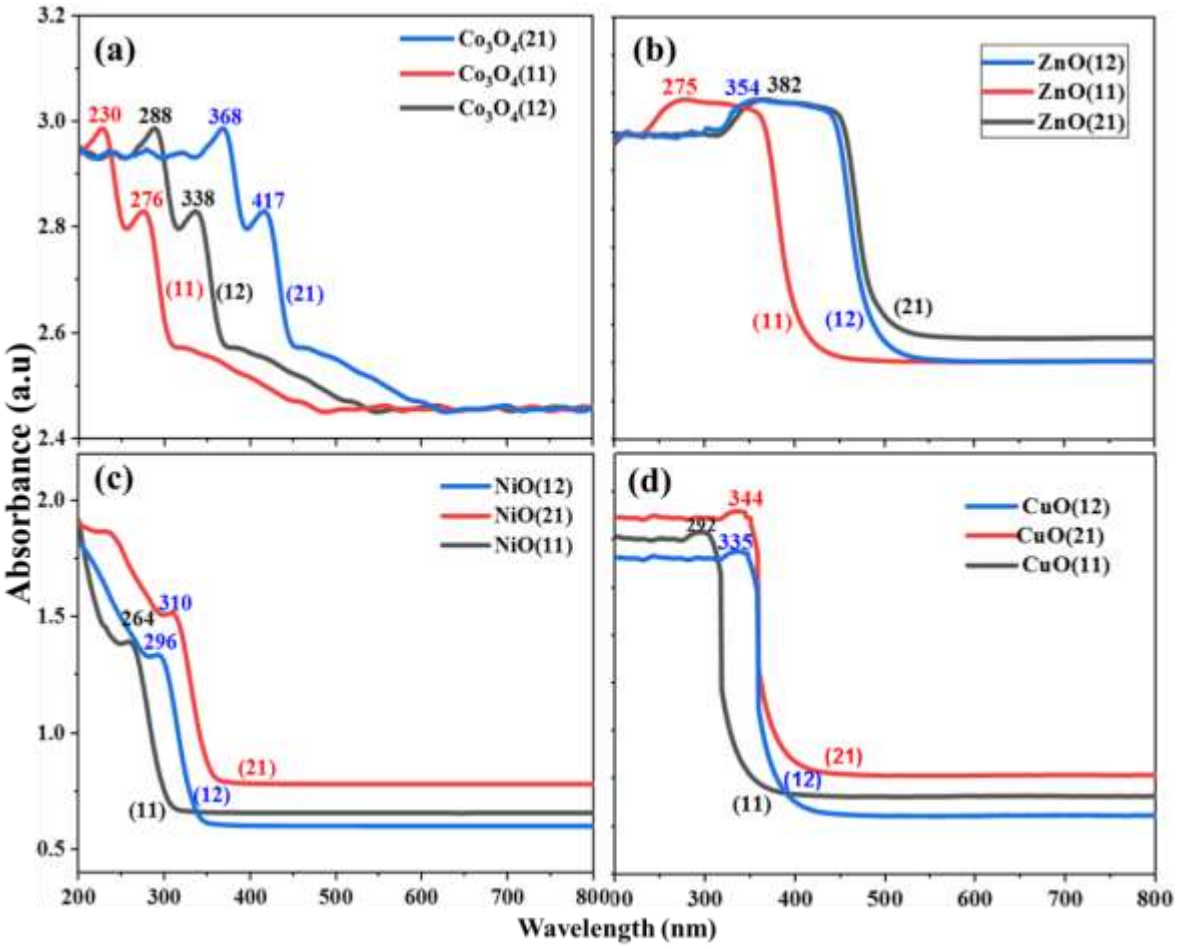

Figure 29: UV-visible absorption spectra of (a) Co_3O_4, (b) ZnO, (c) NiO, and (d) CuO NPs synthesized in (1:1), (1:2), and (2:1) volume ratios.

Additionally, the absorption spectra of NiO(11), NiO(12), and NiO(21) NPs were found at 264, 296, and 310 nm which is represented in Figure 29(c), whereas CuO(11), CuO(12), and CuO(21) NPs were found at 295, 335, and 344 nm as depicted in Figure 29(d). In general, CuO(11) NPs typically exhibit a blue shift in absorption due to quantum effects but show lower intensity at these shorter wavelengths which is believed to be less concentration and dispersion of the particles. The absorption bands that occurred in ZnO, NiO, and CuO NPs analysis were due to the charge transfer from O^{2-} to Zn^{+2}, Ni^{2+}, and Cu^{2+}, respectively (Haq, Dildar, *et al.*, 2021, Aldeen *et al.*, 2022). Furthermore, among the ratios of all MONPs synthesized within three different ratios, (2:1) absorb at a longer wavelength. This is due to its relatively large size. As

shown in Figure 29(a-d), the particle size increases in the order of (1:1), (1:2), and (2:1) volume ratios which enabled the particles to absorb UV-Vis light at different wavelengths.

The band gap energy of metal oxide nanoparticles with small sizes was calculated and further characterized with advanced instruments. The Tauc relation was used to calculate the band gap energy as shown in equation (4) (Haq, Abbasi, *et al*., 2021).

$$F(r)hv = A(hv - Eg)^2 \qquad (4)$$

Where F(r) is the Kubelka-Munk function, hv is the photon energy, and E_g refers to band gap energy. The band gap energy values of all metal oxide nanoparticles were obtained using extrapolation methods. As shown in Figure 30, the band gap of Co_3O_4, ZnO, NiO, and CuO NPs was found to be 3.06, 3.58, 3.45, and 2.88 eV, respectively. The broad absorption band of ZnO NPs is due to the wide range of particle size distribution. In contrast to their corresponding bulk, the band gap value indicates that the MONPs absorb visible light at shorter wavelengths (Safawo *et al*., 2018). The blue shift is because of the large band gap energy between the valance and conduction band in nanoparticles. In general, the band gap energy of Co_3O_4, ZnO, NiO, and CuO NPs was larger than their corresponding parent bulk materials (Ganesan *et al*., 2020, Dewi *et al*., 2019, Karam & Abdulrahman, 2022).

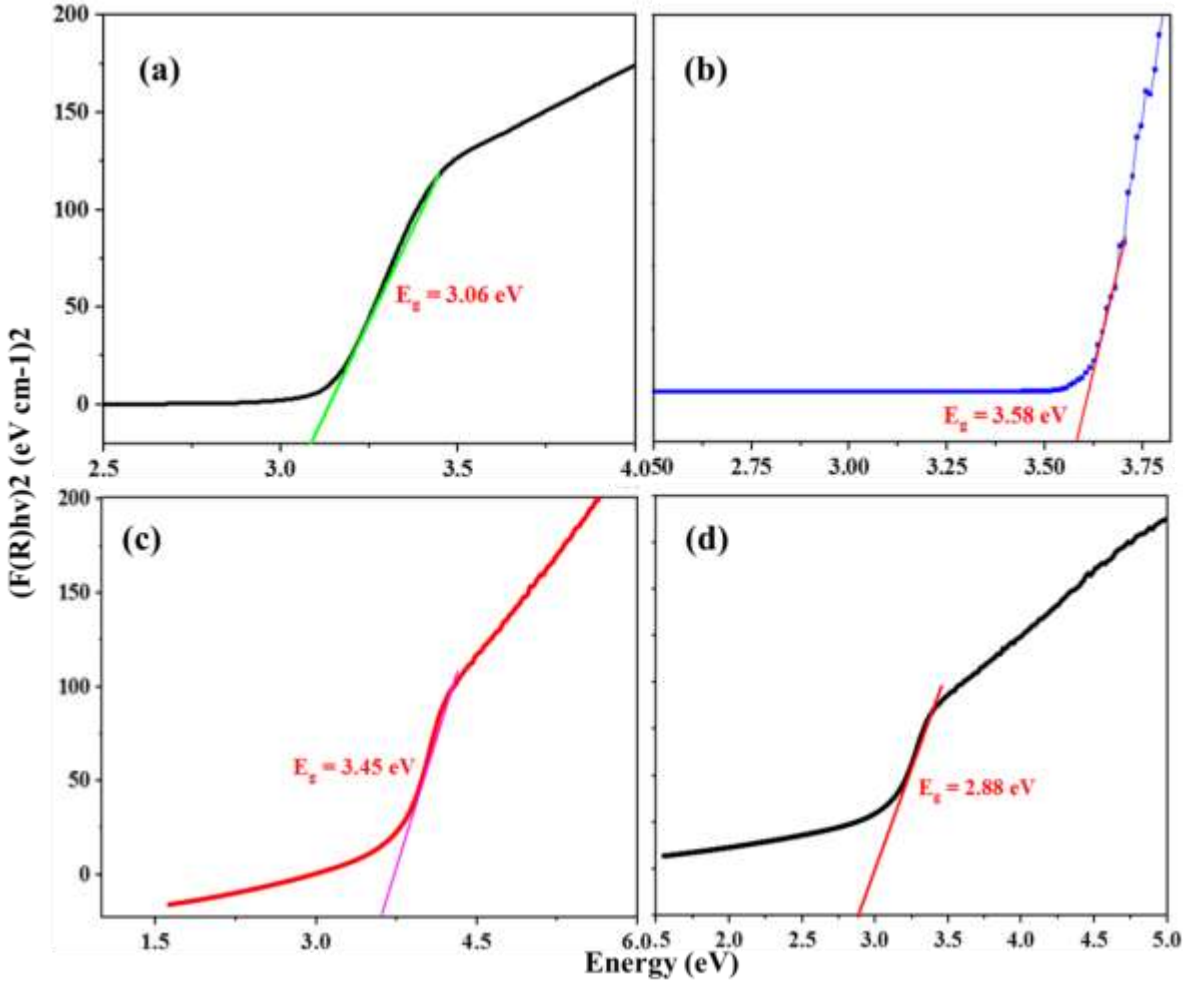

Figure 30: The band gap of (a) Co_3O_4, (b) ZnO, (c) NiO, and (d) CuO metal oxide nanoparticles.

Similarly, the absorption band of synthesized CZ, CN, and CC CSNs measured by using a UV-Vis spectrometer is shown in Figure 31(a-c). In UV-Vis analysis, the metal of the core and shell interact with incident visible light and cause oscillation of conduction electrons. The incident visible light is coupled with the oscillation of conduction electrons of CSNs and the optically active CSNs samples exhibit a plasmon resonance peak. As represented in Figure 31, the spectra show two different absorption bands which are believed to be associated with the absorption of core and shell materials. The absorption band of CZ CSNs synthesized by utilizing salt-to-salt concentration ratios was observed within the range of 230-350 nm. As depicted in Figure 31(a), the absorption peak of (11), (21), and (23) precursor salt concentration ratios were found to be 245, 250, and 254 nm which are associated with shell and 290, 315, and 320 nm that associated with core materials, respectively. Similarly, the CN CSNs absorbed the UV-Vis light at two

different wavelengths. As depicted in Figure 31(b), the characteristic absorption peak appeared at 240 (11), 254 (21), and 260 nm (23) and absorption peak at 306 (11), 322 (21), and 330 nm (23) were associated with NiO shell and Co_3O_4 core nanoparticles, respectively. Additionally, the absorption peak of CC CSNs was determined from the absorbance spectrum in terms of absorbance as a function of wavelength. As indicated in Figure 31(c), the Co_3O_4 core and CuO shell absorb visible light and result in two different absorption peaks. The first spectrum appeared at a shorter wavelength and was formed because of UV-Vis light absorption by the core and the second band is due to shell material. The absorption peak observed at 248 (11), 285 (21), and 288 nm (23) and absorption peak at 312 (11), 354 (21), and 358 (23) nm were believed to be the absorbance due to Co_3O_4 core and with CuO shell nanoparticles, respectively.

In the case of CZ and CN CSNs, the absorption peaks due to the shell appeared at a shorter wavelength, whereas in CC, the peak was observed at a longer wavelength. Relatively, the λ_{max}-shift is due to the size and band gap energy difference of core and shell materials. From the absorption measured in nm, the band gap energy was determined by extrapolation using Tauc plots of the square root of the absorption coefficient as a function of energy. As shown in Figure 31(d-f), the band gap energy of core-shell nanoparticles with small size (11) was calculated from the intercept of an extrapolated line.

As demonstrated in Figure 31(d), the band gap energy of the Co_3O_4 core and ZnO shell were found to be 3.58 and 3.82 eV, respectively. Based on the electronic nature and particle size of the core and shell materials, electrons are excited from the valance band to the conduction band. In the CZ CSNs, the core and shell particles interaction induces a change in the electronic structure and band gap energy arrangement which increases the gap between the valance band and conduction band. The band gap energy of CN CSNs was also investigated and shown in Figure 31(e). The Co_3O_4 core and NiO shell exhibit their characteristic band gap energy. From Figure 31(e), the calculated band gap energy values of 3.68 and 4.52 eV were believed to be associated with the Co_3O_4 core and NiO shell. The band gap energy of CC CSNs was determined from the intersection of the extrapolated line with the x-axis as shown in Figure 31(f). The band gap energies of Co_3O_4 and CuO NPs in CC CSNs were evaluated from the plot to be 3.15 and 2.95 eV, respectively. The increase in energy resulted in absorbing visible light at a shorter wavelength.

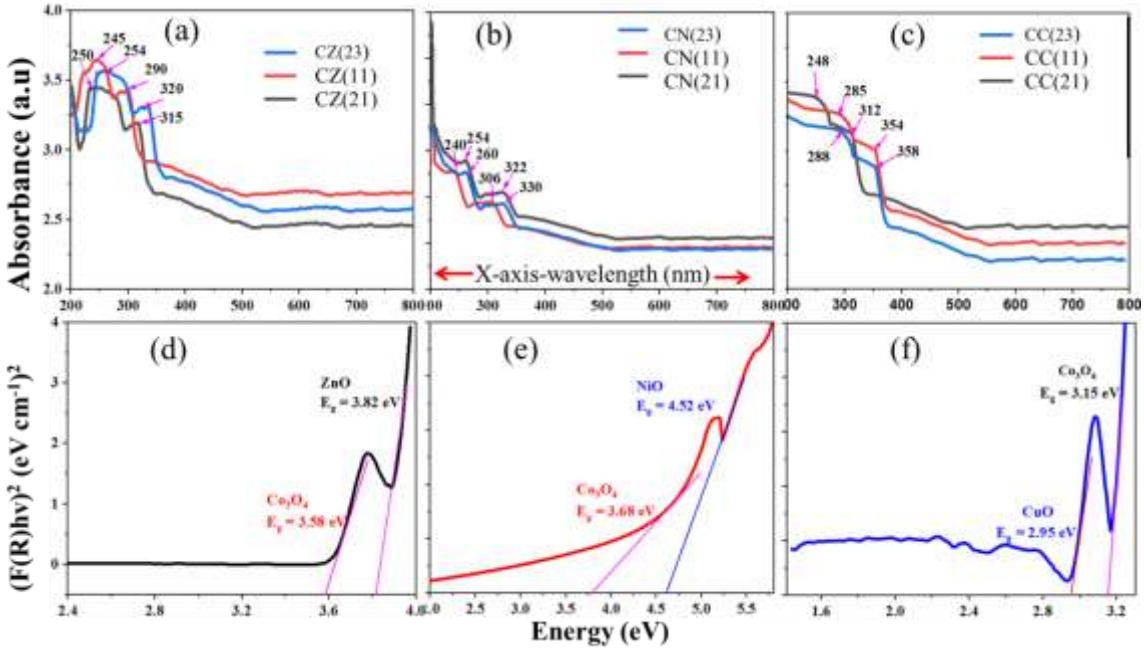

Figure 31: UV-visible optical absorption spectra of (a) CZ, (b) CN, and (c) CC and their band gap energy of (d) CZ, (e) CN, and (f) CC CSNs.

4.2.3. Functional Group Analysis

The different functional groups present in *D. stramonium* leaf extract and the synthesized metal oxide nanoparticles as well as the respective CSNs were assessed using FTIR analysis. The analysis was performed within the range of 4000-400 cm^{-1} and different spectral peaks were observed at different regions of spectra. These spectral data were used to determine the functional group present in the bioactive molecules of plant leaf extract based on the peak value in the region of infrared radiation. The spectra depicted that the bond in these functional groups interacts with infrared allowing the appearance of different spectra at different wave numbers. As shown in Figure 32 the broad absorption band at ~3448 cm^{-1} is due to the stretching of O-H of a phenolic group found in the *D. stramonium* plant (Babiker *et al.*, 2017). The absorption bands at 2925 and 2852 cm^{-1} were due to C-H asymmetric and symmetric stretching vibration groups, respectively (Ikhmal *et al.*, 2018). The symmetric stretching of the -CH_2- groups is characteristic of aliphatic compounds, such as long-chain fatty acids and alkanes. Additionally, the absorption band observed at 1638 cm^{-1} was due to the presence of C=C. The bands that appeared at 1390 cm^{-1} were due to the presence of bending vibration of C-H groups of aldehyde. Similarly, the absorption band of C-O stretching vibrations of the phenolic hydroxyl and C-N vibration of the amide groups were found to be at 1245 and 1045 cm^{-1}, respectively (Younis *et al.*, 2021).

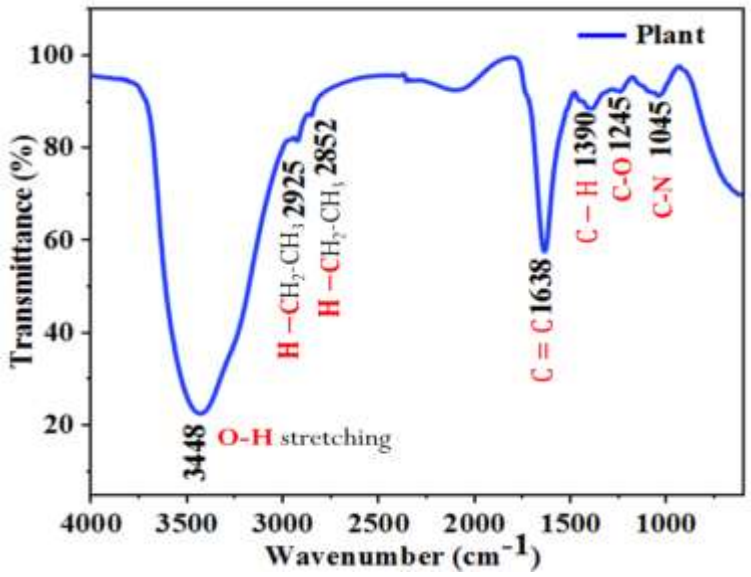

Figure 32: The FTIR spectra of *D. stramonium* plant leaf powder.

The chemical bond vibration of synthesized metal oxide nanoparticles, Co_3O_4, ZnO, NiO, and CuO NPs was predicted by measuring the absorption of infrared rays. The FTIR analysis was done to identify the functional groups that were responsible for the formation of metal oxide nanoparticles. However, most of the secondary metabolites present in *D. stramonium* plant leaf extract were removed during calcination. The metal oxygen bond stretching of Co_3O_4, ZnO, NiO, and CuO NPs was investigated as indicated in Figure 33. In the analysis of all four metal oxides, the spectra of the organic functional groups involved in the reduction and capping of the synthesized NPs were not observed. The disappearance of those functional groups was due to the calcination of synthesized nanoparticles at high temperatures. The metal oxide bonds such as Co-O, Zn-O, Ni-O, and Cu-O were revealed in the spectra. In the case of Co_3O_4 NPs, two successive stretching vibrations were observed. Basically, Co_3O_4 NPs contain two mixed valances, namely Co^{2+} and Co^{3+} ions that form Co^{2+}-O and Co^{3+}-O, respectively. The tetrahedrally coordinated Co^{2+} and octahedrally Co^{3+} ions undergo stretching vibration at 648 and 402 cm^{-1}, respectively. Additionally, two extra spectra were observed along with Co_3O_4 NPs. Due to the large surface area of nanoparticles, CO_2 molecules can be adsorbed and develop intermolecular forces. During FTIR analysis, the adsorbed CO_2 molecules undergo two characteristic bending vibration modes.

As indicated in Figure 33 of Co_3O_4 NPs spectra, CO_2 molecules absorbed from the atmosphere exhibit absorption bands at 1424 and 874 cm^{-1}, respectively, which is due to the fermi resonance

between symmetric stretching and bending and bending vibration of C-O of CO_2. In addition, the FTIR spectrum of synthesized ZnO NPs showed absorption at 405 cm^{-1} wave number which is associated with, the stretching vibration of the Zn-O bond in the sample. The presence of Ni-O and Cu-O bonds was confirmed by FTIR analysis. In the spectrum of NiO NPs the absorption spectra associated with Ni-O stretching vibration appeared at 588 cm^{-1} whereas, Cu-O stretching vibration was observed at 504 cm^{-1} (Olajire & Mohammed, 2020, Mahalakshmi *et al.*, 2020).

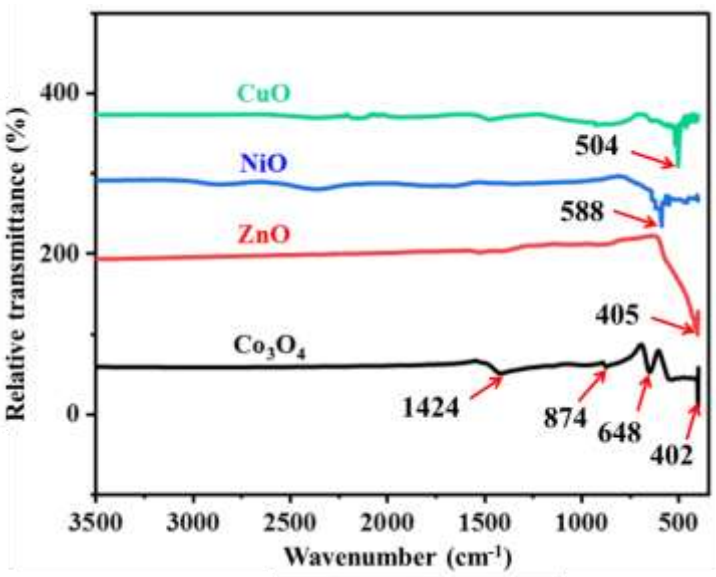

Figure 33: FTIR spectra of Co_3O_4, ZnO, NiO, and CuO NPs from bottom to top order.

Similarly, the FTIR analysis of synthesized CZ, CN, and CC CSNs was done in the same range. As shown in Figure 34, the functional groups seen in the FTIR spectra of the plant extract didn't appear in the spectra of CZ, CN, and CC CSNs. The absence of functional groups of the phytochemicals in the spectra of CSNs indicated that these functional groups involved in the reduction process were removed during calcination. As depicted in Figure 34, different absorption bands of CZ spectra at 864, 470, and 402 cm^{-1}, CN spectra at 1355, 498, and 412 cm^{-1}, and CC 1890, 821, 598 and 424 cm^{-1} were observed. In the case of CZ CSNs, the absence of a broad absorption band was due to the calcination of CZ CSNs at a high temperature that degrades and eliminates the organic functional groups. The characteristic broader peak observed at 864 cm^{-1} was due to the bending vibration of C-O of CO_2 molecules. The stretching vibration modes of Zn-O and $Co^{2/3+}$-O were also found at 470 and 402 cm^{-1}, respectively. The Functional group present in the biogenically synthesized CN CSNs was also analyzed. In the synthesized

CN CSNs prominent groups showed absorption peaks at different wave numbers (cm^{-1}). As shown in Figure 34, the absorption peak that appeared at 1355 cm^{-1} is due to the fermi resonance between symmetry stretching and bending of C-O of CO_2 adsorbed from the atmosphere on the surface of the sample (Lushchikova *et al*., 2021).

Additionally, the absorption peak for the Ni-O stretching vibration bond, and Co-O stretching vibration bond were found at 498, and 412 cm^{-1}, respectively. As shown in Figure 34, at the higher absorption wave number, the absence of peaks indicates that the synthesized sample was calcined for 5 h at which the bioactive molecules were removed. The chemical constituents of CC CSNs were also identified by measuring the absorption band at different wave numbers.

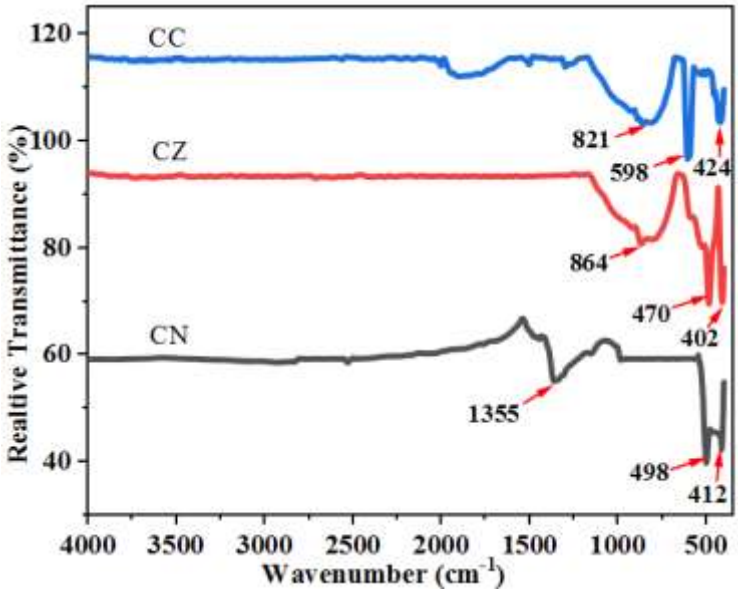

Figure 34: The FTIR spectral analysis of CZ, CN, and CC core-shell nanostructures.

The absorption band seen at 821 cm^{-1} is believed to be the bending of C-O in a CO_2 molecule. Additionally, the distinctive spectra that appeared at 598 and 424 cm^{-1} were associated with Cu-O stretching vibration $Co^{2/3+}$-O groups, respectively (Dewi *et al*., 2019).

4.2.4. X-Ray Diffraction (XRD) Analysis

The valuable information such as crystal structure, average crystallite size, and crystallographic orientation of MONPs and CSNs were investigated by using XRD spectroscopy. The average crystallite sizes of Co_3O_4(12), Co_3O_4(11), and Co_3O_4(21) NPs synthesized utilizing 0.5 M of

$Co(CH_3CO_2)_2.6H_2O$ and plant leaf extract were found to be 14, 11, and 16 nm, respectively. In the synthesis of Co_3O_4 (11), the use of equal volumes of precursor salt and plant extract resulted in a small average crystallite size of the particles. In the case of Co_3O_4(12), the volume of plant extract was twice that of precursor salt, in which the excess amount of phytochemicals interacted with each other rather than reducing the nanoparticles and resulted in the large average crystallite size of the particles in contrast to Co_3O_4(11). The XRD patterns of Co_3O_4(12), Co_3O_4(11), and Co_3O_4(21) NPs were shown in Figure 35(a) and demonstrated strong and distinct diffraction patterns at 2θ with corresponding crystal planes 19° (111), 31.2° (220), 36.82° (311), 38.5° (222), 44.8° (400), 59.32° (511), and 65.24° (440). All the diffraction peaks of Co_3O_4 NPs were indexed and fitted the standard data (JCPDS Card No: 42-1467). The cubic structure of Co_3O_4 NPs was revealed from XRD analysis (space group: Fd-3m). The length of cubic lattice parameters in which a = b = c was calculated using the formula given in equation (5) (in the Appendix section). The calculated lattice parameter value was a = b = c = 0.8074012 nm which matched with a theoretical value of 0.8072904 nm length with angles of α = β = γ = 90°.

Similarly, average crystallite sizes of ZnO(12), ZnO(11), and ZnO(21) synthesized using 0.5 M of $Zn(CH_3CO_2)_2.2H_2O$ and plant leaf extract were found to be 18, 17, and 19 nm, respectively. The XRD peaks of ZnO NPs were depicted in Figure 35(b) which revealed at 2θ of 38.82, 41.48, 43.32, 54.56, 63.66, 70, 75 and 76° and indexed to the (100), (002), (101), (012), (110), (013), (112), and (201) planes, respectively. The hexagonal wurtzite crystal structure of ZnO NPs was also investigated from XRD analysis. The diffraction peaks of ZnO NPs were fitted with their corresponding standard data JCPDS Card No: 01-070-8072. The lattice parameters of the hexagonal wurtzite structure of ZnO NPs (a = b ≠ c) were calculated using the formula shown in equation (6) (in the Appendix section) (Azam *et al.*, 2009).

Where a, b, and c are the axial length of a unit cell, (hkl) is Miller indices and d is the inter-planar spacing of the corresponding planes. The lattice parameter values (a = b) and c for hexagonal structure (α = β = 90°, and γ = 120°) of ZnO NPs were found to be 0.324017 nm and 0.519454 nm, respectively. The calculated length of lattice parameters (a = b) and c of ZnO NPs strongly fit the experimental values of 0.3247814 and 0.5198413 nm, respectively.

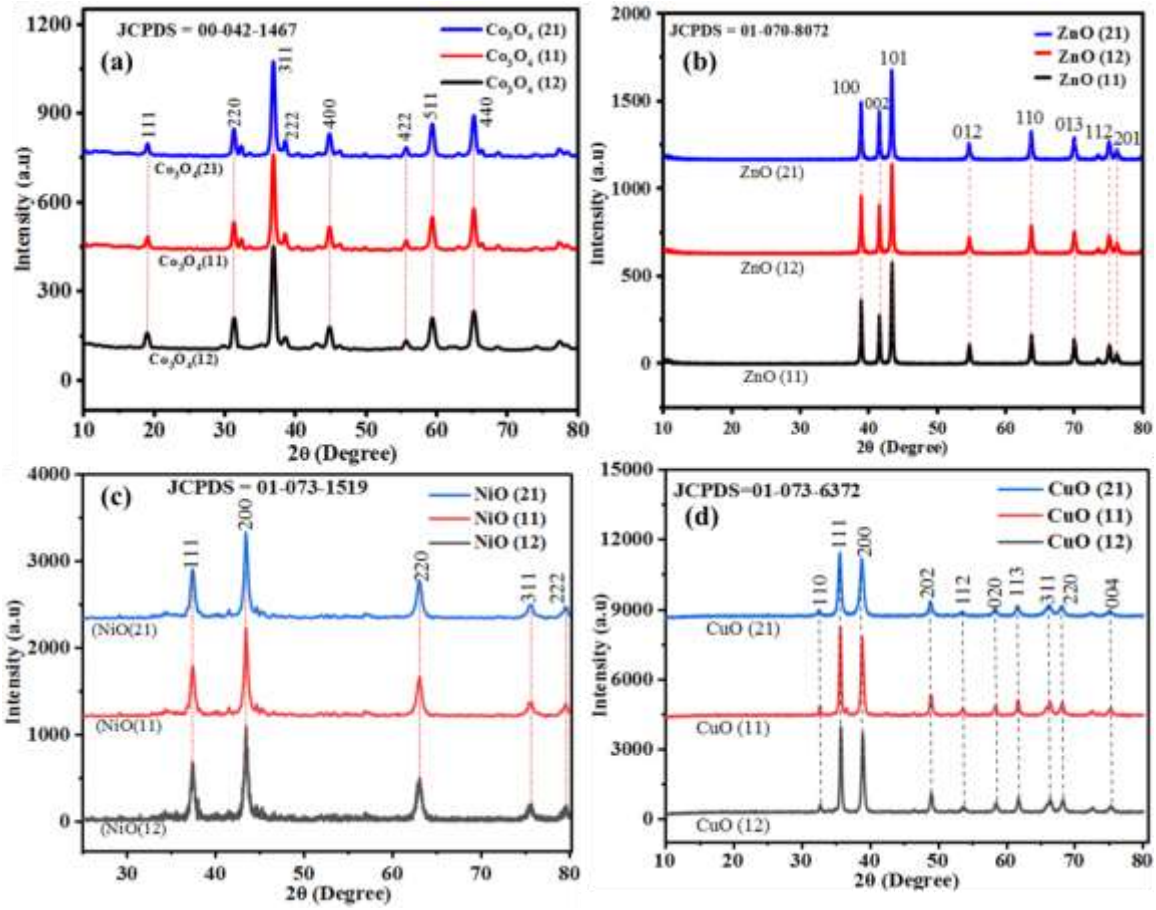

Figure 35: The X-ray diffraction patterns of (a) Co_3O_4, (b) ZnO, (c) NiO, and (d) CuO NPs.

The X-ray diffraction patterns of biogenically synthesized NiO NPs are depicted in Figure 35(c). The diffraction pattern of NiO NPs synthesized in three volume ratios such that (1:2), (1:1), and (2:1) were obtained from XRD analysis. The peaks were obtained at 2θ values of 37.42, 43.42, 63.06, 75.56, and 79.58° which matched with the miller indices of (111), (200), (220), (311), and (222) planes, respectively. The obtained result was complemented with the previous work and properly matched the standard database JCPDS card no. 01-073-1519 of NiO NPs. Furthermore, the average crystallite sizes of biogenically synthesized NiO NPs were calculated using Debye-Scherrer's formula written in equation (1). The calculated average crystallite size of NiO NPs synthesized within volume ratios of NiO (12), NiO(11), and NiO(21) were found to be 15, 12, and 17 nm, respectively. It was also found that the particles have a face-centered cubic structure with space group 225: Fm-3m. In the crystal structure of NiO NPs, the lattice parameter was found to be a=b=c=4.2024 nm with a lattice angle of ($\alpha = \beta = \gamma = 90°$). The calculated lattice parameter values were matched with the theoretical 4.1268 nm.

The formation of CuO NPs was confirmed by the XRD data analysis. As shown in Figure 35(d), the characteristic diffraction peaks of CuO NPs synthesized in (1:2), (1:1), and (2:1) volume ratios were observed which corresponds with the arrangement of atoms in the crystal lattice of the samples. The XRD pattern exhibited peaks at 2θ angles around 32.66, 35.6°, 38.8°, 48.9°, 53.6°, 58.4°, 61.6°, 66.4°, 68.2°, and 75.3° which correspond to the (110), (111), (200), (202), (112), (020), (113), (311), (220), and (004) crystallographic planes of CuO NPs, respectively. The diffraction peaks of all three ratios were found to be in good agreement with standard JCPDS with card number 01-073-6372 which confirms the formation of CuO NPs. The average crystallite particle size of (1:2), (1:1), and (2:1) volume ratios of CuO NPs were calculated using Debye Scherrer's equation written in equitation (1), and the values were found to be 14, 13, 17 nm, respectively. The difference observed in the average crystallite size of the particle is due to the difference in the volume of plant extract. The small size of CuO(11) NPs was because of the sufficient concentration of bioactive molecules required to reduce the metal ions. The diffraction peaks in Figure 35(d) indicated that the CuO NPs have a monoclinic crystal structure with lattice parameters $a \neq b \neq c$ with $\alpha = \gamma \neq \beta$ angles. The lattice parameter of the CuO NPs structure was calculated using equation (12) (in the Appendix section) (Nzilu *et al*., 2023).

Using equation (12), the values of the lattice parameter of $a \neq b \neq c$ of CuO NPs were found to be 4.26, 3.5, and 4.98 nm, respectively. The theoretical values of $a \neq b \neq c$ of were 4.67, 3.43, and 5.12 nm with lattice angle of $\alpha = \gamma = 90 \neq \beta = 99.53°$, respectively which strongly support the experimental results.

The experimental data of the diffraction angle of the newly synthesized particles (2θ), full width at half maximum (FWHM), inter-planar distance (d), and lattice parameter for ZnO NPs have been generated from the XRD diffraction pattern peaks. All the experimentally obtained data were highly matched with the standard values of ZnO NPs. The d-spacing values of ZnO NPs were found to be 0.2809, 0.2597, 0.247, 0.190, 0.1623, 0.148, and 0.137 nm referring to the corresponding planes with indices (100), (002), (101), (012), (110), (013), and (112). All the experimental values found between planes of ZnO NPs obtained from data of XRD were fully matched in the first two decimals in the standard data.

The X-ray diffraction patterns of CZ, CN, and CC CSNs of all concentration ratios are depicted shown in Figure 36(a-c). The XRD patterns of CZ(11) CSNs and parent particles such as Co_3O_4 and ZnO NPs were also shown in Figure 36(d). In XRD analysis, the electrons of both the core and shell nanostructure scattered the X-rays and produced different constructive interference patterns with different intensities. The diffraction peaks observed in separate Co_3O_4 NPs and ZnO NPs have appeared in the biosynthesized core-shell NPs which are consistent with other previous reports. The less intense diffraction peaks were observed at 31.86, 56.66, 59.12, 65.14, and 68.06 of 2θ values which were assigned to the crystal planes with miller indices (220), (442), (511), (440), and (522), respectively, which correspond to Co_3O_4 NPs (Wahab *et al*., 2021). The intense peak of ZnO shell NPs was seen at 2θ values of 34.52, 36.34, 47.71, 56.68, 62.96, and 68.06 which correspond to (002), (101), (012), (110), (112), and (013) planes respectively. As shown in Figure 36(a), all the diffraction peaks of the CZ core-shell NPs within CZ(21), CZ(11), and CZ(23) have fitted the peaks of the corresponding parent particles which is similar to the previous work report (AlTurki, 2018).

In addition to this, the formation of all CZ synthesized in (2:1), (1:1), and (2:3) concentration ratios correctly matched the standard database of JCPDS card no. 01-079-5606. The average crystallite size of *in situ* synthesized CZ core-shell NPs has been calculated using the formula shown in equation (1). The average crystal sizes of CZ(21), CZ(11), and CZ(23) were found to be 24, 22, and 25 nm, respectively. Relatively, the calculated average crystallite size of CZ(11) was found to be 22 nm which is smaller than the two ratios. The difference in the average crystallite size of CZ core-shell NPs is due to the variation in ZnO NPs in their concentration. In the case of CZ(2:1), the excess amount of phytochemicals present in the leaf extract is believed to compete with each other rather than reduce the NPs. But, in CZ(23), the number of phytochemicals present in the extract was less and not enough to reduce and cap the NPs which resulted in the agglomeration of NPs. The calculated lattice parameters of the cubic core were found to be a=b=c=0.868 nm, whereas, the hexagonal wurtzite shell was revealed with a=b=0.318 and c=0.5192 nm. The calculated lattice parameter of the core exceeds the theoretical value by 0.054 nm, which indicates the strain stretching.

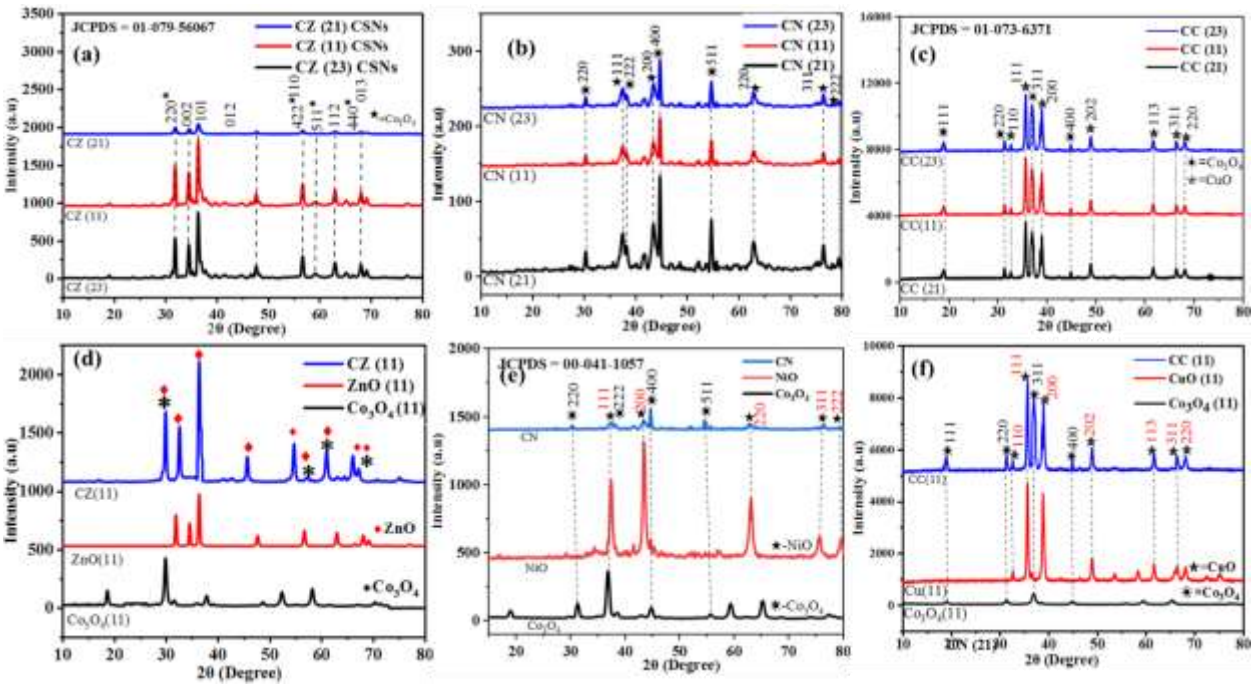

Figure 36: The X-ray diffraction patterns of (a) CZ, (b) CN, (c) CC CSNs, (d) CZ CSNs, Co_3O_4 NPs, and ZnO NPs, (e) CN CSNs, Co_3O_4 NPs and NiO NPs, and (f) CC CSNs, Co_3O_4 NPs, and CuO NPs.

As depicted in Figure 36(e), the diffraction peak with miller indices of (220), (111), (222), (200), (511), (220), (311), and (222) at 2θ values of 30.28, 37.52, 38.2, 43.32, 54.54, 62.72, 76.38, and 79.34°, respectively were obtained. The combination of plane lattice and diffraction patterns of CN CSNs indicated the formation of a core and shell which agreed with the previous work (Sanad *et al.*, 2021). Furthermore, the average crystallite sizes of biogenically synthesized CN CSNs in (21), (11), and (23) concentration ratios were calculated using Debye-Scherrer's formula written in equation (1). The calculated average crystallite size of CN(21), CN(11), and CN(23) CSNs were found to be 14, 13, and 16 nm, respectively. Reasonably, the calculated average crystallite size of CN(11) is smaller than the two ratios due to the optimum concentration and volume ratios of precursor salt to plant extract. In the case of CN(23) CSNs the amount of bioactive molecules present in the extract was not enough to reduce the size and capped the nanoparticles and this led to the agglomeration of particles and resulted in large size. Whereas in CN(21) the excess amount of phytochemicals present in the leaf extract is believed to reduce very small size which can undergo nucleation and agglomeration. As shown in Figure 36(e), the plane of the core material diffracted the X-ray radiation from the plane (220), (222),

(400), and (511) at 2θ values of 31.22, 36.82, 38.48, and 55.64°, whereas the plane of shell material diffracted from the plane (111), (200), (220), (311), and (222) at 2θ of 37.42°, 43.42°, 63.06°, 75.56, and 79.58°, respectively. Some peaks of the shell material are more intense and some are less intense than that of core materials. This indicated that the Co_3O_4 NPs were not fully enclosed by the shell NiO NPs. As shown in Figure 36(b), all the diffraction peaks of biosynthesized CN CSNs within all concentration ratios have fitted the peak of corresponding parent particles which is similar to the previous work report. In addition to this, the formation of all CN CSNs ratios correctly matched the standard database JCPDS card no. 00-041-1057. The face-centered cubic (space group-225:Fm-3m) crystal structure of the shell with a lattice parameter a=b=c=0.368 nm and cubic core with lattice parameter a=b=c=0.768 nm were investigated from XDR analysis. Compared to the theoretical value of the core (0.810 nm), the lattice parameter decreased by 0.042 nm due to strain stress.

The crystalline structure and average crystallite particle size of two-step based CC CSNs were determined using XRD analysis. Figure 36(c) shows the XRD pattern of CC CSNs synthesized in three different concentration ratios, namely (2:1), (1:1), and (2:3) CSNs. The XRD diffraction peak with miller indices of all the three ratios were found to be (111), (220), (110), (111), (311), (200), (400), (202), (113), (311), and (220) at the corresponding 2θ values of 19, 31.2, 32.66, 35.6, 36.82, 38.8, 44.8, 48.9, 61.6, 66.4, and 68.2°, respectively. As indicated in Figure 28(f) the XRD diffraction pattern appeared at 19, 31.2, 36.82, and 44.8 ° belongs to the Co_3O_4 core NPs, whereas 32.66, 35.6, 38.8, 48.9, 61.6, 66.4, and 68.2° belongs to CuO shell NPs. In the XRD analysis of CC CSNs, the peak of the CuO NPs shell is more intense than that of Co_3O_4 core NPs. The intense peak of shell material indicated that CuO NPs were found on the surface of Co_3O_4 core NPs and is believed to be that the shell was thicker and covered Co_3O_4 core NPs. Additionally, the average crystallite sizes CC(21), CC(11), and CC(23) CSNs were found to be 17, 15, and 20 nm, respectively. Figure 38(f) indicates the XRD diffraction peak that appeared in the CC CSNs matches with the peak of single metal oxide nanoparticles. Additionally, the monoclinic crystal structure (15: C12/c1 space group) of the shell was obtained from XRD analysis. The calculated lattice parameters of the CuO shell were found to be a=0.45843, b=0.34012, and c=0.5098 nm, whereas the experimental values were a=0.4674, b=0.34311, and c=0.51222 nm. Similarly, the lattice parameter of the cubic Co_3O_4 core was found to be 0.764 nm and is less than the theoretical value by 0.046 nm.

4.2.5. SEM-EDX Analysis

The morphology of the MONPs (Co_3O_4, ZnO, NiO, and CuO NPs) and the CSNs (CZ, CN, and CC) were analyzed by using the SEM instrument. The SEM images provide an estimate of the average size and size distribution of the nanoparticles present in the synthesized nanoparticles. Figure 37(a, c, e, and g) depicted the SEM image and 29(b, d, f, and h) the EDX spectra of Co_3O_4, ZnO, NiO, and CuO NPs, respectively. The rod-like shape of Co_3O_4, peacock wing-like shape of ZnO, and the spherical shape of NiO, and CuO NPs have been observed from the SEM analysis. The elemental composition of Co_3O_4, ZnO, NiO, and CuO NPs was also determined from energy-dispersive X-ray spectroscopy analysis. As shown in Figure 37(b), the 100% elemental composition of Co_3O_4 NPs confirms the presence of only Co and O which assured that the synthesized nanoparticles were free of any impurity. In Co_3O_4 NPs, the elemental percentages of Co and O were found to be 35 and 65%, respectively. As shown in Figure 37(b), the high intense peak indicated that the oxygen element found in synthesized Co_3O_4 NPs is more in percent. In the stoichiometry of Co_3O_4 NPs, the ratio of Co:O is 3:4 in which the characteristic X-ray emitted by oxygen in the sample resulted in the intense peak. Similarly, the EDX analysis of ZnO NPs indicates the presence of Zn and O elements with their elemental percentage composition of 56.8 and 43.2%, respectively. Unlike that of Co_3O_4 NPs, the elemental percentage of Zn metal is higher than that of oxygen in ZnO NPs. As depicted in Figure 37(d), the most intense peak obtained from EDX corresponds to the number of X-rays detected, which is proportional to the percentage of Zn element in the sample. As shown in Figure 37(f) and (h), the EDX spectra of NiO and CuO NPs were presented respectively. The elemental percentage of Ni and O investigated from the EDX spectrum of NiO was found to be 66.3 and 33.7%, respectively. Additionally, the elemental analysis and purity of CuO NPs were determined by using EDX spectra as shown in Figure 37(h). The sharp and intense peaks of Cu and O atoms confirmed the presence of CuO NPs. The percentage composition of Cu and O was revealed to be 52.4 and 47.6%, respectively, which ensured the absence of any other impurity in the synthesized CuO nanoparticles.

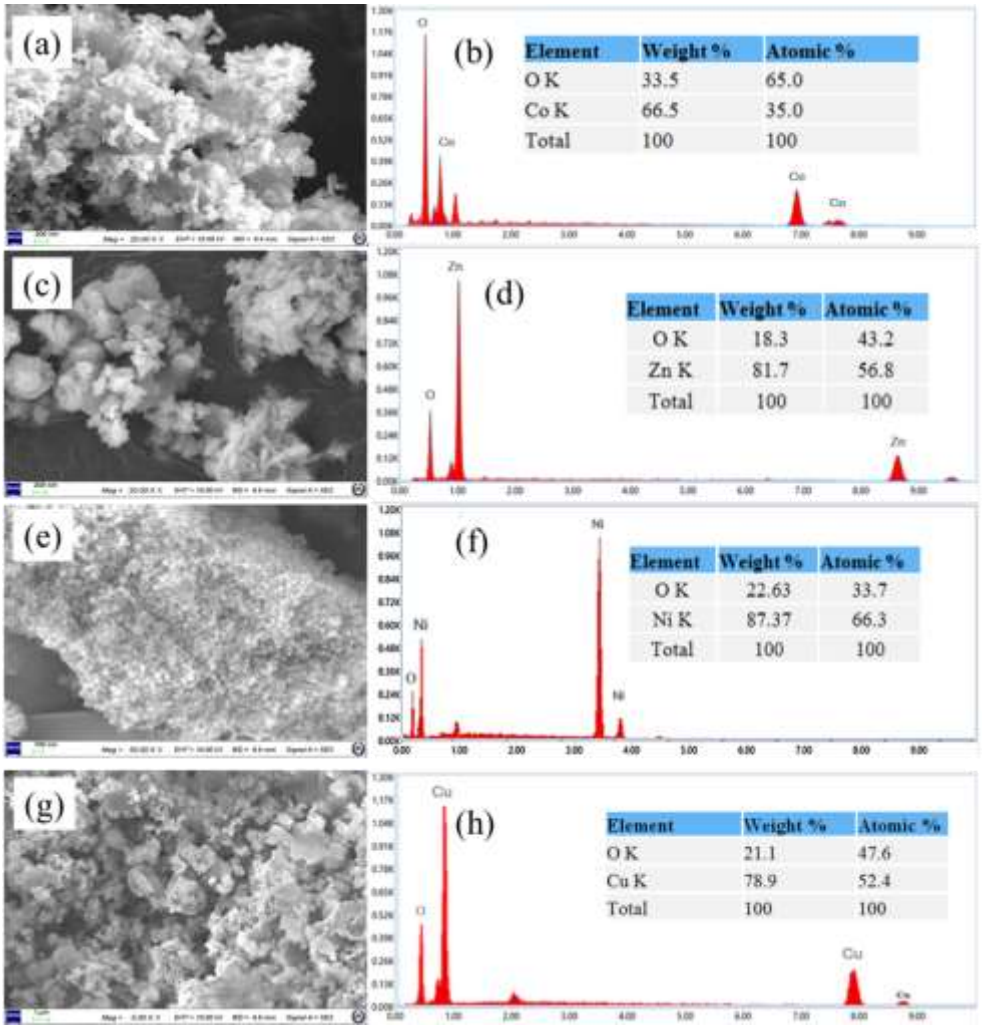

Figure 37: (a) SEM image of Co_3O_4, (b) EDX of Co_3O_4, (c) SEM image of ZnO, (d) EDX of ZnO, (e) SEM of NiO, (f) EDX of NiO, (g) SEM of CuO, and (h) EDX of CuO NPs.

The mean particle size of *D.stramonium* plant leaf extract mediated Co_3O_4, ZnO, NiO, and CuO NPs was calculated from the SEM images depicted in Figure 37(a), (c), (e), and (g), respectively. The individual diameter of the NPs was measured forty times and analyzed using Gatan software. The mean particle size of synthesized nanoparticles obtained from the SEM image was investigated using the Gaussian Fit mode of the histogram graph. All the mean particle sizes of Co_3O_4, ZnO, NiO, and CuO NPs calculated from their SEM images using Gatan software were different.

As depicted in Figure 38(a) the mean particle size of Co_3O_4 NPs was found to be 43.1 ± 1.01 nm. The distribution curve of the histogram graph showed the size distribution within the range of

25-55 nm. The particle size distribution of ZnO NPs within the range of 34-54 nm with a mean particle size of 45.7 ± 0.6 nm is shown in Figure 38(c). Similarly, the mean particle size of NiO (Figure 38(b)) and CuO NPs (Figure 38(d)) were calculated to be, 34.1 ± 1.01 and 43.2 ± 0.4 nm, respectively (Ganesan *et al*., 2020).

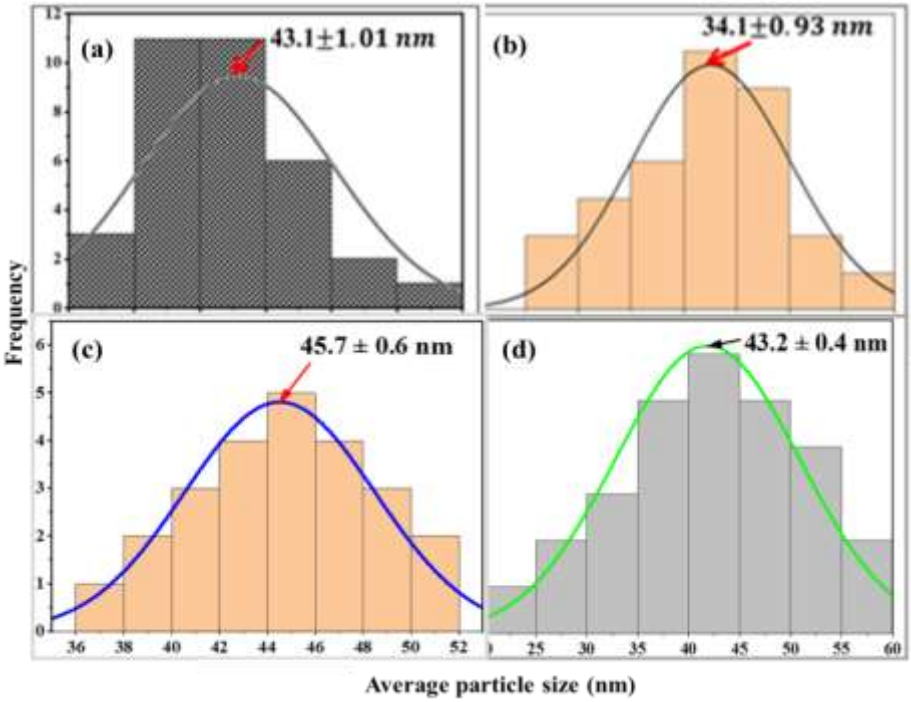

Figure 38: The particle size distribution of (a) Co_3O_4, (b) NiO, (c) ZnO, and (d) CuO metal oxide nanoparticles

The physical features and characteristics of CZ, CN, and CC CSN's surface such as size, shape, and distribution of nanoparticles, as well as the overall quality and uniformity of the CSNs, were revealed from the SEM micrograph shown in Figure 39. As depicted in Figure 39(a) in the SEM analysis, a packet of the electron beam interacts with the surface of samples, and the spherical shape of CZ CSNs was revealed from the scanned surface. The spherically shaped NPs are highly branched from the same point which seems most likely shell material that surrounded the core NPs. The overall shape of CZ NPs shows agglomeration due to the adhesion force developed from the electrostatic interaction between the core and shell NPs. The surface topography of *ex-situ* synthesized CN CSNs was also revealed from the SEM image as indicated in Figure 39(b). The spherical and rod shapes of CN CSNs were found with the indistinct core and shell region. Similarly, the morphology of the synthesized CC CSNs was also found and

analyzed. The rod, spherical, and flake-like structure of CC CSNs was depicted in Figure 39(c). From the SEM image of CC CSNs, the flaked structure was intercalated with each other and distributed in the form of aggregation to some extent.

Additionally, the elemental composition of CZ, CN, and CC CSNs was identified using energy dispersion X-ray spectroscopy within the range of 0 to 10 keV. The relative amount of elements were identified and quantified from the X-ray energy spectrum of EDX analysis as indicated in Figure 39(b), (d), and (f) for CZ, CN, and CC CSNs, respectively. The synthesized CZ CSNs were found to be composed of Co, Zn, O, and C elements. The elements of shell NPs showed an intense peak of ~ 500 at 1 KeV and core NPs ~100 counts at 0.8 KeV. The intensity of the X-ray energy spectrum refers to the concentration of elements found in the sample. As an impurity, carbon element appeared in the analysis and is believed to be from three different sources. Most likely, it is from the atmosphere in the form of carbon dioxide, which is absorbed on the surface of CSNs, formed during the calcination of synthesized materials in a muffle furnace, and from specimen holders, which were used for coating non-conducting materials for analysis. As depicted in Figure 39 (b) the atomic percentages of C, Co, Zn, and O were found to be 4.1, 15.4, 30.6, and 49.9%, respectively.

Similarly, the EDX analysis result of CN CSNs samples indicated that all elements belong to these CSNs particles. As shown in Figure 39(d), the EDX spectrum shows the presence of Co (26.91 wt%), Ni (43.69 wt%), and O (29.40 wt%), and atomic percent of Co (15.03%), Ni (24.49%), and O (60.48%) elements in CN CSNs.

The elemental composition of Co_3O_4 core and CuO shell nanoparticles was also described using EDX as shown in Figure 39(f). As indicated in the EDX spectra of CC, the Co element was appeared at 0.8 and 6.2 KeV, Cu at 0.8, 7.8, and 8.7 KeV, whereas O observed at 0.5 KeV. The evidence for elemental composition of CC CSNs obtained from EDX was in good agreement with XRD data. Additionally, valuable information about the elemental constituent of both core and shell was investigated from the EDX spectrum. In the analysis, a variety of elements have different X-ray emission which gives different peak intensities. As depicted in Figure 39(f) the elements found in CC CSNs in the EDX spectrum were Co, O, and Cu with atomic percentage composition of 15.05, 60.48, and 24.49%, respectively. In CC CSNs the copper atom (Cu) has higher X-ray emission in contrast to cobalt (Co) elements and results in an intense peak. The

higher X-ray emission of Cu and its intense peak indicated that the CuO is a shell and found on the surface of Co_3O_4 which is a core material.

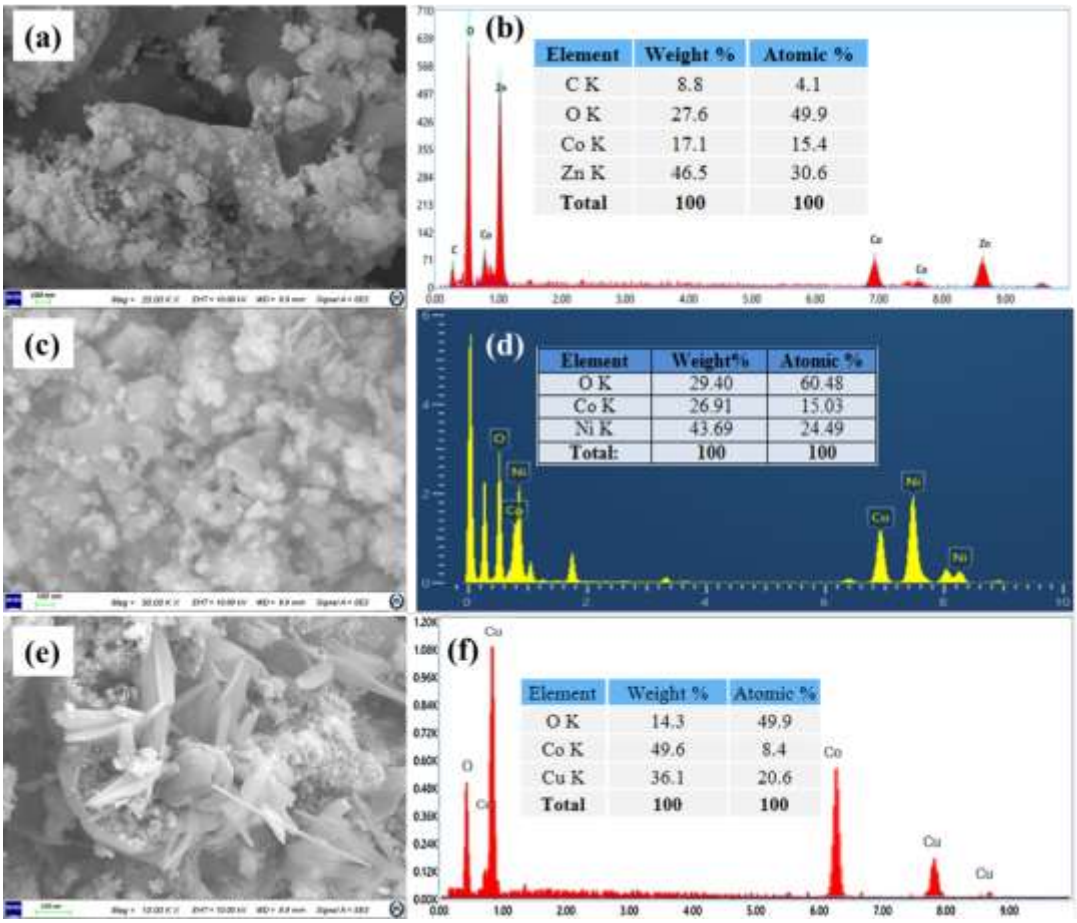

Figure 39: SEM-EDX of (a-b) CZ, (c-d) CN, and (e-f) CC CSNs

Several properties such as reactivity, solubility, stability, and dispersibility of nanoparticles depend on their particle size distribution. The mean particle size of CZ, CN, and CC CSNs were calculated using ImageJ software. In the analysis, an expressive way of plotting a particle size distribution is the histogram, in which the width of a bar indicates the lower and higher group of particle size, and where its height indicates the frequency of particle size. For this purpose, the measured values of the particles are summed up as a count and the average size was determined from the cumulative curve. As depicted in Figure 40(a-c), the mean particle size of CZ, CN, CC CSNs were found to be 63.4, 24.2, and 30.6 nm, respectively.

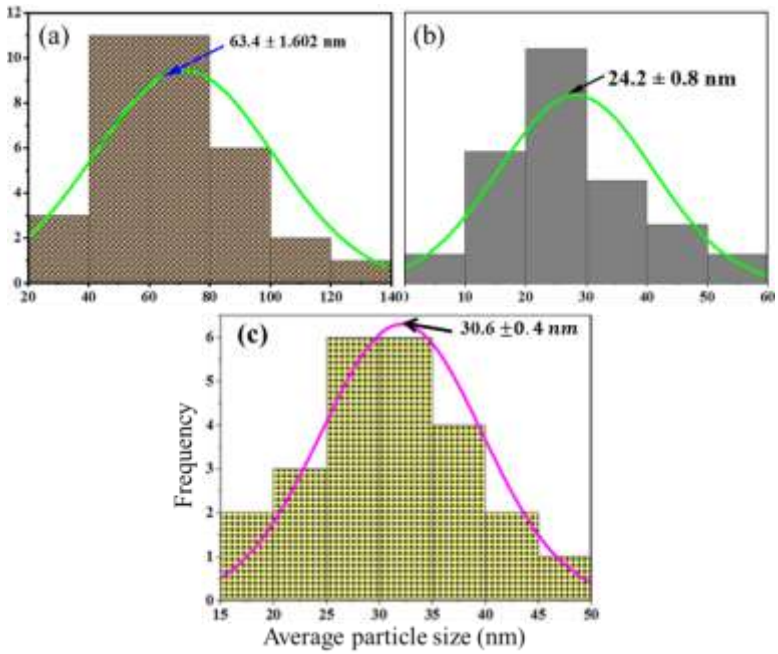

Figure 40: Particle size distribution obtained from SEM image of (a) CZ, (b) CN, and (c) CC CSNs.

In particle size measurement, the cumulative particle size distribution is from the class-dependent values. For this purpose, the quantities for each measurement are determined as mean. This produces a curve with maximum particle size values within different ranges of the curve.

4.2.6. TEM/HR-TEM and SAED Analysis

The *D. stramonium* leaf extract mediated Co_3O_4, ZnO, NiO, and CuO NPs and CZ, CN, and CC CSNs were further analyzed using TEM/HR-TEM and SAED techniques. The TEM and HR-TEM images provided detailed information on the size and shape of the MONPs and CSNs, while the SAED patterns were used to confirm the crystalline nature of the synthesized material. In Figure 40(a-d), the shapes of Co_3O_4, ZnO, NiO, and CuO NPs were investigated. It has been observed from Figure 41(a) that the *D. stramonium* leaf extract mediated Co_3O_4 NPs show semi-spherical and rod like shapes. TEM images of ZnO NPs also provided information such as size, shape, and particle size distribution (Ramesh *et al.*, 2022). As indicated in Figure 41(b), the synthesized ZnO NPs have appeared with semi-spherical shape.

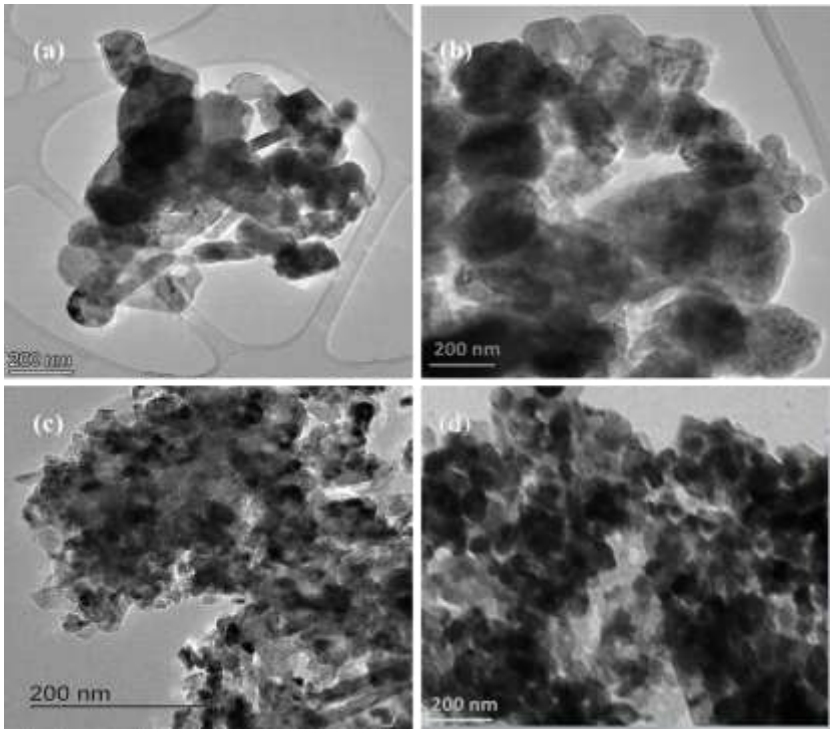

Figure 41: TEM images of (a) Co_3O_4, (b) ZnO, (c) NiO, and (d) CuO metal oxide nanoparticles.

The morphology of the synthesized NiO NPs is also shown in Figure 41(c). The TEM image shows that NiO NPs have appeared with spherical and oval shapes. From the image, the shape of particles is not uniformly distributed which is due to particle aggregation to some extent. The TEM image of CuO nanopowder synthesized in (1:1) volume ratio is shown in Figure 41(d). The spherical shapes of CuO NPs were revealed from the TEM images. In addition to the mean particle size obtained from SEM Images, the mean particle size of MONPs was also determined from TEM images. The mean particle size of Co_3O_4, ZnO, NiO, and CuO NPs were depicted in Figure 42(a-d). In the case of Co_3O_4 NPs, the particle size distribution was found within the 10-25 nm range.

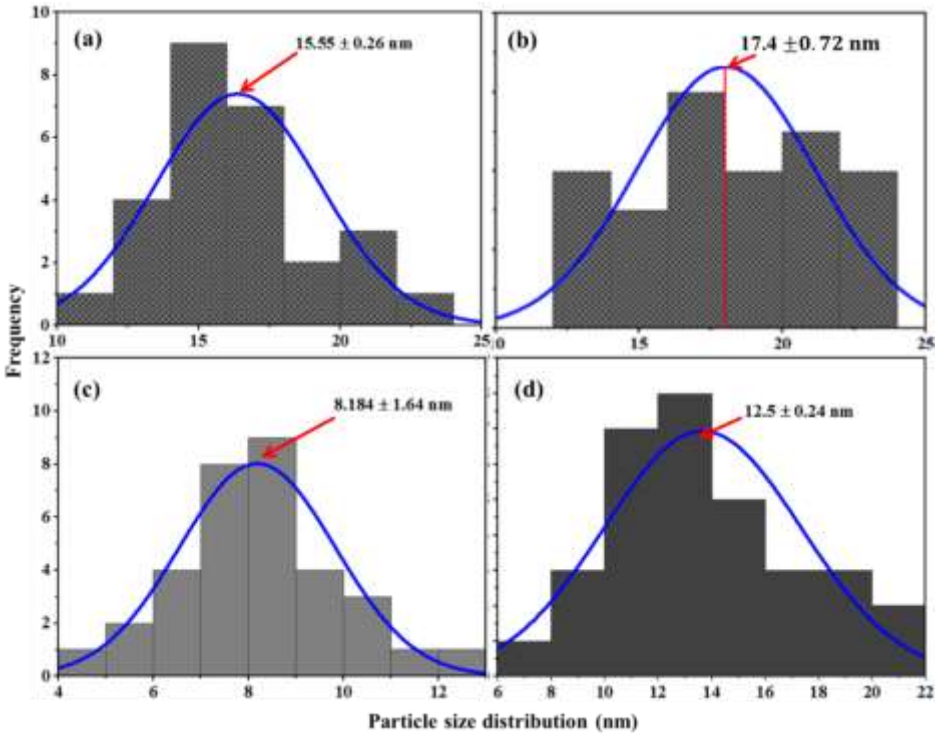

Figure 42: The particle size distribution of (a) Co_3O_4, (b) ZnO, (c) NiO, and (d) CuO metal oxide nanoparticles obtained from the TEM image.

As indicated in Figure 42(a) the mean particle size of Co_3O_4 NPs was found to be 15.55 nm. The diameter measured at the nanoscale was analyzed using the Gaussian Fit model and the mean particle sizes for Co_3O_4 NPs were determined using the equation (13) (in the appendix section). Figure 42(b) is a histogram of ZnO NPs that represents the mean particle size and particle size distribution. The particle size distribution of synthesized ZnO nanopowder was commonly determined by using a transmission electron microscope. The analysis was performed to obtain the appropriate particle size of the synthesized nanoparticles. As shown in Figure 42(b) the size of synthesized ZnO NPs was found less than 25 nm. The diameters of individual particles were found within the 10-25 nm range. Nearly the diameter of 60 particles was measured randomly and the determined mean particle size of synthesized ZnO NPs was found to be 17.4 nm. The difference in particle size is believed to be from nucleation and growth of nanoparticles. The bioactive molecules of *D. stramonium* utilized as a reducing and stabilizing agent act as templates in which aggregation and formation of particles with different sizes take place. The phytochemicals bound to the surface of nanoparticles in a certain crystallographic direction help the nanoparticles to have a particular shape.

Similarly, the mean particle size of NiO NPs synthesized utilizing plant leaf extract was also determined. As shown in Figure 42(c), the particle diameters of NiO NPs were typically within the range of 4-14 nm. The bioactive molecules stabilized the NiO NPs by forming a protective layer and prevented the aggregation which resulted in small size. As shown in Figure 42(c) the mean particle size of NiO NPs was found to be 8.184 with an uncertainty value of ± 1.64 nm. From the value obtained using ImageJ software, the uncertainty of ± 1.64 nm indicated that the actual size of NiO NPs ranged from 6.54-9.82 nm.

The reduction of Cu ions by using the secondary metabolites present in the *D. stramonium* leaf extract was also confirmed using TEM techniques in terms of size. Using Gatan software, the particle size distribution of CuO NPs was found to be within the range of 6-25 nm. As depicted in Figure 42(d), the actual particle size of CuO NPs has been found 12.26-12.74 nm with an mean particle size of 12.5 nm. In contrast to the particle size distribution of Co_3O_4, ZnO, and NiO NPs, the particle size distribution of CuO was consistent. The homogeneity of particle size is mainly due highest reduction potential of Cu^{2+} ion.

Additionally, the samples were analyzed under HR-TEM to determine the number of grains and lattice fringe alignment. The lattice-fringe/structural fingerprint of biologically synthesized Co_3O_4 NPs was found with a long-range arrangement as shown in Figure 43(b). The structural fingerprints developed by the incident electron diffraction after transmitting through the sample were used to determine the inter-planar distance. From the actual HR-TEM image shown in Figure 43(b), the characteristic distance between the fringes was obtained using the Inverted Fast Fourier transform (IFFT) model. The inter-planar distance for Co_3O_4 NPs was found to be 0.3286 nm which refers to the plane (311). The high visibility and long-range alignment of the structural fingerprinting are shown in Figure 43(b) indicating the high crystalline nature of the biologically fabricated Co_3O_4 NPs.

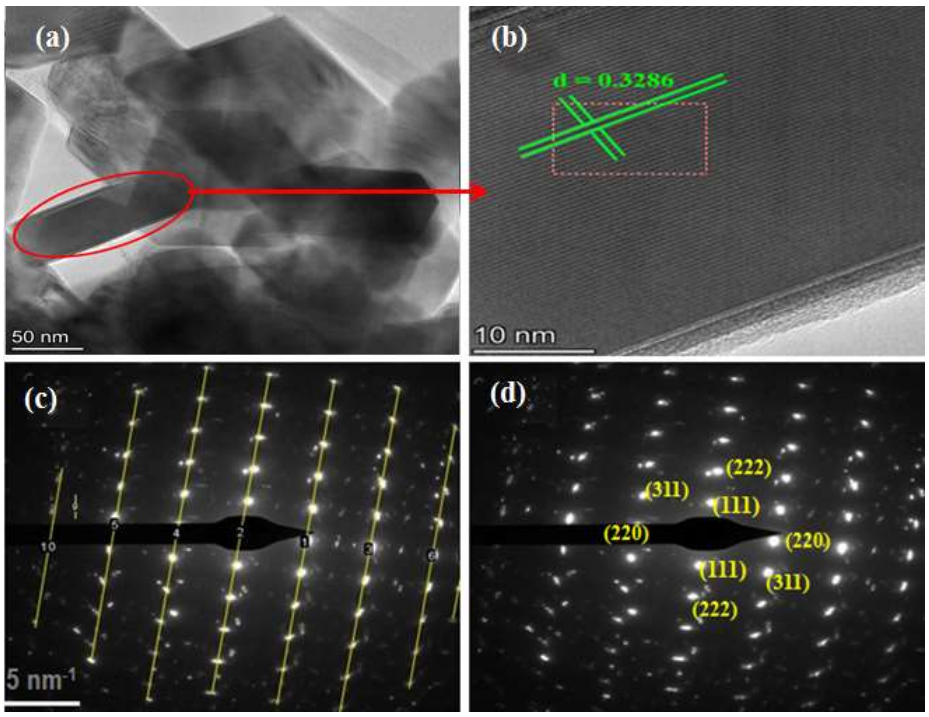

Figure 43: The TEM image (a), HR-TEM image (b), and SAED (c and d) images of Co_3O_4 NPs.

Moreover, the crystallinity nature of the synthesized Co_3O_4 NPs was also explored from the SAED image shown in Figures 43(c) and (d). The diffraction spots are regularly well arranged in the long-range distances and found in the parallel lattice fringe of Co_3O_4 NPs. The spots in the structural fingerprint form parallel lines rather than circular diffraction. As represented in Figure 43(c) the spots in each parallel lattice fringe are arranged at equal distances. Thus, it indicates the atoms in the biologically synthesized Co_3O_4 NPs are ordered regularly and have a high crystalline nature.

The crystallinity nature and structural fingerprint of synthesized ZnO NPs were also analyzed employing SAED and HR-TEM, respectively. The lattice fringe-structural fingerprint of the HR-TEM image is shown in Figure 44b). The inter-planar distance was also determined using Gatan software and was found to be 0.2744 nm which is almost equivalent to the theoretical values (0.28 nm). The experimental value of inter-planar distance obtained from the actual HR-TEM image complies with the calculated value from XRD data. Thus, the comparable result achieved from different characterization techniques helps to confirm the formation of ZnO NPs. The crystalline nature of hexagonal wurtzite ZnO NPs was investigated by employing SAED techniques. As displayed in Figure 44(c) the diffraction spots seem regularly ordered with

unequal distances. The unequal distances between spots were believed to be due to several crystals present in ZnO NPs which designate the poly-crystallinity of the particles.

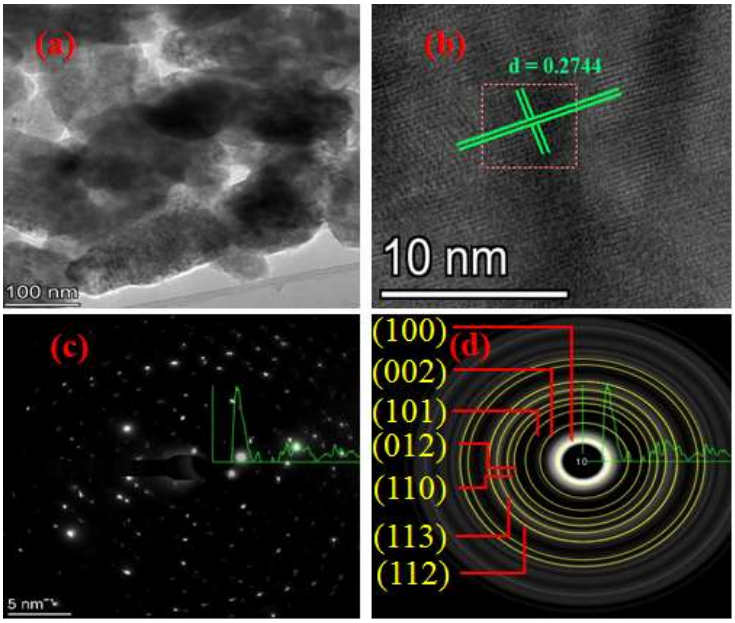

Figure 44: The TEM image (a), HR-TEM image (b), SAED image (c), and miller indices (d) with corresponding planes of ZnO NPs.

The crystalline nature and lattice parameters of NiO NPs were investigated from the high-resolution (HR-TEM). Figure 45(a) and (b) indicate the HR-TEM image and the distance between the lattice fringes. The d-spacing values depicted in Figure 45(b) were calculated using Gatan software. The lattice distance corresponding to the respective miller indices (111) was found to be 0.26 nm. These characteristic (hkl) values of NiO NPs with the d-spacing values obtained from SAED were in good agreement with the standard values of XRD data. Additionally, the crystal structure of synthesized NiO NPs was determined from SAED images shown in Figure 45(c).

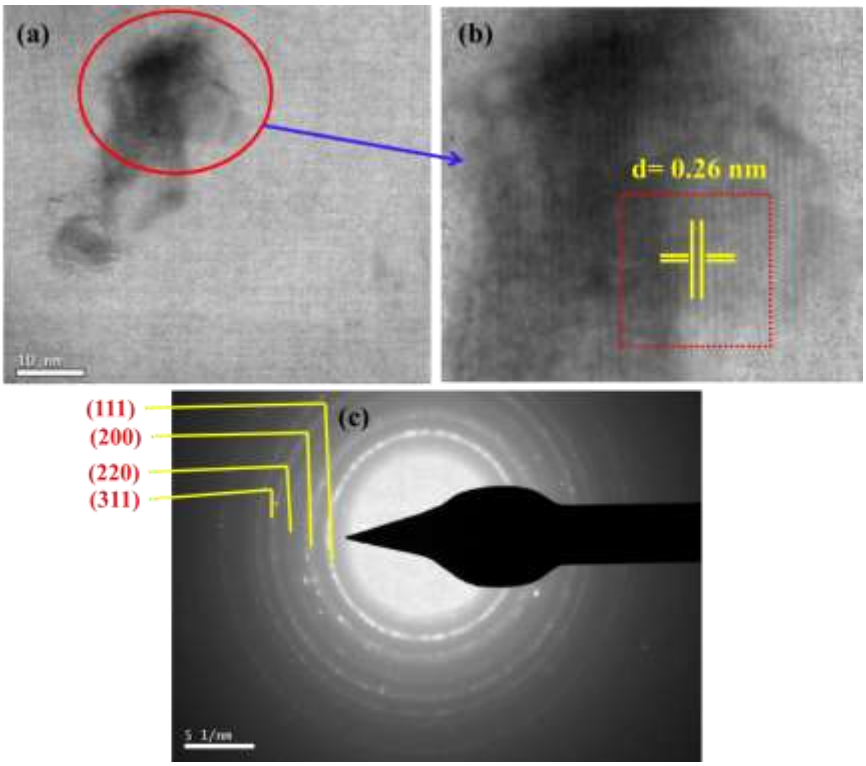

Figure 45: The HR-TEM image (a), interplanar distance (b), SAED image with miller indices (c) of NiO nanoparticles.

Based on the orientation and particle size, the circular diffraction pattern was obtained. The circular diffraction spot corresponds to the lattice points of the crystal structure exhibiting the concentric rings which ensure that the synthesized NiO NPs have a polycrystalline nature.

In addition to HR-TEM, SAED analysis results of CuO NPs shown in Figure 46(a) and (c) also confirm the formation of the particles, respectively. As depicted in Figure 46(b), the lattice fringes in HR-TEM images of CuO NPs were found to be 0.24 nm, associated with the respective miller index (202) which is in good agreement with the d-spacing values of standard and calculated XRD data.

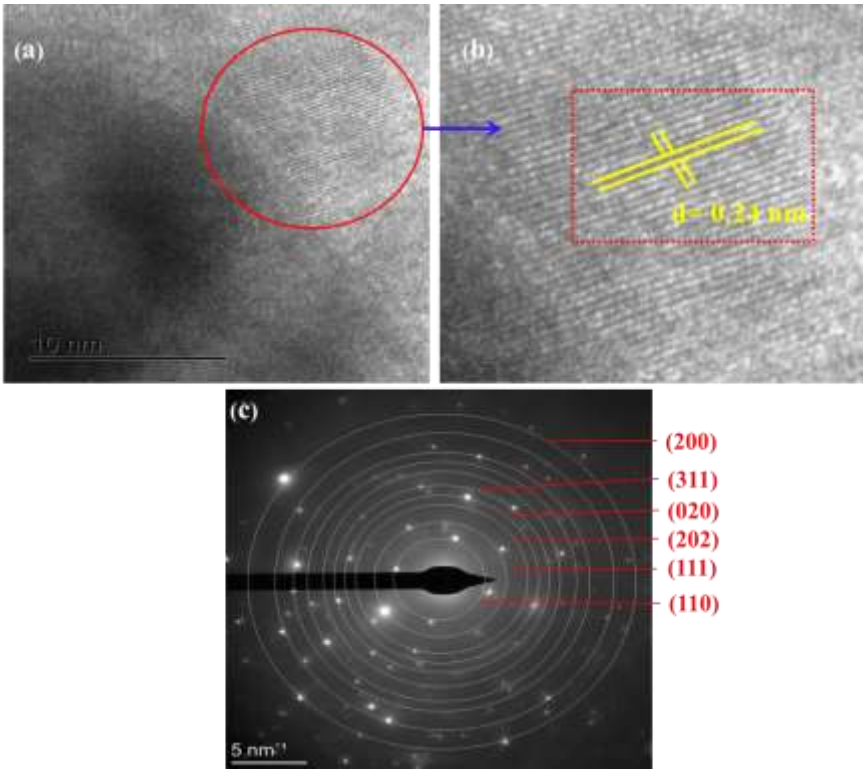

Figure 46: The HR-TEM image (a), interplanar distance (b), SAED image with miller indices (c) of CuO nanoparticles.

Table 5: The particle sizes of Co_3O_4, ZnO, NiO, and CuO NPs obtained from XRD, SEM, and TEM.

Nanoparticles	Particle size -SEM (nm)	Particle size - TEM (nm)	Average crystallite size-XRD (nm)
Co_3O_4	43.1	15.55	11
ZnO	45.7	17.4	17
NiO	34.1	8.184	12
CuO	43.1	12.5	13

The morphology of CZ, CN, and CC CSNs was investigated using TEM characterization techniques. In the case of CZ CSNs, the shape and mean particle size of *in-situ* synthesized particles were revealed with the Co_3O_4 and ZnO NPs as core and shell, respectively. As shown in Figure 47(a) of the TEM image, rod-like and spherical shapes of CZ CSNs were investigated. The TEM images have shown the core and shell NPs. The black area observed in Figure 47(a) is

the Co_3O_4 core particle surrounded by a ZnO shell. In this study, the synthesized CZ CSNs are supported by XDR pattern placement and HR-TEM/SAED results, which are highly similar to those reported in previous studies of sol-gel synthesized CZ CSNs (AlTurki, 2018). The successful synthesis of these features suggests that our synthesis method is effective in producing core-shell NPs with similar properties and characteristics. As indicated in Figure 47(d), the mean particle size was found to be 21.94 nm within the particle size distribution range of 10-35 nm which is determined under the nonlinear curve Gaussian Fit. Furthermore, the mean particle size of the Co_3O_4 core particle was found to be 10.95 nm. The size of the core material was obtained using the normal (Gaussian) distribution formula. The value of the size of the core particle is less than that of the overall size of the CSNs. This indicated that the size of the shell material coating the inner core was larger than the core. The normal Gaussian distribution plot in terms of particle size showed that the value of xc was 10.68 to 11.22 nm which is the size of the Co_3O_4 Core nanoparticle.

Additional information on the precise morphological aspects of CN CSNs was examined using TEM. The TEM images of CN CSNs presented in Figure 47(b) showed spherical and prismatic shapes. As shown in Figure 47(b) the darker area in CN CSNs is believed to be Co_3O_4 NPs which is a core and the lighter area shows NiO NPs which is a shell of synthesized particles. This is because of the difference in the electron sprinkling between the core and shell particles. The distribution of CN CSNs across the TEM image in terms of their size was also obtained. The diameter of 60 particles was measured by using Gatan software and the mean particle size was determined from the histogram. As depicted in Figure 47(e) the mean particle size of CN CSNs was found to be 16.99 nm with a standard deviation of 0.13 nm. The range of particle size distribution was within 5-35 nm which implies that the CN CSNs were found to be agglomerated to some extent which might be attributed to the removal of bioactive molecules during calcination. The originally bioactive capped CN CSNs shrank together after calcination and resulted in agglomeration.

The synthesized CC CSNs was also analyzed using the TEM technique. The analysis has aided in understanding the morphology of CC CSNs. In CC CSNs, the Co_3O_4 NPs form the core and CuO forms the shell. As shown in Figure 47(c) the TEM image showed the contrasted regions surrounding the lighter area. This dark region implies the formation of a Co_3O_4 core surrounded

by the lighter part which is CuO shell nanostructure. From the TEM image of CC CSNs the shape, mean particle size, and particle size distribution were investigated. The TEM image of *D. stramonium* plant leaf extract mediated CC CSNs presented in Figure 47(c) showed semi-spherical and cylindrical shapes. Furthermore, the mean particle size of CC CSNs was calculated and the particle size distribution was revealed within the range of 2-22 nm. The mean size of CC CSNs was found to be 11.07 nm with a standard deviation value of 0.63 nm as shown in Figure 47(f). Additionally, the mean particle size of the core and shell of CC CSNs were found to be 8 and 4 nm, respectively.

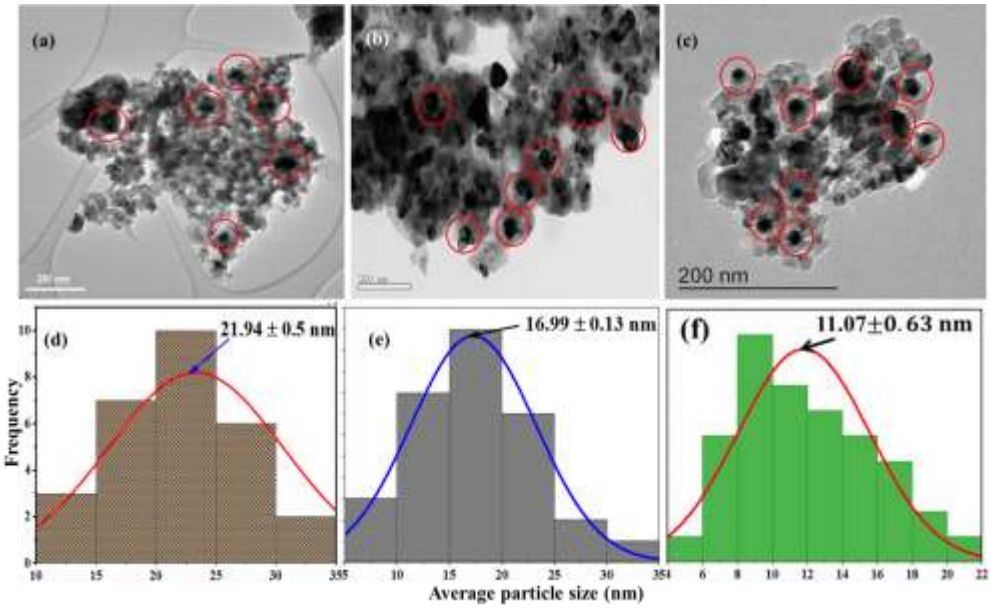

Figure 47: The TEM image of (a) CZ, (b) CN, and (c) CC and particle size distribution (d) CZ, (e) CN, and (f) CC.

The HR-TEM analysis explored the grain distribution of synthesized NPs as depicted in Figure 47(a and b). The distance between fringes (d-spacing) was determined from HR-TEM using Gatan software. The d-spacing for CZ CSNs obtained from IFFT of Gatan software and determined from X-ray diffraction peak using Origin2023/24 were almost equal. As indicated in Figure 48(c) the d-spacing for the ZnO (002) and Co_3O_4 (220) planes was 0.259 and 0.28 nm respectively. The crystalline structure of the CZ CSNs was revealed using selected area electron diffraction (SAED). Figure 48(d) demonstrates the polycrystalline structure of CZ CSNs from the SAED image. Unlike that of XRD, electron beams were diffracted from the highly selected area. In SAED analysis the atoms in the CSNs diffracted by the electrons resulted in small bright

spots that made up of a full ring-like pattern. In XDR analysis the crystallinity was confirmed by the diffraction peaks of X-ray from the atoms found on the planes whereas SAED used diffraction of electrons that showed the regularly ordered spots. The bright ring of SAED refers to the fringe alignment which is equivalent to the plane in which its atoms diffract X-ray. The circular electron diffraction is depicted in Figure. 48(d) has resulted from many crystalline arrangements.

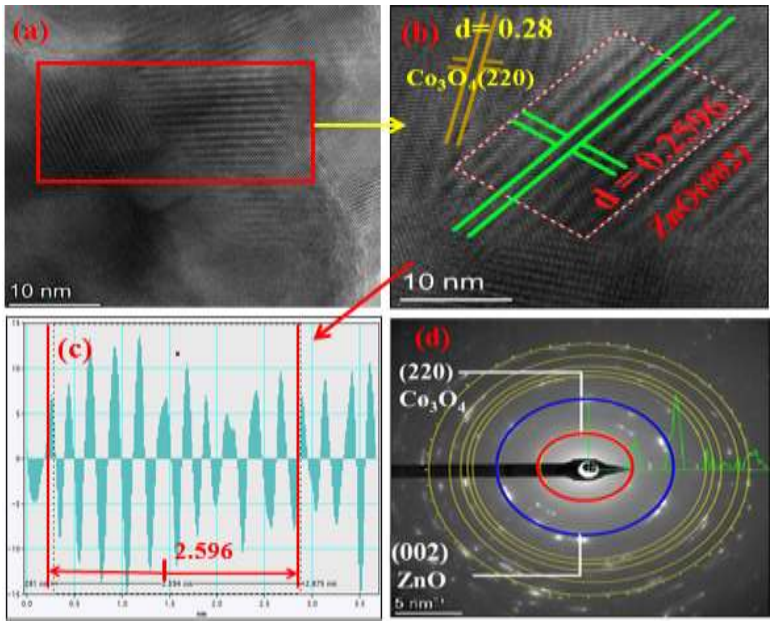

Figure 48: The HR-TEM image (a), selected area of HR-TEM image (b), inverted IFFT (c), and SAED image (d) of CZ CSNs.

In addition to its crystalline nature, SAED is also used for determining the distance between each ring which corresponds to the plane represented by Miller indexes (hkl). The SAED pattern of CZ CSNs indicated the first inner ring with a d-spacing of 0.275 nm and the second 0.258 nm which matched with the d-spacing values of XRD with miller index (220) and (002). In the CZ CSNs the plane with miller index (220) belongs to Co_3O_4 NPs and the (002) plane to ZnO NPs which confirmed that Co_3O_4 NPs were found in the core and ZnO NPs on the shell of CZ CSNs. This investigation indicates good agreement with the CSNs formation obtained from the TEM image and its nanoscale size.

The CN CSNs containing Co_3O_4 core and NiO shell were further examined by using high-resolution TEM. The core-shell structures, interface of core and shell, and the distance between adjacent crystals lattice planes in the nanostructure have been explored. As shown in Figure

48(a) the highly magnified CN CSNs showed the core and shell structure. As shown from the TEM image in Figure 49(a), the HR-TEM image also showed the dark region that ensures the formation of the core and shell nanostructure. In the area where the NiO shell coats the Co_3O_4 core appeared darker in the HR-TEM image. The darker region is believed to be because of higher electron density in the core, resulting in different electron scattering.

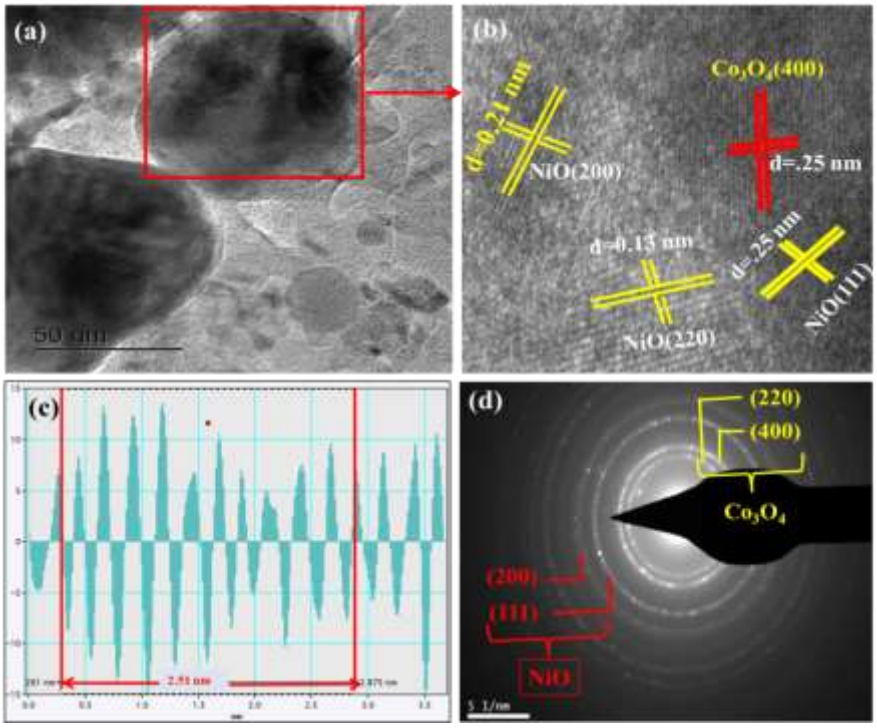

Figure 49: The biologically synthesized (a) HR-TEM image, (b) d-space values of selected fringe (c) inverted IFFT and (d) SAED image of CN NPs.

Under high-resolution detection with the beam of an electron, the incident electron from the electron gun passes through the core of the CN CSNs sample and experiences strong diffraction because of the high density of the electron. The strong diffraction causes a reduction in the intensity of the electron reaching the detector, resulting in a darker region in the HR-TEM image. In contrast, the NiO shell with lower electron density diffracts electrons to some extent whereas most electrons reach the detection and result in brighter regions of the shell observed in Figure 49(a). On the other hand, the shell material, which has a lower atomic number and electron density, scatters electrons to a lesser extent.

As a result, more electrons reach the detector, leading to a brighter appearance in the image. The distance between adjacent crystal lattice planes of the Co_3O_4 core corresponding miller indices

(400) was found to be 0.25 nm, which is presented in Figure 49(b and c). Similarly, the d-spacing for the NiO shell with miller indices (111), (200), and (220) were 0.25, 0.21, and 0.13 nm respectively. The miller indices obtained from HR-TEM and SAED were found in good agreement with the d-spacing values of standard XRD data.

Moreover, Figure 49(d) clarified the SAED image of CN CSNs where miller indices are shown with their corresponding planes. The miller indices were identified from the d-spacing values of the crystal lattice planes of CN CSNs. The calculated lattice space belongs to the miller indices of CN CSNs which are used to confirm the formation of CSNs. In addition, the SAED image explored the crystalline structure of synthesized CN CSNs. As shown in Figure 49(d), the well-defined ring was revealed that shows the polycrystalline nature of CN CSNs.

The structure of *D. stramonium* plant leaf extract mediated CC CSNs containing Co_3O_4 core and CuO shell was also determined by using HR-TEM and SAED analysis. The HR-TEM image of CC CSNs, calcined at 320 ℃ for 5 h was shown in Figure 50(a and b). A similar mode that was found for the structure of CZ and CN CSNs, was also observed in the structure of the CC CSNs. The darker region found in the HR-TEM images of CC CSNs indicates the presence of a core in the synthesized nanoparticle. Additionally, the lattice fringe of both the core and shell with a d-spacing were determined. As shown in Figure 50(b), the distinctive d-spacing value of the Co_3O_4 core corresponding to Miller indices (311) was found to be 0.23 nm. Whereas, the d-spacing values of the CuO shell for corresponding miller indices (111) and (113) were 0.26 and 0.15 nm, respectively. The experimental value obtained for the d-spacing of CC CSNs was in good agreement with standard XRD data. The crystalline nature of CC CSNs which is a periodic function of atoms was characterized and confirmed through SAED in transmission electron microscope. The circular pattern shown in Figure 50(d) indicates that the CC CSNs exhibit a high degree of crystalline which reveals a polycrystalline structure. In SAED analysis, the electron beam interacted with the selected area of CC CSNs and experienced diffraction patterns corresponding with the crystal structure. The crystal structure's circular shape is a consequence of the rotationally symmetric nature of the crystal structure and the random orientation of the nanoparticles in the sample. The presence of a circular pattern indicates that the core-shell nanoparticles have a polycrystalline nature, meaning that they consist of multiple crystalline domains with different crystallographic orientations. Each crystalline domain within the

nanoparticles contributes to the diffraction spots that form the circular pattern in the SAED image.

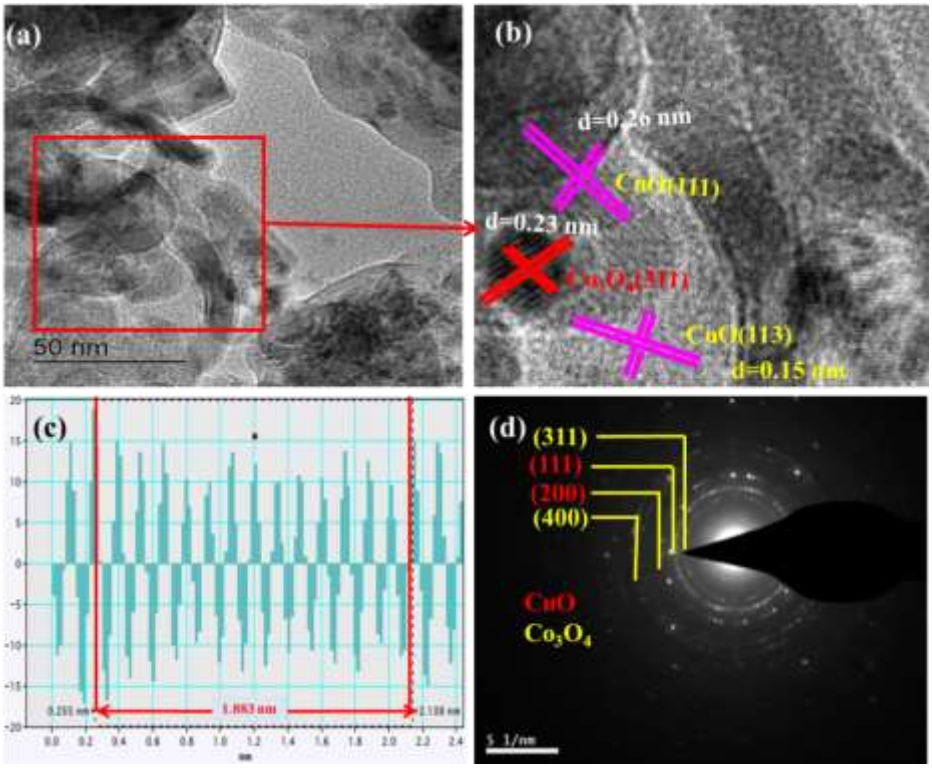

Figure 50: Synthesized (a) HR-TEM image, (b) d-space values calculated from HR-TEM image, and (c) SAED image of CC NPs.

4.3. Anticancer Activity

Nanoparticles (NPs) have emerged as a strong tool in the encounter against cancer, particularly breast cancer, because of their unique physicochemical features. The two most important conditions for breast cancer therapy are efficacy and selective toxicity. To address these issues, MONPs, the most promising alternative to traditional chemotherapy for breast cancer treatment, underwent comprehensive testing. The CSNs have a unique core substance surrounded by a shell layer and offer various benefits for anticancer applications, such as increasing stability, control drug release, and precise targeting capabilities, and recently gained attention for their potential anticancer effects. This indicates that the properties of the core-shell nanoparticles have been modified, and outperform single MONPs in all of their activities. Similarly, in this study, the ZnO, NiO, and CuO NP shells were coated onto Co_3O_4 core NPs.

4.3.1. Cytotoxicity

The cytotoxicity of synthesized CZ, CN, and CC CSNs, as well as Epirubicin (conventional drug), was assessed against breast cancer (MCF-7) cell lines and peripheral blood mononuclear (PBM) cells using an MTT assay. In this work, different concentrations of 12.5, 25, 50, 100, 200, 400, and 800 µg/mL of CZ, CN, and CC CSNs, as well as Epirubicin have been examined on MCF-7 and PBMC. As depicted in Figure 51, the images of untreated MCF-7 cell lines and the treated cell with 100, 200, and 400 µg/mL of CZ, CN, CC CSNs, and conventional drug were taken by using a fluorescence microscope (KFL30LED, India). To determine the cytotoxicity MOCSNs against of the cultured breast cancer cell lines, the micrograph was captured at the wavelength of 520 nm. Consequently, the living cells were observed. Figure 51(a) represents the untreated cancer cell and the treated cell with 100, 200, and 400 µg/mL concentrations of Epirubicin. The micrograph image showed that the number of cancer cell lines decreased with increasing concentration of standard drug. As depicted in Figure 51(b), the *in vitro* cytotoxicity of CZ CSNs against MCF-7 cell lines was examined. The cultured cancer cells treated with 100, 200, and 400 µg/mL concentrations of CZ CSNs showed different morphological changes. As the concentration of the sample increased, the cancer cell population decreased. This indicated that the cell-killing ability of CZ CSNs against the MCF-7 cancer cell line is dose dependent. Similarly, the cytotoxicity of CN and CC CSNs against cancer cell lines showed the same trend as indicated in Figures 51(c) and 51(d). However, cancer cells distributed more densely in the group treated with CN CSNs than in the groups treated with CZ and CC CSNs. As depicted in Figure 51(d), cancer cells treated with the same dose of CC CSNs were effectively destroyed. Overall, the cytotoxicity of the synthesized core-shells was found to be in the order CC > CZ > CN.

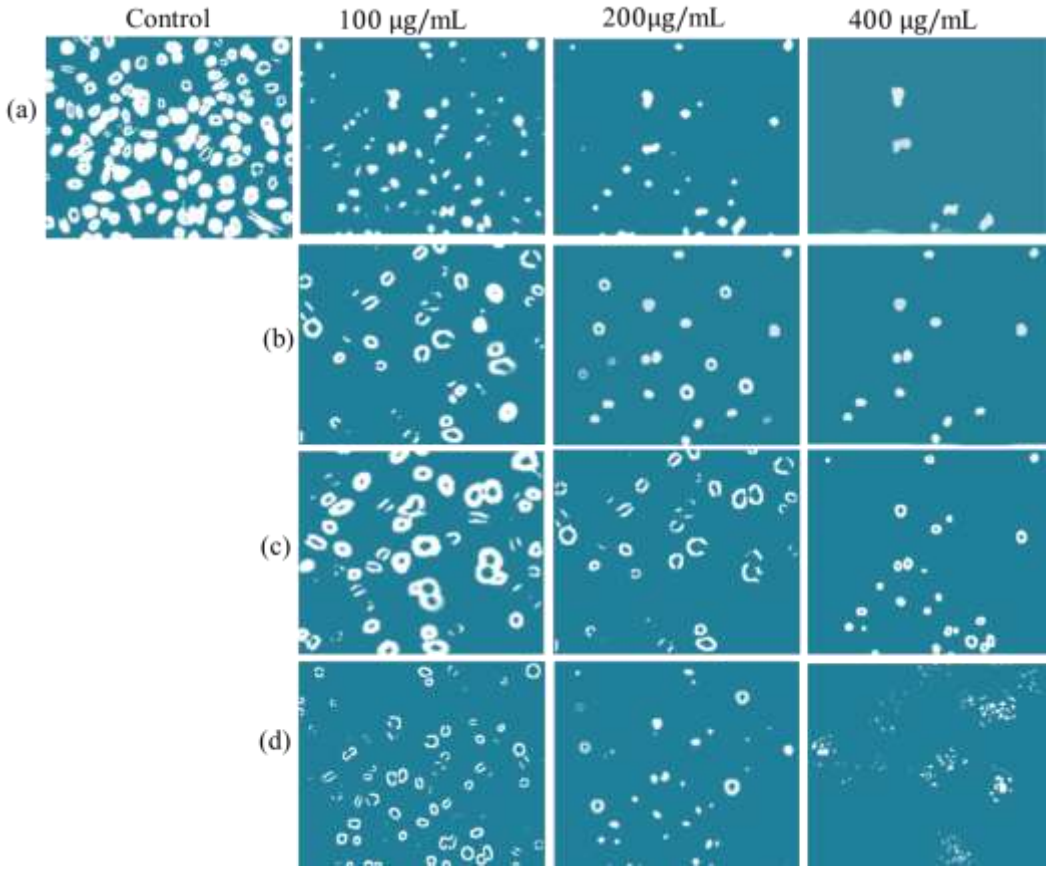

Figure 51: Cytotoxicity on MCF-7 cell lines: (a) untreated cell and the treated cell with 100, 200, and 400 µg/mL of Epirubicin and (b) CZ CSNs, (c) CN CSNs, and (d) CC CSNs treated with the same concretion.

The *in vitro* cytotoxic effect of CZ, CN, and CC CSNs on MCF-7 was measured in terms of percent inhibition, which involves assessing cell viability after treatment with the CSNs and calculating the reduction in viable cells compared to an untreated control. The percent inhibition of CZ, CN, and CC against cancer and healthy cells was determined. Figure 52(a) and Table 6 indicate that CZ CSNs and the Epirubicin inhibit MCF-7 and PBMC cells more effectively as concentration increases. The CZ CSNs inhibit the MCF-7 cells about 35.66, 43.43, 51.54, 68.44, 79.55, 87.77, and 95.22% at 12.5, 25, 50, 100, 200, 400, and 800 µg/mL, respectively. The percentage inhibition of CZ CSNs against healthy cells (PBMC) steadily rises with concentration. At 400 µg/mL, CZ CSNs inhibit MCF-7 and PBMC cells by about 87.77 and 53.28%, respectively, whereas Epirubicin inhibits 86.77 and 53.52%. The percent inhibition of CZ CSNs against PBMC is less than that of the Epirubicin drug; this indicates that Epirubicin has a stronger inhibitory effect on PBMC compared to CZ CSNs. This suggests that Epirubicin, a

chemotherapy drug commonly used to treat breast cancer, has a more potent impact on the viability or function of PBMC than CZ CSNs. Therefore, even though the anticancer activity of CZ CSNs is slightly less than that of Epirubicin, it is less toxic to healthy cells.

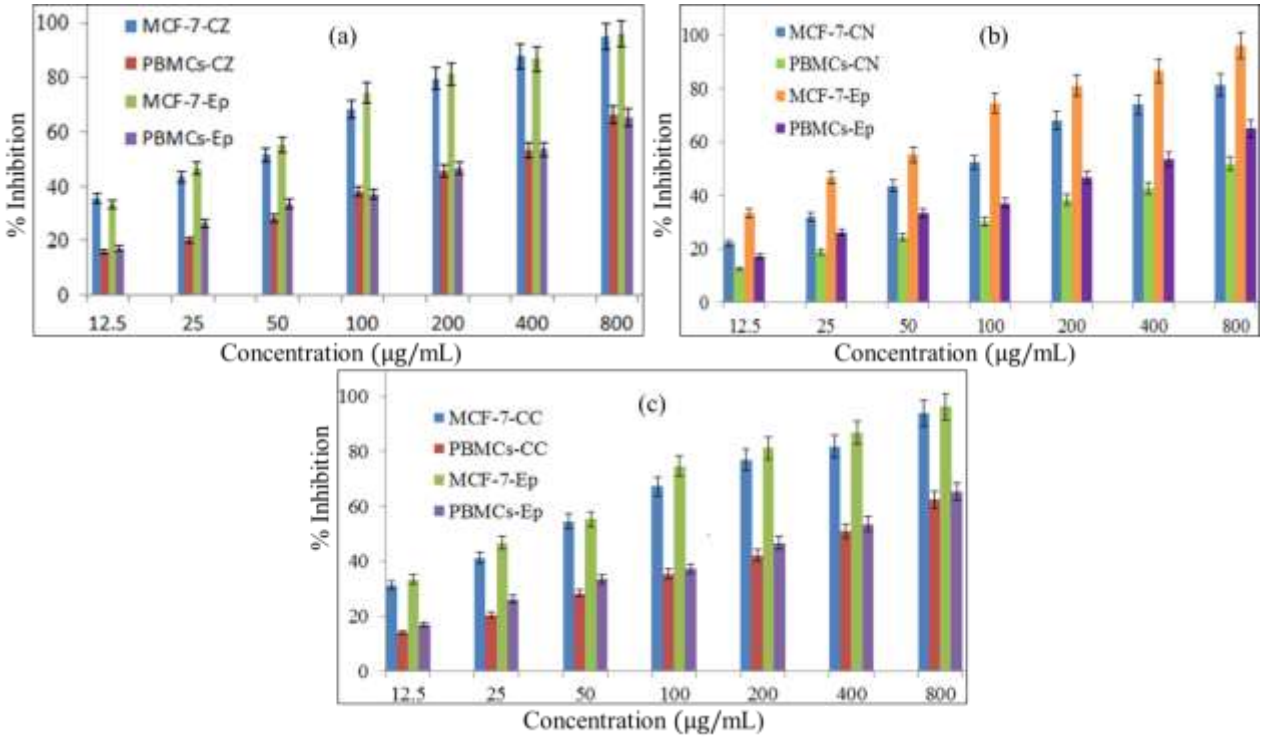

Figure 52: The cytotoxicity of (a) CZ, (b) CN, and (c) CC CSNs with Epirubicin against MCF-7 and PBMC cells.

Additionally, as shown in Figure 52(b), the percent inhibition of CN CSNs against MCF-7 at 12.5, 25, 50, 100, 200, 400, and 800 µg/mL were found to be 22.16, 32.20, 43.62, 52.41, 68.21, 74.11, and 81.38%, respectively, and against PBMC were found to be 12.57, 18.88, 24.44, 30.21, 38.54, 42.67, and 51.94%, respectively. In contrast to CZ CSNs and Epirubicin drugs, CN CSNs is less toxic to both cancer and healthy cells.

Similarly, CC CSNs inhibit the MCF-7 at about 37.33, 49.22, 59.52, 76.23, 83.86, 89.66, and 97.72% at the same concentration used for the CZ CSNs, respectively. As shown in Figure 52(c), the percent inhibition of CC CSNs against PBMC is higher than that of Epirubicin drug but less toxic to PBMC, this implies that CC CSNs have a stronger inhibitory effect on MCF-7 with less side effect on normal cells (PBMC) compared to conventional drug. This suggests that CC CSNs have a greater impact on the viability or growth of MCF-7 as shown in Figure 52. The half-

maximal concentrations (IC_{50}) of CZ, CN, CC CSNs, and Epirubicin used in treating MCF-7 were investigated to be 18.3, 21.25, 17.8, and 18.01 μg/mL, respectively. The minimal IC_{50} of CC CSNs indicates that the concentration needed to suppress breast cancer by 50% is less than that of Epirubicin. This suggests that CC CSNs are more potent and effective at inhibiting breast cancer cells with fewer side effects. The good anticancer activity of CC CSNs is mostly due to the ability of the Cu^{2+} ion to accept an electron to generate ROS that causes cancer cell death.

Table 6: The percentage inhibition of CZ, CN, CC CSNs, and Epirubicin against MCF-7 and PBMC cells.

Conc (μg/mL)	CZ(% In)		CN (% In)		CC (% In)		Epirubicin (% In)	
	MCF-7	PBMCs	MCF-7	PBMCs	MCF-7	PBMCs	MCF-7	PBMCs
DMSO	0.00	0.00	0.00	0.00	0.00	0.00	0.00	0.00
12.5	35.66± 0.01	16.04 ± 0.04	22.16 ± 0.03	12.57 ± 0.01	37.33 ± 0.01	14.11 ± 0.04	33.42 ± 0.03	17.13 ± 0.01
25	43.43 ± 0.03	20.33 ± 0.03	32.20 ± 0.02	18.88 ± 0.02	49.22 ± 0.00	20.43 ± 0.01	46.68 ± 0.01	26.33 ± 0.03
50	51.54 ± 0.04	28.36 ± 0.01	43.62 ± 0.00	24.44 ± 0.01	59.52 ± 0.00	28.35 ± 0.00	55.31 ± 0.02	33.56 ± 0.02
100	68.44 ± 0.03	38.18 ± 0.03	52.41 ± 0.01	30.21 ± 0.01	76.23 ± 0.03	35.40 ± 0.03	74.53 ± 0.03	37.23 ± 0.00
200	79.55 ± 0.01	45.52 ± 0.02	68.21 ± 0.03	38.54 ± 0.03	83.86 ± 0.02	42.13 ± 0.02	81.22 ± 0.01	46.66 ± 0.03
400	87.77 ± 0.01	53.28 ± 0.00	74.11± 0.03	42.67 ± 0.04	89.66 ± 0.01	51.08 ± 0.05	86.77 ± 0.00	53.52 ± 0.02
800	95.22 ± 0.02	66.44 ± 0.00	81.38 ± 0.01	51.94 ± 0.02	97.72 ± 0.02	62.43 ± 0.00	96.15 ± 0.02	65.18 ± 0.04
IC_{50}	18.3	28.5	21.25	38.72	17.8	30.7	18.01	26.40

4.3.2. Cell Viability

The proportion of living cancer cells in a population after being treated with CZ, CN, and CC CSNs has been investigated. As depicted in Figure 53, the treatment of cancer cells with synthesized CSNs has a considerable impact on cell viability. Treatment of cancer cells with increasing concentrations of CZ, CN, and CC CSNs dramatically reduced cell proliferation in a dose-dependent manner. In the treated cancer cells, the metabolically active cell produces an oxidoreductase enzyme that catalyzes Nicotinamide adenine dinucleotide phosphate (NADP/H) to $NADP^+$. The reducing agent NADPH donates a pair of electrons to MTT which is added to the viable cancer cell and forms a purple formazan compound (Carreño *et al*., 2021, S. Hussain *et al*., 2023). The transfer of a pair of electrons from NADPH to the tetrazolium ring of MTT involves breaking the ring and forming the formazan as shown in Figure 53.

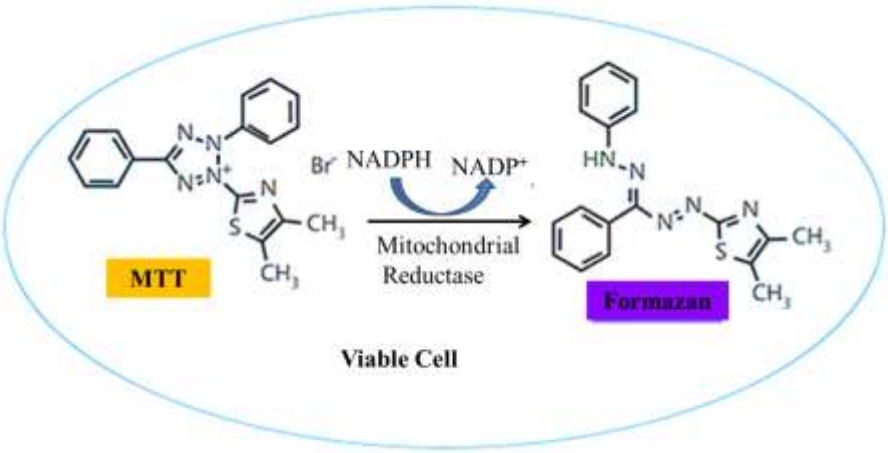

Figure 53: Reduction of MTT to Formazan by using mitochondrial Reductase (Selvakumari *et al*., 2015).

The number of viable cancer cells in percent treated with CZ CSNs at 100, 200, 400, and 800 µg/mL were obtained to be 43.88, 33.23, 26.98, and 18.38%, respectively. In the case of cancer cells treated with CN CSNs, the percentage of viable cells treated with the same concentration was 68.24, 62.69, 58.34, and 48.99%, respectively. This result implies that CN CSNs are less toxic to the breast cancer cells in contrast to the Epirubicin drug.

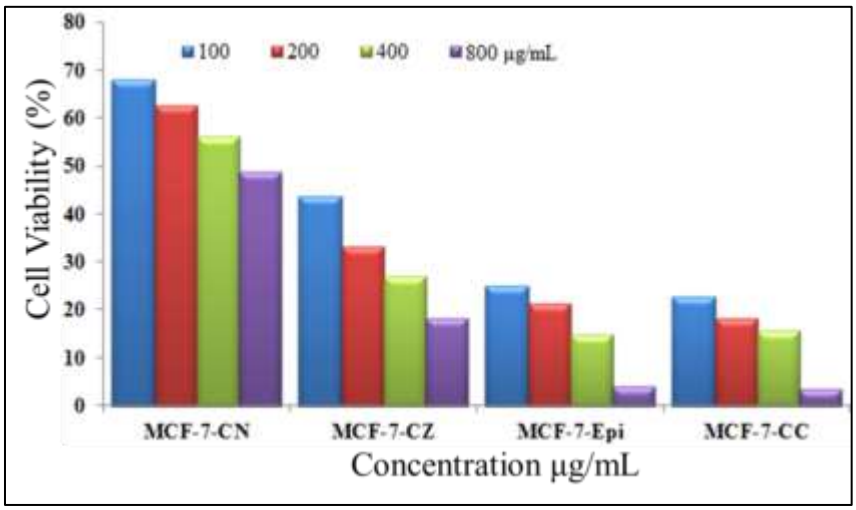

Figure 54: The percent cell viability of cancer cells treated with CSNs and Epirubicin.

Similarly, the percent cell viability of cancer cells treated with CC CSNs at 100, 200, 400, and 800 µg/mL were 22.73, 18.33, 15.73, and 3.63%, respectively. As depicted in Figure 54, the number of metabolically active breast cancer cells is fewer than in cells treated with Epirubicin. This indicates that CC CSNs have more potential activity than conventional drugs.

Table 7: The cell viability percent of breast cancer cells treated with CSNs and Epirubicin

Treated Cells	Concentration (μg/mL)			
	100	200	400	800
MCF-7-CN	68.24 ±0.01	62.69 ±0.01	58.34 ±0.01	48.99 ±0.01
MCF-7-CZ	43.88 ±0.01	33.23 ±0.01	26.98 ±0.01	18.38 ±0.01
MCF-7-Epi	25.18 ±0.01	21.32 ±0.01	14.92 ±0.01	4.21 ±0.01
MCF-7-CC	22.73 ±0.01	18.33 ±0.01	15.73 ±0.01	3.63 ±0.01

4.3.3. Mechanistic Interaction of CSNs with Breast Cancer Cells

The objective of anticancer drugs is to prevent tumor cell growth and cause death without a significant negative impact on healthy cells. The specific molecular mechanisms involved in the interaction between nanoparticles and breast cancer cells can vary depending on the type of nanoparticle, its physicochemical properties, the breast cancer cell line, and the experimental conditions (Andleeb *et al*., 2021, Juan *et al*., 2018). In breast cancer treatment, the type of chemotherapy used is typically determined by the tumor's unique receptor status. The primary receptors evaluated while choosing the proper chemotherapy treatment are hormone receptors (estrogen receptor (ER) and progesterone receptor (PR)), human epidermal growth factor receptor 2 (HER2), and triple-negative breast cancer (TNBC). Chemotherapy is frequently used in conjunction with targeted treatments of ER, PR, and HER2-positive breast cancer. However, chemotherapy remains the major systemic treatment option for triple-negative breast tumors, which has no targeted treatments. TNBC is a particularly difficult kind of breast cancer because it lacks the presence of the hormone receptor and HER2. This implies that TNBC does not react to targeted therapy. Chemotherapy intervenes in cell cycle control, suppresses proliferation, and has a cytotoxic impact, which causes intolerable side effects. Furthermore, this medication is ineffective against a wide variety of malignant tumors. Nanoparticle based therapies are being investigated and developed for a variety of breast cancer subtypes, with the most promising outcomes shown in the treatment of triple-negative breast cancer (TNBC) (Brown *et al*., 2015).

Due to this, the CSNs having unique physicochemical features have emerged as a new hope for cancer therapy. By delivering drugs directly to cancer cells, anticancer treatment can be more effective while minimizing adverse effects. CZ, CN, and CC CSNs inhibit and induce death by

oxidative stress, causing DNA damage, arresting the cell cycle, and inducing cancer cell death by apoptosis as well as nonapoptotic modes of cell death.

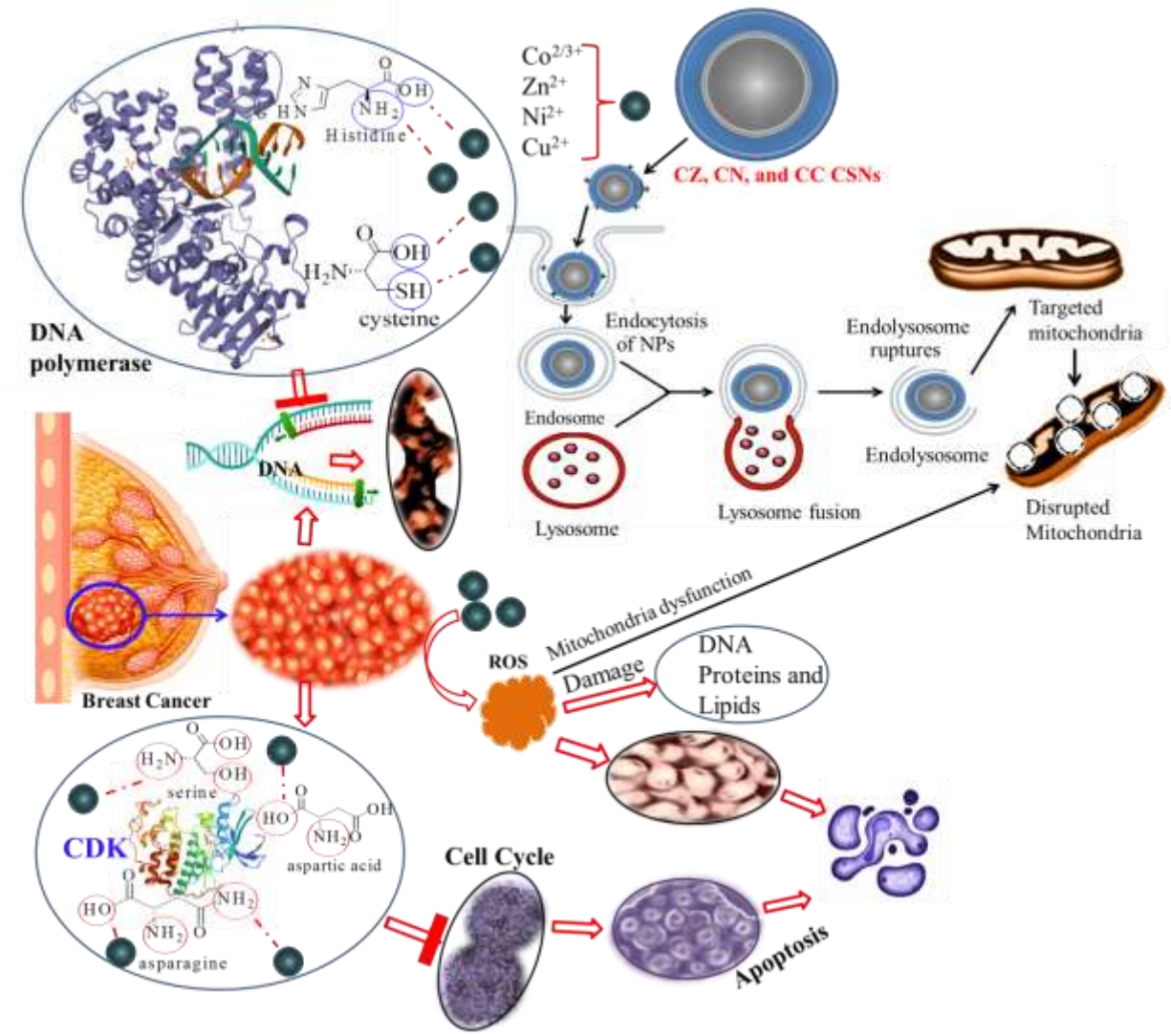

Figure 55: Mechanistic interaction of CZ, CN, and CC CSNs with different parts of breast cancer cells.

In cancer cell proliferation, cyclin-dependent kinase 1/2 (CDK1/2) plays a crucial role in the whole cell cycle. It has become a new target for cancer therapy. CDK1interacts with cyclin B1 to facilitate the transition from the growth (G2) phase into mitosis, whereas CDK2 activates the growth 1/synthesis (G1/S) and synthesis/growth 2 (S/G2) transitions in the interphase stage of the cell cycle. As shown in Figure 55, the delivered metal ion of CSNs is believed to inhibit the activity of CDKs by binding to groups such as imidazole nitrogen of histidine, amide nitrogen

atoms of asparagine and glutamine, carboxylate oxygen atoms of aspartic acid and glutamic acid, hydroxyl oxygen atoms of serine, threonine, and tyrosine residues, and thiol group of cysteine amino acids. Similarly, particular elements inside DNA polymerase, such as the nitrogen, oxygen, and sulfur atoms of amino acids, reacted with metal ions found in CSNs, inhibiting its action.

The other key mechanism of CSNs to induce the death of cancer cells is producing Reactive oxygen species (ROS). Once the CSNs are internalized by the cancer cell through the endocytic pathway and dissolved to metal ions, and disrupts the cellular homeostasis. This homeostasis disruption resulted in the production of excessive ROS within the cancer cells, leading to oxidative stress and mitochondrial dysfunction (Fu *et al*., 2022). Additionally, the core-shell nanoparticles are recognized and taken up by the breast cancer cells through receptor-mediated endocytosis. Once the CSNs are internalized, they become entrapped within the endocytic vesicles, which then fuse with lysosomes to form endolysosomes. The drug is released into the cytoplasm once the endolysosomal membrane is disrupted, and then the drug is targeted to the mitochondria (Wongrakpanich *et al*., 2014).

4.4. Antibacterial Study

The antibacterial activities of Co_3O_4, ZnO, NiO, and CuO NPs and CZ, CN, and CC CSNs against gram-positive (*staphylococcus aureus* and s*treptococcus pyogenes*) and gram-negative (*escherichia coli* and *pseudomonas aeruginosa*) bacterial strains considered in the study has been determined in terms of inhibition mode. The inhibition efficiency of MONPs and CSNs against the bacteria has been evaluated using diffusion methods.

The MONPs and CSNs were believed to inhibit bacterial strains by producing reactive oxygen species (ROS), disrupting cell walls, DNA damage, protein damage, lipid damage, enzyme inhibition, membrane disintegration, etc., (Slavin *et al*., 2017). In this particular study, the inhibited zone were recorded for 25, 50, and 100 µg/mL concentrations as shown in Table 8. 100 µg/mL of Co_3O_4(12) inhibits *S.aureus, S. pyogenes, E.coli, and P. aeruginosa* about (14.5, 13, 13, and 12 mm), Co_3O_4(11) (15, 14.5, 13, and 12.5 mm), and Co_3O_4(21) (14, 13, 11.5, and 8.5 mm), respectively. The inhibition activity of Co_3O_4(11) NPs against both gram-positive and gram-negative is higher than Co_3O_4(12) and Co_3O_4(21) volume ratios at all three concentrations.

Similarly, the inhibition zones of ZnO(11) at 100 μg/mL were found to be 16, 14.5, 13, and 12 mm against *S. aureus*, *S. pyogenes*, *E. coli*, and *P. aeruginosa*, respectively as shown in Figure 56. Among ZnO(12), ZnO(11), and ZnO(21) NPs, ZnO(11) showed high inhibition efficiency in all concentrations. The high efficiency of ZnO(11) NPs is due to their small size which enables them to penetrate the cell wall of bacteria. The CuO(11) NPs was also highly competitive with standard drugs with the inhibition activity of (16, 14, 15, and 11 mm), against *S. aureus and S. pyogenes, E. coli*, and *P. aeruginosa* at 100 μg/mL, respectively. Out of CuO NPs synthesized in three different volume ratios, CuO(11) shows good inhibition activity.

Table 8: Inhibition zone for Co_3O_4, ZnO, NiO, and CuO NPs (in mm).

Nanoparticles	Conc. (μg/mL)	Gram-positive		Gram-negative	
		S.aureus ATCC25923	*S. pyogenes* ATCC19615	*E.coli* ATCC25922	*P. aeruginosa* ATCC27853
Co_3O_4(12)	γ_3 = 100	14.5	13	13	12
	γ_2 =50	12	11	10.5	10
	γ_1 = 25	9	9	8	8
Co_3O_4(11)	β_3 = 100	15	14.5	13	12.5
	β_2 = 50	14	13.12	11.23	10.43
	β_1 = 25	12	12.5	11	9
Co_3O_4(21)	α_3 = 100	14	13	11.2	8.5
	α_2 = 50	12	11.5	9.4	8
	α_1 = 25	10	10.5	7	7.2
$IC_{50(11)}$		22.22	23.88	33.3	34.4
ZnO(12)	V3 = 100	13.7	13	11	10
	V2 = 50	11	10	9	9
	V1 = 25	10	9	7	8
ZnO(11)	U3 = 100	16	14.5	13	12.5
	U2 = 50	14	11.92	10.1	9.22
	U1 = 25	10	11.3	9.87	7.89
ZnO(21)	R3 = 100	14.5	15.5	13	14
	R2 = 50	12.5	13	11	12.5
	R1 = 25	10	9.8	8	8
$IC_{50(11)}$		18.36	19.34	27	26.5
CuO(12)	T_3 = 100	15	14	13	10
	T_2 =50	10	12	11	9.5
	T_1 = 25	9	9	8.5	8
CuO(11)	S_3 = 100	16	14	15	11
	S_2 = 50	15	13.5	13	9
	S_1 = 25	10	8	10	7
CuO(21)	F_3 = 100	14.5	15	10	8
	F_2 = 50	12	11	9.5	7.5
	F_1 = 25	9	7	7	7

$IC_{50(11)}$		17.21	19.86	26	25.4
	P3 = 100	12	11	12	10
NiO (12)	P2 = 50	9	10.5	10	8.5
	P1 = 25	7	8	6.5	7
	D3 = 100	13	12.5	12	11.5
NiO (11)	D2 = 50	11	11.2	11	10
	D1 = 25	8	7.5	7.5	9.5
	H3 = 100	10	10.5	9	9.5
NiO(21)	H2 = 50	9	9.5	8.5	7.5
	H1 = 25	7	8	6.5	6.5
$IC_{50(11)}$		28.55	26.69	36	37
Ampicillin		15	14	12	12

The results of the antibacterial activity of synthesized NiO NPs against these four different bacterial strains are shown in Table 8. The results revealed that the synthesized NiO NPs in (1:1) ratio showed 13, 12.5, 12, and 11.5 mm against *S. aureus and S. pyogenes, E. coli,* and *P. aeruginosa* at 100 μg/mL, respectively. The NiO NPs exhibited less antimicrobial activity than conventional antibacterial drugs. The high inhibition activity of small size MONPs is because of the higher surface area that provides more active sites and interaction points for the nanoparticles to interact with bacterial cells. Among the selected bacterial strains, the growth of gram-positive bacteria primarily *S.aureus* was highly inhibited. As depicted in Figure 56, the drug resisted bacteria; *E.coli* and *P. aeruginosa* were highly susceptible to Co_3O_4, ZnO, and CuO NPs. This designated that these MONPs are a potent antibacterial against both gram-positive and gram-negative. The *in vitro* antibacterial activity of Co_3O_4(11), ZnO(11), NiO(11), and CuO(11) NPs against *S. aureus* showed IC_{50} values of 22.22, 18.36, 28.55, and 17.21 μg/mL and against *E. coli were* 33.3, 27, 36, and 26 μg/mL, respectively. The IC_{50} values of CuO(11) NPs are less than that of the other MONPs, which indicates the high inhibition activity of CuO NPs in contrast to the other.

Generally, the antibacterial activities of Co_3O_4, ZnO, NiO, and CuO NPs synthesized under the same condition were assessed for comparison purposes. The synthesized Co_3O_4 NPs also inhibit the growth of both gram-negative and gram-positive bacteria than ZnO and NiO NPs at the same concentrations. The high efficiency of Co_3O_4 NPs against bacterial strains is due to their small size which allows the particles to penetrate the cell components easily and the availability of Co^{2+} and Co^{3+} that induce cytotoxicity than Zn^{2+} and Ni^{2+}. As shown in Table 8, the high efficiency of MONPs was observed for activities against gram-positive. This is due to the lack of a protective outer membrane and the protein and sugar group of peptidoglycan that can interact

with Co^{2+}, Co^{3+}, Zn^{2+}, Ni^{2+}, and Cu^{2+} metal ions. However, the gram-negative is less inhibited compared to gram-positive strain which reduces the effectiveness of MONPs. The ability to be resistant against MONPs of gram-negative strain is due to the protective outer membrane.

Naturally, the outer part of bacteria is negatively charged due to the teichoic acid in the peptidoglycan and the lipoteichoic acid in the membrane.

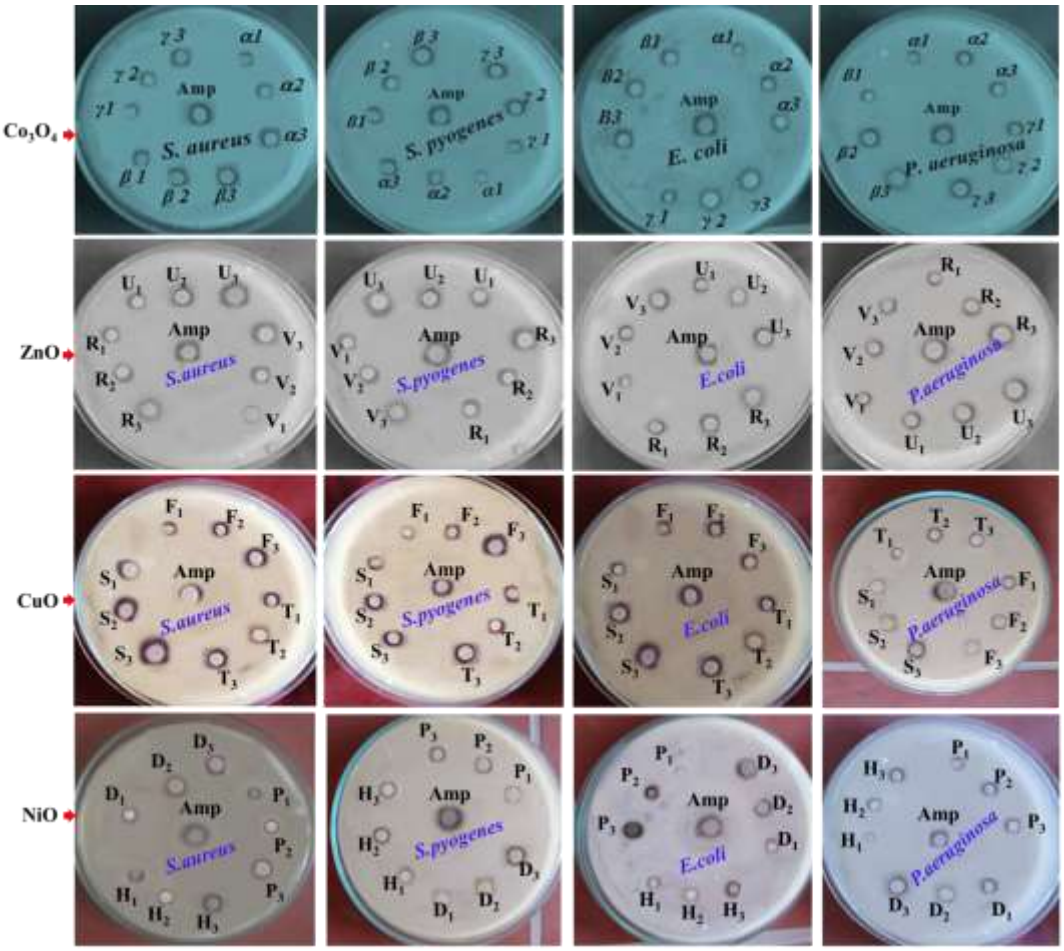

Figure 56: Photograph indicating the inhibition zone of Co_3O_4, ZnO, NiO, and CuO NPs against bacterial strains.

The teichoic acid in peptidoglycan has a negative charge from its phosphate group at the disaccharide head group, carboxylic group from its backbone, and hydroxyl group from its tail group. These function groups can undergo non-covalent interaction with positive charges of MONPs that cause cell wall and cell membrane disruption and lead to death. Additionally, the Co^{2+}, Co^{3+}, Zn^{2+}, Ni^{2+}, and Cu^{2+} penetrate the cell of bacteria to damage protein synthesis and

DNA damage. These charge of MONPs interred the bacteria cells and generate the reactive oxygen species that cause oxidative stress and finally lead to death (Dizaj *et al*., 2014).

Table 9 and Figure 57 depicted the inhibition zone of gram-negative (*S. aureus and S. pyogenes*) and gram-positive (*E. coli and P. aeruginosa*) CSNs. The CSNs synthesized in concentration ratios have been applied to the gram-negative and gram-positive bacteria strains. The zone of inhibition was determined by measuring the diameter of the spot zone shown in Figure 57. The antibacterial activities of biologically synthesized CSNs were increased with increasing the concentration. The inhibition activity of biologically synthesized CZ(21), CZ(11), and CZ(23) CSNs against gram-positive *S. aureus* at 100 μg/mL revealed 19, 21, and 18.17 mm and for gram-negative *E. coli* were found to be 17, 17.5, and 14.5 mm, respectively. The result indicates that the antibacterial activity of CZ CSNs is less effective against gram-negative bacterial strains. This is due to the additional barrier that allows the bacteria to prevent the nanoparticle from entering the bacterial cells.

As depicted in Figure 57 and Table 9 the inhibition activity of CC CSNs against selected bacterial strains was also revealed. The inhibition activity of CC(21) CSNs at 100, 50, and 25 μg/mL against *S.aureu (*17, 14.5, 13.55 mm*), S.pyogenes (*16.5, 14.5, 12.5 mm), *E.coli* (15, 12, 10 mm), and *P.aeruginosa* (14.5, 13, 11.24), respectively. The CC(11) CSNs inhibit *S. aureus, S. pyogenes, E. coli* and *P. aeruginosa* bacterial strains at 100 μg/mL by about 20.5, 18.5, 16, and 16.5 mm, and CC(23) CSNs about 16.5, 16, 15, and 14.5 mm, respectively. The small size CC(11) CSNs can more easily penetrate and enter bacterial cells, resulting in more effective distribution of $Co^{2+,}$ Co^{3+} and Cu^{2+} to the intracellular cell whereas, the larger CC CSNs may have a more difficult time passing bacterial cell walls and membrane barriers, limiting their efficacy. The CC(11) CSNs is highly effective even at lower concentrations in contrast to its parent materials. In general, the potential activities of core-shell against both gram-positive and gram-negative were due to its small nano-scale and synergistic effect which enables it to penetrate the cell wall of bacteria. The core-shell structure has a bigger surface area and more active areas for interacting with bacterial cells than individual nanoparticles. This enhanced surface area and active spots may improve the nanoparticles' potential to break bacterial cell membranes and cause cellular stress. The intimate contact between the Co_3O_4 core and the CuO shell also allows for effective electron transport between the two metal oxide components. This

electron transfer can boost the nanoparticles' redox cycling and catalytic activity, resulting in higher ROS production and antimicrobial properties that resulted in the high antibacterial activity of CSNs.

Table 9: The inhibition activities of CZ, CN and CC core-shell nanostructures (mm).

Nanoparticles	Conc. (μg/mL)	Gram-positive		Gram-negative	
		S.aureus ATCC25923	*S.pyogenes* ATCC19615	*E.coli* ATCC25922	*P.aeruginosa* ATCC27853
CZ (21)	$X_4 = 100$	19	18	17	16
	$X_3 = 75$	18	17.5	16	15.5
	$X_2 = 50$	15.5	16.5	14.5	14
CZ (11)	$Z_4 = 100$	21	18.5	17.5	16.5
	$Z_3 = 75$	18.5	17.2	15	14
	$Z_2 = 50$	15.86	16.5	15	13
CZ (23)	$Y_4 = 100$	18.17	17	14.5	14
	$Y_3 = 75$	15.86	15	13.5	13.5
	$Y_2 = 50$	13.55	14.3	12	13
	$IC_{50(11)}$	11.6	12.23	17.55	19.2
CC(21)	$N_3 = 100$	17	16.5	15	14.5
	$N_2 = 50$	14.5	14.5	12	13
	$N_1 = 25$	13.55	12.5	10	11.24
CC (11)	$L_3 = 100$	20.5	18.5	16	16.5
	$L_2 = 50$	18.5	15.6	14.5	13
	$L_1 = 25$	14.5	14	11	11
CC (23)	$M_3 = 100$	16.5	16	15	14.5
	$M_2 = 50$	16	15	14.5	14
	$M_1 = 25$	13.55	13	11	10.5
	$IC_{50(11)}$	14	15.8	21.76	22
CN(21)	$E_3 = 100$	16	17	14.5	13.5
	$E_2 = 50$	13.5	14.5	13	12.5
	$E_1 = 25$	12	11	10.5	9.5
CN(11)	$K_3 = 100$	16.5	15	14.5	14.7
	$K_2 = 50$	14.5	14.5	12.5	12
	$K_1 = 25$	12	12.24	9.5	9
CN(23)	$J_3 = 100$	14.5	14	12.5	11
	$J_2 = 50$	12.5	13	12	10.5
	$J_1 = 25$	11	10.5	10	9.5
	$IC_{50(11)}$	23.46	25.43	26	28.5
Amp		16±0.99	17±0.87	14±0.65	13±0.44

The antibacterial activity of CN CSNs was also investigated. As indicated in Table 9, the inhibition activity of CN(11) at 100 μg/mL against *S. aureus, S. pyogenes, E. coli* and *P.*

aeruginosa bacterial strains were found to be 16.5, 15, 14.5, and 14.7 mm, respectively. CN CSNs also show good inhibition activity against gram-positive bacteria. However, the inhibition activity of CN CSNs is lower than that of CZ and CC CSNs. Nickel (Ni^{2+}) ions released from the NiO shell in the CN core-shell nanoparticles are less toxic to bacteria than copper (Cu^{2+}) and zinc (Zn^{2+}) ions released from the shell of core-shell nanostructures. The $Cu^{2+)}$ and Zn^{2+} ions can interrupt important cellular processes and cause more damage to bacterial cells, resulting in improved antibacterial activity. The IC_{50} of CZ(11) against *S. aureus, S. pyogenes, E. coli* and *P. aeruginosa* were investigated at about 11.6, 12.23, 17.55, and 19.2 µg/mL, whereas CC(11) was at about 14, 15.8, 21.76, and 22 µg/mL, as well as CN (11) at 23.46, 25.43, 26, and 28.5 µg/mL, respectively.

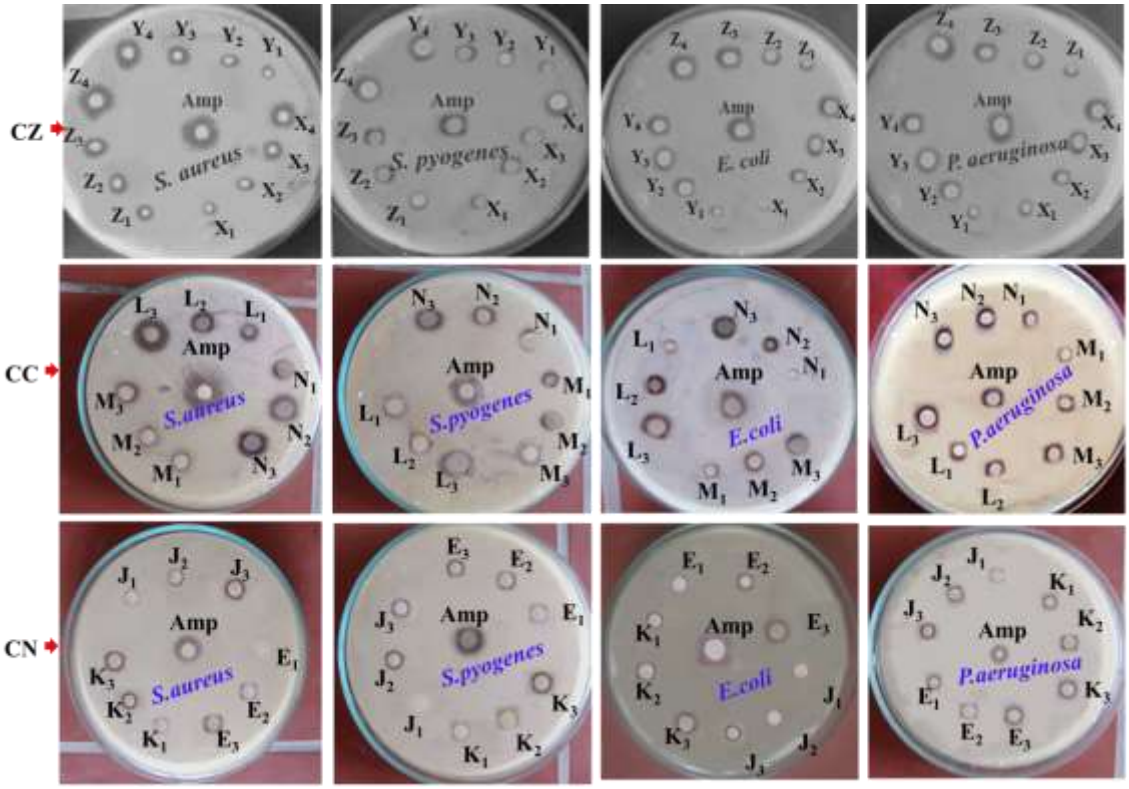

Figure 57: The inhibition zone by biologically synthesized CSNs NPs against gram-negative *(E. coli* and *P. aeruginosa)* and *gram-positive (S. aureus* and *S. pyogenes).*

The lower half-maximal inhibition concentration of CZ CSNs indicates that lower concentration of the nanoparticles utilized to achieve a 50% inhibition of bacterial growth which implies that the CZ CSNs are more potent and effective at inhibiting the target bacterial cells. In contrast to

individual antibacterial activity, the core-shell nanostructure showed better activity. In gram-positive bacteria, the positively charged metal ions from CSNs interact with the thick cell walls of bacteria which are negatively charged and cause necrotic damage. In addition to this, the glycerol phosphate and glucosyl phosphate of peptidoglycan which is an anionic polymer trapped by the metal ions of biologically synthesized CSNs cleaved the glycoside bond of disaccharide peptide Barrera-Ruiz *et al*. 2020. The main feature that made the gram-positive bacteria to be susceptible to biologically synthesized CSNs was the absence of an outer membrane. Unlike gram-positive, gram-negative bacteria are highly resistant to antibacterial drugs. However, the small size CSNs showed good inhibitory activities against gram-negative bacteria than standard drugs (ampicillin). The other reason that gram-negative can't resist the toxicity of biologically synthesized CSNs is the less thickened cell wall, the pore on the outer membrane, and the negatively charged lipopolysaccharide molecules as reported (Shaikh *et al*., 2021).

As reported elsewhere Liang *et al*., (2020), the potential electrical charge of nanoparticles developed the adhesion force which enables it to stick on the surface of the bacterial cell wall. In a similar sense, metal ions from the solution of biologically synthesized CSNs interact with the cell wall of bacteria which causes shrinkage and results in rupturing that leads to cell death. On the other hand, as shown in the report of a mechanistic study of Ag NPs (Feng *et al*., 2000)., the small-size nanoparticles can cross the cell wall of the bacteria. In similar mechanisms, the metal ions of biologically synthesized CSNs can cross the outer membrane through its pore or interact with the thiol groups and deactivate proteins.

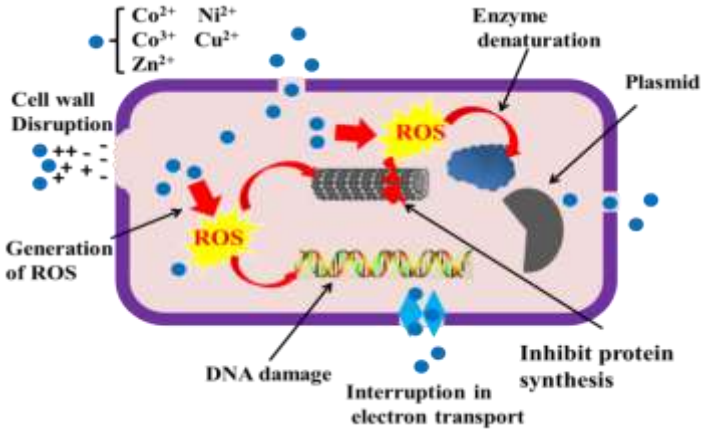

Figure 58: The cellular mechanistic interaction of MONPs and CSNs with bacteria cell.

The CSNs enter the membrane, which can damage the DNA, deactivate the enzymes, and generate the reactive oxygen species molecules. The free radical oxygen reactive molecules such as hydrogen peroxide (H_2O_2), superoxide anion ($O_2^{\cdot-}$), hydroxyl radical (HO·), peroxyl radical ($RO_2^{\cdot}$), and alkoxy radical (RO·). This reactive oxygen produced by *D. stramonium* leaf extract-mediated CSNs caused oxidative stress which inhibits the growth of both gram-negative and gram-positive as shown in Figure 58.

4.5. Antioxidant Study

DPPH Assay. The scavenging activity of *D. stramonium* leaf extract-mediated Co_3O_4, ZnO, NiO, and CuO NPs, as well as CZ, CN, and CC CSNs, was tested against the stable free radical 2, 2-diphenyl-1-picrylhydrazyl (DPPH) using spectroscopic techniques. In the case of the antioxidant activity test of MONPs, the DPPH solution was mixed with 50, 100, 200, 300, and 500 μg/mL concentrations of all MONPs produced at volume ratios of (1:2), (1:1), and (2:1) and analyzed. The ability of antioxidants to donate hydrogen is thought to be the basis for their effect on DPPH. The samples introduced into a violet DPPH solution are reduced to a yellow color depending on concentration. As shown in Figure 59, the absorbance of the reaction mixture at 517 nm was measured using a spectrophotometer and displayed as a function of MONP concentration. The absorbance value reflects the level of DPPH reduction by Co_3O_4, ZnO, NiO, and CuO NPs and is used to assess their antioxidant activity. As depicted in Figure 59, the absorbance of the reference medication (ascorbic acid) and MONPs containing DPPH at 517 nm decreased as their concentration increased. The drop in absorbance suggests that the MONPs are successfully neutralizing the DPPH free radical, validating their antioxidant activity. The greater the decrease in absorbance, the stronger the antioxidant activity of MONPs. Furthermore, because of their significant band gap energy, MONPs with small sizes decrease absorbance quicker than those with large sizes. This ensured that the small-sized particles were powerful antioxidants. Finally, as shown in Figure 59 (a-d), the absorbance order of all MONPs synthesized in three volume ratios is (21) > (12) > (11).

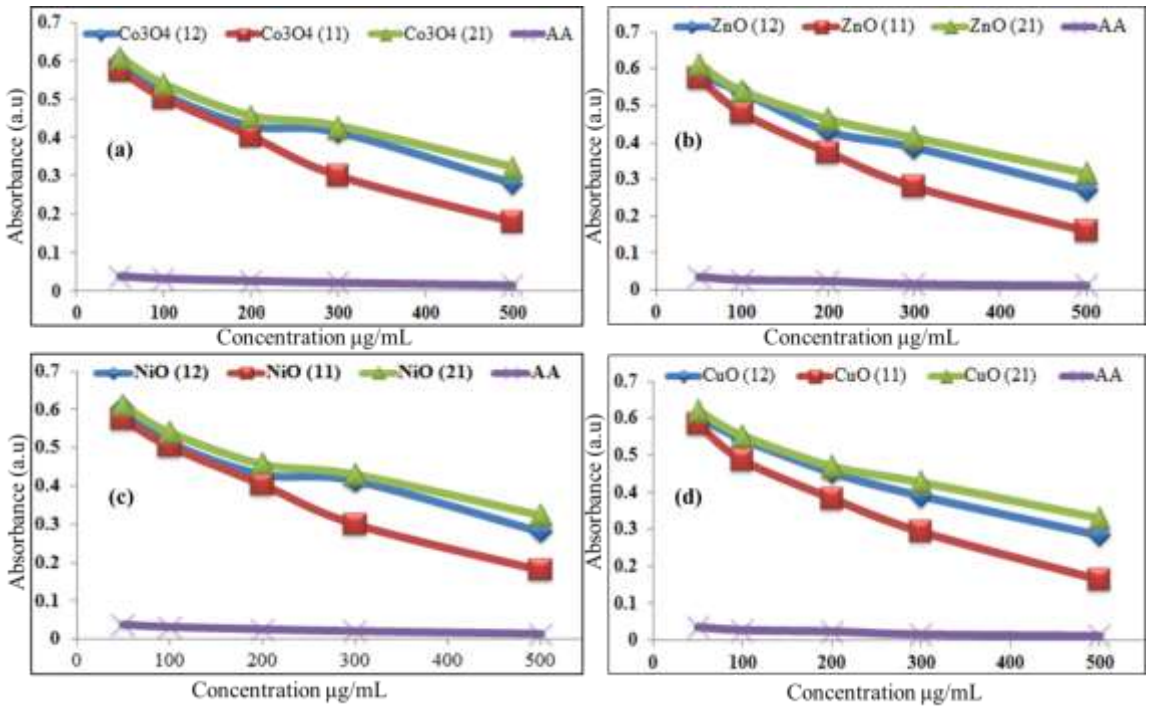

Figure 59: The absorbance of (a) Co_3O_4, (b) ZnO, (c) NiO, and (d) CuO NPs at various concentrations (50, 100, 200, 300, and 500 µg/mL).

The percentage scavenging of Co_3O_4, ZnO, NiO, and CuO NPs against DPPH was measured to determine their antioxidant activity. The percentage scavenging indicates the amount to which these MONPS scavenge the DPPH radicals. Specifically, the percentage of radical scavenging of Co_3O_4, ZnO, NiO, and CuO NPs produced in (1:2), (1:1), and (2:1) volume ratios were calculated. Figure 60 (a) and Table 10 demonstrate that Co_3O_4 NPs produced in a (11) volume ratio inhibit 9.230, 22.564, 37.949, 53.846, and 63.308% at 50, 100, 200, 300, and 500 µg/mL, respectively. As the concentration of Co_3O_4 NPs increases, so does their capacity to scavenge DPPH radicals. Additionally, the percentage scavenging of Co_3O_4 NPs synthesized in (12) ratio was also found to be 4.103 (50), 15.385 (100), 28.205 (200), 36.410 (300), and 54.359% (500 µg/mL), whereas (21) scavenge 4.103 (50), 15.385 (100), 28.205 (200), 36.410 (300), and 54.359% (500 µg/mL). Among the three ratios, Co_3O_4 (11) NPs showed good scavenging potential against the DPPH radical.

The synthesized ZnO NPs showed good radical scavenging ability due to their high electron donating capacity to the radicals. The DPPH scavenging of ZnO (11) NPs at 50, 100, 200, 300, and 500 µg/mL concentration were found to be 11.795, 26.154, 42.564, 56.923, and 75.385%,

respectively. As shown in Figure 60 (b) the scavenging activity of ZnO NPs increases with the concentration increases and shows the same trend in the two remaining ratios.

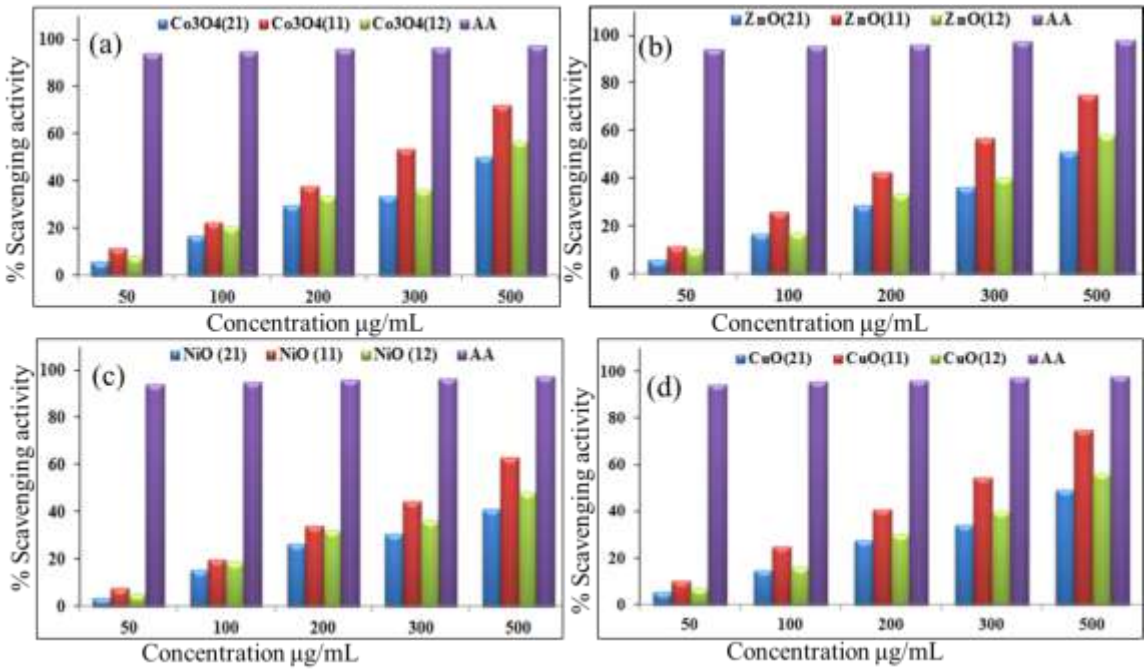

Figure 60: The DPPH free radical scavenging activity of the MONPs.

Similarly, the scavenging activity of NiO and CuO NPs was studied and their activity increases with concentration. The scavenging activity of NiO and CuO NPs synthesized in three volume ratios was raised in the order of (2:1), (1:2), and (1:1). At 500 µg/mL, Co_3O_4 (11), ZnO (11), NiO (11), and CuO (11) NPs demonstrated scavenging activity about 63.308, 75.385, 57.0769, and 74.872%, respectively. ZnO NPs are commonly reported to have stronger antioxidant activity than Co_3O_4, NiO (11), and CuO (11) NPs. This is mostly due to the high redox potential of ZnO NPs. The ZnO NPs with high redox potentials are most likely to donate electrons to the DPPH and inhibit oxidative damage. Similarly, the scavenging activity of CuO nanoparticles was consistent with the prior research. Overall, the percentage scavenging activity of MONPs produced under the same conditions using *D. stramonium* leaf extract was discovered in the following order: ZnO > CuO > Co_3O_4 >> NiO NPs (Shalaby *et al*., 2022)

Table 10: % Scavenging activity Co_3O_4, ZnO, NiO, and CuO NPs

Concentration (µg/mL) NPs	Ratios	50	100	200	300	500	IC_{50} (µg/mL)
	2:1	4.102	13.333	29.744	33.846	47.589	2.68
	1:1	9.230	22.564	37.949	53.846	63.308	2.49
Co_3O_4	1:2	4.103	15.385	31.205	36.410	54.359	2.61
	2:1	6.154	16.923	28.718	36.410	51.282	2.63
ZnO	1:1	11.795	26.154	42.564	56.923	75.385	2.02
	1:2	10.256	17.436	33.846	40.513	58.462	2.52
	2:1	3.589	15.385	26.666	30.769	41.538	3.33
NiO	1:1	7.692	20.002	34.359	44.615	57.0769	2.57
	1:2	5.641	18.974	32.3077	36.410	48.718	2.97
	2:1	5.641	14.872	27.692	34.359	49.230	2.69
CuO	1:1	10.256	25.128	41.026	54.872	74.872	2. 73
	1:2	7.179	16.410	30.256	40.001	56.410	2.58
AA		94.154	95.077	96	96.769	97.846	

The IC_{50} values for DPPH radical scavenging activity of Co_3O_4, ZnO, NiO, and CuO NPs synthesized in (1:1) volume ratio and ascorbic acid were found to be 2.49, 2.02, 2.57, 2.73, and 47.48 µg/mL, respectively. Table 10 demonstrates that NiO NPs with an inhibitory concentration of 365.62 µg/mL scavenged DPPH radicals by about 50%. This means the study shows that NiO NPs have a lower scavenging activity than Co_3O_4, ZnO, and CuO NPs.

The antioxidant activity of synthesized CZ, CN, and CC CSNs was also studied by using the DPPH radical. The Uv-Vis spectra shown in Figure 61 (a-c) were obtained from ultraviolet-visible spectroscopy and the scavenging activity of CSNs was determined. To assess the scavenging activity of CSNs, the DPPH solution was mixed with the concentration of 50, 100, 200, 300, and 500 µg/mL of CSNs synthesized in (2:1), (1:1), and (2:3) concentration ratios and their absorbance were measured at 517 nm. As indicated in Figure 61, the absorption spectra for all synthesized CSNs were obtained and declined with the increment of concentration. Furthermore, the absorbance value of CSNs with small sizes was lower than those with bigger sizes. The absorbance difference is thought to be caused by band gap energy, which comes from the particles' size.

In addition to physical visualization, the percentage scavenging activities of CSNs, and ascorbic acid (AA) at 50, 100, 200, 300, and 500 µg/mL were determined. In the case of the percentage scavenging of CZ CSNs synthesized (21), (11), and (23) concentration ratios tested at 500 µg/mL concentration were found to be 68.63, 86.87, 67.16, and 98.24%, respectively. Among the three ratios, CZ(11) has a high-efficiency performance in scavenging the DPPH free radical. The half-maximal inhibitory concentration (IC_{50}) of CZ(11) was also less than the two ratios that assured the good capacity of these NPs at low concentrations. The half-maximal inhibitory concentrations of CZ CSNs synthesized (21), (11), and (23) concentration ratio were 3.98, 1.68, and 3.8 µg/mL respectively which were obtained by using a mathematical linear equation from $Y=mx\pm b$. Where m is the slope, x is the concentration of the sample, y is the percentage scavenging activity, and b is constant.

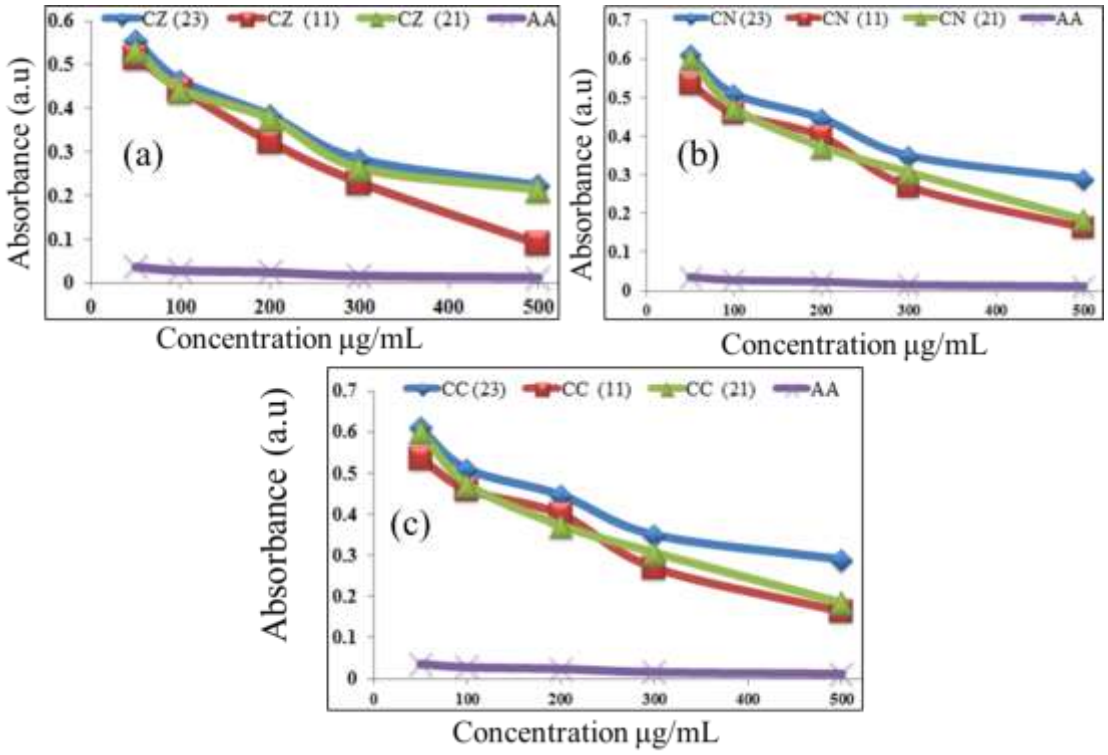

Figure 61: The absorbance of (a) CZ, (b) CN, (c) CC CSNs at various concentrations (50, 100, 200, 300, and 500 µg/mL).

The linear regression value also showed a consistent increment of percentage scavenging activity with increasing concentration.

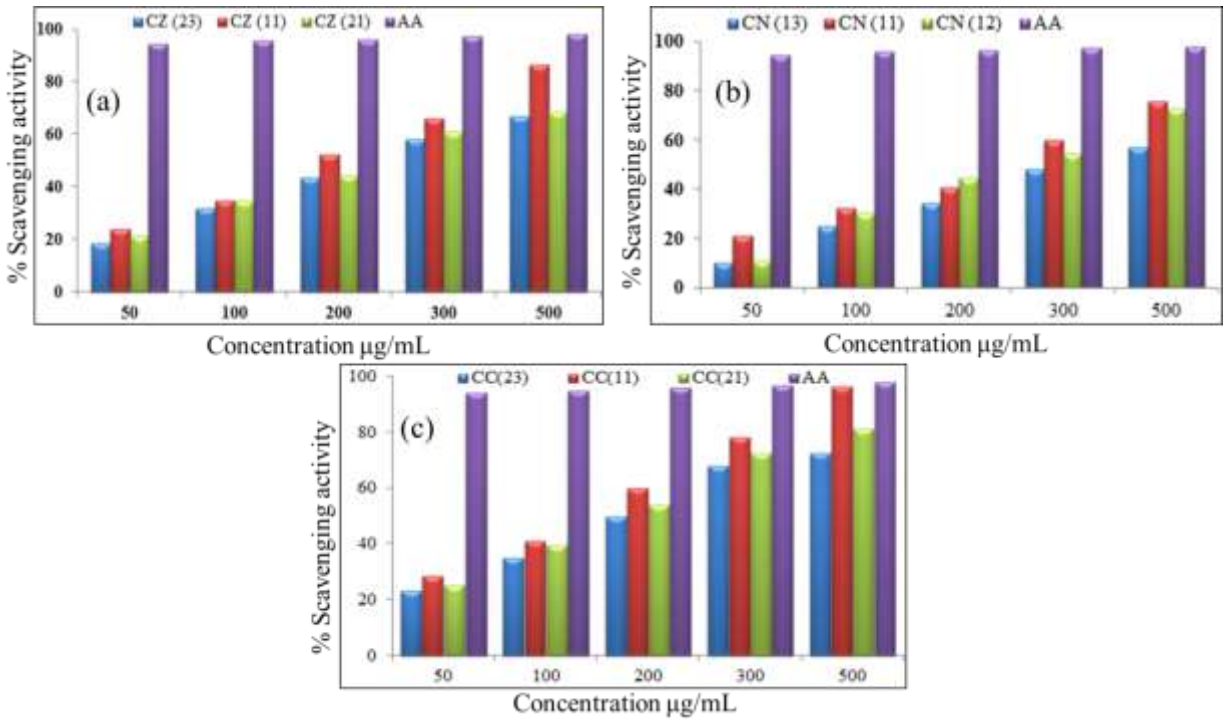

Figure 62: The percent scavenging activity of (a) CZ, (b) CN, and (c) CC CSNs synthesized in core to shell concentration ratios.

Similarly, the antioxidant activity of CN and CC CSNs was investigated as shown in Figure 62(b) and (c), respectively. The percentage scavenging activity of CN (11) at 50, 100, 200, 300, and 500 µg/mL was found to be 15.07, 26.35, 38.18, 56.29, and 65.98%, while CC (11) CSNs scavenged about 16.48, 31.21, 39.98, 61.11, and 76.32% for the corresponding concentrations, as depicted in Figure 62 and Table 11. The result of the percentage scavenging activity achieved by CZ, CN, and CC CSNs was more than that of the parent material. The potent antioxidant activity of CSNs is believed to be due to the synergistic effect, redox potential, and surface area. The shell ZnO, NiO, and CuO NPs enhance the overall antioxidant of CSNs which is a resulted of the synergistic effects (Uddin *et al.*, 2021). Similarly, the shell materials increase the core's redox potential and surface area, allowing for effective electron transport between the Co_3O_4 core and the ZnO, NiO, and CuO NP shells, thus enhancing DPPH scavenging capabilities.

Table 11: Percentage radical scavenging and IC_{50} of CZ, CN, and CC CSNs

Concentration (µg/mL) NPs	Ratios	50	100	200	300	500	IC_{50} (µg/mL)
CZ	2:1	21.46	34.80	44.60	61.27	68.63	3.98
	1:1	24.02	34.80	52.45	66.18	86.87	1.68
	2:3	18.63	31.86	43.63	58.33	67.16	3.8
CN	2:1	10.29	23.01	34.31	48.53	57.52	5.78
	1:1	15.07	26.35	38.18	56.29	65.98	4.01
	2:3	9.27	20.93	31.09	44.91	51.84	7.2
CC	2:1	23.22	33.10	42.83	58.15	66.43	3.69
	1:1	16.48	31.21	49.98	61.11	76.32	2.37
	2:3	17.24	28.56	41.12	54.37	61.17	4.2
AA		94.154	95.077	96	96.769	97.846	

The absorbance of free radicals decreased at 517 nm as the concentration of CSNs increased which increased scavenging capacity. The change in color of DPPH is due to the reduction of the nitrogen atom in the molecule by an electron from the oxygen atom on the CSNs. The electron transition is believed to be from n oxygen orbital to anti-bonding nitrogen orbital (π) ($n \rightarrow \pi^*$) (Rahman *et al*., 2022). According to the mechanism outlined by Mandal *et al*., the unstable purple-colored DPPH• solution was converted into a yellow stable DPPH reduced form during the DPPH• free-radical scavenging process. The mechanistic interaction involves the transition of DPPH• into DPPH free radicals by the donation of electrons from CSNs to the stable DPPH molecules as shown in Figure 63. The electrons supplied to the DPPH radical from MONPs and CSNs reduced nitrogen of DPPH atom (Yamauchi *et al*., 2024)

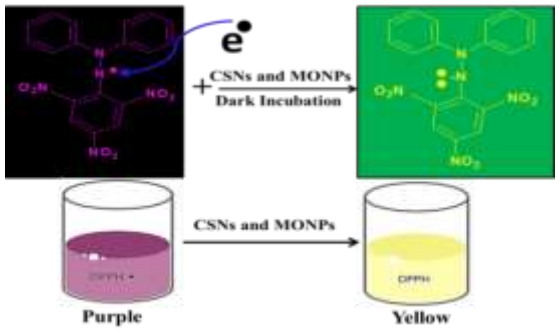

Figure 63: The reduction of DPPH by using CSNs and MONPs.

5. CONCLUSIONS AND RECOMMENDATIONS

5.1. CONCLUSIONS

In this work, Co_3O_4, ZnO, NiO, and CuO MONPs, as well as Co_3O_4@ZnO, Co_3O_4@NiO, and Co_3O_4@CuO CSNs, were synthesized by utilizing their respective precursor salts and *D. stramonium* plant leaf extract. The qualitative test for alkaloids, flavonoids, tannins, saponins, phenols, phytosterols, glycosides, terpenoids, and anthraquinones of aqueous extract showed positive results except for steroids. The calcination temperature of Co_3O_4, ZnO, NiO, and CuO MONPs was found to be 350, 480, 420, and 300 ℃, whereas CZ, CN, and CC CSNs were 360, 400, and 320 ℃, respectively. The O-H stretching vibration commonly found in polyphenolic groups present in plant leaves was observed at 3448 cm^{-1}. The Co^{2+}-O, Co^{+3}-O, Zn-O, Ni-O, and Cu-O bond stretching vibrations were observed at 648, 402, 405, 588, and 504 cm^{-1}, respectively. The formation of cubic Co_3O_4, hexagonal ZnO, face-centered cubic, NiO, monoclinic CuO MONPs, and cubic-hexagonal wurtzite CZ, cubic-face-centered cubic CN, and cubic-monoclinic CC CSNs were confirmed using XRD analysis. A slight peak shift was observed in the XRD diffraction pattern of CSNs due to the grain interaction of the core and shell. TEM investigation indicated the spherical CZ, spherical and prismatic CN, and semi-spherical and cylindrical CC CSNs, with particle diameters of 21.1, 16.99, and 11.07 nm, respectively. Moreover, the HR-TEM images show a low-contrast shell enclosing a dark core, with lattice fringes visible in both regions, indicating a crystalline core-shell structure. Co_3O_4(11), ZnO(11), NiO(11), and CuO(11) MONPs showed antibacterial activity against gram-positive *S. aureus* with IC_{50} values of 22.22, 18.36, 28.55, and 17.21 μg/mL, and against gram-negative *E. coli* with IC_{50} values of 33.3, 27, 36, and 26 μg/mL. The IC_{50} values of CuO(11) NPs are lower than those of other MONPs, indicating that CuO NPs have a higher inhibitory action. The IC_{50} of CZ(11), CN(11), and CC(11) CSNs against *S. aureus* were investigated at 11.6, 23.46, and 14 μg/mL, and against *E. coli were* 17.55, 26, and 21.76 μg/mL, respectively. CSNs had a lower IC_{50} than individual MONPs, indicating a synergistic influence on bacterial strain growth. The IC_{50} values for DPPH radical scavenging activity of Co_3O_4(11), ZnO(11), NiO(11), and CuO(11) MONPs were found to be 2.49, 2.02, 2.57, and 2.37μg/mL, respectively. In comparison to MONPs, CZ(11) and CC(11) CSNs showed better antioxidant activities with IC_{50} values of 1.68 and 2.37 μg/mL, respectively. The *in vitro* cytotoxicity CZ, CN, and CC CSNs against MCF-7 and PBM cell

using an MTT assay was investigated. The percent inhibition of CZ, CN, and CC CSNs against MCF-7 at 800 μg/mL was found to be 95.22, 81.38, and 97.72 %, and against PBMC were 66.44, 51.94, and 62.43%, respectively. In contrast to CZ CSNs and Epirubicin drugs, CN CSNs are less toxic to both cancer and healthy cells. However, CC CSNs showed better anticancer activity due to the ability of Cu^{2+} of shell material to produce ROS that resulted in cancer cell death. Overall, the cytotoxicity of the synthesized core shell nanostructure was found to be in the order CC > CZ > CN.

5.2. RECOMMENDATIONS

The core material concentration, core-shell volume ratio, synthesis pH, and calcination temperature were not optimized. As a result, it is critical to determine the optimal concentration, synthesis pH, core-to-shell volume ratios, and calcination temperature for the synthesis of the core-shell nanostructures. On the other hand, the core-shell nanostructure and its parent materials should be synthesized by utilizing a variety of plants and microorganisms and their biological activity should be investigated. Furthermore, the *in vivo* anticancer and antibacterial investigation of CSNs will be suggested. Finally, the purpose of this work was to synthesize the non-toxic and potent anticancer, antibacterial, and antioxidant core-shell nanostructure using a green approach and recommended to study the *in vivo* test and manufacture at the industry level.

REFERENCES

Abdel-Fattah, W. I., Eid, M. M., Abd El-Moez, S. I., Mohamed, E., & Ali, G. W. (2017). Synthesis of biogenic Ag@Pd Core-shell nanoparticles having anti-cancer/anti-microbial functions. *Life Sciences*, *183*, 28–36. https://doi.org/10.1016/j.lfs.2017.06.017

Aboeita, N. M., Fahmy, S. A., El-Sayed, M. M. H., Azzazy, H. M. E. S., & Shoeib, T. (2022). Enhanced Anticancer Activity of Nedaplatin Loaded onto Copper Nanoparticles Synthesized Using Red Algae. *Pharmaceutics*, *14*(2). https://doi.org/10.3390/pharmaceutics14020418

Abu‐Serie, M. M., & Eltarahony, M. (2021). Novel nanoformulation of disulfiram with bacterially synthesized copper oxide nanoparticles for augmenting anticancer activity: an in vitro study. *Cancer Nanotechnology*, *12*(1), 1–17. https://doi.org/10.1186/s12645-021-00097-5

Ahmadi Bakhtiari, S., Abdoos, H., & Karimzadeh, F. (2022). Green synthesis of ZnO@ZnS core–shell nanoparticles for detection of lead and iron ions in aqueous solutions by colorimetric paper sensors. *Chemical Papers*, *76*(1), 99–109. https://doi.org/10.1007/s11696-021-01840-3

Ahmadi, H., Ebrahimi, A., & Ahmadi, F. (2021). Antibiotic Therapy in Dentistry. *International Journal of Dentistry*, *2021*. https://doi.org/10.1155/2021/6667624

Ajarem, J. S., Maodaa, S. N., Allam, A. A., Taher, M. M., & Khalaf, M. (2021). Benign Synthesis of Cobalt Oxide Nanoparticles Containing Red Algae Extract: Antioxidant, Antimicrobial, Anticancer, and Anticoagulant Activity. *Journal of Cluster Science*, *9*. https://doi.org/10.1007/s10876-021-02004-9

Ajarem, J. S., Maodaa, S. N., Allam, A. A., Taher, M. M., & Khalaf, M. (2022). Benign Synthesis of Cobalt Oxide Nanoparticles Containing Red Algae Extract: Antioxidant, Antimicrobial, Anticancer, and Anticoagulant Activity. *Journal of Cluster Science*, *33*(2), 717–728. https://doi.org/10.1007/s10876-021-02004-9

Akintelu, S. A., Folorunso, A. S., Folorunso, F. A., & Oyebamiji, A. K. (2020). Green synthesis of copper oxide nanoparticles for biomedical application and environmental remediation. *Heliyon*, *6*(7), e04508. https://doi.org/10.1016/j.heliyon.2020.e04508

Al-Enazi, N. M., Alsamhary, K., Kha, M., & Ameen, F. (2023). In vitro anticancer and antibacterial performance of biosynthesized Ag and Ce co-doped ZnO NPs. *Bioprocess and Biosystems Engineering*, *46*(1), 89–103. https://doi.org/10.1007/s00449-022-02815-8

Al-Sheddi, E. S., Farshori, N. N., Al-Oqail, M. M., Al-Massarani, S. M., Saquib, Q., Wahab, R., Musarrat, J., Al-Khedhairy, A. A., & Siddiqui, M. A. (2018). Anticancer potential of green synthesized silver nanoparticles using extract of nepeta deflersiana against human cervical cancer cells (HeLA). *Bioinorganic Chemistry and Applications*, *2018*. https://doi.org/10.1155/2018/9390784

Al-Snafi, P. D. A. E. (2017). Medical importance of Datura fastuosa (syn: Datura metel) and Datura stramonium - A review. *IOSR Journal of Pharmacy (IOSRPHR)*, *07*(02), 43–58. https://doi.org/10.9790/3013-0702014358

Alarifi, I. M. (2022). Metal oxide nanomaterials. In *Synthetic Engineering Materials and Nanotechnology* (Vol. 2). https://doi.org/10.1016/b978-0-12-824001-4.00007-7

Alarifi, S., Ali, D., Alkahtani, S., & Alhader, M. S. (2014). Iron oxide nanoparticles induce oxidative stress, DNA damage, and caspase activation in the human breast cancer cell line. *Biological Trace Element Research*, *159*(1–3), 416–424. https://doi.org/10.1007/s12011-014-9972-0

Alavi, M., Rai, M., Martinez, F., Kahrizi, D., Khan, H., Rose Alencar de Menezes, I., Douglas Melo Coutinho, H., & Costa, J. (2022). The efficiency of metal, metal oxide, and metalloid nanoparticles against cancer cells and bacterial pathogens: different mechanisms of action. *Cellular, Molecular and Biomedical Reports*, *2*(1), 10–21. https://doi.org/10.55705/cmbr.2022.147090.1023

Aldeen, T. S., Ahmed Mohamed, H. E., & Maaza, M. (2022). ZnO nanoparticles prepared via a green synthesis approach: Physical properties, photocatalytic and antibacterial activity.

Journal of Physics and Chemistry of Solids, *160*(February 2021), 110313. https://doi.org/10.1016/j.jpcs.2021.110313

Ali, A., Sattar, M., Hussain, F., Tareen, M. H. K., Militky, J., & Noman, M. T. (2021). Single-step green synthesis of highly concentrated and stable colloidal dispersion of core-shell silver nanoparticles and their antimicrobial and ultra-high catalytic properties. *Nanomaterials*, *11*(4). https://doi.org/10.3390/nano11041007

Ali, K., Saquib, Q., Ahmed, B., Siddiqui, M. A., Ahmad, J., Al-Shaeri, M., Al-Khedhairy, A. A., & Musarrat, J. (2020). Bio-functionalized CuO nanoparticles induced apoptotic activities in human breast carcinoma cells and toxicity against Aspergillus flavus: An in vitro approach. *Process Biochemistry*, *91*(September 2019), 387–397. https://doi.org/10.1016/j.procbio.2020.01.008

Ali, M. A., & Endalew, S. A. (2021). *Chemical Constituents of Datura stramonium L . Leaves and Its Antibacterial Activity against Human Pathogenic Bacteria*. *6*(2), 15–21.

Ali Thamer, N., & Tareq Barakat, N. (2019). Cytotoxic activity of green synthesis copper oxide nanoparticles using cordia myxa L. aqueous extract on some breast cancer cell lines. *Journal of Physics: Conference Series*, *1294*(6). https://doi.org/10.1088/1742-6596/1294/6/062104

Almisbah, S. R. E., & Mohammed, A. M. A. (2023). *Green synthesis of CuO nanoparticles using Hibiscus sabdariffa L . extract to treat wastewater in Soba Sewage Treatment Plant , Sudan*. *87*(12), 3059–3071. https://doi.org/10.2166/wst.2023.153

Alqarni, L. S., Alghamdi, M. D., Alshahrani, A. A., & Nassar, A. M. (2022). Green Nanotechnology: Recent Research on Bioresource-Based Nanoparticle Synthesis and Applications. *Journal of Chemistry*, *2022*. https://doi.org/10.1155/2022/4030999

Alrubaie, E. A. A. A., & Kadhim, R. E. (2019). Synthesis of zno nanoparticles from olive plant extract. *Plant Archives*, *19*, 339–344.

Altameme, H. J., Hameed, I. H., & Kareem, M. A. (2015). Analysis of alkaloid phytochemical

compounds in the ethanolic extract of Datura stramonium and evaluation of antimicrobial activity. *African Journal of Biotechnology*, *14*(19), 1668–1674. https://doi.org/10.5897/AJB2015.14536

AlTurki, A. M. (2018). Low-temperature synthesis of core/shell of Co3O4@ZnO nanoparticle characterization and dielectric properties. *Journal of Nanostructure in Chemistry*, *8*(2), 153–158. https://doi.org/10.1007/s40097-018-0260-y

Álvarez-Chimal, R., García-Pérez, V. I., Álvarez-Pérez, M. A., & Arenas-Alatorre, J. Á. (2021). Green synthesis of ZnO nanoparticles using a Dysphania ambrosioides extract. Structural characterization and antibacterial properties. *Materials Science and Engineering C*, *118*, 111540. https://doi.org/10.1016/j.msec.2020.111540

Alzahrani, K. E., Aniazy, A., Alswieleh, A. M., Wahab, R., El-Toni, A. M., & Alghamdi, H. S. (2018). Antibacterial activity of trimetal (CuZnFe) oxide nanoparticles. *International Journal of Nanomedicine*, *13*, 77–87. https://doi.org/10.2147/IJN.S154218

Amaliyah, S., Pangesti, D. P., Masruri, M., Sabarudin, A., & Sumitro, S. B. (2020). Green synthesis and characterization of copper nanoparticles using Piper retrofractum Vahl extract as bioreductor and capping agent. *Heliyon*, *6*(8), e04636. https://doi.org/10.1016/j.heliyon.2020.e04636

Amina, M., Al Musayeib, N. M., Alarfaj, N. A., El-Tohamy, M. F., Oraby, H. F., Al Hamoud, G. A., Bukhari, S. I., & Moubayed, N. M. S. (2020). Biogenic green synthesis of MgO nanoparticles using Saussurea costus biomasses for a comprehensive detection of their antimicrobial, cytotoxicity against MCF-7 breast cancer cells and photocatalysis potentials. *PLoS ONE*, *15*(8 August), 1–23. https://doi.org/10.1371/journal.pone.0237567

Ananda Murthy, H. C., Abebe, B., C H, P., & Shantaveerayya, K. (2018). A Review on Green Synthesis and Applications of Cu and CuO Nanoparticles. *Material Science Research India*, *15*(3), 279–295. https://doi.org/10.13005/msri/150311

Andleeb, A., Andleeb, A., Asghar, S., Zaman, G., Tariq, M., Mehmood, A., Nadeem, M., Hano, C., Lorenzo, J. M., & Abbasi, B. H. (2021). *A Systematic Review of Biosynthesized Metallic*

Nanoparticles as a Promising Anti-Cancer-Strategy. 1–22.

Angel Ezhilarasi, A., Judith Vijaya, J., Kaviyarasu, K., John Kennedy, L., Ramalingam, R. J., & Al-Lohedan, H. A. (2018). Green synthesis of NiO nanoparticles using Aegle marmelos leaf extract for the evaluation of in-vitro cytotoxicity, antibacterial and photocatalytic properties. *Journal of Photochemistry and Photobiology B: Biology*, *180*, 39–50. https://doi.org/10.1016/j.jphotobiol.2018.01.023

Ansari, M. A., Khan, H. M., Alzohairy, M. A., Jalal, M., Ali, S. G., Pal, R., & Musarrat, J. (2015). Green synthesis of Al2O3 nanoparticles and their bactericidal potential against clinical isolates of multi-drug resistant Pseudomonas aeruginosa. *World Journal of Microbiology and Biotechnology*, *31*(1), 153–164. https://doi.org/10.1007/s11274-014-1757-2

Anuradha, C. T., & Raji, P. (2021). Citrus limon fruit juice-assisted biomimetic synthesis, characterization and antimicrobial activity of cobalt oxide (Co3O4) nanoparticles. *Applied Physics A: Materials Science and Processing*, *127*(1), 1–9. https://doi.org/10.1007/s00339-020-04209-7

Aravind, M., Amalanathan, M., & Mary, M. S. M. (2021). Synthesis of TiO2 nanoparticles by chemical and green synthesis methods and their multifaceted properties. *SN Applied Sciences*, *3*(4), 1–10. https://doi.org/10.1007/s42452-021-04281-5

Arriagada, F., Günther, G., Nos, J., Nonell, S., Olea-Azar, C., & Morales, J. (2019). Antioxidant nanomaterial based on core–shell silica nanospheres with surface-bound caffeic acid: A promising vehicle for oxidation-sensitive drugs. *Nanomaterials*, *9*(2). https://doi.org/10.3390/nano9020214

Arsalan, N., Kashi, E. H., Hasan, A., Doost, M. E., Rasti, B., Paray, B. A., Nakhjiri, M. Z., Sari, S., Sharifi, M., Shahpasand, K., Akhtari, K., Haghighat, S., & Falahati, M. (2020). Exploring the interaction of cobalt oxide nanoparticles with Albumin, leukemia cancer cells and pathogenic bacterial by multispectroscopic, docking, cellular and antibacterial approaches. *International Journal of Nanomedicine*, *15*, 4607–4623. https://doi.org/10.2147/IJN.S257711

Asamoah, R. B., Annan, E., Mensah, B., Nbelayim, P., Apalangya, V., Onwona-Agyeman, B., & Yaya, A. (2020). A Comparative Study of Antibacterial Activity of CuO/Ag and ZnO/Ag Nanocomposites. *Advances in Materials Science and Engineering*, *2020*. https://doi.org/10.1155/2020/7814324

Azam, A., Ahmed, F., Arshi, N., Chaman, M., & Naqvi, A. H. (2009). Low temperature synthesis of ZnO nanoparticles using mechanochemical route : A green chemistry approach. *International Journal of Theoretical & Applied Sciences*, *1*(2), 12–14.

Aziz, S. B., Hussein, G., Brza, M. A., Mohammed, S. J., Abdulwahid, R. T., Saeed, S. R., & Hassanzadeh, A. (2019). Fabrication of interconnected plasmonic spherical silver nanoparticles with enhanced localized surface plasmon resonance (Lspr) peaks using quince leaf extract solution. *Nanomaterials*, *9*(11). https://doi.org/10.3390/nano9111557

Azizi, M., Ghourchian, H., Yazdian, F., Dashtestani, F., & AlizadehZeinabad, H. (2017). Cytotoxic effect of albumin coated copper nanoparticle on human breast cancer cells of MDA-MB 231. *PLoS ONE*, *12*(11), 1–21. https://doi.org/10.1371/journal.pone.0188639

Babiker, F., Jamal, P., Mirghani, M. E. S., & Ansari, A. H. I. (2017). Characterization, purification and identification of some Alkaloids in Datura stramonium. *International Food Research Journal*, *24*(December), 540–543.

Baig, N., Kammakakam, I., Falath, W., & Kammakakam, I. (2021). Nanomaterials: A review of synthesis methods, properties, recent progress, and challenges. *Materials Advances*, *2*(6), 1821–1871. https://doi.org/10.1039/d0ma00807a

Barzan, G., Kokalari, I., Gariglio, G., Ghibaudi, E., Devocelle, M., Monopoli, M. P., Sacco, A., Greco, A., Giovannozzi, A. M., Rossi, A. M., & Fenoglio, I. (2022). Molecular Aspects of the Interaction with Gram-Negative and Gram-Positive Bacteria of Hydrothermal Carbon Nanoparticles Associated with Bac8c2,5LeuAntimicrobial Peptide. *ACS Omega*. https://doi.org/10.1021/acsomega.2c00305

Barzinjy, A. A., Hamad, S. M., Aydın, S., Ahmed, M. H., & Hussain, F. H. S. (2020). Green and eco-friendly synthesis of Nickel oxide nanoparticles and its photocatalytic activity for

methyl orange degradation. *Journal of Materials Science: Materials in Electronics*, *31*(14), 11303–11316. https://doi.org/10.1007/s10854-020-03679-y

Batool, A., Batool, Z., Qureshi, R., & Raja, N. I. (2020). Phytochemicals , Pharmacological Properties and Biotechnological Aspects of Highly Medicinal Plant : Datura stramonium. *Journal of Plant Sciences*, *8*(2), 29–40. https://doi.org/10.11648/j.jps.20200802.12

Bayal, N., & Jeevanandam, P. (2012). Synthesis of CuO@NiO core-shell nanoparticles by homogeneous precipitation method. *Journal of Alloys and Compounds*, *537*, 232–241. https://doi.org/10.1016/j.jallcom.2012.05.086

Bayat, M., Chudinova, E., Zargar, M., Lyashko, M., Louis, K., & Adenew, F. K. (2019). Phyto-assisted green synthesis of zinc oxide nanoparticles and its antibacterial and antifungal activity. *Research on Crops*, *20*(4), 725–730. https://doi.org/10.31830/2348-7542.2019.107

Behera, N., Arakha, M., Priyadarshinee, M., Pattanayak, B. S., Soren, S., Jha, S., & Mallick, B. C. (2019). Oxidative stress generated at nickel oxide nanoparticle interface results in bacterial membrane damage leading to cell death. *RSC Advances*, *9*(43), 24888–24894. https://doi.org/10.1039/c9ra02082a

Bekele, E. T., Murthy, H. C. A., Muniswamy, D., Lemenh, Y. A., Shume, M. S., Tadesse Ayanie, G., Kumar, A. P., Ravikumar, C. R., Balachandran, R., & Roy, A. (2022). Solanum tuberosum Leaf Extract Templated Synthesis of Co3O4Nanoparticles for Electrochemical Sensor and Antibacterial Applications. *Bioinorganic Chemistry and Applications*, *2022*(16 mm). https://doi.org/10.1155/2022/8440756

Benhammada, A., & Trache, D. (2021). Green synthesis of CuO nanoparticles using Malva sylvestris leaf extract with different copper precursors and their effect on nitrocellulose thermal behavior. *Journal of Thermal Analysis and Calorimetry*, *0123456789*. https://doi.org/10.1007/s10973-020-10469-5

Bhuvaneshwari, V., Vaidehi, D., & Logpriya, S. (2018). Green synthesis of copper oxide nanoparticles for biological applications. *Microbiology: Current Research*, *2*(1), 2–3.

Bibi, I., Nazar, N., Iqbal, M., Kamal, S., Nawaz, H., Nouren, S., Safa, Y., Jilani, K., Sultan, M.,

Ata, S., Rehman, F., & Abbas, M. (2017). Green and eco-friendly synthesis of cobalt-oxide nanoparticle: Characterization and photo-catalytic activity. *Advanced Powder Technology*, *28*(9), 2035–2043. https://doi.org/10.1016/j.apt.2017.05.008

Bouafia, A., Laouini, S. E., & Ouahrani, M. R. (2020). A Review on Green Synthesis of CuO Nanoparticles using Plant Extract and Evaluation of Antimicrobial Activity. *Asian Journal of Research in Chemistry*, *13*(1), 65. https://doi.org/10.5958/0974-4150.2020.00014.0

Bridges, D. F., Lacombe, A., & Wu, V. C. H. (2020). Integrity of the Escherichia coli O157:H7 Cell Wall and Membranes After Chlorine Dioxide Treatment. *Frontiers in Microbiology*, *11*(May), 1–11. https://doi.org/10.3389/fmicb.2020.00888

Bridier, A., Le Coq, D., Dubois-Brissonnet, F., Thomas, V., Aymerich, S., & Briandet, R. (2011). The spatial architecture of Bacillus subtilis biofilms deciphered using a surface-associated model and in Situ imaging. *PLoS ONE*, *6*(1). https://doi.org/10.1371/journal.pone.0016177

Brown, N. R., Korolchuk, S., Martin, M. P., Stanley, W. A., Moukhametzianov, R., Noble, M. E. M., & Endicott, J. A. (2015). *features of the essential cell cycle CDK*. 1–12. https://doi.org/10.1038/ncomms7769

Bukhari, S. I., Hamed, M. M., Al-Agamy, M. H., Gazwi, H. S. S., Radwan, H. H., & Youssif, A. M. (2021). Biosynthesis of Copper Oxide Nanoparticles Using Streptomyces MHM38 and Its Biological Applications. *Journal of Nanomaterials*, *2021*. https://doi.org/10.1155/2021/6693302

Cai, D., Huang, H., Wang, D., Liu, B., Wang, L., Liu, Y., Li, Q., & Wang, T. (2014). High-performance supercapacitor electrode based on the unique ZnO@Co3O4 core/shell heterostructures on nickel foam. *ACS Applied Materials and Interfaces*, *6*(18), 15905–15912. https://doi.org/10.1021/am5035494

Carpa, R., Dumitru, D.-V., Burtescu, R. F., Maior, M. C., Dobrotă, C., & Olah, N.-K. (2017). Bio-chemical analysis of Datura stramonium extract. *Studia Universitatis Babeş-Bolyai Biologia*, *62*(2), 5–19. https://doi.org/10.24193/subbbiol.2017.2.01

Carreño, E. A., Viana, A., Alberto, P., Alves, C., Souza, D., Mello, H. L. De, Henriques-pons, A., & Alves, L. A. (2021). *applied sciences Considerations and Technical Pitfalls in the Employment of the MTT Assay to Evaluate Photosensitizers for Photodynamic Therapy*.

Casais-Molina, M. L., Cab, C., Canto, G., Medina, J., & Tapia, A. (2018). Carbon Nanomaterials for Breast Cancer Treatment. *Journal of Nanomaterials*, *2018*. https://doi.org/10.1155/2018/2058613

Chakra, C. S., Rajendar, V., Rao, K. V., & Kumar, M. (2017). Enhanced antimicrobial and anticancer properties of ZnO and TiO2 nanocomposites. *3 Biotech*, *7*(2), 1–8. https://doi.org/10.1007/s13205-017-0731-8

Chan Park, J., Kim, A. Y., Kim, J. Y., Park, S., Park, K. H., & Song, H. (2012). ZnO-CuO core-branch nanocatalysts for ultrasound-assisted azide-alkyne cycloaddition reactions. *Chemical Communications*, *48*(68), 8484–8486. https://doi.org/10.1039/c2cc31654d

Chang, S. H., Yang, P. Y., Lai, C. M., Lu, S. C., Li, G. A., Chang, W. C., & Tuan, H. Y. (2016). Synthesis of Cu/ZnO core/shell nanocomposites and their use as efficient photocatalysts. *CrystEngComm*, *18*(4), 616–621. https://doi.org/10.1039/c5ce01944c

Chen, J. S., Zhu, T., Hu, Q. H., Gao, J., Su, F., Qiao, S. Z., & Lou, X. W. (2010). Shape-controlled synthesis of cobalt-based nanocubes, nanodiscs, and nanoflowers and their comparative lithium-storage properties. *ACS Applied Materials and Interfaces*, *2*(12), 3628–3635. https://doi.org/10.1021/am100787w

Chen, R. X., Zhu, S. L., Mao, J., Cui, Z. D., Yang, X. J., Liang, Y. Q., & Li, Z. Y. (2015). Synthesis of CuO/Co3O4 coaxial heterostructures for efficient and recycling photodegradation. *International Journal of Photoenergy*, *2015*. https://doi.org/10.1155/2015/183468

Chikkanna, M. M., Neelagund, S. E., & Rajashekarappa, K. K. (2019). Green synthesis of Zinc oxide nanoparticles (ZnO NPs) and their biological activity. *SN Applied Sciences*, *1*(1), 1–10. https://doi.org/10.1007/s42452-018-0095-7

Chung, I., Rahuman, A. A., Marimuthu, S., Kirthi, A. V., Anbarasan, K., Padmini, P., &

Rajakumar, G. (2017). Green synthesis of copper nanoparticles using eclipta prostrata leaves extract and their antioxidant and cytotoxic activities. *Experimental and Therapeutic Medicine*, *14*(1), 18–24. https://doi.org/10.3892/etm.2017.4466

Cornelius, G., Lohiya, G., & Sharma, R. (2019). *Chemical Constituents and Pharmacological Properties of Datura Stramonium (Thorn Apple)-A Review*. *8*(11), 512–515. www.ijert.org

Costas, A., Florica, C., Preda, N., Kuncser, A., & Enculescu, I. (2020). Photodetecting properties of single CuO–ZnO core–shell nanowires with p–n radial heterojunction. *Scientific Reports*, *10*(1), 1–12. https://doi.org/10.1038/s41598-020-74963-4

Cox, G., & Wright, G. D. (2013). Intrinsic antibiotic resistance: Mechanisms, origins, challenges and solutions. *International Journal of Medical Microbiology*, *303*(6–7), 287–292. https://doi.org/10.1016/j.ijmm.2013.02.009

D.lowy, F., & M.D. (1998). Lowy1998. *The New England Journal of Medicine*, *339*(8), 520–532.

Dagne, S., Abate, S. M., Tigeneh, W., & Engidawork, E. (2019). Assessment of breast cancer treatment outcome at Tikur Anbessa Specialized Hospital Adult Oncology Unit, Addis Ababa, Ethiopia. *European Journal of Oncology Pharmacy*, *2*(2), e13. https://doi.org/10.1097/op9.0000000000000013

Das, R. K., Pachapur, V. L., Lonappan, L., Naghdi, M., Pulicharla, R., Maiti, S., Cledon, M., Dalila, L. M. A., Sarma, S. J., & Brar, S. K. (2017). Biological synthesis of metallic nanoparticles: plants, animals and microbial aspects. *Nanotechnology for Environmental Engineering*, *2*(1), 1–21. https://doi.org/10.1007/s41204-017-0029-4

Das, S., Kumar, P., & Basu, S. P. (2012). Phytoconstituents and Therapeutic Potentials of Datura Stramonium Linn. *Journal of Drug Delivery and Therapeutics*, *2*(3), 4–7. https://doi.org/10.22270/jddt.v2i3.141

De Souza, R. C., Haberbeck, L. U., Riella, H. G., Ribeiro, D. H. B., & Carciofi, B. A. M. (2019). Antibacterial activity of zinc oxide nanoparticles synthesized by solochemical process. *Brazilian Journal of Chemical Engineering*, *36*(2), 885–893. https://doi.org/10.1590/0104-

6632.20190362s20180027

Dessen, A., Di Guilmi, A. M., Vernet, T., & Dideberg, O. (2001). Molecular mechanisms of antibiotic resistance in gram-positive pathogens. *Current Drug Targets. Infectious Disorders*, *1*(1), 63–77. https://doi.org/10.2174/1568005013343272

Devi, A. B., Moirangthem, D. S., Talukdar, N. C., Devi, M. D., Singh, N. R., & Luwang, M. N. (2014). Novel synthesis and characterization of CuO nanomaterials: Biological applications. *Chinese Chemical Letters*, *25*(12), 1615–1619. https://doi.org/10.1016/j.cclet.2014.07.014

Dewi, N. O. M., Yulizar, Y., & Bagus Apriandanu, D. O. (2019). Green synthesis of Co3O4 nanoparticles using Euphorbia heterophylla L. leaves extract: Characterization and photocatalytic activity. *IOP Conference Series: Materials Science and Engineering*, *509*(1). https://doi.org/10.1088/1757-899X/509/1/012105

Din, M. I., Arshad, F., Hussain, Z., & Mukhtar, M. (2017). Green Adeptness in the Synthesis and Stabilization of Copper Nanoparticles: Catalytic, Antibacterial, Cytotoxicity, and Antioxidant Activities. *Nanoscale Research Letters*, *12*. https://doi.org/10.1186/s11671-017-2399-8

Din, M. I., Nabi, A. G., Rani, A., Aihetasham, A., & Mukhtar, M. (2018). Single step green synthesis of stable nickel and nickel oxide nanoparticles from Calotropis gigantea: Catalytic and antimicrobial potentials. *Environmental Nanotechnology, Monitoring and Management*, *9*(November 2017), 29–36. https://doi.org/10.1016/j.enmm.2017.11.005

Ding, J., Cheng, F., Meng, Z., Cao, Y., Han, F., & Chen, D. (2021). *Core-Shell-Like Structured Co 3 O 4 @ SiO 2 Catalyst for Highly Ef fi cient Catalytic Elimination of Ozone*. *9*(December), 1–6. https://doi.org/10.3389/fchem.2021.803464

Dinga, E., Mthiyane, D. M. N., Marume, U., Botha, T. L., Horn, S., Pieters, R., Wepener, V., Ekennia, A., & Onwudiwe, D. C. (2022). Biosynthesis of ZnO nanoparticles using Melia azedarach seed extract: Evaluation of the cytotoxic and antimicrobial potency. *OpenNano*, *8*(June), 100068. https://doi.org/10.1016/j.onano.2022.100068

Dizaj, S. M., Lotfipour, F., Barzegar-Jalali, M., Zarrintan, M. H., & Adibkia, K. (2014).

Antimicrobial activity of the metals and metal oxide nanoparticles. *Materials Science and Engineering C*, *44*, 278–284. https://doi.org/10.1016/j.msec.2014.08.031

Dobrucka, R. (2018). Antioxidant and Catalytic Activity of Biosynthesized CuO Nanoparticles Using Extract of Galeopsidis herba. *Journal of Inorganic and Organometallic Polymers and Materials*, *28*(3), 812–819. https://doi.org/10.1007/s10904-017-0750-2

Dubale, S., Kebebe, D., Zeynudin, A., Abdissa, N., & Suleman, S. (2023). Phytochemical Screening and Antimicrobial Activity Evaluation of Selected Medicinal Plants in Ethiopia. *Journal of Experimental Pharmacology*, *15*(January), 51–62. https://doi.org/10.2147/JEP.S379805

El-Toni, A. M., Habila, M. A., Labis, J. P., Alothman, Z. A., Alhoshan, M., Elzatahry, A. A., & Zhang, F. (2016). Design, synthesis and applications of core-shell, hollow core, and nanorattle multifunctional nanostructures. *Nanoscale*, *8*(5), 2510–2531. https://doi.org/10.1039/c5nr07004j

El-toni, A. M., Habila, M. A., Sheikh, M., & El-mahrouky, M. (2023). *core-mesoSiO 2 / TiO 2 Double Shell Nanoparticles for Methylene Blue Adsorption : Kinetic , Isotherms and Thermodynamic Characterization*.

Elbaz, N. M., Ziko, L., Siam, R., & Mamdouh, W. (2016). Core-Shell Silver/Polymeric Nanoparticles-Based Combinatorial Therapy against Breast Cancer In-vitro. *Scientific Reports*, *6*(October 2015), 1–9. https://doi.org/10.1038/srep30729

Elsayed, A. M., Sherif, N. M., Hassan, N. S., Althobaiti, F., Hanafy, N. A. N., & Sahyon, H. A. (2021). Novel quercetin encapsulated chitosan functionalized copper oxide nanoparticles as anti-breast cancer agent via regulating p53 in rat model. *International Journal of Biological Macromolecules*, *185*(June), 134–152. https://doi.org/10.1016/j.ijbiomac.2021.06.085

Ezhilarasi, A. A., Vijaya, J. J., Kaviyarasu, K., Maaza, M., Ayeshamariam, A., & Kennedy, L. J. (2016). Green synthesis of NiO nanoparticles using Moringa oleifera extract and their biomedical applications: Cytotoxicity effect of nanoparticles against HT-29 cancer cells. *Journal of Photochemistry and Photobiology B: Biology*, *164*, 352–360.

https://doi.org/10.1016/j.jphotobiol.2016.10.003

Fatimah, I., Pradita, R. Y., & Nurfalinda, A. (2016). Plant Extract Mediated of ZnO Nanoparticles by Using Ethanol Extract of Mimosa Pudica Leaves and Coffee Powder. *Procedia Engineering*, *148*, 43–48. https://doi.org/10.1016/j.proeng.2016.06.483

Florica, C., Costas, A., Preda, N., Beregoi, M., Kuncser, A., Apostol, N., Popa, C., Socol, G., Diculescu, V., & Enculescu, I. (2019). Core-shell nanowire arrays based on ZnO and CuxO for water stable photocatalysts. *Scientific Reports*, *9*(1), 1–15. https://doi.org/10.1038/s41598-019-53873-0

Fu, L., Mou, J., Deng, Y., Ren, X., & Qiu, S. (2022). *Design , Synthesis , and Activity Assays of Cyclin-Dependent Kinase 1 Inhibitors With Flavone Scaffolds*. *10*(August), 1–16. https://doi.org/10.3389/fchem.2022.940427

Ganesan, K., Jothi, V. K., Natarajan, A., Rajaram, A., Ravichandran, S., & Ramalingam, S. (2020). Green synthesis of Copper oxide nanoparticles decorated with graphene oxide for anticancer activity and catalytic applications. *Arabian Journal of Chemistry*, *13*(8), 6802–6814. https://doi.org/10.1016/j.arabjc.2020.06.033

García-Sánchez, A., Miranda-Díaz, A. G., & Cardona-Muñoz, E. G. (2020). The Role of Oxidative Stress in Physiopathology and Pharmacological Treatment with Pro- And Antioxidant Properties in Chronic Diseases. *Oxidative Medicine and Cellular Longevity*, *2020*. https://doi.org/10.1155/2020/2082145

Gawande, M. B., Goswami, A., Asefa, T., Guo, H., Biradar, A. V., Peng, D. L., Zboril, R., & Varma, R. S. (2015). Core-shell nanoparticles: synthesis and applications in catalysis and electrocatalysis. *Chemical Society Reviews*, *44*(21), 7540–7590. https://doi.org/10.1039/c5cs00343a

George, B. P., Rajendran, N. K., Houreld, N. N., & Abrahamse, H. (2022). Rubus Capped Zinc Oxide Nanoparticles Induce Apoptosis in MCF-7 Breast Cancer Cells. *Molecules*, *27*(20). https://doi.org/10.3390/molecules27206862

Ghosh Chaudhuri, R., & Paria, S. (2012). Core/shell nanoparticles: Classes, properties, synthesis

mechanisms, characterization, and applications. *Chemical Reviews*, *112*(4), 2373–2433. https://doi.org/10.1021/cr100449n

Ghosh, M. K., Sahu, S., Gupta, I., & Ghorai, T. K. (2020). Green synthesis of copper nanoparticles from an extract ofJatropha curcasleaves: characterization, optical properties, CT-DNA binding and photocatalytic activity. *RSC Advances*, *10*(37), 22027–22035. https://doi.org/10.1039/d0ra03186k

Gnanavel, V., Palanichamy, V., & Roopan, S. M. (2017a). Biosynthesis and characterization of copper oxide nanoparticles and its anticancer activity on human colon cancer cell lines (HCT-116). *Journal of Photochemistry and Photobiology B: Biology*, *171*(May), 133–138. https://doi.org/10.1016/j.jphotobiol.2017.05.001

Gnanavel, V., Palanichamy, V., & Roopan, S. M. (2017b). Biosynthesis and characterization of copper oxide nanoparticles and its anticancer activity on human colon cancer cell lines (HCT-116). *Journal of Photochemistry and Photobiology B: Biology*, *171*, 133–138. https://doi.org/10.1016/j.jphotobiol.2017.05.001

Goutam, S. P., Saxena, G., Roy, D., Yadav, A. K., & Bharagava, R. N. (2020). Green Synthesis of Nanoparticles and Their Applications in Water and Wastewater Treatment. In *Bioremediation of Industrial Waste for Environmental Safety* (Issue Dm). https://doi.org/10.1007/978-981-13-1891-7_16

Govindasamy, R., Raja, V., Singh, S., Govindarasu, M., & Sabura, S. (2022). *Green Synthesis and Characterization of Cobalt Oxide Nanoparticles Using Psidium guajava Leaves Extracts and Their Photocatalytic and Biological Activities*. 1–16.

Govindasamy, R., Raja, V., Singh, S., Govindarasu, M., Sabura, S., Rekha, K., Rajeswari, V. D., Alharthi, S. S., Vaiyapuri, M., Sudarmani, R., Jesurani, S., Venkidasamy, B., & Thiruvengadam, M. (2022). Green Synthesis and Characterization of Cobalt Oxide Nanoparticles Using Psidium guajava Leaves Extracts and Their Photocatalytic and Biological Activities. *Molecules*, *27*(17), 1–16. https://doi.org/10.3390/molecules27175646

Grigorie, A. C., Muntean, C., Vlase, T., Locovei, C., & Stefanescu, M. (2017). ZnO-SiO2 based

nanocomposites prepared by a modified sol-gel method. *Materials Chemistry and Physics*, *186*, 399–406. https://doi.org/10.1016/j.matchemphys.2016.11.011

Guisbiers, G., Mejía-Rosales, S., & Leonard Deepak, F. (2012). Nanomaterial properties: Size and shape dependencies. *Journal of Nanomaterials*, *2012*. https://doi.org/10.1155/2012/180976

Guo, R., Liu, Y., Xu, Z. P., Xia, Y. G., Yang, B. Y., & Kuang, H. X. (2018). Withanolides from the leaves of Datura metel L. *Phytochemistry*, *155*(March), 136–146. https://doi.org/10.1016/j.phytochem.2018.08.005

Gupta, M., Tomar, R. S., Kaushik, S., Mishra, R. K., & Sharma, D. (2018). Effective antimicrobial activity of green ZnO nano particles of Catharanthus roseus. *Frontiers in Microbiology*, *9*(SEP), 1–13. https://doi.org/10.3389/fmicb.2018.02030

Habtemariam, A. B. (2021). Synthesis of WO3 Nanoparticles using Rhamnus Prinoides Leaf Extract and Evaluation of its Antibacterial Activities. *Biointerface Research in Applied Chemistry*, *12*(1), 529–536. https://doi.org/10.33263/briac121.529536

Hafeez, M., Shaheen, R., Akram, B., Ahmed, M. N., Zain-Ul-Abdin, Haq, S., Din, S. U., Zeb, M., & Khan, M. A. (2021). Green Synthesis of Nickel Oxide Nanoparticles using Populus ciliata Leaves Extract and their Potential Antibacterial Applications. *South African Journal of Chemistry*, *75*, 168–173. https://doi.org/10.17159/0379-4350/2021/v75a21

Hafeez, M., Shaheen, R., Akram, B., Zain-Ul-Abdin, Haq, S., Mahsud, S., Ali, S., & Khan, R. T. (2020). Green synthesis of cobalt oxide nanoparticles for potential biological applications. *Materials Research Express*, *7*(2). https://doi.org/10.1088/2053-1591/ab70dd

Haider, A., Ijaz, M., Ali, S., Haider, J., Imran, M., Majeed, H., Shahzadi, I., Ali, M. M., Khan, J. A., & Ikram, M. (2020). Green Synthesized Phytochemically (Zingiber officinale and Allium sativum) Reduced Nickel Oxide Nanoparticles Confirmed Bactericidal and Catalytic Potential. *Nanoscale Research Letters*, *15*(1). https://doi.org/10.1186/s11671-020-3283-5

Hammouda, M. M., Alanazi, A. A., & Elattar, K. M. (2024). Mentha suaveolens Leaves Extract-Mediated Synthesis of CoO@TiO2 and Fe2O3@TiO2 Core/Shell Nanoparticles with

Synergistic Antimicrobial and Antioxidant Activities. *ChemistrySelect*, *9*(17). https://doi.org/10.1002/slct.202401385

Han, D. Y., Wang, C. Q., Li, D. D., & Cao, Z. B. (2016). NiO/ZnO Core-Shell Nanoparticles in Situ Synthesis Via Microemulsion Method. *Synthesis and Reactivity in Inorganic, Metal-Organic and Nano-Metal Chemistry*, *46*(5), 794–797. https://doi.org/10.1080/15533174.2014.989595

Happy, A., Soumya, M., Kumar, S. V., Rajeshkumar, S., Sheba, R. D., Lakshmi, T., & Nallaswamy, V. D. (2019). Phyto-assisted synthesis of zinc oxide nanoparticles using Cassia alata and its antibacterial activity against Escherichia coli. *Biochemistry and Biophysics Reports*, *17*(September 2018), 208–211. https://doi.org/10.1016/j.bbrep.2019.01.002

Haq, S., Abbasi, F., Ben Ali, M., Hedfi, A., Mezni, A., Rehman, W., Waseem, M., Khan, A. R., & Shaheen, H. (2021). Green synthesis of cobalt oxide nanoparticles and the effect of annealing temperature on their physiochemical and biological properties. *Materials Research Express*, *8*(7). https://doi.org/10.1088/2053-1591/ac1187

Haq, S., Dildar, S., Ali, M. Ben, Mezni, A., Hedfi, A., Shahzad, M. I., Shahzad, N., & Shah, A. (2021). Antimicrobial and antioxidant properties of biosynthesized of NiO nanoparticles using Raphanus sativus (R. sativus) extract. *Materials Research Express*, *8*(5). https://doi.org/10.1088/2053-1591/abfc7c

Hariharan, D., Srinivasan, K., & Lc, N. (2017). Synthesis and Characterization of Tio2 Nanoparticles Using Cynodon Dactylon Leaf Extract for Antibacterial and Anticancer (A549 Cell Lines) Activity. *Journal of Nanomedicine Research*, *5*(6), 4–8. https://doi.org/10.15406/jnmr.2017.05.00138

Harwood, C. R., Crawshaw, S. G., & Wipat, A. (2001). From genome to function: Systematic analysis of the soil bacterium Bacillus subtilis. *Comparative and Functional Genomics*, *2*(1), 22–24. https://doi.org/10.1002/cfg.69

Hashami, M., Nazhipkyzy, M., Seitkazinova, A. R., & Kerimkulova, A. R. (2024). *Synthesis of*

Co 3 O 4 Nanoparticles through Solution Combustion Method and Their Applications : A Review Synthesis of Co 3 O 4 Nanoparticles through Solution Combustion Method and Their Applications : https://doi.org/10.20944/preprints202403.1118.v1

Hashmi, H. F., Bibi, S., Anwar, M., & Rashid Khan, M. (2021). Qualitative and Quantitative Analysis of Phytochemicals in Lepidium Pinnatifidum Ledeb. *Abbreviated Key Title: Sch Int J Tradit Complement Med*, *4*(5), 67–75. https://doi.org/10.36348/sijtcm.2021.v04i05.002

Hossain, M., Hamza, A., Polash, S. A., Tushar, M. H., Takikawa, M., Piash, A. B., Dekiwadia, C., Saha, T., Takeoka, S., & Sarker, S. R. (2024). *As featured in : RSC Pharmaceutics Green synthesis of silver nanoparticles using Phyllanthus emblica extract : investigation of antibacterial activity and biocompatibility in vivo †*. https://doi.org/10.1039/d3pm00077j

Huang, X., Cai, H., Zhou, H., Li, T., Jin, H., Evans, C. E., Cai, J., & Pi, J. (2021). Cobalt oxide nanoparticle-synergized protein degradation and phototherapy for enhanced anticancer therapeutics. *Acta Biomaterialia*, *121*, 605–620. https://doi.org/10.1016/j.actbio.2020.11.036

Huang, X., & El-Sayed, M. A. (2010). Gold nanoparticles: Optical properties and implementations in cancer diagnosis and photothermal therapy. *Journal of Advanced Research*, *1*(1), 13–28. https://doi.org/10.1016/j.jare.2010.02.002

Huang, Y., Du, Z., Bao, G., Fang, G., Cappadona, M., McClements, L., Tuch, B. E., Lu, H., & Xu, X. (2023). Smart Drug-Delivery System of Upconversion Nanoparticles Coated with Mesoporous Silica for Controlled Release. *Pharmaceutics*, *15*(1). https://doi.org/10.3390/pharmaceutics15010089

Hussain, A., Oves, M., Alajmi, M. F., Hussain, I., Amir, S., Ahmed, J., Rehman, M. T., El-Seedi, H. R., & Ali, I. (2019). Biogenesis of ZnO nanoparticles using: Pandanus odorifer leaf extract: Anticancer and antimicrobial activities. *RSC Advances*, *9*(27), 15357–15369. https://doi.org/10.1039/c9ra01659g

Hussain, S., Ali Muazzam, M., Ahmed, M., Ahmad, M., Mustafa, Z., Murtaza, S., Ali, J., Ibrar, M., Shahid, M., & Imran, M. (2023). Green synthesis of nickel oxide nanoparticles using

Acacia nilotica leaf extracts and investigation of their electrochemical and biological properties. *Journal of Taibah University for Science*, *17*(1). https://doi.org/10.1080/16583655.2023.2170162

Huth, M. E., Ricci, A. J., & Cheng, A. G. (2011). Mechanisms of Aminoglycoside Ototoxicity and Targets of Hair Cell Protection. *International Journal of Otolaryngology*, *2011*, 1–19. https://doi.org/10.1155/2011/937861

Ijaz, F., Shahid, S., Khan, S. A., Ahmad, W., & Zaman, S. (2017). Green synthesis of copper oxide nanoparticles using abutilon indicum leaf extract: Antimicrobial, antioxidant and photocatalytic dye degradation activities. *Tropical Journal of Pharmaceutical Research*, *16*(4), 743–753. https://doi.org/10.4314/tjpr.v16i4.2

Ikhmal, W. M. K. W. M., Yasmin, M. Y. N., Fazira, M. F. M., Rafizah, W. A. W., Wan Nik, W. B., & Sabri, M. G. M. (2018). Anticorrosion Coating using Olea sp. Leaves Extract. *IOP Conference Series: Materials Science and Engineering*, *344*(1). https://doi.org/10.1088/1757-899X/344/1/012028

Iqbal, J., Abbasi, B. A., Mahmood, T., Hameed, S., Munir, A., & Kanwal, S. (2019). Green synthesis and characterizations of Nickel oxide nanoparticles using leaf extract of Rhamnus virgata and their potential biological applications. *Applied Organometallic Chemistry*, *33*(8), 0–2. https://doi.org/10.1002/aoc.4950

Jabeen, K., Nizamuddin, S., Irfan, S., Khan, E., Malik, F., & Zafar, A. (2011). Increasing trend of resistance to penicillin, tetracycline, and fluoroquinolone resistance in Neisseria gonorrhoeae from Pakistan (1992-2009). *Journal of Tropical Medicine*, *2011*. https://doi.org/10.1155/2011/960501

Jacob, V., & P, R. (2019). in Vitro Analysis: the Antimicrobial and Antioxidant Activity of Zinc Oxide Nanoparticles From Curcuma Longa. *Asian Journal of Pharmaceutical and Clinical Research*, *12*(1), 200. https://doi.org/10.22159/ajpcr.2019.v12i1.28808

Jayasimha, H. N., Chandrappa, K. G., Sanaulla, P. F., & Dileepkumar, V. G. (2024). Green synthesis of CuO nanoparticles : A promising material for photocatalysis and

electrochemical sensor. *Sensors International*, *5*(September 2023), 100254. https://doi.org/10.1016/j.sintl.2023.100254

Jia, H., Yang, D., Han, X., Cai, J., Liu, H., & He, W. (2016). Peroxidase-like activity of the Co3O4 nanoparticles used for biodetection and evaluation of antioxidant behavior. *Nanoscale*, *8*(11), 5938–5945. https://doi.org/10.1039/c6nr00860g

Jiang, J., Pi, J., & Cai, J. (2018). The Advancing of Zinc Oxide Nanoparticles for Biomedical Applications. *Bioinorganic Chemistry and Applications*, *2018*. https://doi.org/10.1155/2018/1062562

Johnston, N., Mukhtar, T., & Wright, G. (2005). Streptogramin Antibiotics: Mode of Action and Resistance. *Current Drug Targets*, *3*(4), 335–344. https://doi.org/10.2174/1389450023347678

Juan, A., Cimas, F. J., Pandiella, A., Ocaña, A., & Alonso-moreno, C. (n.d.). *Antibody Conjugation of Nanoparticles as Therapeutics for Breast Cancer Treatment*. *Figure 1*, 1–21.

Juma, A. O., Arbab, E. A. A., Muiva, C. M., Lepodise, L. M., & Mola, G. T. (2017). Synthesis and characterization of CuO-NiO-ZnO mixed metal oxide nanocomposite. *Journal of Alloys and Compounds*, *723*(June), 866–872. https://doi.org/10.1016/j.jallcom.2017.06.288

Kadam, S. D., Chavhan, S. A., Shinde, S. A., & Sapkal, P. N. (2018). Pharmacognostic Review on Datura. *Research Journal of Pharmacology and Pharmacodynamics*, *10*(4), 171. https://doi.org/10.5958/2321-5836.2018.00032.0

Kalpana, V. N., & Devi Rajeswari, V. (2018). A Review on Green Synthesis, Biomedical Applications, and Toxicity Studies of ZnO NPs. *Bioinorganic Chemistry and Applications*, *2018*. https://doi.org/10.1155/2018/3569758

Kalska-Szostko, B., Wykowska, U., & Satuła, D. (2015). Magnetic nanoparticles of core-shell structure. *Colloids and Surfaces A: Physicochemical and Engineering Aspects*, *481*, 527–536. https://doi.org/10.1016/j.colsurfa.2015.05.040

Kamurai, B., Mombeshora, M., & Mukanganyama, S. (2020). Repurposing of Drugs for Antibacterial Activities on Selected ESKAPE Bacteria Staphylococcus aureus and Pseudomonas aeruginosa. *International Journal of Microbiology, 2020*. https://doi.org/10.1155/2020/8885338

Kantelhardt, E. J., Zerche, P., Mathewos, A., Trocchi, P., Addissie, A., Aynalem, A., Wondemagegnehu, T., Ersumo, T., Reeler, A., Yonas, B., Tinsae, M., Gemechu, T., Jemal, A., Thomssen, C., Stang, A., & Bogale, S. (2014). Breast cancer survival in Ethiopia: A cohort study of 1,070 women. *International Journal of Cancer*, *135*(3), 702–709. https://doi.org/10.1002/ijc.28691

Karam, S. T., & Abdulrahman, A. F. (2022). Green Synthesis and Characterization of ZnO Nanoparticles by Using Thyme Plant Leaf Extract. *Photonics*, *9*(8). https://doi.org/10.3390/photonics9080594

Keat, C. L., Aziz, A., Eid, A. M., & Elmarzugi, N. A. (2015). Biosynthesis of nanoparticles and silver nanoparticles. *Bioresources and Bioprocessing*, *2*(1). https://doi.org/10.1186/s40643-015-0076-2

Kebede Urge, S., Tiruneh Dibaba, S., & Belay Gemta, A. (2023). Green Synthesis Method of ZnO Nanoparticles using Extracts of Zingiber officinale and Garlic Bulb (Allium sativum) and Their Synergetic Effect for Antibacterial Activities. *Journal of Nanomaterials*, *2023*. https://doi.org/10.1155/2023/7036247

Kganyago, P., Mahlaule-Glory, L. M., Mathipa, M. M., Ntsendwana, B., Mketo, N., Mbita, Z., & Hintsho-Mbita, N. C. (2018). Synthesis of NiO nanoparticles via a green route using Monsonia burkeana: The physical and biological properties. *Journal of Photochemistry and Photobiology B: Biology*, *182*, 18–26. https://doi.org/10.1016/j.jphotobiol.2018.03.016

Khalil, A. T., Ovais, M., Ullah, I., Ali, M., Shinwari, Z. K., & Maaza, M. (2020). Physical properties, biological applications and biocompatibility studies on biosynthesized single phase cobalt oxide (Co3O4) nanoparticles via Sageretia thea (Osbeck.). *Arabian Journal of Chemistry*, *13*(1), 606–619. https://doi.org/10.1016/j.arabjc.2017.07.004

Khan, S. A., Shahid, S., Ayaz, A., Alkahtani, J., Elshikh, M. S., & Riaz, T. (2021). Phytomolecules-coated NiO nanoparticles synthesis using abutilon indicum leaf extract: Antioxidant, antibacterial, and anticancer activities. *International Journal of Nanomedicine*, *16*, 1757–1773. https://doi.org/10.2147/IJN.S294012

Khan, S., Ansari, A. A., Khan, A. A., Ahmad, R., Al-Obaid, O., & Al-Kattan, W. (2015). In vitro evaluation of anticancer and antibacterial activities of cobalt oxide nanoparticles. *Journal of Biological Inorganic Chemistry*, *20*(8), 1319–1326. https://doi.org/10.1007/s00775-015-1310-2

Khan, S. U., Saleh, T. A., Wahab, A., Khan, M. H. U., Khan, D., Khan, W. U., Rahim, A., Kamal, S., Khan, F. U., & Fahad, S. (2018). Nanosilver: New ageless and versatile biomedical therapeutic scaffold. *International Journal of Nanomedicine*, *13*(February), 733–762. https://doi.org/10.2147/IJN.S153167

Khandel, P., Yadaw, R. K., Soni, D. K., Kanwar, L., & Shahi, S. K. (2018). Biogenesis of metal nanoparticles and their pharmacological applications: present status and application prospects. In *Journal of Nanostructure in Chemistry* (Vol. 8, Issue 3). Springer Berlin Heidelberg. https://doi.org/10.1007/s40097-018-0267-4

Khatami, M., Alijani, H. Q., Nejad, M. S., & Varma, R. S. (2018). Core@shell nanoparticles: Greener synthesis using natural plant products. *Applied Sciences (Switzerland)*, *8*(3), 1–17. https://doi.org/10.3390/app8030411

Kiani, M., Rabiee, N., Bagherzadeh, M., Ghadiri, A. M., Fatahi, Y., Dinarvand, R., & Webster, T. J. (2021). Improved green biosynthesis of chitosan decorated Ag- and Co3O4-nanoparticles: A relationship between surface morphology, photocatalytic and biomedical applications. *Nanomedicine: Nanotechnology, Biology, and Medicine*, *32*, 102331. https://doi.org/10.1016/j.nano.2020.102331

Kim, D. W., Thawng, C. N., Lee, K., Wellington, E. M. H., & Cha, C. J. (2019). A novel sulfonamide resistance mechanism by two-component flavin-dependent monooxygenase system in sulfonamide-degrading actinobacteria. *Environment International*, *127*(January), 206–215. https://doi.org/10.1016/j.envint.2019.03.046

Kirubha, E., & Palanisamy, P. K. (2014). Green synthesis, characterization of Au-Ag core-shell nanoparticles using gripe water and their applications in nonlinear optics and surface enhanced Raman studies. *Advances in Natural Sciences: Nanoscience and Nanotechnology*, *5*(4). https://doi.org/10.1088/2043-6262/5/4/045006

Kishore, M., Rao, M. V., Rao, Y. H., Venkateswara Rao, M., Hanumantha Rao, Y., & Kishore, M. (2016). Green nanoparticles synthesized from roots of Datura metel and evaluation of anti microbial activity. *Journal of Pharmacy Research*, *10*(10), 730–734.

Kolodziejczak-Radzimska, A., & Jesionowski, T. (2014). Zinc oxide-from synthesis to application: A review. *Materials*, *7*(4), 2833–2881. https://doi.org/10.3390/ma7042833

Kouhbanani, M. A. J., Sadeghipour, Y., Sarani, M., Sefidgar, E., Ilkhani, S., Amani, A. M., & Beheshtkhoo, N. (2021). The inhibitory role of synthesized Nickel oxide nanoparticles against Hep-G2, MCF-7, and HT-29 cell lines: the inhibitory role of NiO NPs against Hep-G2, MCF-7, and HT-29 cell lines. *Green Chemistry Letters and Reviews*, *14*(3), 443–453. https://doi.org/10.1080/17518253.2021.1939435

Kovács, D., Igaz, N., Marton, A., Rónavári, A., Bélteky, P., Bodai, L., Spengler, G., Tiszlavicz, L., Rázga, Z., Hegyi, P., Vizler, C., Boros, I. M., Kónya, Z., & Kiricsi, M. (2020). Core-shell nanoparticles suppress metastasis and modify the tumour-supportive activity of cancer-associated fibroblasts. *Journal of Nanobiotechnology*, *18*(1), 1–20. https://doi.org/10.1186/s12951-020-0576-x

Kumar, H., Bhardwaj, K., Kuča, K., Kalia, A., Nepovimova, E., Verma, R., & Kumar, D. (2020). Flower-based green synthesis of metallic nanoparticles: Applications beyond fragrance. *Nanomaterials*, *10*(4). https://doi.org/10.3390/nano10040766

Lagashetty, A., Ganiger, S. K., R. K., P., Reddy, S., & Pari, M. (2020). Microwave-assisted green synthesis, characterization and adsorption studies on metal oxide nanoparticles synthesized using: Ficus Benghalensis plant leaf extracts. *New Journal of Chemistry*, *44*(33), 14095–14102. https://doi.org/10.1039/d0nj01759k

Lan, J., Gou, N., Gao, C., He, M., & Gu, A. Z. (2014). Comparative and mechanistic

genotoxicity assessment of nanomaterials via a quantitative toxicogenomics approach across multiple species. *Environmental Science and Technology*, *48*(21), 12937–12945. https://doi.org/10.1021/es503065q

Lee, K. X., Shameli, K., Nagao, Y., Yew, Y. P., Teow, S. Y., & Moeini, H. (2022). Potential use of gold-silver core-shell nanoparticles derived from Garcinia mangostana peel for anticancer compound, protocatechuic acid delivery. *Frontiers in Molecular Biosciences*, *9*(October), 1–15. https://doi.org/10.3389/fmolb.2022.997471

Li, G., & Tang, Z. (2014). Noble metal nanoparticle@metal oxide core/yolk-shell nanostructures as catalysts: Recent progress and perspective. *Nanoscale*, *6*(8), 3995–4011. https://doi.org/10.1039/c3nr06787d

Li, X., Du, X., Ma, X., Wang, Z., Hao, X., Abudula, A., Yoshida, A., & Guan, G. (2017). CuO nanowire@Co3O4 ultrathin nanosheet core-shell arrays: An effective catalyst for oxygen evolution reaction. *Electrochimica Acta*, *250*, 77–83. https://doi.org/10.1016/j.electacta.2017.08.063

Liang, J., Wu, M., Chen, C., Mai, M., Huang, J., Zhu, P., & Agnetti, G. (2020). Roles of Reactive Oxygen Species in Cardiac Differentiation, Reprogramming, and Regenerative Therapies. *Oxidative Medicine and Cellular Longevity*, *2020*. https://doi.org/10.1155/2020/2102841

Lizundia, E., Armentano, I., Luzi, F., Bertoglio, F., Restivo, E., Visai, L., Torre, L., & Puglia, D. (2020). Synergic Effect of Nanolignin and Metal Oxide Nanoparticles into Poly(l-lactide) Bionanocomposites: Material Properties, Antioxidant Activity, and Antibacterial Performance. *ACS Applied Bio Materials*, *3*(8), 5263–5274. https://doi.org/10.1021/acsabm.0c00637

Lushchikova, O. V., Szalay, M., Tahmasbi, H., Juurlink, L. B. F., Meyer, J., Höltzl, T., & Bakker, J. M. (2021). IR spectroscopic characterization of the co-adsorption of CO2and H2onto cationic Cu: N+clusters. *Physical Chemistry Chemical Physics*, *23*(47), 26661–26673. https://doi.org/10.1039/d1cp03119h

Mahalakshmi, S., Hema, N., & Vijaya, P. P. (2020). In Vitro Biocompatibility and Antimicrobial activities of Zinc Oxide Nanoparticles (ZnO NPs) Prepared by Chemical and Green Synthetic Route— A Comparative Study. *BioNanoScience*, *10*(1), 112–121. https://doi.org/10.1007/s12668-019-00698-w

Mahendra, C., Chandra, M. N., Murali, M., Abhilash, M. R., Singh, S. B., Satish, S., & Sudarshana, M. S. (2020). Phyto-fabricated ZnO nanoparticles from Canthium dicoccum (L.) for antimicrobial, anti-tuberculosis and antioxidant activity. *Process Biochemistry*, *89*, 220–226. https://doi.org/10.1016/j.procbio.2019.10.020

Maheswari, P., Ponnusamy, S., Harish, S., Ganesh, M. R., & Hayakawa, Y. (2020). Hydrothermal synthesis of pure and bio modified TiO2: Characterization, evaluation of antibacterial activity against gram positive and gram negative bacteria and anticancer activity against KB Oral cancer cell line. *Arabian Journal of Chemistry*, *13*(1), 3484–3497. https://doi.org/10.1016/j.arabjc.2018.11.020

Mallikarjunaswamy, C., Lakshmi Ranganatha, V., Ramu, R., Udayabhanu, & Nagaraju, G. (2020). Facile microwave-assisted green synthesis of ZnO nanoparticles: application to photodegradation, antibacterial and antioxidant. *Journal of Materials Science: Materials in Electronics*, *31*(2), 1004–1021. https://doi.org/10.1007/s10854-019-02612-2

Manikandan, V., Velmurugan, P., Park, J. H., Chang, W. S., Park, Y. J., Jayanthi, P., Cho, M., & Oh, B. T. (2017). Green synthesis of silver oxide nanoparticles and its antibacterial activity against dental pathogens. *3 Biotech*, *7*(1). https://doi.org/10.1007/s13205-017-0670-4

Mansournia, M., & Ghaderi, L. (2017). CuO@ZnO core-shell nanocomposites: Novel hydrothermal synthesis and enhancement in photocatalytic property. *Journal of Alloys and Compounds*, *691*, 171–177. https://doi.org/10.1016/j.jallcom.2016.08.267

Marslin, G., Siram, K., Maqbool, Q., Selvakesavan, R. K., Kruszka, D., Kachlicki, P., & Franklin, G. (2018). Secondary metabolites in the green synthesis of metallic nanoparticles. *Materials*, *11*(6), 1–25. https://doi.org/10.3390/ma11060940

Mendes, C. R., Dilarri, G., Forsan, C. F., Moraes, V. De, Sapata, R., Renato, P., Lopes, M.,

Moraes, P. B. De, Montagnolli, R. N., Ferreira, H., & Bidoia, E. D. (2022). Antibacterial action and target mechanisms of zinc oxide nanoparticles against bacterial pathogens. *Scientific Reports*, 1–10. https://doi.org/10.1038/s41598-022-06657-y

Mittal, A. K., Chisti, Y., & Banerjee, U. C. (2013). Synthesis of metallic nanoparticles using plant extracts. *Biotechnology Advances*, *31*(2), 346–356. https://doi.org/10.1016/j.biotechadv.2013.01.003

Moavi, J., Buazar, F., & Sayahi, M. H. (2021). Algal magnetic nickel oxide nanocatalyst in accelerated synthesis of pyridopyrimidine derivatives. *Scientific Reports*, *11*(1), 1–14. https://doi.org/10.1038/s41598-021-85832-z

Mohd Yusof, H., Mohamad, R., Zaidan, U. H., & Abdul Rahman, N. A. (2019). Microbial synthesis of zinc oxide nanoparticles and their potential application as an antimicrobial agent and a feed supplement in animal industry: A review. *Journal of Animal Science and Biotechnology*, *10*(1), 1–22. https://doi.org/10.1186/s40104-019-0368-z

Mousa, A. B., Moawad, R., Abdallah, Y., Abdel-Rasheed, M., & Zaher, A. M. A. (2023). Zinc Oxide Nanoparticles Promise Anticancer and Antibacterial Activity in Ovarian Cancer. *Pharmaceutical Research*, *40*(10), 2281–2290. https://doi.org/10.1007/s11095-023-03505-0

Mubarik, S., Sharma, R., Hussain, S. R., Iqbal, M., Nawsherwan, Liu, X., & Yu, C. (2022). Breast Cancer Mortality Trends and Predictions to 2030 and Its Attributable Risk Factors in East and South Asian Countries. *Frontiers in Nutrition*, *9*(March), 1–15. https://doi.org/10.3389/fnut.2022.847920

Murali, M., Kalegowda, N., Gowtham, H. G., Ansari, M. A., Alomary, M. N., Alghamdi, S., Shilpa, N., Singh, S. B., Thriveni, M. C., Aiyaz, M., Angaswamy, N., Lakshmidevi, N., Adil, S. F., Hatshan, M. R., & Amruthesh, K. N. (2021). Plant-mediated zinc oxide nanoparticles: Advances in the new millennium towards understanding their therapeutic role in biomedical applications. *Pharmaceutics*, *13*(10). https://doi.org/10.3390/pharmaceutics13101662

Murray, A. J., Rogers, J. C., Katshu, M. Z. U. H., Liddle, P. F., & Upthegrove, R. (2021).

Oxidative Stress and the Pathophysiology and Symptom Profile of Schizophrenia Spectrum Disorders. *Frontiers in Psychiatry*, *12*(July), 1–16. https://doi.org/10.3389/fpsyt.2021.703452

Nabera, C. K. (2009). Staphylococcus aureus bacteremia: Epidemiology, pathophysiology, and management strategies. *Clinical Infectious Diseases*, *48*(SUPPL. 4), 231–237. https://doi.org/10.1086/598189

Nabil, A., Elshemy, M. M., Asem, M., Abdel-Motaal, M., Gomaa, H. F., Zahran, F., Uto, K., & Ebara, M. (2020). Zinc Oxide Nanoparticle Synergizes Sorafenib Anticancer Efficacy with Minimizing Its Cytotoxicity. *Oxidative Medicine and Cellular Longevity*, *2020*. https://doi.org/10.1155/2020/1362104

Nagajothi, D. (2022). *Biosynthesis and Characterization of Co 3 O 4 NPs Utilizing Prickly Pear Fruit Extract and its Biological Activities*. *9*(4), 1117–1128.

Nagajyothi, P. C., Cha, S. J., Yang, I. J., Sreekanth, T. V. M., Kim, K. J., & Shin, H. M. (2015). Antioxidant and anti-inflammatory activities of zinc oxide nanoparticles synthesized using Polygala tenuifolia root extract. *Journal of Photochemistry and Photobiology B: Biology*, *146*, 10–17. https://doi.org/10.1016/j.jphotobiol.2015.02.008

Nagajyothi, P. C., Muthuraman, P., Sreekanth, T. V. M., Kim, D. H., & Shim, J. (2017). Green synthesis: In-vitro anticancer activity of copper oxide nanoparticles against human cervical carcinoma cells. *Arabian Journal of Chemistry*, *10*(2), 215–225. https://doi.org/10.1016/j.arabjc.2016.01.011

Nagajyothi, P. C., Pandurangan, M., Kim, D. H., Sreekanth, T. V. M., & Shim, J. (2017). Green Synthesis of Iron Oxide Nanoparticles and Their Catalytic and In Vitro Anticancer Activities. *Journal of Cluster Science*, *28*(1), 245–257. https://doi.org/10.1007/s10876-016-1082-z

Nagaraj, E., Karuppannan, K., Shanmugam, P., & Venugopal, S. (2019). Exploration of Bio-synthesized Copper Oxide Nanoparticles Using Pterolobium hexapetalum Leaf Extract by Photocatalytic Activity and Biological Evaluations. *Journal of Cluster Science*, *30*(4),

1157–1168. https://doi.org/10.1007/s10876-019-01579-8

Nalluri, S. R., Nagarjuna, R., Patra, D., Ganesan, R., & Balaji, G. (2019). Large Scale Solid-state Synthesis of Catalytically Active Fe 3 O 4 @M (M = Au, Ag and Au-Ag alloy) Core-shell Nanostructures. *Scientific Reports*, *9*(1), 1–11. https://doi.org/10.1038/s41598-019-43116-7

Naseer, M., Aslam, U., Khalid, B., & Chen, B. (2020). Green route to synthesize Zinc Oxide Nanoparticles using leaf extracts of Cassia fistula and Melia azadarach and their antibacterial potential. *Scientific Reports*, *10*(1), 1–10. https://doi.org/10.1038/s41598-020-65949-3

Nasrollahzadeh, M., Sajjadi, M., Iravani, S., & Varma, R. S. (2020). Trimetallic nanoparticles: Greener synthesis and their applications. *Nanomaterials*, *10*(9), 1–27. https://doi.org/10.3390/nano10091784

Navarro-Yepes, J., Burns, M., Anandhan, A., Khalimonchuk, O., Del Razo, L. M., Quintanilla-Vega, B., Pappa, A., Panayiotidis, M. I., & Franco, R. (2014). Oxidative stress, redox signaling, and autophagy: Cell death versus survival. *Antioxidants and Redox Signaling*, *21*(1), 66–85. https://doi.org/10.1089/ars.2014.5837

Neupane, K., Rayamajhee, B., Acharya, J., Rijal, N., Shrestha, D., G C, B., Pant, M. R., & Shah, P. K. (2018). Comparison of Nasal Colonization of Methicillin-Resistant Staphylococcus aureus in HIV-Infected and Non-HIV Patients Attending the National Public Health Laboratory of Central Nepal. *Canadian Journal of Infectious Diseases and Medical Microbiology*, *2018*. https://doi.org/10.1155/2018/4508757

Nomoev, A. V., Bardakhanov, S. P., Schreiber, M., Bazarova, D. G., Romanov, N. A., Baldanov, B. B., Radnaev, B. R., & Syzrantsev, V. V. (2015). Structure and mechanism of the formation of core-shell nanoparticles obtained through a one-step gas-phase synthesis by electron beam evaporation. *Beilstein Journal of Nanotechnology*, *6*(1), 874–880. https://doi.org/10.3762/bjnano.6.89

Nomura, K., Terwilliger, P., Saeed, M., Akram, N., Ali, S., Naqvi, R., Usman, M., & Abbas, M. A. (2019). *Self-dual Leonard pairs Green and eco-friendly synthesis of Co a O*. 382–390.

Nzilu, D. M., Madivoli, E. S., Makhanu, D. S., Wanakai, S. I., Kiprono, G. K., & Kareru, P. G. (2023). Green synthesis of copper oxide nanoparticles and its efficiency in degradation of rifampicin antibiotic. *Scientific Reports*, *13*(1), 1–18. https://doi.org/10.1038/s41598-023-41119-z

Ogunyemi, S. O., Abdallah, Y., Zhang, M., Fouad, H., Hong, X., Ibrahim, E., Masum, M. M. I., Hossain, A., Mo, J., & Li, B. (2019). Green synthesis of zinc oxide nanoparticles using different plant extracts and their antibacterial activity against Xanthomonas oryzae pv. oryzae. *Artificial Cells, Nanomedicine and Biotechnology*, *47*(1), 341–352. https://doi.org/10.1080/21691401.2018.1557671

Olajire, A. A., & Mohammed, A. A. (2020). Green synthesis of nickel oxide nanoparticles and studies of their photocatalytic activity in degradation of polyethylene films. *Advanced Powder Technology*, *31*(1), 211–218. https://doi.org/10.1016/j.apt.2019.10.012

Omran, B. A., Nassar, H. N., Younis, S. A., El-Salamony, R. A., Fatthallah, N. A., Hamdy, A., El-Shatoury, E. H., & El-Gendy, N. S. (2020). Novel mycosynthesis of cobalt oxide nanoparticles using Aspergillus brasiliensis ATCC 16404—optimization, characterization and antimicrobial activity. *Journal of Applied Microbiology*, *128*(2), 438–457. https://doi.org/10.1111/jam.14498

Ong, H. R., Rahman Khan, M. M., Ramli, R., & Yunus, R. M. (2015). Effect of CuO Nanoparticle on Mechanical and Thermal Properties of Palm Oil Based Alkyd/Epoxy Resin Blend. *Procedia Chemistry*, *16*, 623–631. https://doi.org/10.1016/j.proche.2015.12.101

Pal, S., Mondal, S., Maity, J., & Mukherjee, R. (2018). Green Synthesis of silver nanoparticles using Moringa Oleifera leaf extract: Investigation of Photocatalytic activity. *Journal of Nanoscience Nanoengineering and Applications*, *8*(2), 60–68.

Pathak, B., Choudhury, J. P. R., Kalita, P. K., & Aomoa, N. (2019). Optical properties of PbO/ZnO core/shell dispersed in PVP matrix. *Materials Today: Proceedings*, *46*(xxxx), 6196–6200. https://doi.org/10.1016/j.matpr.2020.04.158

Paul, D., Mangla, S., & Neogi, S. (2020). Antibacterial study of CuO-NiO-ZnO trimetallic oxide

nanoparticle. *Materials Letters*, *271*, 127740. https://doi.org/10.1016/j.matlet.2020.127740

Perumal, P., Sathakkathulla, N. A., Kumaran, K., Ravikumar, R., Selvaraj, J. J., Nagendran, V., Gurusamy, M., Shaik, N., Gnanavadivel Prabhakaran, S., Suruli Palanichamy, V., Ganesan, V., Thiraviam, P. P., Gunalan, S., & Rathinasamy, S. (2024). Green synthesis of zinc oxide nanoparticles using aqueous extract of shilajit and their anticancer activity against HeLa cells. *Scientific Reports*, *14*(1), 1–11. https://doi.org/10.1038/s41598-024-52217-x

Peterson, E., & Kaur, P. (2018). Antibiotic resistance mechanisms in bacteria: Relationships between resistance determinants of antibiotic producers, environmental bacteria, and clinical pathogens. *Frontiers in Microbiology*, *9*(NOV), 1–21. https://doi.org/10.3389/fmicb.2018.02928

Pizzino, G., Irrera, N., Cucinotta, M., Pallio, G., Mannino, F., Arcoraci, V., Squadrito, F., Altavilla, D., & Bitto, A. (2017). Oxidative Stress: Harms and Benefits for Human Health. *Oxidative Medicine and Cellular Longevity*, *2017*. https://doi.org/10.1155/2017/8416763

Pleńkowska, J., Gabig-Cimińska, M., & Mozolewski, P. (2020). Oxidative stress as an important contributor to the pathogenesis of psoriasis. *International Journal of Molecular Sciences*, *21*(17), 1–15. https://doi.org/10.3390/ijms21176206

Poller, J. M., Zaloga, J., Schreiber, E., Unterweger, H., Janko, C., Radon, P., Eberbeck, D., Trahms, L., Alexiou, C., & Friedrich, R. P. (2017). Selection of potential iron oxide nanoparticles for breast cancer treatment based on in vitro cytotoxicity and cellular uptake. *International Journal of Nanomedicine*, *12*, 3207–3220. https://doi.org/10.2147/IJN.S132369

Pugazhendhi, A., Prabhu, R., Muruganantham, K., Shanmuganathan, R., & Natarajan, S. (2019). Anticancer, antimicrobial and photocatalytic activities of green synthesized magnesium oxide nanoparticles (MgONPs) using aqueous extract of Sargassum wightii. *Journal of Photochemistry and Photobiology B: Biology*, *190*(May), 86–97. https://doi.org/10.1016/j.jphotobiol.2018.11.014

Punnoose, A., Dodge, K., Rasmussen, J. W., Chess, J., Wingett, D., & Anders, C. (2014).

Cytotoxicity of ZnO Nanoparticles Can Be Tailored by Modifying Their Surface Structure: A Green Chemistry Approach for Safer Nanomaterials. https://doi.org/10.1021/sc500140x

Rabiei, M. M., Asadi, K., Shokouhi, S., Nasiri, M. J., & Alavi Darazam, I. (2020). Antipseudomonal β-Lactams Resistance in Iran. *International Journal of Microbiology*, *2020*. https://doi.org/10.1155/2020/8818315

Raeisi, M., Alijani, H. Q., Peydayesh, M., Khatami, M., Bagheri Baravati, F., Borhani, F., Šlouf, M., & Soltaninezhad, S. (2021). Magnetic cobalt oxide nanosheets: green synthesis and in vitro cytotoxicity. *Bioprocess and Biosystems Engineering*, *44*(7), 1423–1432. https://doi.org/10.1007/s00449-021-02518-6

Rahman, F., Majed Patwary, M. A., Bakar Siddique, M. A., Bashar, M. S., Haque, M. A., Akter, B., Rashid, R., Haque, M. A., & Royhan Uddin, A. K. M. (2022). Green synthesis of zinc oxide nanoparticles using Cocos nucifera leaf extract: characterization, antimicrobial, antioxidant and photocatalytic activity. *Royal Society Open Science*, *9*(11). https://doi.org/10.1098/rsos.220858

Rahmoune, B., Zerrouk, I. Z., Morsli, A., Slaoui, M. K., Khelifi, L., & Do Amarante, L. (2017). Phenylpropanoids and Fatty Acids Levels in Roots and Leaves of Datura Stramonium and Datura Innoxia. *International Journal of Pharmacy and Pharmaceutical Sciences*, *9*(7), 150. https://doi.org/10.22159/ijpps.2017v9i7.15946

Raj Preeth, D., Shairam, M., Suganya, N., Hootan, R., Kartik, R., Pierre, K., Suvro, C., & Rajalakshmi, S. (2019). Green synthesis of copper oxide nanoparticles using sinapic acid: an underpinning step towards antiangiogenic therapy for breast cancer. *Journal of Biological Inorganic Chemistry*, *24*(5), 633–645. https://doi.org/10.1007/s00775-019-01676-z

Rajeshkumar, S., Menon, S., Venkat Kumar, S., Tambuwala, M. M., Bakshi, H. A., Mehta, M., Satija, S., Gupta, G., Chellappan, D. K., Thangavelu, L., & Dua, K. (2019). Antibacterial and antioxidant potential of biosynthesized copper nanoparticles mediated through Cissus arnotiana plant extract. *Journal of Photochemistry and Photobiology B: Biology*, *197*, 111531. https://doi.org/10.1016/j.jphotobiol.2019.111531

Rajith Kumar, C. R., Betageri, V. S., Nagaraju, G., Pujar, G. H., Onkarappa, H. S., & Latha, M. S. (2020). Synthesis of Core/Shell (ZnO/Ag) Nanoparticles Using Calotropis gigantea and Their Applications in Photocatalytic and Antibacterial Studies. *Journal of Inorganic and Organometallic Polymers and Materials*, *30*(9), 3410–3417. https://doi.org/10.1007/s10904-020-01507-8

Rakgalakane, B. P., & Moloto, M. J. (2011). Aqueous synthesis and characterization of CdSe/ZnO core-shell nanoparticles. *Journal of Nanomaterials*, *2011*. https://doi.org/10.1155/2011/514205

Ramalingam, V., Harshavardhan, M., Dinesh Kumar, S., & Malathi devi, S. (2020). Wet chemical mediated hematite α-Fe2O3 nanoparticles synthesis: Preparation, characterization and anticancer activity against human metastatic ovarian cancer. *Journal of Alloys and Compounds*, *834*, 155118. https://doi.org/10.1016/j.jallcom.2020.155118

Ramesh, A. M., Pal, K., Kodandaram, A., Manjula, B. L., Ravishankar, D. K., Gowtham, H. G., Murali, M., Rahdar, A., & Kyzas, G. Z. (2022). Antioxidant and photocatalytic properties of zinc oxide nanoparticles phyto-fabricated using the aqueous leaf extract of Sida acuta. *Green Processing and Synthesis*, *11*(1), 857–867. https://doi.org/10.1515/gps-2022-0075

Rao, P. V., Nallappan, D., Madhavi, K., Rahman, S., Jun Wei, L., & Gan, S. H. (2016). Phytochemicals and Biogenic Metallic Nanoparticles as Anticancer Agents. *Oxidative Medicine and Cellular Longevity*, *2016*. https://doi.org/10.1155/2016/3685671

Ravi Dhas, C., Venkatesh, R., Jothivenkatachalam, K., Nithya, A., Suji Benjamin, B., Moses Ezhil Raj, A., Jeyadheepan, K., & Sanjeeviraja, C. (2015). Visible light driven photocatalytic degradation of Rhodamine B and Direct Red using cobalt oxide nanoparticles. *Ceramics International*, *41*(8), 9301–9313. https://doi.org/10.1016/j.ceramint.2015.03.238

Rehana, D., Mahendiran, D., Kumar, R. S., & Rahiman, A. K. (2017). Evaluation of antioxidant and anticancer activity of copper oxide nanoparticles synthesized using medicinally important plant extracts. *Biomedicine and Pharmacotherapy*, *89*, 1067–1077. https://doi.org/10.1016/j.biopha.2017.02.101

Reta, A., Bitew Kifilie, A., & Mengist, A. (2019). Bacterial Infections and Their Antibiotic Resistance Pattern in Ethiopia: A Systematic Review. *Advances in Preventive Medicine*, *2019*(Cdc), 1–10. https://doi.org/10.1155/2019/4380309

Rezk, N., Abdelsattar, A. S., Makky, S., Hussein, A. H., Kamel, A. G., & El-Shibiny, A. (2022). New formula of the green synthesised Au@Ag core@shell nanoparticles using propolis extract presented high antibacterial and anticancer activity. *AMB Express*, *12*(1). https://doi.org/10.1186/s13568-022-01450-6

Robertson, A. D., Paustian, K., Ogle, S., Wallenstein, M. D., Lugato, E., & Cotrufo, M. F. (2019). *Unifying soil organic matter formation and persistence frameworks : the MEMS model*. 1225–1248.

Rocchetti, L., Amato, A., & Beolchini, F. (2016). Recovery of indium from liquid crystal displays. *Journal of Cleaner Production*, *116*(May 2019), 299–305. https://doi.org/10.1016/j.jclepro.2015.12.080

Ruiz-Garcia, H., Alvarado-Estrada, K., Krishnan, S., Quinones-Hinojosa, A., & Trifiletti, D. M. (2020). Nanoparticles for Stem Cell Therapy Bioengineering in Glioma. *Frontiers in Bioengineering and Biotechnology*, *8*(December). https://doi.org/10.3389/fbioe.2020.558375

Sabouri, Z., Akbari, A., Hosseini, H. A., Khatami, M., & Darroudi, M. (2021). Green-based bio-synthesis of nickel oxide nanoparticles in Arabic gum and examination of their cytotoxicity, photocatalytic and antibacterial effects. *Green Chemistry Letters and Reviews*, *14*(2), 402–412. https://doi.org/10.1080/17518253.2021.1923824

Sadollahkhani, A., Kazeminezhad, I., Lu, J., Nur, O., Hultman, L., & Willander, M. (2014). Synthesis, structural characterization and photocatalytic application of ZnO@ZnS core-shell nanoparticles. *RSC Advances*, *4*(70), 36940–36950. https://doi.org/10.1039/c4ra05247a

Safawo, T., Sandeep, B. V., Pola, S., & Tadesse, A. (2018). Synthesis and characterization of zinc oxide nanoparticles using tuber extract of anchote (Coccinia abyssinica (Lam.) Cong.) for antimicrobial and antioxidant activity assessment. *OpenNano*, *3*(May), 56–63.

https://doi.org/10.1016/j.onano.2018.08.001

Safdar, A., Mohamed, H. E. A., Hkiri, K., Muhaymin, A., & Maaza, M. (2023). Green Synthesis of Cobalt Oxide Nanoparticles Using Hyphaene thebaica Fruit Extract and Their Photocatalytic Application. *Applied Sciences (Switzerland)*, *13*(16). https://doi.org/10.3390/app13169082

Saif, S., Tahir, A., Asim, T., & Chen, Y. (2016). Plant mediated green synthesis of CuO nanoparticles: Comparison of toxicity of engineered and plant mediated CuO nanoparticles towards Daphnia magna. *Nanomaterials*, *6*(11), 1–15. https://doi.org/10.3390/nano6110205

Salari, S., & Neamati, A. (2019). *Green-synthesized Zinc oxide nanoparticle , an efficient safe anticancer compound for human breast MCF7 cancer cells*. *November*, 1–8. https://doi.org/10.1002/aoc.5417

Samal, A. K., Polavarapu, L., Rodal-Cedeira, S., Liz-Marzán, L. M., Pérez-Juste, J., & Pastoriza-Santos, I. (2013). Size tunable Au@Ag core-shell nanoparticles: Synthesis and surface-enhanced raman scattering properties. *Langmuir*, *29*(48), 15076–15082. https://doi.org/10.1021/la403707j

Samy, A., El-Sherbiny, A. E., & Menazea, A. E. R. A. (2019). Green synthesis of high impact zinc oxide nanoparticles. *Egyptian Journal of Chemistry*, *62*, 29–37. https://doi.org/10.21608/EJCHEM.2019.12863.1802

Sanad, M. F., Meneses-Brassea, B. P., Blazer, D. S., Pourmiri, S., Hadjipanayis, G. C., & El-Gendy, A. A. (2021). Superparamagnetic fe/au nanoparticles and their feasibility for magnetic hyperthermia. *Applied Sciences (Switzerland)*, *11*(14). https://doi.org/10.3390/app11146637

Sánchez-López, E., Gomes, D., Esteruelas, G., Bonilla, L., Lopez-Machado, A. L., Galindo, R., Cano, A., Espina, M., Ettcheto, M., Camins, A., Silva, A. M., Durazzo, A., Santini, A., Garcia, M. L., & Souto, E. B. (2020). Metal-based nanoparticles as antimicrobial agents: An overview. *Nanomaterials*, *10*(2), 1–39. https://doi.org/10.3390/nano10020292

Sankar, R., Maheswari, R., Karthik, S., Shivashangari, K. S., & Ravikumar, V. (2014).

Anticancer activity of Ficus religiosa engineered copper oxide nanoparticles. *Materials Science and Engineering C*, *44*(February 2008), 234–239. https://doi.org/10.1016/j.msec.2014.08.030

Santhoshkumar, M., & Balupillai, A. (n.d.). *Biological Fabrication and Characterization of Zinc Oxide Nanoparticles Using Gymnema Sylvestre Potentially Produces Toxicity in Breast Cancer Cells*. 1–11.

Selim, Y. A., Azb, M. A., Ragab, I., & H. M. Abd El-Azim, M. (2020). Green Synthesis of Zinc Oxide Nanoparticles Using Aqueous Extract of Deverra tortuosa and their Cytotoxic Activities. *Scientific Reports*, *10*(1), 1–9. https://doi.org/10.1038/s41598-020-60541-1

Selvakumari, D., Deepa, R., Mahalakshmi, V., Subhashini, P., & Lakshminarayan, N. (2015). Anti cancer activity of zno nanoparticles on MCF7 (breast cancer cell) and A549 (lung cancer cell). *ARPN Journal of Engineering and Applied Sciences*, *10*(12), 5418–5421.

Shafey, A. M. El. (2020). Green synthesis of metal and metal oxide nanoparticles from plant leaf extracts and their applications: A review. *Green Processing and Synthesis*, *9*(1), 304–339. https://doi.org/10.1515/gps-2020-0031

Shaikh, J. R., & Patil, M. (2020). Qualitative tests for preliminary phytochemical screening: An overview. *International Journal of Chemical Studies*, *8*(2), 603–608. https://doi.org/10.22271/chemi.2020.v8.i2i.8834

Shalaby, E. A., Shanab, S. M. M., El-Raheem, W. M. A., & Hanafy, E. A. (2022). Biological activities and antioxidant potential of different biosynthesized nanoparticles of Moringa oleifera. *Scientific Reports*, *12*(1), 1–14. https://doi.org/10.1038/s41598-022-23164-2

Shamhari, N. M., Wee, B. S., Chin, S. F., & Kok, K. Y. (2018). Synthesis and characterization of zinc oxide nanoparticles with small particle size distribution. *Acta Chimica Slovenica*, *65*(3), 578–585. https://doi.org/10.17344/acsi.2018.4213

Shanmugasundaram, T., Radhakrishnan, M., Poongodi, A., Kadirvelu, K., & Balagurunathan, R. (2018). Bio-inspired synthesis of superparamagnetic iron oxide nanoparticles for enhanced in vitro anticancer therapy. *MRS Communications*, *8*(2), 604–609.

https://doi.org/10.1557/mrc.2018.36

Sharifi, M., Sharifi, M., Jafari, S., Hasan, A., Hasan, A., Paray, B. A., Gong, G., Zheng, Y., & Falahati, M. (2020). Antimetastatic Activity of Lactoferrin-Coated Mesoporous Maghemite Nanoparticles in Breast Cancer Enabled by Combination Therapy. *ACS Biomaterials Science and Engineering*, *6*(6), 3574–3584. https://doi.org/10.1021/acsbiomaterials.0c00086

Sharma, B., Sonam, M., & Sarma, T. K. (2013). Biogenic growth of alloys and core-shell nanostructures using urease as a nanoreactor at ambient conditions. *Scientific Reports*, *3*, 1–8. https://doi.org/10.1038/srep02601

Sharma, G., Kumar, A., Sharma, S., Naushad, M., Prakash Dwivedi, R., ALOthman, Z. A., & Mola, G. T. (2019). Novel development of nanoparticles to bimetallic nanoparticles and their composites: A review. *Journal of King Saud University - Science*, *31*(2), 257–269. https://doi.org/10.1016/j.jksus.2017.06.012

Sharma, J. K., Akhtar, M. S., Ameen, S., Srivastava, P., & Singh, G. (2015). Green synthesis of CuO nanoparticles with leaf extract of Calotropis gigantea and its dye-sensitized solar cells applications. *Journal of Alloys and Compounds*, *632*, 321–325. https://doi.org/10.1016/j.jallcom.2015.01.172

Sharmila, G., Muthukumaran, C., Sandiya, K., Santhiya, S., Pradeep, R. S., Kumar, N. M., Suriyanarayanan, N., & Thirumarimurugan, M. (2018). Biosynthesis, characterization, and antibacterial activity of zinc oxide nanoparticles derived from Bauhinia tomentosa leaf extract. *Journal of Nanostructure in Chemistry*, *8*(3), 293–299. https://doi.org/10.1007/s40097-018-0271-8

Sharmila, G., Sakthi Pradeep, R., Sandiya, K., Santhiya, S., Muthukumaran, C., Jeyanthi, J., Manoj Kumar, N., & Thirumarimurugan, M. (2018). Biogenic synthesis of CuO nanoparticles using Bauhinia tomentosa leaves extract: Characterization and its antibacterial application. *Journal of Molecular Structure*, *1165*, 288–292. https://doi.org/10.1016/j.molstruc.2018.04.011

Sharmila, G., Thirumarimurugan, M., & Sivakumar, V. M. (2016). Optical, catalytic and antibacterial properties of phytofabricated CuO nanoparticles using Tecoma castanifolia leaf extract. *Optik*, *127*(19), 7822–7828. https://doi.org/10.1016/j.ijleo.2016.05.142

Shivappa, P., Gangaiah, V., & Siddaramanna, A. (2018). Materials Science in Semiconductor Processing Mesoporous CeO 2 nanoparticles modi fi ed Glassy carbon electrode for individual and simultaneous determination of Cu (II) and Hg (II): Application to environmental samples. *Materials Science in Semiconductor Processing*, *84*(January), 157–166. https://doi.org/10.1016/j.mssp.2018.05.010

Shobhaa, N., Nandab, N., & Nagabhushana, B. M. (2017). Nano ZnO and its Perspective in Anti-Cancer Activities. *Mapana - Journal of Sciences*, *16*(2), 41–52. https://doi.org/10.12723/mjs.41.5

Siegel, R. L., Miller, K. D., Fuchs, H. E., & Jemal, A. (2022). Cancer statistics, 2022. *CA: A Cancer Journal for Clinicians*, *72*(1), 7–33. https://doi.org/10.3322/caac.21708

Singh, A., Singh, N. B., Hussain, I., & Singh, H. (2017). Effect of biologically synthesized copper oxide nanoparticles on metabolism and antioxidant activity to the crop plants Solanum lycopersicum and Brassica oleracea var. botrytis. *Journal of Biotechnology*, *262*, 11–27. https://doi.org/10.1016/j.jbiotec.2017.09.016

Singh, H., Desimone, M. F., Pandya, S., Jasani, S., George, N., Adnan, M., Aldarhami, A., Bazaid, A. S., & Alderhami, S. A. (2023). *Revisiting the Green Synthesis of Nanoparticles : Uncovering Influences of Plant Extracts as Reducing Agents for Enhanced Synthesis Efficiency and Its Biomedical Applications*. *August*, 4727–4750.

Sirelkhatim, A., Mahmud, S., Seeni, A., Kaus, N. H. M., Ann, L. C., Bakhori, S. K. M., Hasan, H., & Mohamad, D. (2015). Review on zinc oxide nanoparticles: Antibacterial activity and toxicity mechanism. *Nano-Micro Letters*, *7*(3), 219–242. https://doi.org/10.1007/s40820-015-0040-x

Sivaraj, R., Rahman, P. K. S. M., Rajiv, P., Salam, H. A., & Venckatesh, R. (2014). Biogenic copper oxide nanoparticles synthesis using Tabernaemontana divaricate leaf extract and its

antibacterial activity against urinary tract pathogen. *Spectrochimica Acta - Part A: Molecular and Biomolecular Spectroscopy*, *133*, 178–181. https://doi.org/10.1016/j.saa.2014.05.048

Slavin, Y. N., Asnis, J., Häfeli, U. O., & Bach, H. (2017). Metal nanoparticles: Understanding the mechanisms behind antibacterial activity. *Journal of Nanobiotechnology*, *15*(1), 1–20. https://doi.org/10.1186/s12951-017-0308-z

Slavin, Y. N., & Bach, H. (2022). Mechanisms of Antifungal Properties of Metal Nanoparticles. *Nanomaterials*, *12*(24). https://doi.org/10.3390/nano12244470

Snezhkina, A. V., Kudryavtseva, A. V., Kardymon, O. L., Savvateeva, M. V., Melnikova, N. V., Krasnov, G. S., & Dmitriev, A. A. (2020). ROS generation and antioxidant defense systems in normal and malignant cells. *Oxidative Medicine and Cellular Longevity*, *2019*. https://doi.org/10.1155/2019/6175804

Soni, P., Siddiqui, A. A., Dwivedi, J., & Soni, V. (2012). Pharmacological properties of Datura stramonium L. as a potential medicinal tree: An overview. *Asian Pacific Journal of Tropical Biomedicine*, *2*(12), 1002–1008. https://doi.org/10.1016/S2221-1691(13)60014-3

Sorbiun, M., Shayegan Mehr, E., Ramazani, A., & Mashhadi Malekzadeh, A. (2018). Biosynthesis of metallic nanoparticles using plant extracts and evaluation of their antibacterial properties ARTICLE INFO. *Nanochem Res*, *3*(1), 1–16. https://doi.org/10.22036/ncr.2018.01.001

Stephen, A., & Seethalakshmi, S. (2013). Phytochemical Synthesis and Preliminary Characterization of Silver Nanoparticles Using Hesperidin. *Journal of Nanoscience*, *2013*, 1–6. https://doi.org/10.1155/2013/126564

Sugihartono, I., Retnoningtyas, A., Rustana, C., Umiatin, Yudasari, N., Isnaeni, Imawan, C., & Kurniadewi, F. (2019). The influence of calcination temperature on optical properties of ZnO nanoparticles. *AIP Conference Proceedings*, *2169*(November 2019). https://doi.org/10.1063/1.5132688

Sun, Y. S., Zhao, Z., Yang, Z. N., Xu, F., Lu, H. J., Zhu, Z. Y., Shi, W., Jiang, J., Yao, P. P., &

Zhu, H. P. (2017). Risk factors and preventions of breast cancer. *International Journal of Biological Sciences*, *13*(11), 1387–1397. https://doi.org/10.7150/ijbs.21635

Sundram, S., Baskar, S., & Subramanian, A. (2022). Green synthesized nickel doped cobalt ferrite nanoparticles exhibit antibacterial activity and induce reactive oxygen species mediated apoptosis in MCF-7 breast cancer cells through inhibition of PI3K/Akt/mTOR pathway. *Environmental Toxicology*, *37*(12), 2877–2888. https://doi.org/10.1002/tox.23644

Sundrarajan, M., Ambika, S., & Bharathi, K. (2015). Plant-extract mediated synthesis of ZnO nanoparticles using Pongamia pinnata and their activity against pathogenic bacteria. *Advanced Powder Technology*, *26*(5), 1294–1299. https://doi.org/10.1016/j.apt.2015.07.001

Sushma, N. J., Mahitha, B., Mallikarjuna, K., & Raju, B. D. P. (2016). Bio-inspired ZnO nanoparticles from Ocimum tenuiflorum and their in vitro antioxidant activity. *Applied Physics A: Materials Science and Processing*, *122*(5), 1–10. https://doi.org/10.1007/s00339-016-0069-9

Ta, T. T., Doan, T. N., Pham, D. C., & Tran, H. N. (2022). Factors affecting the professional skepticism of independent auditors in Viet Nam. *Cogent Business and Management*, *9*(1). https://doi.org/10.1080/23311975.2022.2059043

Tagde, P., Najda, A., Nagpal, K., Kulkarni, G. T., Shah, M., Ullah, O., Balant, S., & Rahman, M. H. (2022). Nanomedicine-Based Delivery Strategies for Breast Cancer Treatment and Management. *International Journal of Molecular Sciences*, *23*(5). https://doi.org/10.3390/ijms23052856

Tahir, M., Pan, L., Zhang, R., Wang, Y. C., Shen, G., Aslam, I., Qadeer, M. A., Mahmood, N., Xu, W., Wang, L., Zhang, X., & Zou, J. J. (2017). High-Valence-State NiO/Co3O4 Nanoparticles on Nitrogen-Doped Carbon for Oxygen Evolution at Low Overpotential. *ACS Energy Letters*, *2*(9), 2177–2182. https://doi.org/10.1021/acsenergylett.7b00691

Tamanis, E., Sledevskis, E., Ogurcovs, A., Gerbreders, V., & Paskevics, V. (2015). Synthesis of Core/Shell CuO-Zno Nanoparticles and Their Second-Harmonic Generation Performance. *Latvian Journal of Physics and Technical Sciences*, *52*(5), 41–46.

https://doi.org/10.1515/lpts-2015-0027

Tang, X., Loc, W. S., Dong, C., Matters, G. L., Butler, P. J., Kester, M., Meyers, C., Jiang, Y., & Adair, J. H. (2017). The use of nanoparticulates to treat breast cancer. *Nanomedicine*, *12*(19), 2367–2388. https://doi.org/10.2217/nnm-2017-0202

Tanwar, J., Das, S., Fatima, Z., & Hameed, S. (2014). Multidrug resistance: An emerging crisis. *Interdisciplinary Perspectives on Infectious Diseases*, *2014*. https://doi.org/10.1155/2014/541340

Tao, L., Chen, X., Sun, J., & Wu, C. (2021). *Silver nanoparticles achieve cytotoxicity against breast cancer by regulating long-chain noncoding RNA XLOC _ 006390-mediated pathway*. *January*, 123–133. https://doi.org/10.1093/toxres/tfaa090

Tavassolifar, M. J., Vodjgani, M., Salehi, Z., & Izad, M. (2020). The Influence of Reactive Oxygen Species in the Immune System and Pathogenesis of Multiple Sclerosis. *Autoimmune Diseases*, *2020*. https://doi.org/10.1155/2020/5793817

Teshome, A., Alemayehu, T., Deriba, W., & Ayele, Y. (2020). Antibiotic Resistance Profile of Bacteria Isolated from Wastewater Systems in Eastern Ethiopia. *Journal of Environmental and Public Health*, *2020*. https://doi.org/10.1155/2020/2796365

Thatyana, M., Dube, N. P., Kemboi, D., Manicum, A. E., Mokgalaka-fleischmann, N. S., & Tembu, J. V. (2023). *Advances in Phytonanotechnology : A Plant-Mediated Green Synthesis of Metal Nanoparticles Using Phyllanthus Plant Extracts and Their Antimicrobial and Anticancer Applications*.

Tilahun, E., Yilkal, B., Sintayehu, D., Murthy, H. C. A., & Shegaw, M. (2022). Synthesis of ZnO nanoparticles mediated by natural products of Acanthus sennii leaf extract for electrochemical sensing and photocatalytic applications : a comparative study of volume ratios. *Chemical Papers*, *76*(9), 5967–5983. https://doi.org/10.1007/s11696-022-02301-1

Tong, S. Y. C., Davis, J. S., Eichenberger, E., Holland, T. L., & Fowler, V. G. (2015). Staphylococcus aureus infections: Epidemiology, pathophysiology, clinical manifestations, and management. *Clinical Microbiology Reviews*, *28*(3), 603–661.

https://doi.org/10.1128/CMR.00134-14

Torres-Román, J. S., Ybaseta-Medina, J., Loli-Guevara, S., Bazalar-Palacios, J., Valcarcel, B., Arce-Huamani, M. A., Alvarez, C. S., & Hurtado-Roca, Y. (2023). Disparities in breast cancer mortality among Latin American women: trends and predictions for 2030. *BMC Public Health*, *23*(1), 1–9. https://doi.org/10.1186/s12889-023-16328-w

Turakhia, B., Divakara, M. B., Santosh, M. S., & Shah, S. (2020). Green synthesis of copper oxide nanoparticles: a promising approach in the development of antibacterial textiles. *Journal of Coatings Technology and Research*, *17*(2), 531–540. https://doi.org/10.1007/s11998-019-00303-5

Turna, F., Aksakal, S., Vales, G., Creus, A., & Marcos, R. (2014). *Zinc oxide nanoparticles : Genotoxicity , interactions with UV-light and cell-transforming potential*. *264*, 420–429. https://doi.org/10.1016/j.jhazmat.2013.11.043

Uddin, S., Safdar, L. Bin, Anwar, S., Iqbal, J., Laila, S., Abbasi, B. A., Saif, M. S., Ali, M., Rehman, A., Basit, A., Wang, Y., & Quraishi, U. M. (2021). Green synthesis of nickel oxide nanoparticles from berberis balochistanica stem for investigating bioactivities. *Molecules*, *26*(6), 1–14. https://doi.org/10.3390/molecules26061548

Ullah, N., Ansir, R., Muhammad, W., & Jabeen, S. (2019). Mechanistic Approaches and Current Trends in the Green Synthesis of Cobalt Oxide Nanoparticles and their Applications. *Asian Journal of Green Chemistry*, *0*, 340–354. https://doi.org/10.33945/SAMI/AJGC.2019.185995.1158

Urabe, A. A., & Aziz, W. J. (2019). *Biosynthesis of cobalt oxide (Co 3 O 4) nanoparticles using plant extract of Camellia sinensis (L .) Kuntze and Apium graveolens L . as the antibacterial application*. *24*(April), 357–365.

Uribe López, M. C., Alvarez Lemus, M. A., Hidalgo, M. C., López González, R., Quintana Owen, P., Oros-Ruiz, S., Uribe López, S. A., & Acosta, J. (2019). Synthesis and characterization of ZnO-ZrO2 nanocomposites for photocatalytic degradation and mineralization of phenol. *Journal of Nanomaterials*, *2019*.

https://doi.org/10.1155/2019/1015876

Usmani 1, A., Dash 2, P. P., & Mishra 1, A. (2018). Metallic nanoformulations: Green synthetic approach for advanced drug delivery. *Materials Science: Advanced Composite Materials*, *2*(2). https://doi.org/10.18063/msacm.v2i1.729

Üstün, E., Önbaş, S. C., Çelik, S. K., Ayvaz, M. Ç., & Şahin, N. (2022). Green synthesis of iron oxide nanoparticles by using ficus carica leaf extract and its antioxidant activity. *Biointerface Research in Applied Chemistry*, *12*(2), 2108–2116. https://doi.org/10.33263/BRIAC122.21082116

van Beek, J. G. M., Ramdas, W. D., Angi, M., van Rij, C. M., Naus, N. C., Kacperek, A., Errington, R. D., Damato, B., Heimann, H., & Kiliç, E. (2021). Local tumour control and radiation side effects for fractionated stereotactic photon beam radiotherapy compared to proton beam radiotherapy in uveal melanoma. *Radiotherapy and Oncology*, *157*, 219–224. https://doi.org/10.1016/j.radonc.2021.01.030

Van den Bosch, L., van der Schaaf, A., van der Laan, H. P., Hoebers, F. J. P., Wijers, O. B., van den Hoek, J. G. M., Moons, K. G. M., Reitsma, J. B., Steenbakkers, R. J. H. M., Schuit, E., & Langendijk, J. A. (2021). Comprehensive toxicity risk profiling in radiation therapy for head and neck cancer: A new concept for individually optimised treatment. *Radiotherapy and Oncology*, *157*, 147–154. https://doi.org/10.1016/j.radonc.2021.01.024

Vasantharaj, S., Sathiyavimal, S., Saravanan, M., Senthilkumar, P., Gnanasekaran, K., Shanmugavel, M., Manikandan, E., & Pugazhendhi, A. (2019). Synthesis of ecofriendly copper oxide nanoparticles for fabrication over textile fabrics: Characterization of antibacterial activity and dye degradation potential. *Journal of Photochemistry and Photobiology B: Biology*, *191*(December 2018), 143–149. https://doi.org/10.1016/j.jphotobiol.2018.12.026

Veisi, H., Nikseresht, A., Rostami, A., & Hemmati, S. (2019). Fe3O4@PEG core/shell nanoparticles as magnetic nanocatalyst for acetylation of amines and alcohols using ultrasound irradiations under solvent-free conditions. *Research on Chemical Intermediates*, *45*(2), 507–520. https://doi.org/10.1007/s11164-018-3614-7

Venkateswarlu, S., Natesh Kumar, B., Prathima, B., Anitha, K., & Jyothi, N. V. V. (2015). A novel green synthesis of Fe3O4-Ag core shell recyclable nanoparticles using Vitis vinifera stem extract and its enhanced antibacterial performance. *Physica B: Condensed Matter*, *457*, 30–35. https://doi.org/10.1016/j.physb.2014.09.007

Vijaya Kumar, P., Jafar Ahamed, A., & Karthikeyan, M. (2019). Synthesis and characterization of NiO nanoparticles by chemical as well as green routes and their comparisons with respect to cytotoxic effect and toxicity studies in microbial and MCF-7 cancer cell models. *SN Applied Sciences*, *1*(9), 1–15. https://doi.org/10.1007/s42452-019-1113-0

Villalobos-Noriega, J. M. A., Rodríguez-León, E., Rodríguez-Beas, C., Larios-Rodríguez, E., Plascencia-Jatomea, M., Martínez-Higuera, A., Acuña-Campa, H., García-Galaz, A., Mora-Monroy, R., Alvarez-Cirerol, F. J., Rodríguez-Vázquez, B. E., Carillo-Torres, R. C., & Iñiguez-Palomares, R. A. (2021). Au@Ag Core@Shell Nanoparticles Synthesized with Rumex hymenosepalus as Antimicrobial Agent. *Nanoscale Research Letters*, *16*(1). https://doi.org/10.1186/s11671-021-03572-5

Vinardell, M. P., & Mitjans, M. (2015). Antitumor activities of metal oxide nanoparticles. *Nanomaterials*, *5*(2), 1004–1021. https://doi.org/10.3390/nano5021004

Wahab, R., Siddiqui, M. A., Ahmad, J., Saquib, Q., & Al-Khedhairy, A. A. (2021). Cytotoxic and molecular assessment against breast (MCF-7) cancer cells with cobalt oxide nanoballs. *Journal of King Saud University - Science*, *33*(5), 101467. https://doi.org/10.1016/j.jksus.2021.101467

Wang, J., Lee, J. S., Kim, D., & Zhu, L. (2017). Exploration of Zinc Oxide Nanoparticles as a Multitarget and Multifunctional Anticancer Nanomedicine. *ACS Applied Materials and Interfaces*, *9*(46), 39971–39984. https://doi.org/10.1021/acsami.7b11219

Wang, J., Ma, W., & Wang, X. (2021). Insights into the structure of Escherichia coli outer membrane as the target for engineering microbial cell factories. *Microbial Cell Factories*, *20*(1), 1–17. https://doi.org/10.1186/s12934-021-01565-8

Wanjala Wafula, K., Kiambi Mworia, J., & Piero Ngugi, M. (2023). Phytochemical Screening

and In Vitro Evaluation of the Antioxidant Potential of Dichloromethane Extracts of Strychnos henningsii Gilg. and Ficus sycomorus L. *The Scientific World Journal*, *2023*, 1–12. https://doi.org/10.1155/2023/8494176

Wardani, M., Yulizar, Y., Abdullah, I., & Bagus Apriandanu, D. O. (2019). Synthesis of NiO nanoparticles via green route using Ageratum conyzoides L. leaf extract and their catalytic activity. *IOP Conference Series: Materials Science and Engineering*, *509*(1). https://doi.org/10.1088/1757-899X/509/1/012077

Waris, A., Din, M., Ali, A., Afridi, S., Baset, A., Khan, A. U., & Ali, M. (2021). Green fabrication of Co and Co3O4nanoparticles and their biomedical applications: A review. *Open Life Sciences*, *16*(1), 14–30. https://doi.org/10.1515/biol-2021-0003

Widatalla, H. A., Yassin, L. F., Alrasheid, A. A., Rahman Ahmed, S. A., Widdatallah, M. O., Eltilib, S. H., & Mohamed, A. A. (2022). Green synthesis of silver nanoparticles using green tea leaf extract, characterization and evaluation of antimicrobial activity. *Nanoscale Advances*, *4*(3), 911–915. https://doi.org/10.1039/d1na00509j

Wongrakpanich, A., Joiner, M. A., Anderson, M. E., & Salem, A. K. (2014). *Mitochondria-targeting particles*. *9*, 2531–2543.

Wu, D., Wang, W., He, X., Jiang, M., Lai, C., Hu, X., Xi, J., & Wang, M. (2019). Biofabrication of nano copper oxide and its aptamer bioconjugate for delivery of mRNA 29b to lung cancer cells. *Materials Science and Engineering C*, *97*, 827–832. https://doi.org/10.1016/j.msec.2018.12.009

Xia, X., Tu, J., Zhang, Y., Wang, X., Gu, C., Zhao, X. B., & Fan, H. J. (2012). High-quality metal oxide core/shell nanowire arrays on conductive substrates for electrochemical energy storage. *ACS Nano*, *6*(6), 5531–5538. https://doi.org/10.1021/nn301454q

Xiong, H., Xu, Y., Ren, Q., & Xia, Y. (2008). *Stable Aqueous ZnO@Polymer Core-Shell Nanoparticles with Tunable.pdf*. 7522–7523.

Xu, H., Liu, W., Zhao, Y., Wang, D., & Zhao, J. (2019). Ammonia-induced synergistic construction of Co 3 O 4 @CuO microsheets: An efficient electrocatalyst for oxygen

evolution reaction. *Journal of Colloid and Interface Science*, *540*, 585–592. https://doi.org/10.1016/j.jcis.2019.01.066

XU, N. N., ZHANG, Q., GUO, W., LI, Q. T., & XU, J. (2016). Au@PVP Core-Shell Nanoparticles Used as Surface-Enhanced Raman Spectroscopic Substrate to Detect Malachite Green. *Chinese Journal of Analytical Chemistry*, *44*(9), 1378–1384. https://doi.org/10.1016/S1872-2040(16)60956-8

Yagoub, A. E. A., Al-shammari, G. M., Al-harbi, L. N., & Fattiny, S. Z. A. (2022). *applied sciences Antimicrobial Properties of Zinc Oxide Nanoparticles Synthesized from Lavandula pubescens Shoot Methanol Extract*.

Yamauchi, M., Kitamura, Y., Nagano, H., Kawatsu, J., & Gotoh, H. (2024). DPPH Measurements and Structure—Activity Relationship Studies on the Antioxidant Capacity of Phenols. *Antioxidants*, *13*(3). https://doi.org/10.3390/antiox13030309

Yang, Q., Lu, Z., Li, T., Sun, X., & Liu, J. (2014). Hierarchical construction of core-shell metal oxide nanoarrays with ultrahigh areal capacitance. *Nano Energy*, *7*, 170–178. https://doi.org/10.1016/j.nanoen.2014.03.005

Yang, S., & Lian, G. (2020). ROS and diseases: role in metabolism and energy supply. *Molecular and Cellular Biochemistry*, *467*(1–2), 1–12. https://doi.org/10.1007/s11010-019-03667-9

Yilmaz, A., & Yilmaz, M. (2020). Bimetallic core–shell nanoparticles of gold and silver via bioinspired polydopamine layer as surface-enhanced raman spectroscopy (SERS) platform. *Nanomaterials*, *10*(4). https://doi.org/10.3390/nano10040688

Yin, X., Zhi, C., Sun, W., Lv, L. P., & Wang, Y. (2019). Multilayer NiO@Co3O4@graphene quantum dots hollow spheres for high-performance lithium-ion batteries and supercapacitors. *Journal of Materials Chemistry A*, *7*(13), 7800–7814. https://doi.org/10.1039/c8ta11982a

Younis, U., Rahi, A. A., Danish, S., Ali, M. A., Ahmed, N., Datta, R., Fahad, S., Holatko, J., Hammerschmiedt, T., Brtnicky, M., Zarei, T., Baazeem, A., Sabagh, A. E. L., & Glick, B.

R. (2021). Fourier Transform Infrared Spectroscopy vibrational bands study of Spinacia oleracea and Trigonella corniculata under biochar amendment in naturally contaminated soil. *PLoS ONE*, *16*(6 June 2021). https://doi.org/10.1371/journal.pone.0253390

Yugandhar, P., Vasavi, T., Uma Maheswari Devi, P., & Savithramma, N. (2017). Bioinspired green synthesis of copper oxide nanoparticles from Syzygium alternifolium (Wt.) Walp: characterization and evaluation of its synergistic antimicrobial and anticancer activity. *Applied Nanoscience (Switzerland)*, *7*(7), 417–427. https://doi.org/10.1007/s13204-017-0584-9

Zhang, L., Feng, Q., Nie, A., Liu, J., Wang, H., & Fang, Y. (2014). In situ study of thermal stability of copper oxide nanowires at anaerobic environment. *Journal of Nanomaterials*, *2014*. https://doi.org/10.1155/2014/670849

Zhang, L., Li, H., Yang, B., Zhou, Y., Zhang, Z., & Wang, Y. (2019). Photo-deposition of ZnO/Co3O4 core-shell nanorods with p-n junction for efficient oxygen evolution reaction. *Journal of Solid State Electrochemistry*, *23*(12), 3287–3297. https://doi.org/10.1007/s10008-019-04444-w

Zhao, X., Wang, P., & Li, B. (2010). CuO/ZnO core/shell heterostructure nanowire arrays: Synthesis, optical property, and energy application. *Chemical Communications*, *46*(36), 6768–6770. https://doi.org/10.1039/c0cc01610a

Zhu, L., Hao, C., Zhou, S., Wang, X., Zhou, T., & Guo, Y. (2021). Ternary ZnO/Co3O4/NiO inherited layered core-shell structure from a double template for high performanced supercapacitor. *Journal of Materiomics*, *7*(4), 708–720. https://doi.org/10.1016/j.jmat.2021.01.003

Zubair, M., Wang, S., & Ali, N. (2021). Advanced Approaches to Breast Cancer Classification and Diagnosis. *Frontiers in Pharmacology*, *11*(February), 1–24. https://doi.org/10.3389/fphar.2020.632079

RESEARCH WORK

Research articles

1. Gezahegn Tadesse, Tegene Desalegn, HC Ananda Murthy, CR Ravikumar, T Naveen Kumar, Lema Teshome (2023). *In Situ* Green Synthesis of Co_3O_4@ZnO Core-Shell Nanoparticles Using *Datura stramonium* Leaf Extract: Antibacterial and Antioxidant Studies. *Bioinorganic Chemistry and Applications*, 2023(18), Hindawi. (Impact factor = 3.8, Q1 Journal, Scopus and SCIE indexed). https://doi.org/10.1155/2023/5019838
2. Gezahegn Tadesse, Tegene Desalegn, H. C. Ananda Murthy, C. R. Ravikumar, T. Naveen Kumar, Lemma Teshome. Phyto-mediated Green Synthesis and Characterization of Co_3O_4 and ZnO Nanoparticles for Antibacterial Performance Applications. *Journal of Nanostructures, Iranian.* (Impact factor = 1.8, Q2, Journal, Scopus and SCIE indexed).
   - **Accepted**
3. In-vitro Anti-cancer (MCF-7 breast cancer cell line) and Antioxidant Activity of Biogenically Synthesized Co_3O_4@NiO Core-shell Nanostructures. Journal of Nanomedicine, *Iranian*, (Impact factor = 1.5, Q2, Journal, Scopus and SCIE indexed).
   - **Accepted**

APPENDIX
Mass Calculation

To synthesize MONPs, 0.5 M of $Co(CH_3CO_2)_2 \cdot 6H_2O$, $Zn(CH_3CO_2)_2 \cdot 2H_2O$, $Ni(CH_3CO_2)_2 \cdot 2H_2O$, and $Cu(CH_3CO_2)_2\ 2H_2O$ precursor salt were used for their respective nanoparticles. The mass of $Co(CH_3CO_2)_2 \cdot 6H_2O$, 0.5 M solution in 100 mL, was calculated in these steps.

- Mole determination

  Molarity (c) $= \frac{moles\ of\ solute\ (n)}{liters\ of\ solution\ (v)}$

  $n = cv$

  n=0.5 M x 0.1 L= 0.05 moles

- Molar mass of $Co(CH_3CO_2)_2 \cdot 6H_2O$

  Cobalt (Co): 58.93 g/mol

  Carbon (C): 12.01 g/mol (4C in $2CH_3CO_2$)

  Hydrogen (H): 1.01 g/mol (6H in $2CH_3CO_2$ + 12H in $6H_2O$)

  Oxygen (O): 16.00 g/mol (4O in $2CH_3CO_2$ + 6O in $6H_2O$)

Molar mass = 58.93 + (4 x 12.01) + (10 x 1.01) + (10 × 16.00)

=58.93 + 48.04 + 10.10 + 160.00

= 277.07 g/mol

- mass=moles x molar mass

  mass=0.05 moles x 277.07 g/mol

  =13.85 g

Therefore, 13.85 g of $Co(CH_3CO_2)_2 \cdot 6H_2O$ was utilized for Co_3O_4 NPs synthesized in (1:1), (1:2), and (2:1) volume ratios. Similarly, 7.78, 7.44, and 7.68 g of $Zn(CH_3CO_2)_2 \cdot 2H_2O$, $Ni(CH_3CO_2)_2 \cdot 2H_2O$, and $Cu(CH_3CO_2)_2\ 2H_2O$ precursor salt, respectively were used to synthesize their respective NPs.

The lattice parameters of the crystal structure investigated from XRD were calculated using the equation mentioned in this section.

Cubic structure:

$$\frac{1}{d^2} = \frac{h^2 + k^2 + l^2}{a^2} \quad \text{.....(5)}$$

Hexagonal structure:

$$\frac{1}{d^2} = \frac{4(h^2 + hk + k^2)}{3a^2} + \frac{l^2}{c^2} \quad \text{.....(6)}$$

Monoclinic structure:

$$\frac{1}{d^2{}_{hkl}} = \left(\frac{h^2}{a^2} + \frac{k^2 sin^2\beta}{b^2} + \frac{l^2}{c^2} - \frac{2hlcos\beta}{ac}\right) csc^2\beta \quad \text{.....(7)}$$

The particle size were determined from TEM and SEM images by using ImageJ. In the analysis, the xc value is calculated by using equation (12).

$$Y = y0 + A/(w\sqrt{(\pi/(4\ln(2)))}) \exp(-4\ln(2)(x - xc)^2 2/w^2) \qquad (8)$$

Where $y0$ is offset, xc is the center of size distribution, w is the width of the curve, and A is the amplitude of the curve.